Study on hydrogen storage performance of as-milled Ti-V-Cr-Fe-Mn high entropy alloys

A thesis submitted in fulfilment
of the requirements for the degree
of
Doctor of Philosophy in Materials and Processing Engineering
At
The University of Waikato
By

Yutao Zhai

THE UNIVERSITY OF
WAIKATO
Te Whare Wānanga o Waikato

2025

Chief Supervisor: Professor Fei Yang

Co-Supervisor: Associate Professor Leandro Bolzoni

Dr. John Kennedy

Dr. Ajit Pal Singh

Abstract

This study aims to fabricate and optimize BCC-based high-entropy hydrogen storage alloys through mechanical alloying. The research systematically investigates the effects of processing parameters (including milling time, ball-to-powder ratio, rotation speed, and process control agent (PCA) addition), alloy composition, and heat treatment on the phase structure, thermodynamic stability, and hydrogen storage performance of the fabricated alloys. Furthermore, the study compares the microstructure and hydrogen storage properties of alloys fabricated by different methods (mechanical alloying and arc melting).

Firstly, the study optimizes the mechanical alloying parameters, revealing the critical roles of milling time, ball-to-powder ratio, and rotation speed in forming BCC structures and nanocrystalline grains in Ti-V-Cr-Mn-Fe alloys. The regulatory effects of PCA addition on powder yield and particle size are also analyzed. Subsequently, the impact of composition on hydrogen storage properties, including hydrogen absorption/desorption kinetics, thermodynamic behavior, and cycling stability, are explored by varying the Ti content and Mn/Cr ratios. It is found that increasing Ti content enhances the proportion of C14 Laves phases, while increasing Mn content effectively suppresses Laves phase formation, thereby increasing the BCC phase fraction and improving hydrogen storage kinetics.

Additionally, the role of heat treatment is examined. Microstructural evolution analysis reveals the phase transformation behavior among BCC, FCC, and Laves phases under different heat treatment conditions and their effects on hydrogen storage capacity. Specifically, as the temperature increases, the BCC structure first decomposes into a BCC + FCC dual-phase structure, followed by the precipitation of the Laves-2 phase within the FCC phase. After high-temperature treatment, the lattice constant of the BCC phase decreases, and the synergistic effect of the Laves and FCC phases results in a slight reduction in the hydrogen absorption and desorption capacity of the alloy. Finally, by comparing different fabricating process, the differences in microstructure and hydrogen storage performance of $Ti_{25}V_{35}(CrMnFe)_{40}$ alloys prepared by these methods are investigated. The results suggested that Mechanical alloying

significantly enhances initial the activation performance and hydrogen absorption kinetics of the as-milled alloys are improved compared to the counterparts of as-cast alloys.

Acknowledgments

As my doctoral journey draws to a close, I find myself reflecting on the challenges, choices, and growth that have defined this path. Each step bears the marks of effort, and every milestone is inseparable from the support of those around me. With profound gratitude, I extend my heartfelt thanks to everyone who has offered me help, encouragement, and strength throughout this journey.

First and foremost, I would like to express my deepest gratitude to my parents and grandmother. You have been my greatest source of support. From my childhood to adulthood, your unconditional love and infinite patience have been the foundation of my pursuits, both academic and personal. Your encouragement has given me the courage to forge ahead, no matter the challenges. During my years abroad, your care and thoughtful words provided warmth and strength, even in the most difficult times. I also want to pay my deepest respects to the memory of my late grandfather, grandmother, and grandfather. Although you could not witness my achievements today, the love and teachings you imparted to me have become an irreplaceable spiritual pillar in my life. Whenever I face tough decisions or challenges, I think of your guidance, which has consistently renewed my confidence and determination to move forward.

I would like to extend my sincere gratitude to my advisor, Professor Fei Yang. Over the past seven years, from my undergraduate studies to my master's and doctoral research, your guidance has not only enriched my academic knowledge but also taught me how to face challenges and make decisions. Your patience and trust have transformed me from a confused undergraduate into a researcher capable of independent thought and exploration. During these seven years, you have been more than just my academic mentor; you have been a guide and friend in life. Your support during my studies abroad made me feel a sense of belonging, which was a vital source of motivation that kept me going through this long journey. Without your guidance and support, I would not be who I am today. Being your student has been an immense

honor and privilege.

I would also like to express my gratitude to Dr. Yiming Li. During my experimental work in China, your support and assistance were invaluable, especially during the experiments conducted at the School of Rare Earths. Your professional guidance and meticulous coordination of experimental equipment ensured the smooth progress of my research. Your patience and attention to detail enabled me to gain a deeper understanding of experimental procedures in a short period.

The three years of the pandemic made this journey particularly challenging. The prolonged inability to return home often left me feeling lonely and helpless. Yet, in this solitude, I learned how to engage in self-reflection and how to face pressure and challenges with greater resilience. These years honed my perseverance and deepened my appreciation for family and companionship. Looking back, these three years not only fostered my academic growth but also brought unprecedented inner strength and development.

I am deeply grateful to my senior peers and colleagues who have supported and accompanied me along the way: Senior brothers Qin-Yang Zhao, Lei Lei, Ying-Chao Guo, Qi-Wen Zhou, Run-Qi Zhang as well as my friends and fellow students: Hao Liu ,Zhuang Li, Jing-Nan Ma, Pan Gao, Zi-Yao Fan, Shan Zhou, Ya-Qi Chang, Qing-He Zheng, Jun-Qi Liu, Xin Hu, and Ze-Min Li, among others. While I cannot list everyone individually, your help and encouragement have made my academic journey less lonely. Late-night discussions, teamwork in the lab, and encouragement after setbacks—all these memories have made my academic journey warmer and more fulfilling.

The doctoral journey has taught me the hardship and beauty of growth. From being an ordinary student to standing at the threshold of earning a doctoral degree, this path has been filled with choices, perseverance, and challenges. None of this would have been possible without the help

and support of those around me. Today marks not only the conclusion of this journey but also the beginning of a new chapter in my life. As I leave behind my identity as a student, I will embrace the unknown challenges and opportunities ahead with greater maturity and resilience. I believe the future will be even more exciting, and I hope to always carry a heart full of gratitude, using what I have learned to contribute to society and to continue striving for my dreams.

Finally, with this acknowledgment, I once again extend my sincerest thanks to everyone who has helped, supported, encouraged, or even challenged me along the way!

Table of content

List of figures

List of tables

List of publications

Publications related to PhD research:

1. ***Y.T. Zhai***, Y.M. Li, L. Bolzoni, J. Kennedy, ***F. Yang***, Effect of heat treatment on microstructural evolution and hydrogen storage performance of as-milled $Ti_{5+x}V_{35}(CrMnFe)_{60-x}$ (x=0, 10, 20, 30) high-entropy alloys, International Journal of Hydrogen Energy, Volume 81, 2024, Pages584-594. (**IF: 8.3**) https://doi.org/10.1016/j.ijhydene.2024.07.298.
2. ***Y.T. Zhai***, Y. M. Li, S. H. Wei, I. Tolj, J. Kennedy, ***F. Yang***, Progress in V-BCC Based Solid Solution Hydrogen Storage Alloys, Journal of Energy Storage, Volume 109, 2025, 115103. (**IF: 9.8**) https://doi.org/10.1016/j.est.2024.115103.
3. ***Y.T. Zhai***, Y.M. Li, Z.C. Liu, L. Bolzoni, J. Kennedy, ***F. Yang***, Hydrogen ab/desorption behavior of the mechanical alloyed Ti-V-Cr-Mn-Fe HEAs with varying Mn/Cr ratio, International Journal of Hydrogen Energy, Volume 109, 2025, Pages 1008-1022. (**IF: 8.3**) https://doi.org/10.1016/j.ijhydene.2025.02.139.
4. ***Y.T. Zhai***, Y. M. Li, S. H. Wei, I. Tolj, J. Kennedy, ***F. Yang***, Investigation of different fabrication methods on the phase structure, thermal stability, and hydrogen storage kinetic performance of $Ti_{25}V_{35}(CrMnFe)_{40}$ high entropy alloy, International Journal of Hydrogen Energy, Preparation (**IF: 8.3**)

Other publications during the PhD research:

1. ***Y. T. Zhai,*** A. P. Singh, L. Bolzoni, Y. D. Qu, Y. M. Li, F. Yang, Direct fabrication of titanium matrix composites from the recycled Ti-6Al-4V swarf using a rapid hot-pressing approach, Metals 2022, 12(12), 2038. **(IF: 2.9)** https://doi.org/10.3390/met12122038.

2. X. Dong, ***Y.T. Zhai***, Z. C. Liu, Y.Z. Li, G. F. Zhang, Y. P. Ji, ***F. Yang***, Y.M. Li, Poisoning effect of CO on hydrogen storage cycling stability of Mg80Ni16-xAlxY4 (x=2, 4, 8) alloys, International Journal of Hydrogen Energy. **(IF: 8.3)** https://doi.org/10.1016/j.ijhydene.2025.04.172.
3. Dong, X.; Li, Y.***;*** ***Zhai***, ***Y***.; Liu, Z.; Zhang, G.; ***Yang, F***. Study on Microstructure and Hydrogen Storage Properties of Mg80Ni16−xAlxY4 (x = 2, 4, 8) Alloys. Metals 2024, 14, 126. **(IF: 2.9)** https://doi.org/10.3390/met14010126.
4. Qiwen Zhou, Guanglong Li, Yingdong Qu, Shan Zhou, Zimu Wang, Yu Zhao, ***Yutao Zhai***, Rongde Li, ***Fei Yang***, Improvement of thermophysical and machinability properties of Al matrix composites with CFs-D hybrid reinforcement, Materials Characterization ,209,2024,113725. **(IF:5.5)** https://doi.org/10.1016/j.matchar.2024.113725.

Contributions to international conferences:

1. ***Y. T. Zhai***, J. Kennedy, ***F. Yang***, Study on hydrogen storage performance of as-milled Ti-V-Cr-Mn-Fe high entropy alloys, 3rd New Zealand Hydrogen Symposium 2025, Christchurch, New Zealand, ***Poster***.
2. ***Y. T. Zhai***, Y. M. Li, J. Kennedy, ***F. Yang***, Effect of Mechanical Alloying on Phase Synthesis and Hydrogen Absorption/ Desorption Behavior of TiVCrMnFe Alloys, 2nd New Zealand Hydrogen Symposium 2024, Wellington, New Zealand, ***Poster***.
3. ***Y. T. Zhai, F. Yang***, Turning waste to useful: Cost-effective titanium matrix composites produced from recycled Ti-6Al-4V swarf using rapid hot-pressing approach, 2nd Engineering Innovation Cooperation Forum & International Conference on New Energy and Advanced Materials, 2021, Shijing Zhuang, China, **Oral presentation**

1. Introduction

The global warming crisis has become the most significant issue affecting human survival [1-3]. Coal, oil, natural gas, and other fossil fuels are on the brink of depletion. It is imperative to develop clean, renewable, and non-polluting energy sources [4, 5]. Hydrogen, the most abundant energy source in nature, holds promise as the ideal new energy source of the 21st century [6-8]. However, ensuring the safe and efficient storage and transportation of hydrogen is a key challenge in advancing hydrogen energy applications. The primary forms of hydrogen storage include liquid hydrogen storage [9, 10], compressed hydrogen storage [11, 12], and hydrogen storage alloys [13-16], with hydrogen storage alloys emerging as a research hotspot in the field of hydrogen storage due to their high hydrogen storage density and small volume [17, 18]. The development of multi-component hydrogen storage alloys has emerged as a mainstream approach, primarily due to the greater compositional design flexibility offered by multi-component alloys compared to traditional binary alloys, which are limited by adjustments through microalloying [19-22]. Serving as a representative of multi-component alloys, high-entropy alloys not only possess significant compositional design space but also exhibit lattice distortions arising from differences in the sizes of constituent elements, which may provide additional storage sites for hydrogen atoms [23-26]. Therefore, high-entropy hydrogen storage alloys are poised to become the most promising hydrogen storage alloys in the future.

High entropy alloys (HEAs), also known as multi principal element alloys (MPEAs), were first introduced by Yeh et al. [18] in 2004. Unlike traditional alloys, they typically consist of five or more elements, each comprising between 5 at% and 35 at%. The mixture of multiple principal elements increases the configurational entropy, favoring the formation of a disordered single phase solid solution [27]. As an emerging class of alloys, high-entropy alloys (HEAs) have attracted increasing attention from the materials science community due to their unique

physical, chemical, and mechanical properties, particularly in the field of hydrogen storage [28]. High-entropy alloy hydrogen storage materials mainly include BCC base solid solution and Laves base solid solution. Sahlberg et al. [23] first discovered the hydrogen storage capacity of TiVZrNbHf high-entropy alloys, and found that the TiVZrNbHf equimolar alloy exists in a single phase BCC structure. The alloy absorbs 2.7 wt% H_2 at 300 °C, reaching H/M = 2.5, it is higher than traditional V (BCC) -based hydrogen storage alloys (H/M=2) [19, 29]. The lattice transformation from BCC → body-centered tetragonal (BCT) → FCC during hydrogenation of this alloy is the same as the typical lattice transformation behavior of conventional V-based alloys [14, 17, 30]. On the other hand, due to the large atomic radius different of the alloy (δ = 6.82%), it is favorable for hydrogen to occupy the octahedral interstitial sites, which may be the driving force for opening new interstitial sites for hydrogen. The Laves phase high entropy alloy system is another widely studied high-entropy hydrogen storage alloy, and the maximum hydrogen storage capacity (1.8 wt%) of the alloy is similar to traditional AB_2 type ($TiCr_2$ [31], $ZrMn_2$ [32]) hydrogen storage alloy. Compared with BCC high entropy alloy, Laves high entropy alloys have better hydrogen storage kinetics performance [33], easier activation [34] and longer cycle life [35]. However, due to the more complex and densely packed crystal structure of Laves phases compared to BCC structures, they exhibit lower hydrogen storage capacity [32, 36].

Currently, the fabrication of hydrogen storage alloys primarily relies on melting processes, where various metal elements are combined at high temperatures to produce the desired alloy [28, 37-40]. However, studies exploring the effects of different preparation methods on the microstructure and performance of hydrogen storage alloys remain limited, especially regarding mechanical alloying (ball milling) [28, 40]. Mechanical alloying, as a solid-state powder metallurgy technique [41], offers several distinct advantages: it enables uniform mixing of multiple elements at relatively low temperatures [42, 43], thereby minimizing issues like elemental evaporation and compositional segregation typically encountered in high-temperature melting processes [44]. Furthermore, by adjusting ball milling parameters, the

technique allows for control over particle size, phase composition, and microstructure, and it can produce nanocrystalline or amorphous materials [45, 46], opening new possibilities for enhancing hydrogen storage performance. HEAs have garnered significant attention in the field of hydrogen storage due to their unique structures and exceptional properties. However, current research has primarily focused on their hydrogen storage capacity, while systematic studies on the microstructural evolution during hydrogenation, alloy composition optimization, and the effects of different processing conditions on phase stability and transformation mechanisms remain insufficient. Therefore, in this research, mechanical alloying is employed to fabricate high-entropy hydrogen storage alloy samples, with a focus on systematically investigating the effects of ball milling parameters on the alloy's phase composition and microstructure. Additionally, the hydrogen storage performance of mechanically alloyed samples subjected to various heat treatments is extensively examined. To broaden the understanding, a comparative analysis between mechanically alloyed samples and arc-melting is conducted. This research aims to provide new insights for optimizing hydrogen storage alloy fabrication techniques and enhancing their hydrogen storage performance.

2. Literature Review

The structural characteristics and fabrication methods of hydrogen storage alloys significantly influence their hydrogen absorption/desorption performance. To thoroughly investigate the hydrogen storage performance of high-entropy alloys (HEAs) and other hydrogen storage materials, this chapter first systematically reviews the fundamental principles, thermodynamic, and kinetic characteristics of hydrogen storage process. By summarizing various alloy types, including AB_5, AB_2, AB, A_2B, and BCC solid solutions, a foundational understanding of the potential applications of different hydrogen storage alloys is established. Additionally, the key factors affecting hydrogen storage performance, such as phase composition, lattice constants, and lattice distortion, are examined to further elucidate how the microstructure of materials influences hydrogen absorption/desorption behavior.

Moreover, this chapter provides an in-depth analysis of the unique characteristics and design principles of HEAs, with a particular focus on their advantages in hydrogen storage applications. Finally, the chapter discusses the primary fabrication methods for HEAs, including vacuum arc melting, vacuum induction melting, selective laser melting, and mechanical ball milling. This literature review provides theoretical support and reference for the subsequent experimental design and materials characterization, contributing to a more comprehensive understanding of the hydrogen absorption/desorption mechanisms and optimization pathways for HEAs and other hydrogen storage materials.

Partial contents in this chapter have been published in journal:

Y.T. Zhai, Y. M. Li, S. H. Wei, I. Tolj, J. Kennedy, ***F. Yang***, Progress in V-BCC Based Solid Solution Hydrogen Storage Alloys, Journal of Energy Storage, Volume 109, 2025, 115103. https://doi.org/10.1016/j.est.2024.115103.

2.1 Principle of hydrogen absorption/desorption

In the periodic table, nearly all A-side metal elements can react with hydrogen to form hydrides. However, not all hydrides are suitable for hydrogen storage. Only hydrides that can absorb and desorb significant amounts of hydrogen under mild conditions can be used as hydrogen storage materials [47, 48]. Figure 2.1 illustrates the schematic process of hydrogen absorption and desorption in alloys. Taking the hydrogen absorption process as an example, it involves the following steps: (1) Surface/interface control stage (surface activation stage), hydrogen molecules dissociate into hydrogen atoms, which are adsorbed onto the alloy surface [49]; (2) Nucleation and growth of initial hydrides, this step is accompanied by lattice expansion as the hydride forms [50]; (3) hydrogen atom diffusion, hydrogen atoms diffuse into the alloy until the maximum hydrogen capacity is reached [51]. Beyond this point, even if the external hydrogen pressure continues to increase, the hydride concentration (wt%) remains largely unchanged, marking the end of the absorption process. Upon reducing the external hydrogen pressure or increasing the temperature, the metal hydride gradually decomposes. Hydrogen atoms diffuse to the surface, recombine into hydrogen molecules, and are released from the alloy[52]. Overall, the hydrogen absorption/desorption process in hydrogen storage alloys is reversible.

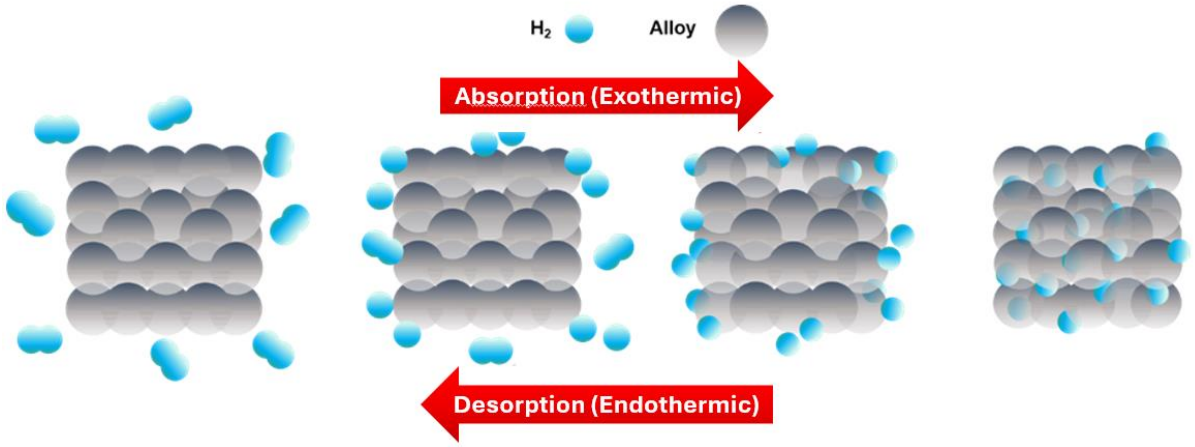

Fig. 2.1. Schematic model of hydrogen absorption/desorption processing of hydrogen storage alloys

2.2 Thermodynamics of hydrogen absorption/desorption

The study of the thermodynamic properties of hydrogen storage alloys primarily focuses on the enthalpy of formation ($\triangle$H) of metal hydrides. As seen from Fig 2.1, the hydrogen absorption/desorption process involves both exothermic and endothermic reactions. Specifically, the forward reaction (hydrogenation) is exothermic, whereas the reverse reaction (dehydrogenation) is endothermic. By examining the relationship between Gibbs free energy and other thermodynamic parameters, the following expression can be derived [53-55]:

$$\triangle \boldsymbol{G} = \triangle \boldsymbol{H} - \boldsymbol{T} * \triangle \boldsymbol{S} \quad \textbf{(2-1)}$$

$$\triangle \boldsymbol{G} = -\boldsymbol{R} * \boldsymbol{T} * \boldsymbol{lnK_p} \quad \textbf{(2-2)}$$

Through the integration of formula **(2-1)** and formula **(2-2)**, the following formula can be obtained:

$$\boldsymbol{lnP_{H2}} = \frac{\triangle \boldsymbol{H}}{\boldsymbol{RT}} - \frac{\triangle \boldsymbol{S}}{\boldsymbol{R}} \quad \textbf{(2-3)}$$

In the formula, $\triangle \boldsymbol{H}$is the enthalpy of formation of the metal hydride; $\triangle \boldsymbol{S}$ is the entropy; $\boldsymbol{R}$ (8.314J/(mol·K)) is the gas constant; $\boldsymbol{P_{H2}}$ is hydrogen pressure; $\boldsymbol{T}$ is temperature in Kelvin (K). Using formula (2-8), the relationship between $\boldsymbol{lnP_{H2}}$ and $\frac{\boldsymbol{1}}{\boldsymbol{T}}$ is Van't Hoff curve (Fig.2.2).

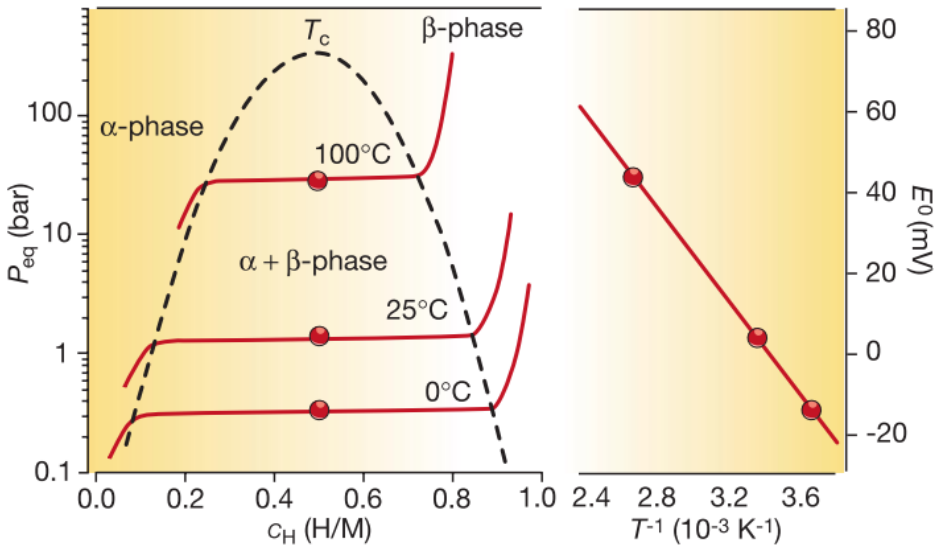

Fig. 2.2 Pressure–concentration–temperature (PCT) plot and a Van't Hoff curve [56]

Thermodynamic parameters provide insight into the ease with which an alloy absorbs and desorbs hydrogen. A higher enthalpy of formation (△H) indicates greater stability of the metal hydride, making the hydrogenation reaction more difficult. Conversely, a lower enthalpy of formation corresponds to reduced thermal stability of the metal hydride, resulting in improved hydrogen absorption and desorption performance of the hydrogen storage alloy. The entropy of formation (△S) reflects the stability of the metal hydride system, while Gibbs free energy (△G) indicates the spontaneity of the hydrogen absorption/desorption reaction in the hydrogen storage alloy.

In the quantitative study of the thermodynamic properties of hydrogen storage materials, PCT curves at different temperatures are used to establish a logarithmic relationship between equilibrium hydrogen pressure and temperature (the relationship between and 1/T). This relationship should result in a straight line, as shown on the right side of Fig 2.2. From this relationship, the slope and intercept of the line can be obtained, allowing for the calculation of the thermodynamic parameters for the hydrogen absorption process (ΔG_a, ΔH_a, ΔS_a) and for the desorption process (ΔG_d, ΔH_d ΔS_d). Additionally, this curve provides a direct and intuitive reflection of the properties of the hydride. The magnitude of the enthalpy of formation is

directly related to the plateau pressure in the PCT curves for hydrogen absorption and desorption: a larger enthalpy of formation corresponds to a higher plateau pressure, which favors hydrogen desorption but hinders absorption. Conversely, a smaller enthalpy of formation leads to a lower plateau pressure, facilitating hydrogen absorption but hindering desorption.

2.3 Kinetics of hydrogen absorption/desorption

The hydrogen absorption/desorption kinetics of hydrogen storage materials is a key physical quantity that measures the rate of hydrogen absorption and desorption, making it an important indicator for assessing the practical application potential of these materials. The hydrogen absorption reaction in alloys is essentially a chemical reaction between a solid phase and a gas phase, which can be divided into three main stages (as mentioned in Section 2.1). Studies on the kinetics of hydrogen storage materials often focus on how factors such as material composition [57], preparation methods [58], and the addition of catalysts [59] influence the rate of hydrogenation and dehydrogenation reactions. However, the kinetic performance of hydrogen storage alloys is influenced not only by the phase composition and intrinsic (lattice constant, electronegativity etc.) feature of the alloy but also by external factors such as hydrogen pressure, ambient temperature, and particle size. Generally, a higher instantaneous pressure, higher ambient temperature, and smaller particle size lead to faster hydrogen absorption and desorption rates [60]. However, these factors also interact with each other. For example, during the hydrogen absorption process, excessively high temperatures can increase the absorption plateau pressure of the alloy, reducing the difference between the ambient pressure and the plateau pressure. This decrease in pressure differential reduces the driving force for hydrogen absorption, ultimately slowing down the absorption rate [61]. The kinetic models of hydrogen storage materials during the hydrogen absorption/desorption process can be categorized into several types, as summarized in Table 2-1. Different models can be selected to analyze the kinetic mechanisms of hydrogen absorption and desorption based on the specific characteristics of each material.

Table 2.1 The solid–gas reaction models for the hydrogen absorption/ desorption in the hydrogen storage alloy [62-65]

Reaction models	Formulas
Chemisorption (surface reaction)	$-ln(1-\alpha) = kt$
Johnson-Mehl-Avrami (nucleation and growth)	$\alpha = 1 - expk(-kt)^{\eta}$
Contracting Volume (geometrical contraction)	$1-(1-\alpha)^{1/2} = kt$ $1-(1-\alpha)^{1/3} = kt$
Ginstiling-Brounshtein (geometrical contraction)	$1-\left(\frac{2\alpha}{3}\right)-(1-\alpha)^{\frac{1}{3}} = kt$

PS: t = time; α = reaction fraction; k is the reaction rate constant; η is the Avrami exponent.

For most hydrogen storage materials, the hydrogen absorption and desorption processes are most commonly and widely described using the nucleation and growth kinetic mechanism, known as the JMAK model, which is also the most recognized model in this field. The following section provides a detailed explanation of the principles of this model and its specific application. The specific expression of the JMAK model is as follows:

$$\alpha = 1 - expk(-kt)^{\eta} \quad \textbf{(2-4)}$$

Taking the logarithm of both sides' yields:

$$ln[-ln\,(1-\alpha)] = \eta lnk + \eta lnt \quad \textbf{(2-5)}$$

Where k is the rate constant of the hydrogenation/dehydrogenation reaction, α represents the fraction of hydrogen absorbed by the material at time t, and η defines the ***Avrami exponent*** of the model. From equation **(2-5)**, a linear relationship between $ln[-ln\,(1-\alpha)]$ and lnt can be established. The slope of this line gives the value of η, while the intercept can be used to calculate the rate constant k. It is well known that hydrogen storage materials must overcome

a certain energy barrier for hydrogenation/dehydrogenation to occur. This energy barrier, known as the activation energy (E_a), can be determined using the Arrhenius equation (equation 2-6) [66]:

$$k = Ae^{-Ea/RT} \quad \textbf{(2-6)}$$

Taking the logarithm of equation **(2-7)** gives:

$$lnk = -\frac{E_a}{RT} + ln\,A \quad \textbf{(2-7)}$$

It is clear that lnk has a linear relationship with $1/T$, with a slope of E_a/R. By calculating the rate constant k at different temperatures using equation **(2-5)**, and plotting the lnk versus $1/T$ curve using equation **(2-7)**, a linear fit can be performed to determine the activation energy E_a. The E_a is an explanation of the changes in the kinetic behavior of hydrogen absorption/desorption mechanisms from the perspective of activation energy.

2.3 Classification of hydrogen storage alloys

Hydrogen storage alloys, particularly those based on intermetallic compounds, are effective, safe, and efficient materials for hydrogen storage. To date, the main types of hydrogen storage alloys that have been developed and studied include: AB_5 type (rare earth hydrogen storage alloys), AB_2 type (Laves phase hydrogen storage alloys), AB type (titanium-based hydrogen storage alloys), A_2B type (magnesium-based hydrogen storage alloys), AB_2 type (with Laves structure), solid solution alloys (with BCC structure), and high-entropy alloys.

2.3.1 AB_5 type (rare earth hydrogen storage alloys)

In AB_5 type rare earth hydrogen storage alloys, A elements typically refers to rare earth elements [67-70], while B elements denotes transition metals [71-73]. $LaNi_5$, a well-known typical example of this alloy type, features a $CaCu_5$ type crystal structure with six tetrahedral

sites and belongs to the space group P6/mmm. It was first discovered by the Dutch Philips laboratory. The theoretical hydrogen storage capacity of $LaNi_5$ is 1.4 wt%, and the enthalpy of hydride decomposition is 30 kJ/mol H_2 [74].

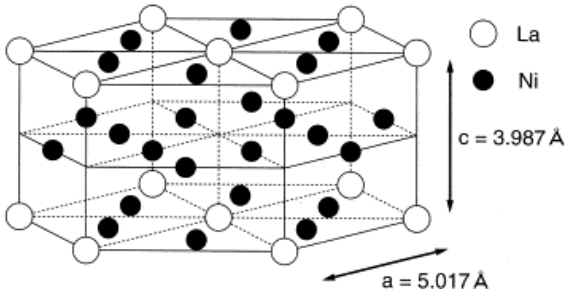

Fig. 2.3 The crystal structure of $LaNi_5$ with the hexagonal $CaCu_5$ structure [70]

$LaNi_5$ exhibits an easy activation process, moderate hydrogen absorption/desorption plateau pressure, and low hysteresis during hydrogen absorption/desorption [70, 74]. However, the alloy is prone to pulverization due to significant lattice expansion (23 vol%) after hydrogen absorption, caused by its small lattice gaps [74]. To improve hydrogen absorption/desorption capacity and resistance to pulverization, researchers often substitute elements on the A and B sites. For example, Liu et al. [67] fabricated a series of $LaNi_{5-x}Al_x$ (x = 0, 0.25, 0.5, 0.75, 1) hydrogen storage alloys via arc melting and investigated the effect of substituting Ni with Al on hydrogen storage performance. The results showed that as the Al content increased, the stability of the metal hydride improved and the plateau pressure decreased due to the expansion of the unit cell (lattice constant). However, the substitution of Al for Ni reduced the number of available interstitial sites in $LaNi_{5-x}Al_x$, leading to a decrease in the maximum hydrogen storage capacity. Additionally, due to the high cost of La, some researchers have substituted pure La with Ce or La (Mm) mixed rare earth elements to reduce alloy costs. Studies have demonstrated that mixed rare earth (Mm) hydrogen storage alloys exhibit hydrogen storage properties comparable to those of $LaNi_5$ [75-79].

2.3.2 AB_2 type (Laves structure hydrogen storage alloys)

AB_2 type hydrogen storage alloys possess a Laves structure (with seven tetrahedral sites), which in most conditions exist in two forms: the hexagonal close-packed C14 structure and the face-centered cubic C15 structure show in Fig 2.4 [80, 81]. The A site is typically occupied by elements with relatively large atomic radii, such as Ti [82] and Zr [83], while the B site consists of smaller transition metals like Mn, Ni, and Cr. The atomic radius ratio between A and B elements (r_A/r_B) generally falls between 1.1 and 1.6 [84]. In 1966, Pebler et al. [85] were the first to investigate binary Zr-based Laves-phase alloys as potential hydrogen storage materials. AB_2 type hydrogen storage alloys that have shown promise for practical applications include $TiCr_2$ [31, 86], $TiMn_2$ [87], $ZrCr_2$ [83], and $ZrMn_2$ [32], among others. These alloys are characterized by high hydrogen storage capacities (1.8 wt% to 2.4 wt%), ease of activation, and favorable kinetic properties. However, the hydrides formed by these alloys are often overly stable, making hydrogen release difficult. The researchers began to modify binary Laves structure alloys by substituting multiple elements on both the A and B sites to tailor the properties of the alloys [88-90]. Liu et al. [91] explored the effects of replacing Mn with Cr, V, Cu, Ni, and Fe in Ti-Zr-Mn-V-Cr-based alloys. The study found that Cr reduced hydrogen absorption hysteresis, V lowered the plateau pressure without compromising hydrogen storage capacity, and Cu decreased the slope of the plateau pressure. These findings demonstrate that multi-element alloying is an important and effective strategy for improving the hydrogen storage performance of AB_2 type alloys.

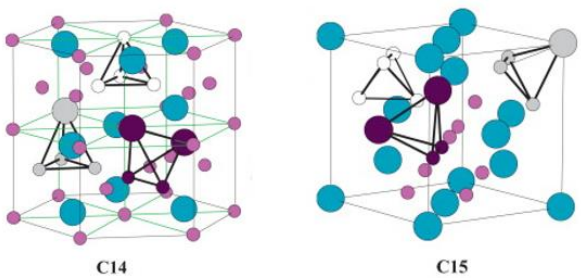

Fig. 2.4 Different tetrahedral interstitial sites in C14 (hexagonal) and C15 (cubic) Laves structure [81]

2.3.3 AB type (titanium based hydrogen storage alloys)

AB type (titanium based) hydrogen storage alloys primarily include TiFe [92], TiCo [93], TiNi [94], and multi-element alloys in which other elements partially substitute the A or B site. The most representative AB type hydrogen storage alloy is TiFe, which was first discovered by Reilly and Wiswall at Brookhaven National Laboratory in 1973 [95]. TiFe crystallizes in a CsCl type cubic structure (space group Pm-3m), where hydrogen atoms are stored exclusively in the octahedral sites formed by four titanium (Ti) atoms and two iron (Fe) atoms (show in Fig 2.5). Upon hydrogenation, the Pressure-Composition-Temperature (PCT) curves exhibit two distinct plateau pressures, corresponding to the successive formation of the monohydride β-TiFeH (orthorhombic, space group P2221) and the dihydride γ-$TiFeH_2$ (orthorhombic, space group Cmmm) [92, 96, 97]. TiFe alloys offer several advantages, including abundant raw material availability, low cost, high hydrogen storage capacity (1.86 wt%), and moderate hydrogen absorption plateau pressure. However, the alloy faces challenges such as difficult activation and poor resistance to impurity gases. To address these limitations, extensive research has been conducted. Studies have shown that partially substituting Ti or Fe with metals such as Ni [94, 98], Zr [96, 99], Nb [97, 100], Co [93, 97] and Mn [101, 102] can significantly improve the alloy's activation properties and resistance to impurity gases.

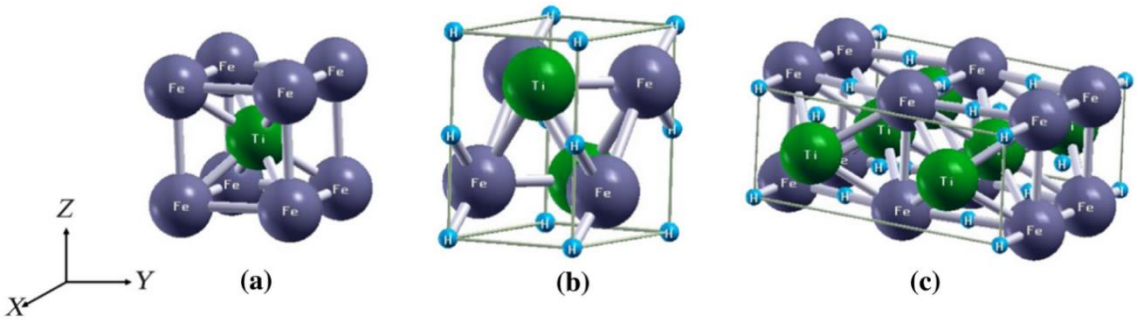

Fig. 2.5 The crystal structure of TiFe with the CsCl type structure: (a) before hydrogenation; (b) monohydride β-TiFeH; (c) dihydride γ-$TiFeH_2$ [103]

2.3.4 A_2B type (magnesium based hydrogen storage alloy)

A_2B type Mg based hydrogen storage alloys are regarded as highly promising for high-capacity hydrogen storage, particularly in applications such as fuel cells and hydrogen-powered vehicles [104]. Magnesium based hydrogen storage materials (MgH_2) have garnered significant attention due to their high gravimetric hydrogen density (7.6 wt%), excellent reversibility, natural abundance, and low cost [105]. However, the development of MgH_2 has been hindered by challenges related to its unsatisfactory thermodynamic stability and slow kinetics. Specifically, the dehydrogenation enthalpy (75 kJ/mol H_2) and entropy (135 J/mol H_2) of MgH_2 are high, primarily due to the stable Mg-H bond [105], making it difficult to fully release hydrogen at temperatures below 623 K. Moreover, the dehydrogenation activation energy (Ea) of MgH_2 is as high as 156 kJ/mol H_2 [106]. As a result, current research is focused on improving the kinetic and thermodynamic properties of MgH_2. Studies have shown that alloying with other elements can significantly enhance the hydrogen storage characteristics of magnesium [54, 107-109]. One typical example is Mg_2Ni in magnesium-based alloys, which reacts with H_2 to form Mg_2NiH_4 (3.6 wt%). Mg_2NiH_4 not only exhibits a lower formation enthalpy (64.5 kJ/mol H_2) but can also release hydrogen completely at 523 K, a temperature significantly lower than that required for MgH_2 [110].

2.3.5 BCC solid solution (V-based) hydrogen storage alloys

A solid solution alloy refers to a solid phase in which one or more solute elements are dissolved into a solvent matrix element. The most representative body-centered cubic (BCC) solid solution hydrogen storage alloy is the vanadium-based alloys. Vanadium crystallizes in the space group Im-3m with a BCC structure and a lattice constant of a = 3.028 Å. When pure vanadium absorbs hydrogen, hydrogen atoms initially occupy the tetrahedral interstitial sites. Since the BCC phase contains 12 tetrahedral interstitials, the theoretical hydrogen storage capacity of this type of solid solution is relatively high (3.8 wt%) [111]. During the initial hydrogen absorption by vanadium, a hydrogen-containing solid solution phase (α phase) with

a deformed BCC structure is formed, where H atoms mainly occupy the tetrahedral sites. Subsequently, the monohydride VH (β phase) with a body-centered tetragonal structure (BCT) is formed, with H atoms gradually filling more tetrahedral sites, leading to lattice expansion and deformation. Finally, the dihydride VH_2 (γ phase) with a face-centered cubic structure (FCC) is formed, and H atoms tend to preferentially occupy octahedral sites due to relative larger volume compared to BCC structure [48, 112]. However, due to the low plateau pressure of VH, the hydride formed is too stable, making hydrogen release difficult [48]. To optimize the hydrogen storage properties, additional elements are introduced to form ternary (Ti-Cr/Mn/Fe/Ni-V) [29, 113-117] or quaternary (Ti-Fe/Mn/Zr-Cr-V) [36, 118-121] alloy systems. Yan et al. [20, 118] studied the structure and hydrogen storage properties of Vx–(Ti–Cr–Fe)100−x (Ti/(Cr+Fe) = 1.0, Cr/Fe = 2.5, x = 20–55). Their research revealed that, as the lattice parameter increases, the hydrogen absorption and desorption capacities improve, reaching a maximum capacity (C_{ab} = 3.4 wt%, C_{de} = 1.8 wt%) when a = 3.03 Å.

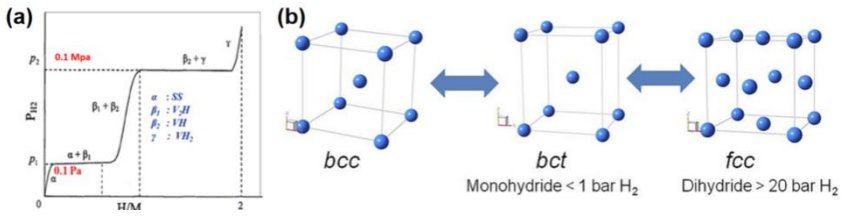

Fig. 2.6 (a) Schematic of PCT curve for vanadium; (b) The crystal structure of V-BCC solid solution during hydrogenation processing [48, 122]

2.3.6 High-entropy hydrogen storage alloys

High entropy alloys (HEAs), also referred to as multi-principal element alloys (MPEAs), were first introduced by Yeh et al. in 2004 [123]. Unlike conventional alloys, which are typically composed of one or two principal elements, HEAs consist of five or more elements, each contributing between 5 at% and 35 at%. These alloys lack a single dominant element and are characterized by a random distribution of elements. The high configurational entropy resulting from multiple principal elements promotes the formation of a disordered single-phase solid solution [27]. As a novel class of materials, HEAs have garnered significant attention due to

their unique physical, chemical, and mechanical properties, particularly in hydrogen storage applications [28]. Sahlberg et al. [23] were the first to identify the hydrogen storage potential of the TiVZrNbHf HEA, which possesses a body-centered cubic (BCC) structure and exhibits a hydrogen-to-metal ratio (H/M) of 2.5. This H/M ratio surpasses that of traditional BCC-based hydrogen storage alloys (H/M = 2), suggesting enhanced hydrogen storage potential, potentially attributed to substantial lattice distortion, which enables both tetrahedral and octahedral sites to accommodate hydrogen atoms. However, the alloy demonstrates a relatively low hydrogen storage weight percentage (wt%). Zlotea et al. [122] explored the hydrogen storage mechanism of the TiZrNbHfTa HEA, noting that the alloy undergoes a lattice transformation from BCC to body-centered tetragonal (BCT) and eventually to face-centered cubic (FCC), a behavior similar to that observed in conventional V-BCC hydrogen storage alloys. With the continued development of BCC-based HEAs for hydrogen storage, a wider range of compositions and properties are being investigated. Di Wan et al. [124] examined the cycling performance of $Ti_{25}V_{30}Nb_{10}Cr_{35-x}Ni_x$ (x=2, 4, and 6) HEAs, finding that all samples followed similar trends in cycle performance, with capacity decay rates decreasing as the number of cycles increased, eventually stabilizing. After 110 cycles, the Ni6 sample retained 87.1% of its initial hydrogen storage capacity (1.81 wt%), demonstrating excellent cycling stability. Additionally, Luo Long et al. [125] investigated the hydrogen storage performance of V35Ti35Cr10Fe10M10 (M = Mn, Co, Sc, and Ni) HEAs, finding that all alloys could be activated after a single hydrogen absorption/desorption cycle, a process significantly more efficient than that observed in traditional V-BCC hydrogen storage alloys.

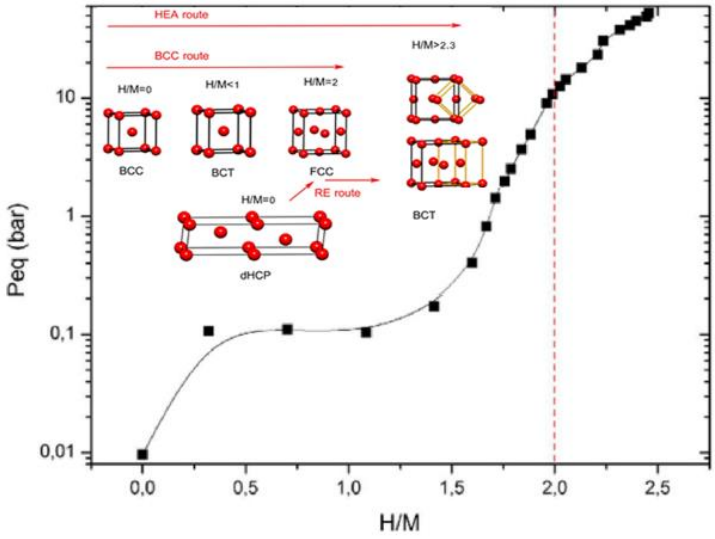

Fig. 2.7 Isothermal hydrogen absorption curve for TiVZrNbHf at 299 °C and crystal structure transformation during hydrogenation [23]

The Laves phase high entropy alloy (HEA) system is another extensively studied as a hydrogen storage material [34, 35, 126], exhibiting a maximum hydrogen storage capacity of 1.8 wt%, similar to traditional AB_2 type alloys, such as $TiCr_2$ [31] and $TiMn_2$ [87]. In a study by Edalati et al. [34], thermodynamic calculations were employed to develop a TiZrCrMnFeNi HEA, which was found to reversibly store 1.7 wt% hydrogen at room temperature with rapid kinetics, without requiring an activation process. This favorable behavior is likely attributed to a valence electron concentration (VEC) of 6.4. Moreover, Yuan et al. [35] investigated the cyclic hydrogen storage performance of a TiZrFeMnCrV HEA, which achieved a hydrogen storage capacity of 1.8 wt% under 7 MPa pressure at 30 °C. After 50 cycles, the alloy retained a reversible hydrogen storage capacity of 1.76 wt% and exhibited a fast hydrogenation rate, demonstrating excellent cyclic stability. Compared to BCC HEAs, Laves phase HEAs offer superior kinetic performance, including higher hydrogen absorption/desorption rates [33, 127], easier activation [34]. However, due to their more complex and densely packed crystal structures, Laves phase HEAs tend to have lower hydrogen storage capacities than BCC HEAs [35, 48].

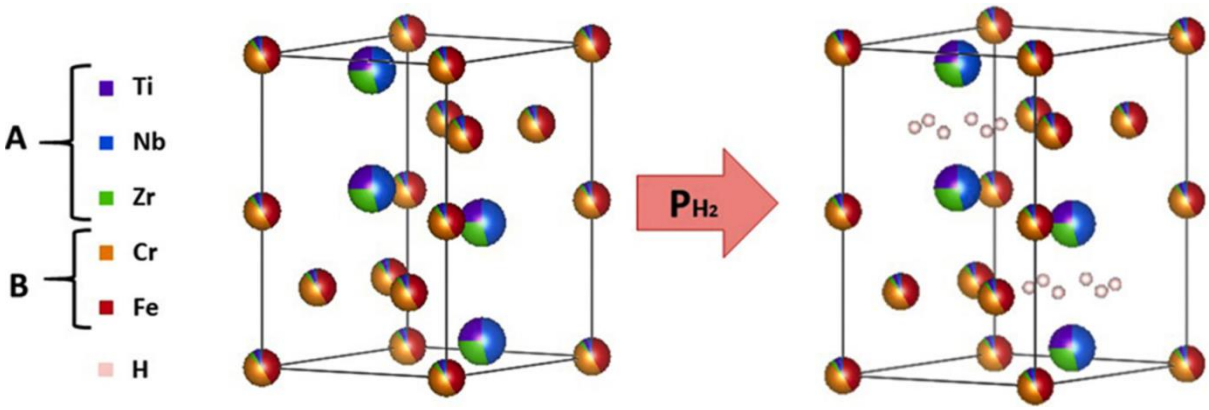

Fig. 2.8 The crystal structure transformation during hydrogenation of TiZrNbCrFe C14 structure HEA

2.4 Influence factors on hydrogen storage performance

2.4.1 Phase composition and morphology

A minor presence of a second phase can significantly enhance the activation process and improve the hydrogen storage kinetics of alloys during hydrogen absorption and desorption [118, 128, 129]. R.R. Chen et al. [39] systematically studied the microstructure and hydrogen absorption/desorption properties of $TiMn_{(100-x,\ Ti/Mn=5/8)}V_x$ (x = 25, 30, 35, 40, 45, and 50) alloys. Their findings revealed that the proportion of BCC and Laves phases varies with V content, with the BCC phase increasing as V content rises. The presence of the Laves phase contributes to improved kinetics, as the brittle Laves phase surrounds the BCC matrix. During hydrogen absorption, cracks form in the Laves phase due to lattice expansion and propagate into the BCC phase, facilitating the diffusion of hydrogen atoms into the BCC matrix (Fig. 31). However, the theoretical hydrogen storage capacity of the Laves phase (H/M≈1.4) is lower than that of the BCC solid solution (H/M≈2), so an excessive amount of Laves phase leads to a marked reduction in the alloy's hydrogen storage capacity [118, 129]. Composite hydrogen storage materials, composed of materials with different kinetic behaviors, can effectively enhance the activation properties of the alloy and mitigate the negative effects of air exposure on hydrogen absorption/desorption performance, which is crucial for industrial applications [57].

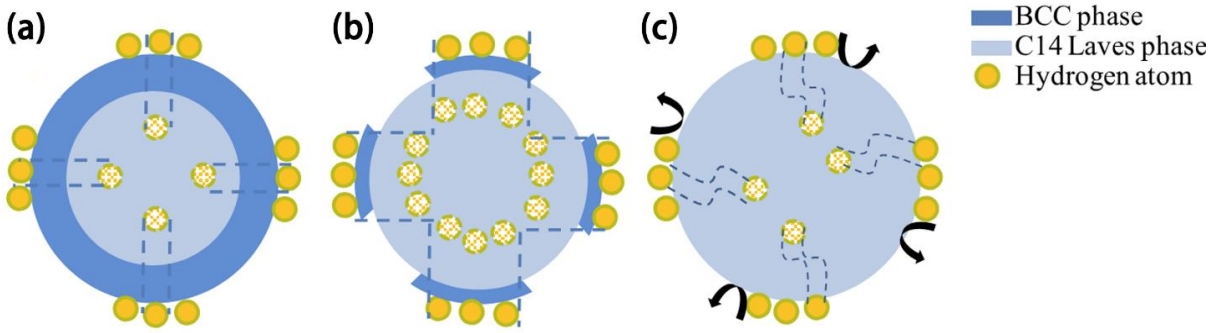

Fig. 2.9 The schematic diagram of effect of phase proportion on hydrogen absorption capacity of Ti-V-Mn alloys [39]

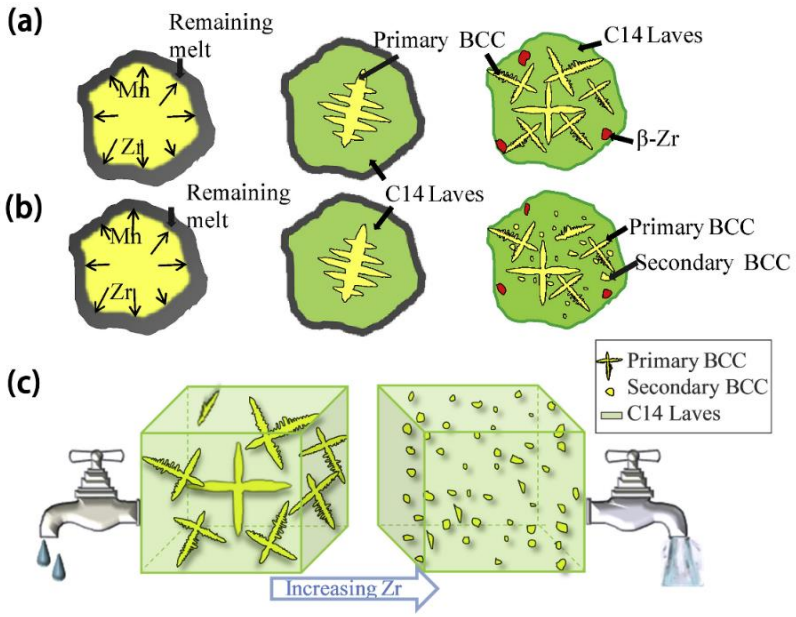

Fig. 2.10 Schematically illustration of the evolving microstructure of $Ti_{23-x}Zr_xV_{40}Mn_{37}$ alloys: (a) x = 2,4; (b) x = 6, 8 and 10; The schematic diagram of effect of BCC phase size on hydrogen diffusion of Ti-Zr-V-Mn alloys[130]

Chen et al. [130] investigated the effect of phase morphology on the hydrogen storage properties of $Ti_{10}V_{84-x}Fe_6Zr_x$ alloys, where x ranges from 1 to 8 at%. Their study revealed that increasing the Zr content results in a reduction of the primary dendritic BCC phase and an increase in the C14 Laves phase (as shown in Fig. 2.10 a and b). Notably, when the Zr content exceeds 6 at%, a secondary blocky BCC phase emerges. In alloys with higher Zr content, the small blocky BCC phases are completely surrounded by the C14 Laves phase, offering shorter diffusion paths for hydrogen atoms from the interior to the exterior of the blocky BCC phase, compared to the larger dendritic BCC phase. This morphology facilitates easier hydrogen desorption with minimal pressure reduction. Conversely, in alloys with lower Zr contents (2 and 4 at%), only a limited amount of hydrogen desorbs from the dendritic BCC phase (as shown in Fig. 2.10 c). Alloys with a higher proportion of the secondary blocky BCC phase exhibit greater effective hydrogen storage capacity. The alloy composition $Ti_{21}Zr_2V_{40}Mn_{37}$ achieved the highest effective hydrogen storage capacity of 1.85 wt% at 293 K. Furthermore, as Zr content increases beyond 6 at%, two desorption plateaus appear, with the upper plateau widening as Zr content increases, owing to faster hydrogen diffusion in the smaller secondary

blocky BCC phases. However, increasing Zr content also amplifies hysteresis and raises the plateau slope, which is attributed to the increase in interstitial strain energy and the alloy's affinity for hydrogen.

2.4.2 Lattice constants

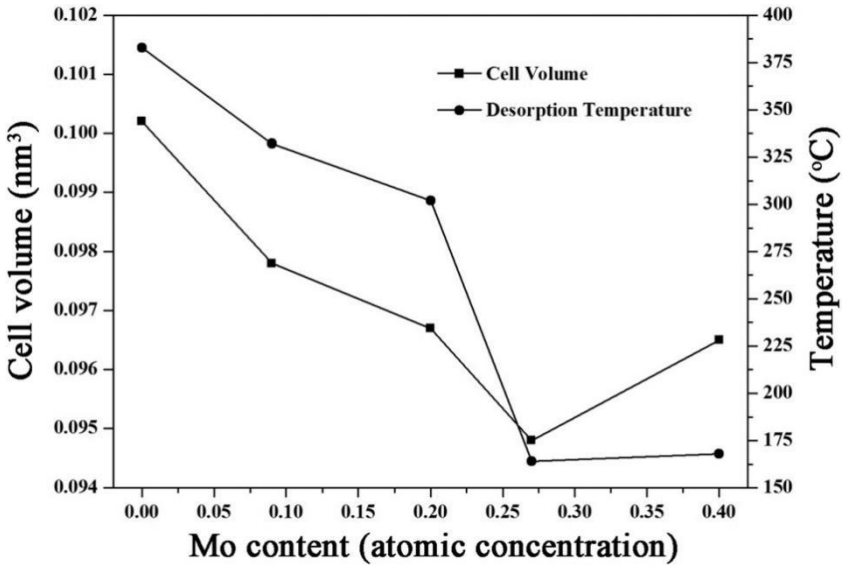

Fig 2.11 Dependence of cell volume and hydrogen desorption temperature of Ti-Zr-Hf-Mo-Nb hydrides on the Mo concentration [131]

The influence of lattice constants on the stability of metal hydrides has been extensively studied [20, 132]. A decrease in the primary lattice constant (BCC lattice) reduces the stability of metal hydrides, resulting in an increase in plateau pressure. Conversely, as the stability of metal hydrides increases, the plateau pressure decreases [133-135]. Huahai et al. [131] explored the effect of Mo substitution for Nb on the hydrogen storage properties of Ti-Zr-Hf-Nb BCC solid solution alloys. Their findings indicate that the thermal stability of metal hydrides decreases with increasing Mo concentration, which is primarily attributed to the reduced bonding energy between the alloy and hydrogen atoms due to the reduction in lattice constant. Moreover, changes in lattice constants also influence the pulverization and cycle life of alloys during hydrogen absorption/desorption cycles. During these cycles, the expansion and contraction of the lattice cause relaxation in the crystal structure, leading to partial structural damage and a

subsequent decline in cyclic hydrogen storage performance. An increase in the lattice constant mitigates the volume expansion of the lattice during hydrogen absorption/desorption, thereby stabilizing the crystal structure and slowing the degradation of cyclic capacity [61].

Liu et al. [61] investigated the hydrogen storage cycle stability, absorption/desorption plateau, and degradation mechanisms of the $LaNi_{5-x}Al_x$ (x = 0, 0.25, 0.5) alloy system. Fig 2.12 (a)–(c) presents the PCT isotherms of $LaNi_{5-x}Al_x$ (x = 0, 0.25, 0.5) alloys after 10, 100, 300, and 1000 cycles. As the Al content increases, the rise in the plateau pressure diminishes with an increasing number of cycles, indicating that Al stabilizes the $LaNi_5$ lattice structure. Notably, the $LaNi_{4.5}Al_{0.5}$ alloy retains 98.2% of its hydrogen storage capacity even after 1000 cycles.

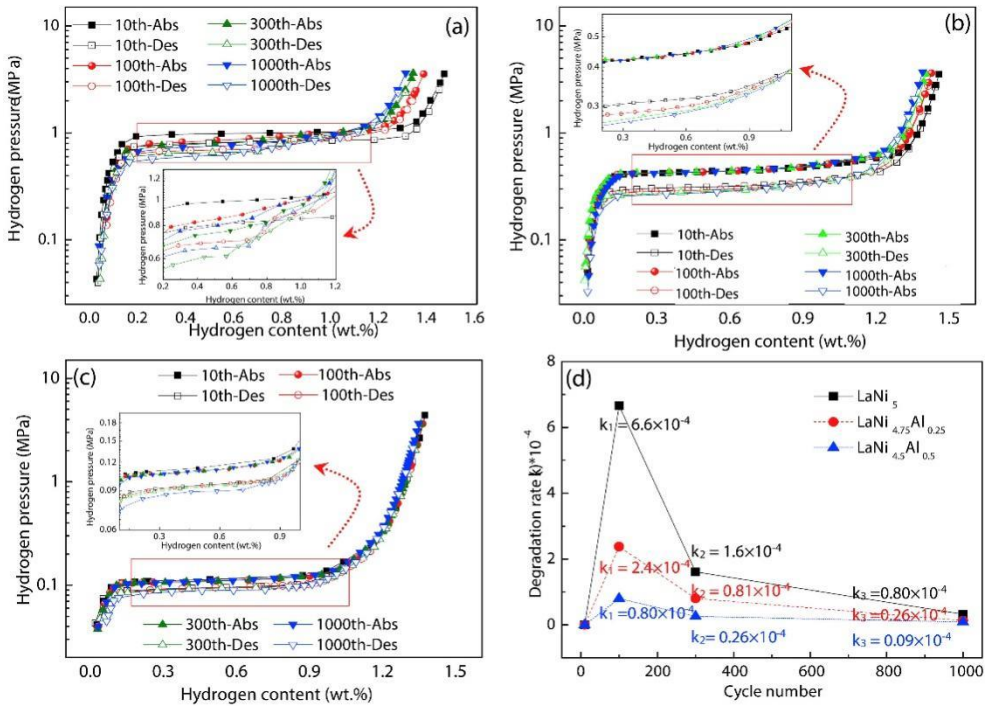

Fig. 2.12 P-C-T curves of $LaNi_{5-x}Al_x$ (x = 0, 0.25, 0.50) alloys after 10, 100, 300, and 1000 cycles at 343 K (a)–(c), and degradation rate with cycling (d) [61]

2.4.3 Lattice distortion

Sahlberg et al. [23] investigated the hydrogenation behavior of the high entropy alloy (HEA) TiVZrNbHf. The observed maximum hydrogen-to-metal (H/M) ratio of 2.5 indicates that hydrogen occupies both tetrahedral sites and approximately 50% of the octahedral sites, a phenomenon that is unique and has not been previously observed in pure transition metal hydrides. These findings clearly demonstrate that the TiVZrNbHf alloy exhibits behavior distinct from that of typical transition metals. The formation of a distorted face-centered cubic (FCC) or body-centered tetragonal (BCT) structure in the fully hydrogenated state is also reminiscent of the structures found in rare-earth compounds. It is proposed that the remarkable hydrogen storage capacity is a result of lattice strain in the distorted HEA, which promotes hydrogen occupancy in both tetrahedral and octahedral sites. However, the observed H/M ratio of 2.5 corresponds to only about 2.7 wt% hydrogen, primarily due to the high atomic mass of Hf, Nb, and Zr. Higher hydrogen storage capacities (by weight percentage) could potentially be achieved in other HEAs by substituting these heavier elements with lighter alternatives.

2.5 High entropy alloys (HEAs)

High entropy alloys (HEAs) are characterized by four key features: (1) high entropy effect in thermodynamics, which stabilizes single-phase solid solutions; (2) severe lattice distortion, resulting from the significant atomic size differences among constituent elements; (3) sluggish diffusion effect in kinetics;and (4) the "cocktail" effect.

2.5.1 Characteristics of high entropy alloys

2.5.1.1 High entropy effect

As implied by the name, high entropy alloys (HEAs) are primarily defined by their high entropy, which is one of their core effects. This effect promotes the formation of solid solution phases, simplifying the microstructure more than was previously anticipated. According to Gibbs' phase rule, when the pressure of a system is constant, the relationship between the number of phases and the number of elements in the alloy can be expressed by the following equation [136]:

$$\boldsymbol{P = C + 1 - F} \quad \textbf{(2-8)}$$

where $\boldsymbol{C}$ represents the number of elements in the alloy, $\boldsymbol{P}$ is the number of phases formed, and $\boldsymbol{F}$ is the degree of freedom of the system. Based on equation (2-8), with a constant degree of freedom, the number of phases is expected to increase as the number of elements increases. However, studies have shown that the actual number of phases formed in high entropy alloys is significantly lower than what is predicted by Gibbs' phase rule [137-139]. Fig 2.13 presents the XRD pattern of the Cu-Ni-Al-Co-Cr-Fe-Si alloy system. It reveals that as the number of elements increases, the alloy system predominantly forms a simple FCC structure or a mixed solid solution structure of FCC and BCC phases. According to Gibbs' phase rule, an alloy containing seven elements should theoretically form eight phases. Moreover, given the highly negative formation enthalpy of Si with other metals, intermetallic compounds would be expected. However, experimental results indicate that the alloy

exhibits only FCC and BCC phases. This discrepancy is primarily attributed to the high configurational entropy, which enhances mutual solubility among elements and inhibits the formation of intermetallic compounds.

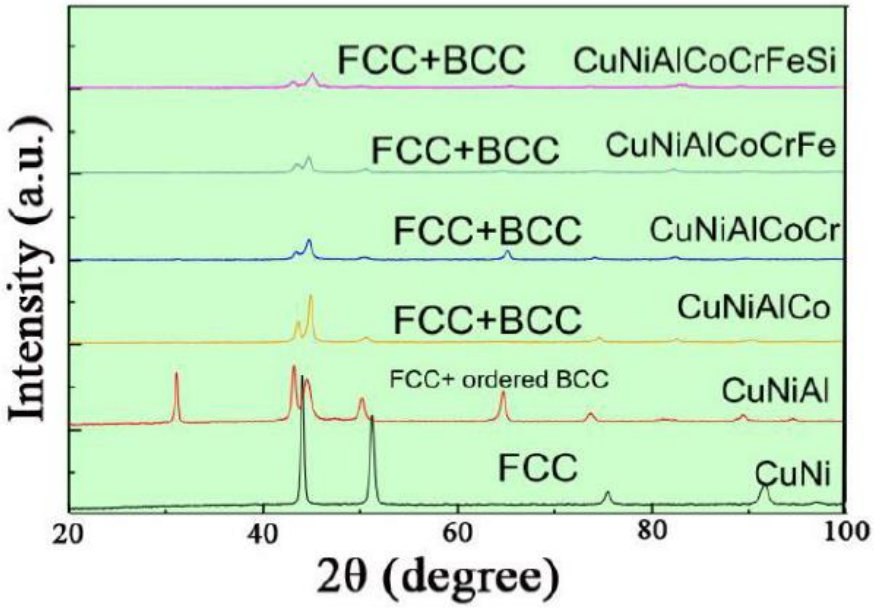

Fig. 2.13 XRD patterns of Cu–Ni–Al–Co–Cr–Fe–Si alloy series with increasing number of incorporated principal elements [137]

2.5.1.2 Severe lattice distortion effect

The solid solution in high-entropy alloys is composed of multiple elements, with atoms from each element randomly occupying lattice positions within the crystal structure [140, 141]. In this solid solution, all atoms can be considered either solute or solvent atoms, and each atom varies in size and character. These differences lead to significant lattice distortion (schematic in Fig. 2.14). The severe lattice distortion causes atoms to deviate from their equilibrium positions, resulting in increased potential energy and a rise in the system's overall free energy.

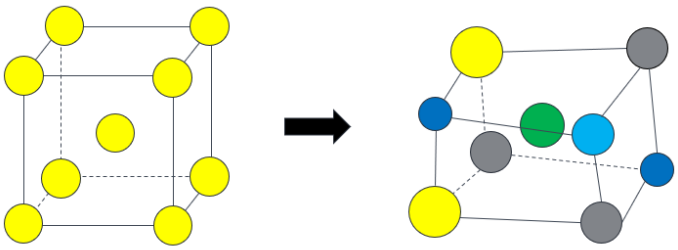

Fig. 2.14 Schematic of the transition from pure metal BCC structure to five element high-entropy alloys BCC structure

The significant lattice distortion in high-entropy alloys has a profound impact on their mechanical, thermodynamic, electrical, and chemical properties. Most high-entropy alloys exhibit high strength and hardness, primarily due to the large lattice distortions, which increase internal stress and hinder dislocation movement [138]. Additionally, the elevated internal stress enhances electron scattering, thereby increasing the electrical resistivity of the alloy. Similarly, heat conduction in solid materials occurs through lattice vibrations (phonons) and free electrons. Severe lattice distortion intensifies phonon and lattice scattering, which in turn reduces the thermal conductivity of the material [137].

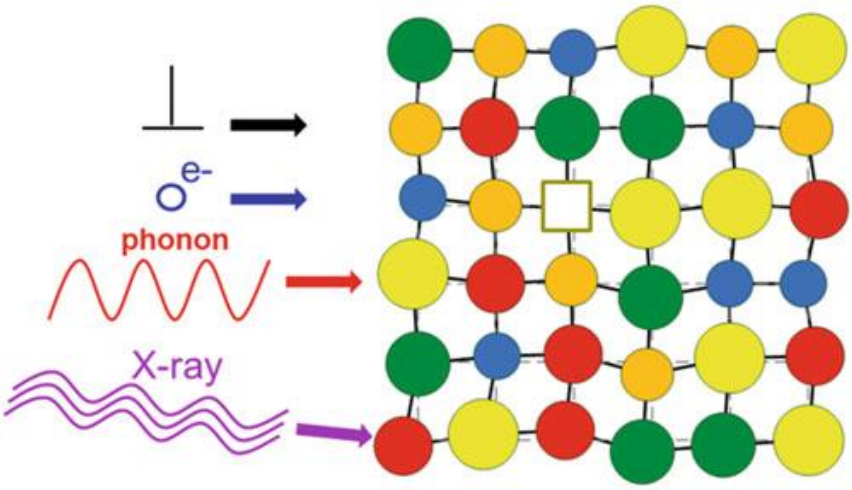

Fig. 2.15 Schematic diagram showing the severely distorted lattice and the various interactions with dislocations, electrons, phonons, and x-ray beam [142]

Yeh et al. [137] investigated the unusual decrease in XRD diffraction peak intensity in the Cu-

Ni-Al-Co-Cr-Fe-Si series of high-entropy alloys as the number of constituent elements increased. As illustrated in Figure 2.16, this reduction in intensity is attributed to the presence of atoms of varying sizes occupying the crystal lattice, which results in rough and uneven diffracting crystal planes. Consequently, during Bragg diffraction, the X-rays are significantly scattered, leading to a marked decrease in diffraction intensity.

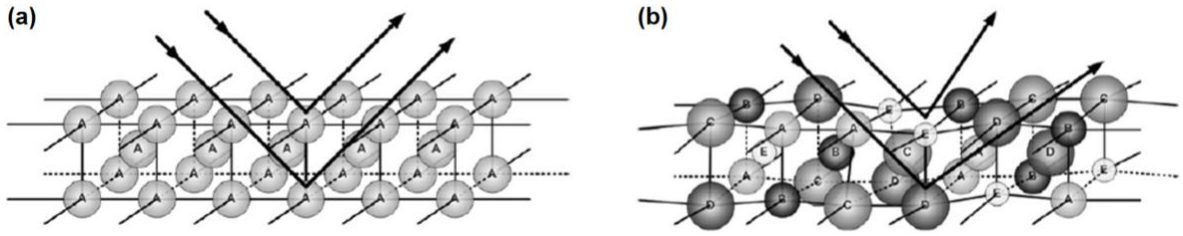

Fig 2.16 Schematic illustration of intrinsic lattice distortion effect on Bragg diffraction: (a) perfect lattice with the same atoms; (b) distorted lattice with solid-solution of different-sized atoms which are expected to randomly distribute in the crystal lattice according to a statistical average probability of occupancy [137]

2.5.1.3 Sluggish diffusion effect

Several studies have demonstrated that the self-diffusion coefficients of elements in multicomponent alloys are lower by an order of magnitude compared to traditional alloys. Yeh et al [143] validated this observation by designing three diffusion couple pairs Cr-Mn, Fe-Co, and Fe-Ni. As shown in Fig. 2.17, the Q/T (activation energies) values for Cr, Mn, Fe, Co, and Ni in the CrMnFeCoNi high-entropy alloy are the highest, indicating the smallest diffusion coefficients. This suggests that atomic diffusion rates in high-entropy alloys (HEAs) are significantly slower than in conventional alloys. The slower diffusion is primarily attributed to the interaction between atoms of different sizes and the severe lattice distortion in HEAs, which hinder effective atomic diffusion.

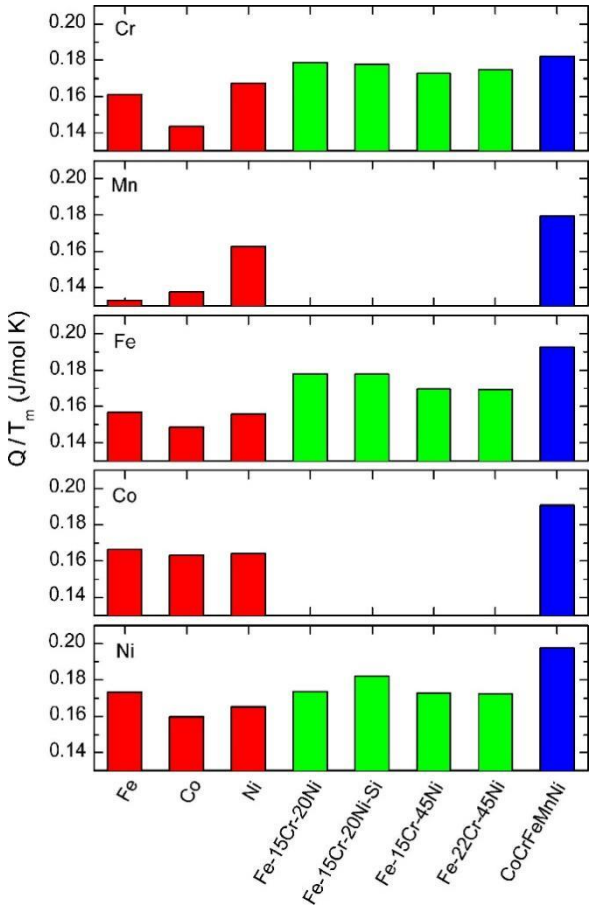

Fig 2.17 Normalized activation energies of diffusion for Cr, Mn, Fe, Co and Ni in different matrices [143]

Phase transformations typically require coordinated diffusion of the constituent elements to reach phase equilibrium, and thus, the sluggish diffusion effect in HEAs can delay the formation of new phases. From a kinetic perspective, in conventional alloys, the bonding between solute and solvent atoms after vacancy filling remains the same as before. However, in HEAs, diffusion primarily occurs through a vacancy mechanism [141-143]. Due to the variation in melting points and bonding strengths between different atoms, more mobile atoms tend to diffuse more easily into vacant positions. Nevertheless, the bonding strength between atoms differs, affecting the diffusion process. Generally, atomic diffusion involves continuous vacancy filling (as shown in Fig. 2.18). If the energy decreases after a vacancy is filled, further atomic diffusion becomes difficult; if the energy increases, it becomes harder for atoms to occupy the vacancies. Consequently, the diffusion rate and phase transformation rate in HEA

solid solutions are significantly reduced [142].

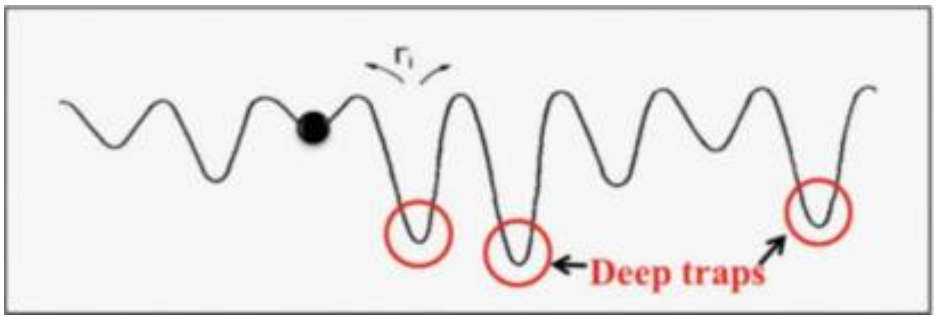

Fig 2.18 Schematic diagram showing the fluctuation of lattice potential energy along the diffusion path for an atom in the lattice (deep traps are indicated) [142]

2.5.1.4 “Cocktail” effect

The "cocktail effect" in multicomponent high-entropy alloys (HEAs) was first proposed by Indian scientist Ranganathan [144]. This effect arises from the fundamental properties of the constituent elements and their interactions, leading to a composite effect that influences the overall performance of HEAs. Essentially, this effect considers how the multiple elements at the atomic scale contribute to the macroscopic properties of the alloy, such as density, strength, oxidation resistance, and corrosion resistance. Furthermore, depending on the composition and processing methods, HEAs can form single-phase, dual-phase, or even multiphase structures. The properties of the alloy are affected by a combination of factors, including grain morphology, grain size, grain boundaries, phase boundaries, and the characteristics of each phase. Therefore, the overall performance is not a simple sum of the individual phases and elements. The "cocktail effect" emphasizes the emergent properties that go beyond what any individual element could exhibit. In the as-cast AlxCoCeFeNi HEA, the phase structure transitions from FCC to BCC as the Al content increases (show in Fig. 2.19). This results in a "cocktail effect" where the alloy’s microhardness increases, particularly as the BCC phase content rises, leading to a rapid increase in hardness [145].

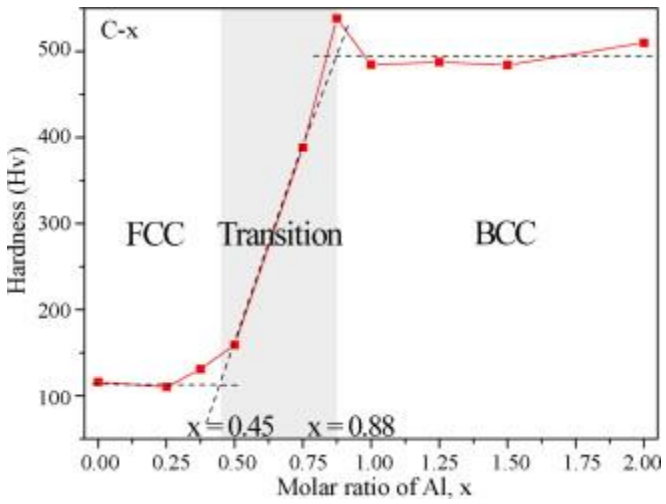

Fig 2.19 Hardness of C-x vs. x plot with the schematic plot (dashed line) for determining the boundaries of the transition region in C-x [145]

2.5.2 Design of high-entropy alloys

The design of high-entropy alloys should make the constituent elements obtain solid solutions with similar contents in some way according to a certain proportion. The type of solid solution is mostly face-centered cubic (FCC) [146], body-centered cubic (BCC) [147], hexagonal close packed (HCP) [148] or a phase composed of them. During the fabrication of high-entropy alloys, the volume fraction of the solid solution phase should be increased as much as possible. Avoid the formation of intermetallic compounds, and non-metallic inclusions, and other impurities.

2.5.2.1 Mixing enthalpy (ΔH_{mix}) and atomic size difference (δ)

In the formula (2-9), $\triangle H_{ij}^{mix}$ is the mixing enthalpy of the binary liquid alloy composed of the *i*-th element and the j-th element, and its value is calculated based on the Miedema macroscopic model [149] of the binary liquid alloy. c_i and c_j are the atomic percentages of the *i*-th element and the *j*-th element. For the alloys, the enthalpy of mixing can be positive or negative. When the $\triangle H_{mix} > 0$, it will cause dissolution gaps between the different liquid phases and reduce the solid solubility of the alloy. In addition, phase separation or component

segregation will be occurred, when the $\triangle H_{mix} > 0$. When the $\triangle H_{mix} < 0$, the bond force between the elements is strong, which easily produce intermetallic compounds. In summary, no matter whether $\triangle H_{mix}$ is negative or positive, the formation of solid solution is inhibited, but the high entropy effect in high-entropy alloys weakens this trend.

$$\triangle \boldsymbol{H_{mix}} = \sum_{i\neq j}^{n} \boldsymbol{4} \triangle \boldsymbol{H_{ij}^{mix}} \boldsymbol{c_i c_j} \quad \textbf{(2-9)}$$

In addition to the mixing enthalpy ($\triangle \boldsymbol{H_{mix}}$), the atomic size difference ($\boldsymbol{\delta}$) of elements will also affect the stability of the solid solution phase (2-10). A large difference in atomic size will increase the degree of lattice distortion in the alloy, increasing the strain energy of the crystal, which is not conducive to the stability of the solid solution phase. On the other hand, a large atomic size difference ($\boldsymbol{\delta}$) will cause slow diffusion between the components, which will reduce the phase transition rate and form an amorphous phase. Only when the atomic size difference of the alloy is within a certain range, the atoms of each element can replace each other to form a disordered solid solution phase.

$$\boldsymbol{\delta} = \sqrt{\sum_{i=1}^{n} \boldsymbol{c_i}(\boldsymbol{1} - \boldsymbol{r_i}/\bar{\boldsymbol{r}})^{\boldsymbol{2}}} \quad \textbf{(2-10)}$$

$$\bar{\boldsymbol{r}} = \sum_{i=1}^{n} \boldsymbol{c_i r_i} \quad \textbf{(2-11)}$$

Yong et al. [150] extended the "Hume-Rothery rules" to the study of high-entropy alloys (HEAs). According to this extended rule, the formation of solid solutions in HEAs is primarily influenced by the mixing enthalpy ($\triangle \boldsymbol{H_{mix}}$) and atomic size difference ($\boldsymbol{\delta}$). Through statistical analysis and calculations, a relationship between the atomic size difference and mixing enthalpy was established, as illustrated in Fig. 2.20 The figure demonstrates that for a solid solution phase to form (represented by regions S and S'), the following conditions must be satisfied: (1) $\boldsymbol{\delta}$ < 6.5%, and (2) -15 kJ/mol < $\boldsymbol{\Delta H_{mix}}$ < 5 kJ/mol.

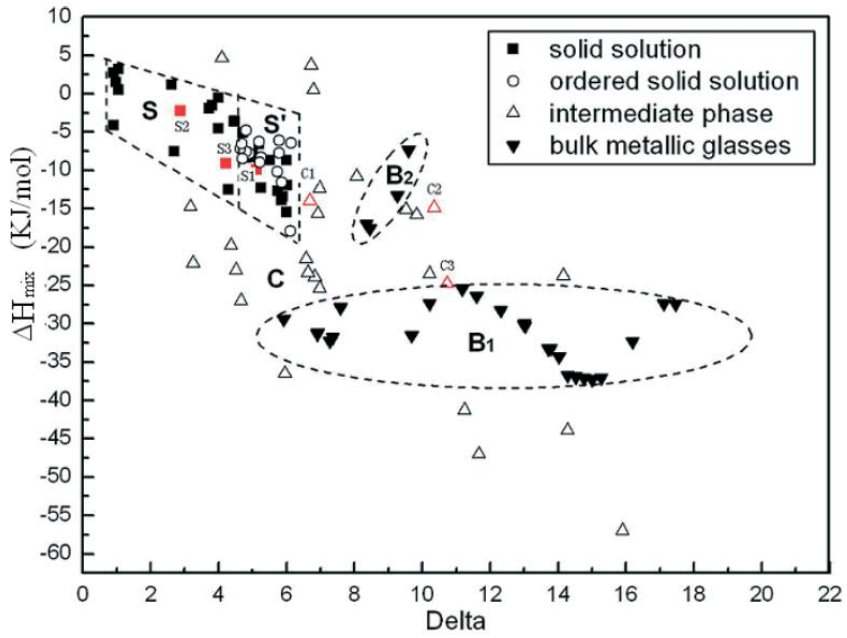

Fig 2.20 Relationship between Delta (δ) and $\triangle H_{mix}$ for MHAs and typical multicomponent bulk metallic glasses[150]

2.5.2.2 Ω criterion and atomic size difference (δ)

The $\boldsymbol{\delta}$ -$\triangle \boldsymbol{H_{mix}}$ criterion for solid solution phase formation takes into account atomic size mismatch and thermodynamic stability but does not consider the influence of configurational entropy (ΔS) on solid solution formation. To address this limitation, a new parameter (Ω) has been introduced (2-12), and its expression is as follows[27, 151]:

$$\boldsymbol{\Omega} = \frac{\boldsymbol{T_{mix}\triangle S_{conf}}}{|\triangle \boldsymbol{H_{mix}}|} \tag{2-12}$$

$$\mathbf{T}_{\boldsymbol{mix}} = \sum_{\boldsymbol{i=1}}^{\boldsymbol{n}} \boldsymbol{C_i}(\boldsymbol{T_m})_{\boldsymbol{i}} \tag{2-13}$$

In the formula, $\mathbf{T}_{\boldsymbol{mix}}$ is the melting point of the high-entropy alloy; $(\boldsymbol{T_m})_{\boldsymbol{i}}$ is the melting point of the *i*-th element in the alloy; $\boldsymbol{C_i}$ is the atomic percentage of the ***i***-th element in the alloy. As shown in Figure 2.21, the value of **Ω** is positive, indicating the alloy's ability to form a solid solution phase. **Ω** = 1 can be considered a critical threshold for high-entropy alloys to form a solid solution, where the influence of configurational entropy **(ΔS)** is equal to that of the mixing

enthalpy (ΔH_{mix}). When $\Omega > 1$, the effect of configurational entropy on solid solution formation surpasses that of the mixing enthalpy, making it easier for the alloy to form a solid solution phase. Conversely, when $\Omega < 1$, the influence of configurational entropy is weaker than that of mixing enthalpy, leading to the inhibition of solid solution nucleation and the preferential formation of intermetallic compounds. Therefore, $\Omega > 1$ can be used as a criterion for predicting the formation of a solid solution phase.

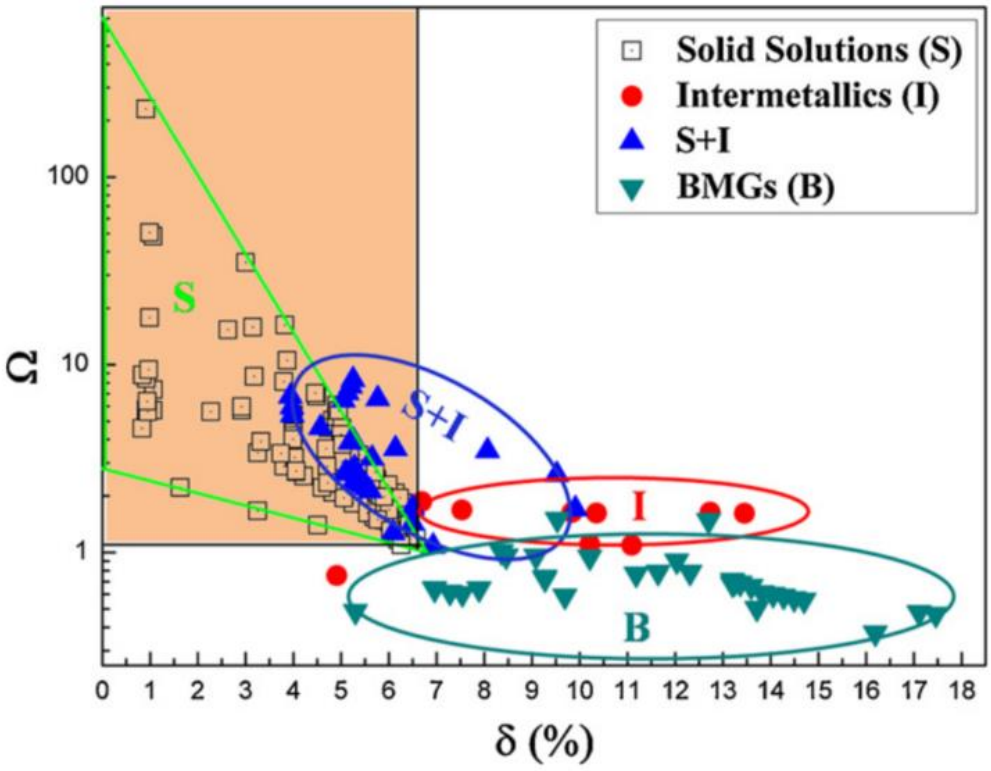

Fig 2.21 Phase selection diagram of HEAs and BMGs based on Ω and δ [27]

2.5.2.3 Valence electron concentration (VEC) criterion

When the atomic valence of each element is similar, the solid solubility between the elements increases, leading to a more stable solid solution phase within the alloy. However, as the electron concentration exceeds a certain threshold, the bonding between elements becomes disordered, and the stability of the solid solution decreases. The valence electron concentration (VEC) of high-entropy alloys can be calculated using the following formula [152]:

$$VEC = \sum_{i=1}^{n} C_i (VEC)_i \quad \textbf{(2-14)}$$

In formula (2-14), C_i is the atomic percentage of the i-th element, and $(VEC)_i$ is the electron valence concentration of the **i-th** element. The specific relationship is shown in Fig 2.22.

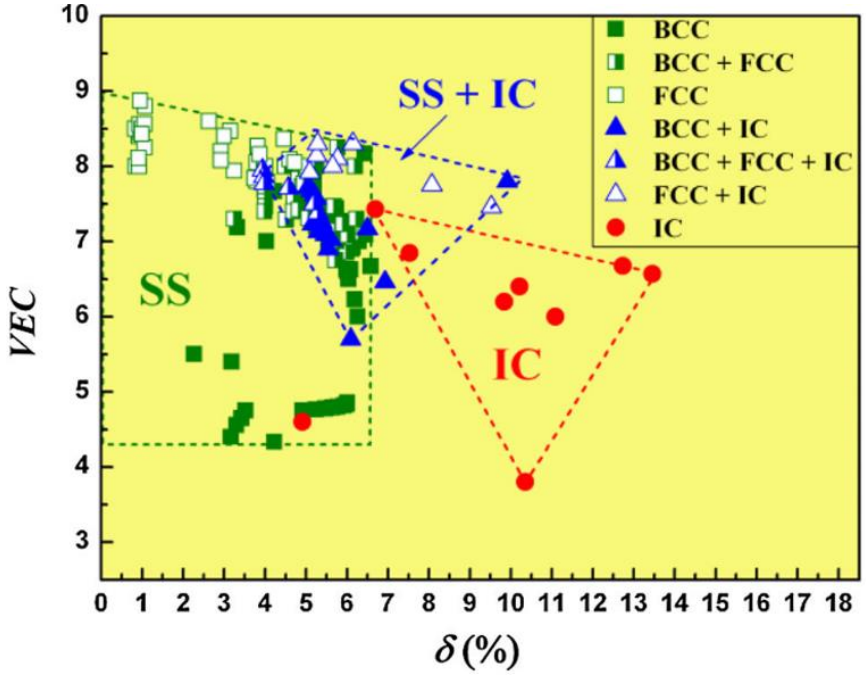

Fig 2.22 The relationship between parameters δ and VEC [152]

Sheng Guo et al. [153] investigated the correlation between valence electron concentration (VEC) and the stability of FCC and BCC solid solutions in high-entropy alloys (show in Fig 2.23). Their findings indicate that when the VEC exceeds 8.6, the FCC solid solution phase is more stable, whereas a VEC below 6.87 favors the stability of the BCC solid solution phase.

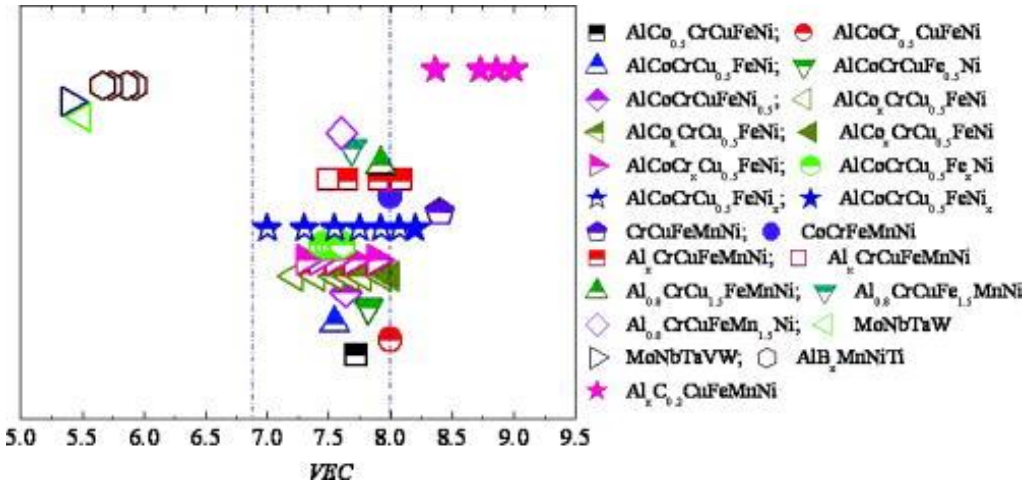

Fig 2.23 Relationship between VEC and the fcc, bcc phase stability for more HEA systems [153]

2.6 Fabrication process of high-entropy alloy

High-entropy alloys (HEAs) are alloys with a high configurational entropy, composed of multiple principal and supplementary elements. They typically exhibit a solid solution phase, with the grain structure ranging from conventional (μm) sizes [154-157] to nanocrystalline [158-162], and in some cases, amorphous phases [163-166] may also be present. The melting point, density, and atomic radius of the constituent elements can either be similar or vary significantly. Based on current research and application experience, the preparation methods for HEAs are largely similar to those used for conventional alloys, though there are certain specificities. The preparation methods for high-entropy alloys are generally divided into two categories: casting (melting) [167-169] and powder metallurgy (mechanical ball milling) [162, 170-172].

2.6.1 Vacuum arc melting

Arc melting is a metallurgical technique that utilizes electrical energy to generate an electric arc between two electrodes or between an electrode and the material being processed. The arc can be produced using either direct current (DC) or alternating current (AC). However, when using AC, momentary zero-voltage conditions occur between the electrodes, which can easily extinguish the arc in vacuum environments. Therefore, vacuum arc smelting typically employs DC power. Currently, vacuum arc melting is the most commonly used method for preparing high-entropy alloys [37, 173]. Nonetheless, due to the complexity of alloy compositions and the significant differences in melting points among the constituent elements, high-entropy alloys often experience elemental segregation during the solidification and cooling process. Additionally, as-cast samples are prone to casting defects, necessitating further post-processing treatments [38, 169, 174, 175].

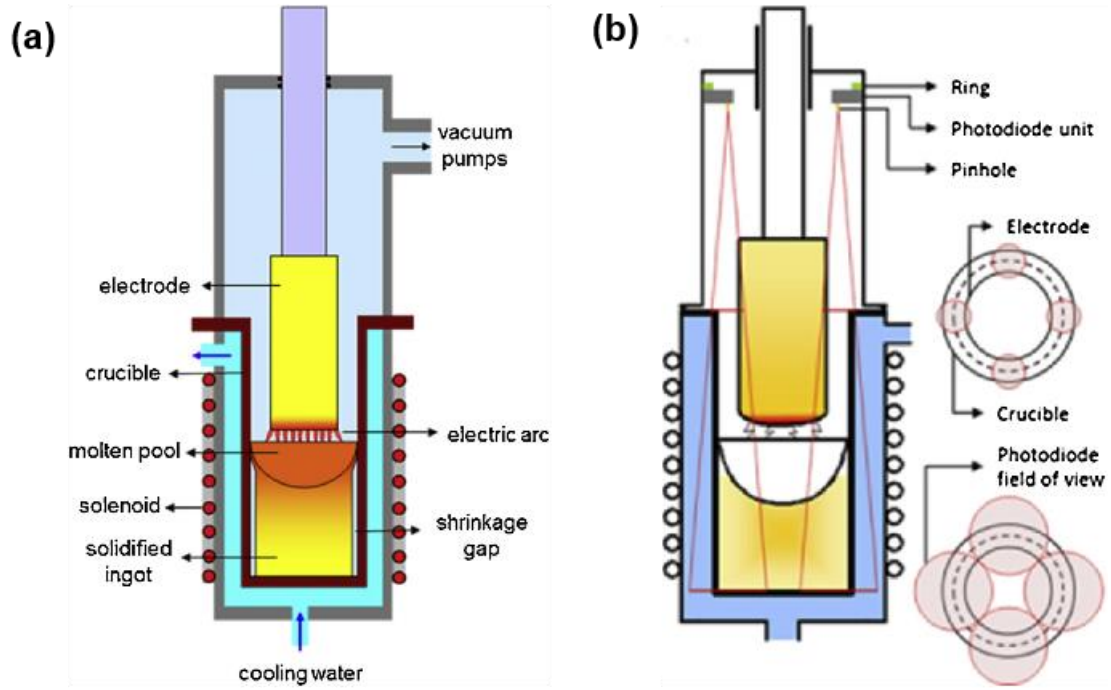

Figure 2.24 (a) VAR process schematic representational; (b) Schematic representation of the instrumentation of a VAR furnace with photodiodes showing the view field of each photodiode

2.6.2 Vacuum induction melting

The principle of induction melting is based on electromagnetic induction. In this process, a wire is wound into a coil and a current is applied, creating a magnetic field. The object placed inside the coil generates an opposing current due to the electromagnetic effect, resulting in the formation of eddy currents within the material. These currents heat the object internally as a result of its own electrical resistance, gradually increasing the temperature to achieve the smelting effect [176]. The heat generated through electromagnetic induction and electrothermal conversion occurs inside the metal, which helps minimize the loss of volatile elements [177]. Additionally, the power adjustment is straightforward, and furnace temperature can be precisely controlled, making it easy to carry out smelting in vacuum or controlled atmospheres [178]. However, despite its many advantages, induction smelting also has certain drawbacks. For instance, compared to other smelting methods, the equipment costs are higher, requiring additional infrastructure such as power supplies and vacuum glove boxes. Furthermore, issues

such as elemental segregation or uneven distribution within the melt can arise during the process [179].

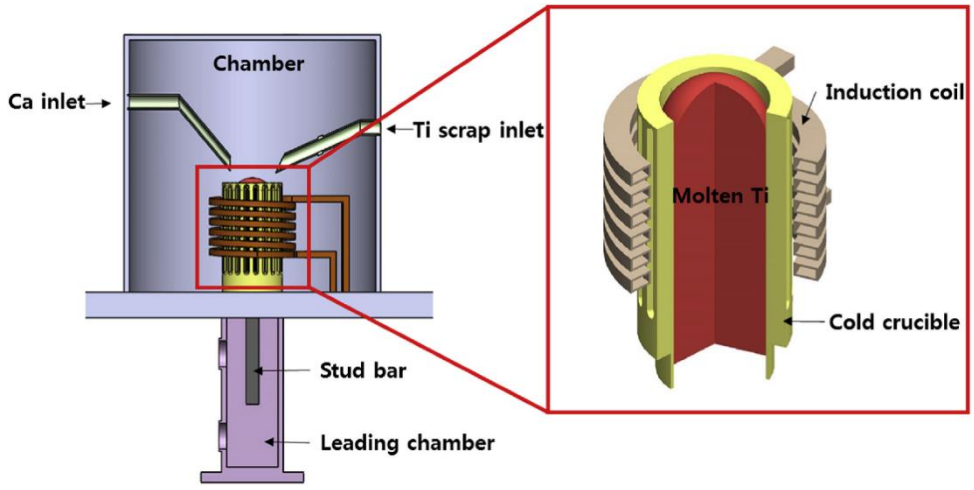

Fig 2.25 Schematic of the refined vacuum induction melting process [180]

2.6.3 Selective laser melting

The Selective Laser Melting (SLM) process is an advanced additive manufacturing technique that utilizes high-energy lasers to selectively melt metal powders layer by layer, thereby building complex three-dimensional structures[181]. The primary steps include powder deposition, laser scanning, and layer-by-layer accumulation until the final part is formed. This technique offers a highly efficient approach for manufacturing geometrically intricate structures and operates on principles similar to welding. During laser irradiation, metal powders undergo melting and solidification through processes such as absorption, reflection, radiation, and heat conduction. Due to the rapid movement of the laser beam and the molten pool, cooling rates can reach 10^4 to 10^6 K/s [182]. Compared to traditional casting methods, SLM does not significantly increase production costs in small batch manufacturing and provides flexibility in producing complex shapes. However, it also faces challenges such as high equipment costs, complex operational procedures, and the tendency to generate defects like balling, porosity, and cracking during fabrication [183].

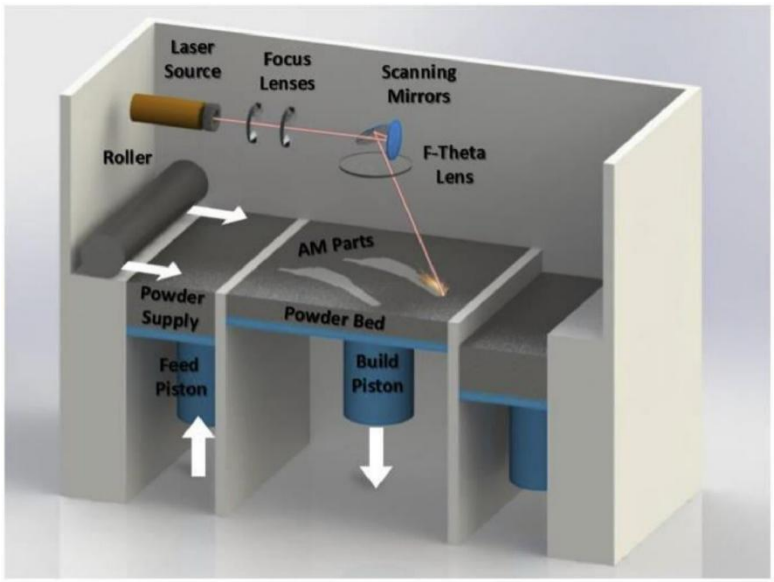

Fig 2. 26 Selective laser melting process [184]

2.6.4 Mechanical ball milling

Mechanical alloying (MA) is a solid-state powder processing technique that involves repeated welding, fracturing, and rewelding of powder particles in a high-energy ball mill to achieve atomic-level alloying [170]. This complex process, driven by both physical and chemical reactions, causes the powders to undergo extensive deformation, cold welding, and fragmentation, enabling the mixing and alloying of elements at the atomic scale [41]. Initially developed for the aerospace industry to produce oxide dispersion-strengthened (ODS) nickel-based and iron-based superalloys, MA has since proven effective in synthesizing various equilibrium and non-equilibrium alloy phases from mixed elemental or pre-alloyed powders [185-187].

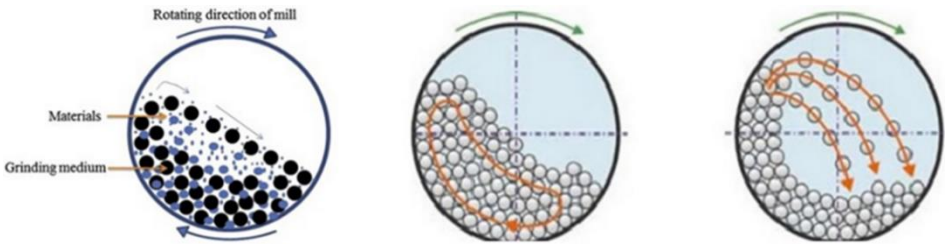

Fig 2.27 Ball milling process and different stages in MA [44]

MA offers several advantages in the synthesis of high-melting-point alloys and intermetallic

compounds. Firstly, it avoids the high-temperature melting and solidification processes associated with conventional metallurgical methods, enabling alloy formation at room temperature [42, 188]. Secondly, it produces uniform alloys with fine microstructures, often at the nanoscale [45, 46]. Additionally, MA is relatively simple to operate and is well-suited for both experimental and industrial applications. However, the process is not without challenges, including the potential for contamination, impurity introduction, and extended processing times [188]. Three main types of ball mills are commonly used for mechanical alloying: SPEX mills [189], shaker rod mills [190], and planetary ball mills [191]. Among these, planetary ball mills are the most widely used due to their efficiency and versatility [41, 46, 170].

2.7 Research gaps and objectives

2.7.1 Research gaps

1. Research on the mechanical alloying fabrication of high-entropy hydrogen storage alloys is still limited.

Through the above literature review, it can be observed that a significant amount of research has focused on the fabrication of high-entropy hydrogen storage alloys using the melting process, while studies on high-entropy hydrogen storage alloys prepared via ball milling remain extremely limited. This indicates a notable research gap in this area.

2. Research on the effects of heat treatment processes on the performance of mechanically alloyed high-entropy hydrogen storage alloys remains insufficient.

Currently, most studies focus on the hydrogen storage performance and phase structure changes of alloys after fabrication (as-casting), while research on the effects of heat treatment on the phase evolution and hydrogen storage performance of high-entropy hydrogen storage alloys remain limited. In particular, studies on as-milled high-entropy hydrogen storage alloys are almost nonexistent.

3. Research on the effects of B-side (non-hydrogen-affinitive) elements on the phase structure and hydrogen storage performance of ball-milled high-entropy hydrogen storage alloys remain limited.

The research on high-entropy hydrogen storage alloys focuses on the effects of A-group elements, such as Ti, V, Zr, Nb, Ta, Hf, and Mg. However, studies on the effects of B-group element addition and substitution on the phase structure and hydrogen storage properties remain limited.

4. Research on the influence of different fabrication methods on the hydrogen storage performance of HEAs remains limited.

2.7.2 Research objectives

1. Investigation on fabrication of Ti-V-Cr-Mn-Fe HEAs via mechanical milling.

Through a systematic study, the effects of milling media, milling time, ball-to-powder ratio, rotation speed, and process control agent on key factors such as phase structure, elemental distribution, particle size, and powder yield were investigated, leading to the optimization of the ball milling parameters for as-milled high-entropy alloys.

2. Investigating the effect of heat treatment on microstructural evolution and hydrogen storage performance of as-milled Ti-V-Cr-Mn-Fe HEAs.

Investigate the effect of heat treatment on the microstructural stability and hydrogen storage performance of as-milled HEAs.

3. Investigation of the varying Mn/Cr ratio on hydrogen ab/desorption behavior of the mechanical alloyed Ti-V-Cr-Mn-Fe HEAs.

Building upon previous experimental research, the alloy composition (Cr/Mn ratio) was systematically adjusted to investigate its effects on the hydrogen storage kinetics and thermodynamic performance of as-milled HEAs.

4. Investigation of the influence of fabrication methods on the phase structure, thermal stability, and hydrogen storage performance of Ti-V-Cr-Mn-Fe HEAs.

By comparing alloys fabricated via mechanical alloying and arc-melting, this study systematically evaluates the differences in microstructure, lattice distortion, and hydrogen storage performance between the two processing methods. Furthermore, the underlying mechanisms influencing these variations are analyzed. Based on the experimental results, proposed a potential reasons or hypotheses regarding the impact of different fabrication methods on hydrogen storage performance, providing insights for further optimization of ball-milled hydrogen storage materials.

3. Research methodology

This chapter primarily presents the composition design, fabrication methods, microstructural characterization techniques, thermodynamic testing methods, and hydrogen storage performance evaluation using the Sieverts method. The detailed experimental workflow is outlined below:

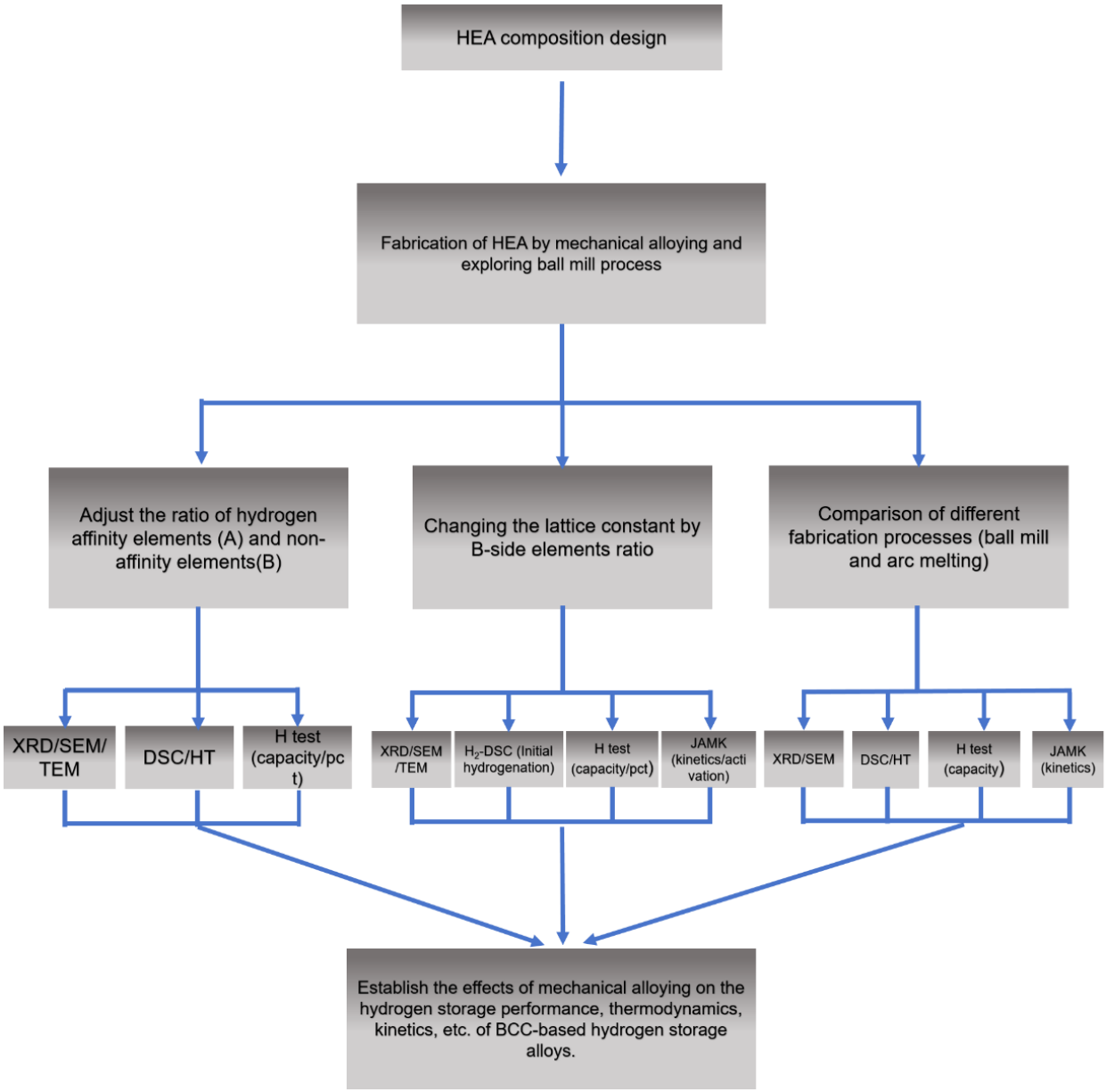

Fig 3.1 Schematic diagram of the whole research methodology design

3.1 Raw materials (elements) and HEAs fabrication

3.1.1 Elements selection

The elements within the yellow-bordered region are classified as hydrogen-affinitive, indicating their strong tendency to form stable bonds with hydrogen. These elements play a crucial role in hydrogen storage materials due to their ability to absorb hydrogen efficiently [192]. In contrast, the elements within the red-bordered region are considered non-hydrogen-affinitive, meaning they exhibit minimal or no attraction to hydrogen atoms. Their inclusion in alloys generally hinders hydrogen absorption [193]. The delineation of hydrogen-affinitive and non-affinitive elements is essential for optimizing the composition and performance of hydrogen storage alloys, as the balance between these two groups determines the material's overall hydrogen storage capacity and efficiency.

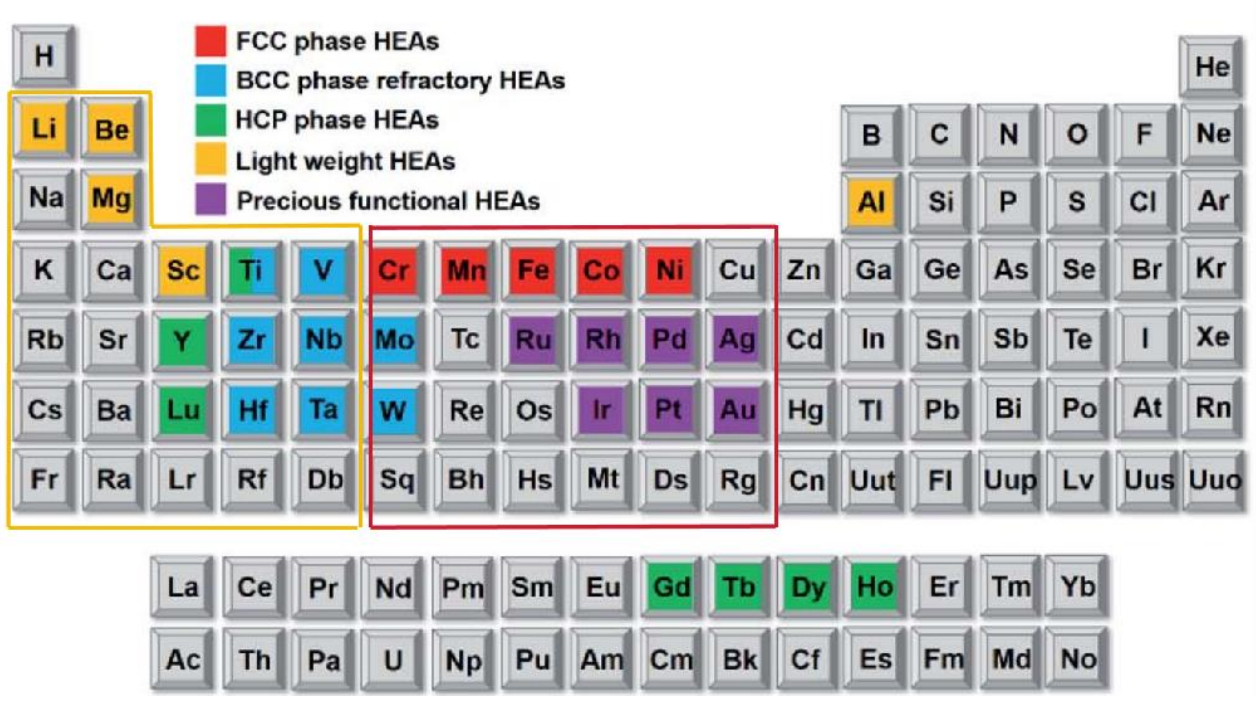

Fig 3.2 Common elements included in the HEAs and classification of various HEAs [194]

Ti and V were selected as hydrogen-absorbing elements primarily due to their excellent hydrogen affinity and compatibility during alloy formation. Firstly, both Ti and V exhibit

significant hydrogen absorption capabilities, allowing them to form stable hydride structures. Additionally, Ti and V have a high solid solubility, up to 80 wt% [195], which facilitates the formation of a stable body-centered cubic (BCC) phase in the alloy. The BCC structure, known for its unique crystal configuration, provides ample interstitial sites for hydrogen atoms, making it one of the most promising structures for achieving high theoretical hydrogen storage capacities [48]. This offers a substantial potential for maximizing the hydrogen storage capacity in HEAs design.

The non-hydrogen-affinitive elements Cr, Mn, and Fe are incorporated into the alloy system with the goal of optimizing its hydrogen desorption performance. Although these elements exhibit low affinity for hydrogen, they play a crucial role in modulating the thermodynamic stability of hydrides, thereby facilitating hydrogen release and enhancing the desorption rate of the alloy. Moreover, Cr, Mn, and Fe exhibit broad compatibility with Ti and V in phase diagrams, enabling the formation of stable body-centered cubic (BCC) structures across a wide compositional range, with Laves phases acting as secondary phases. The presence of a small amount of Laves phase can significantly improve the activation and kinetics properties of hydrogen absorption/desorption process. Therefore, through the careful design of hydrogen-affinitive and non-hydrogen-affinitive elements, it is possible not only to maintain the alloy's high hydrogen storage capacity but also to significantly enhance the kinetic and thermodynamic properties of hydrogen absorption and desorption. The specific parameters of the materials used in the experiment are as follows:

Table 3.1 Physical characteristics of raw elemental powders

Elements	Purity (wt%)	Powder sizes (μm)	Company
V	> 99.5	< 75	Chengdu Jinchun Metallic Materials Co, LTD, China
Ti	> 99.4	< 75	Good Fellow Cambridge Limited, England
Cr	> 99.8	< 45	Sigma Aldrich, St Louis, MO, USA
Mn	> 99.8	< 45	Sigma Aldrich, St Louis, MO, USA
Fe	> 99.8	< 10	Good Fellow Cambridge Limited, England

3.1.2 Fabrication process

Ball milling is a crucial solid-state alloying technique in materials science, where mechanical energy is used to repeatedly weld, fracture, and reweld powder particles, leading to alloying or refinement of microstructures. The fundamental principle of ball milling involves the repeated impact and friction of metallic powders with milling media (usually balls made of hard materials) within a high-energy ball mill (show in Fig 3.3). This process induces severe plastic deformation and localized heating, which can occur at room temperature, breaking the temperature limitations of traditional metallurgical methods. As a result, many high-melting-point alloys and composite materials can be synthesized effectively.

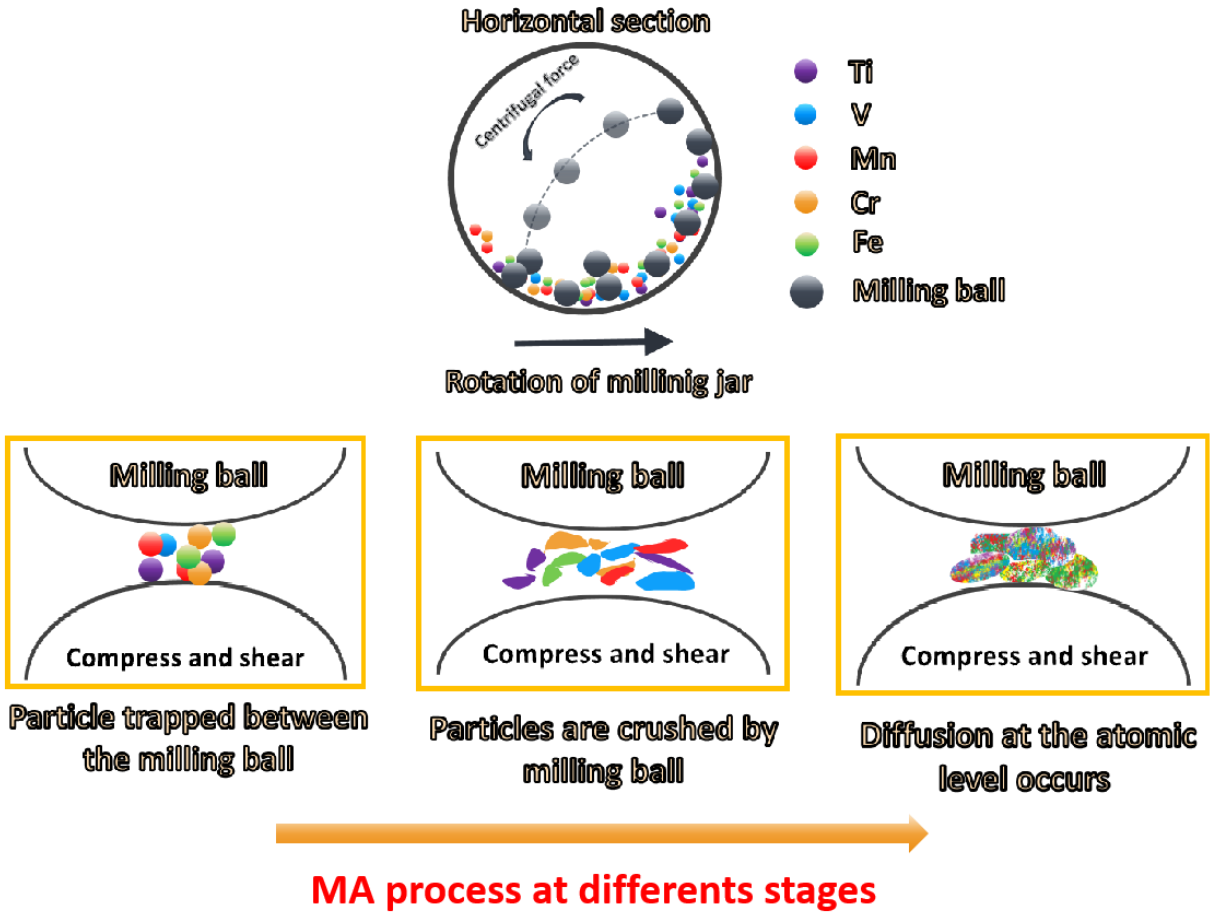

Fig 3.3 Schematic diagram of the different stages of the ball milling process

The advantage of ball milling lies in its ability to produce refined microstructures, such as nanocrystalline structures, while ensuring a homogeneous distribution of elements. This technique is widely applied in the fabrication of high-entropy alloys [196], nanocrystalline materials [197], intermetallic compounds [198], and other materials with special properties. However, certain challenges persist in the ball milling process, such as the potential introduction of impurities and extended experimental durations. Thus, optimizing the ball milling parameters is essential for achieving desirable material properties.

In this study, various ball milling parameters, including the manufacturing material, ball-to-powder ratio, milling time, and rotation speed, were explored to assess their impact on the mechanical alloying process. The optimal ball milling parameters will be discussed in detail in the research discussion section. The specific milling equipment model and parameter

adjustments are listed in the following table:

Table 3.2 Specific parameters of ball milling process
(The optimized ball milling parameters are provided in the Table 4.5 in Chapter 4)

Milling parameters	Details
Model	Fritsch Pulverisetter-6, Idhar-Oberstien, Germany
Milling jar	500ml
Milling ball radius	Half ft. (1.5cm)
Manufacturing material	304 stainless steel/high Cr steel
Ball milling time	0-60 hrs
Ball to powder weight ratio	5:1, 10:1, 20:1
Milling speed	0 - 500 rpm
Milling atmosphere	Ar gas (99.99 wt%)
Process control agents	Ethanol (C_2H_5OH)

3.2 Microstructure characterizations

3.2.1 Preparation of observation samples

In the experimental methodology, sample preparation is crucial for accurate microstructural analysis. To ensure that samples remain undamaged during microscopy (such as scanning electron microscopy (SEM)) and present a stable, clear surface for observation, embedding (mounting) techniques are typically employed to encapsulate the sample. In this experiment, a combination of resin and hardener was used to embed the samples, ensuring structural integrity and facilitating further processing and analysis.

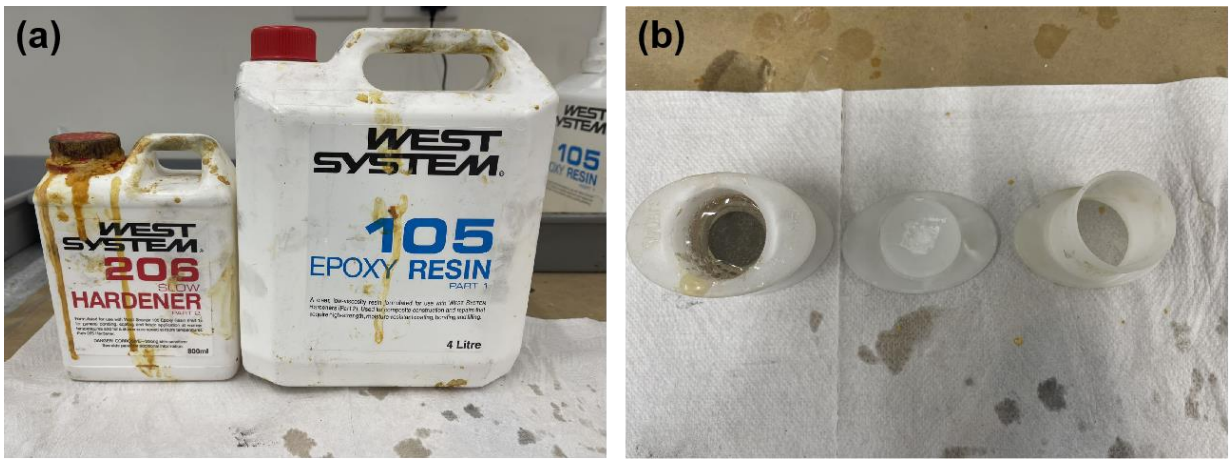

Fig 3.4 (a) Hardener and Epoxy resin; (b) mounting mold

First, the sample is placed in a mounting mold (Fig 3.4 b), ensuring that the critical observation surface is oriented correctly. The embedding material, typically epoxy resin or acrylic resin [199] (Fig 3.4 a), is selected due to its excellent mechanical strength and stability, providing robust protection once cured. To ensure full coverage of the sample during embedding, the resin and hardener are mixed according to the recommended ratio (hardener: resin = 4.44:1), with careful stirring to avoid the formation of air bubbles, which could create voids and negatively affect the quality of the sample surface after curing. Next, the mixed resin is poured into the mold, completely covering the sample. The sample and mold are left to cure at room temperature or slightly elevated temperatures, depending on the properties of the resin and hardener used. Curing times vary from several hours to a full day, during which care is taken to avoid contamination or mechanical damage to the sample's surface.

3.2.2 Sample grinding and polishing

In the sample preparation process, grinding and polishing are essential to achieve a smooth and defect-free surface suitable for microstructural analysis. In this experiment, a manual grinder (Fig 3.5 a) was used with progressively finer sandpapers, starting from 200 mesh, followed by 500 mesh, 1000 mesh, and finally 2000 mesh sandpaper. This approach effectively removes excess resin and surface imperfections, ensuring a flat, less scratch surface that is ready for the polishing stage. After grinding, an automatic polishing machine (Fig 3.5 b) was employed for

a 30 minutes polishing process. An OPS-Non dry (oxide polishing suspension, Fig 3.5 c) was used during polishing, containing fine particles (0.25 μm) that help further smooth the surface and eliminate micro-scratches left from the sanding process. The automatic polishing machine ensures even and consistent pressure (20 N) throughout the process, resulting in a mirror-like surface ideal for SEM and other microstructural analyses.

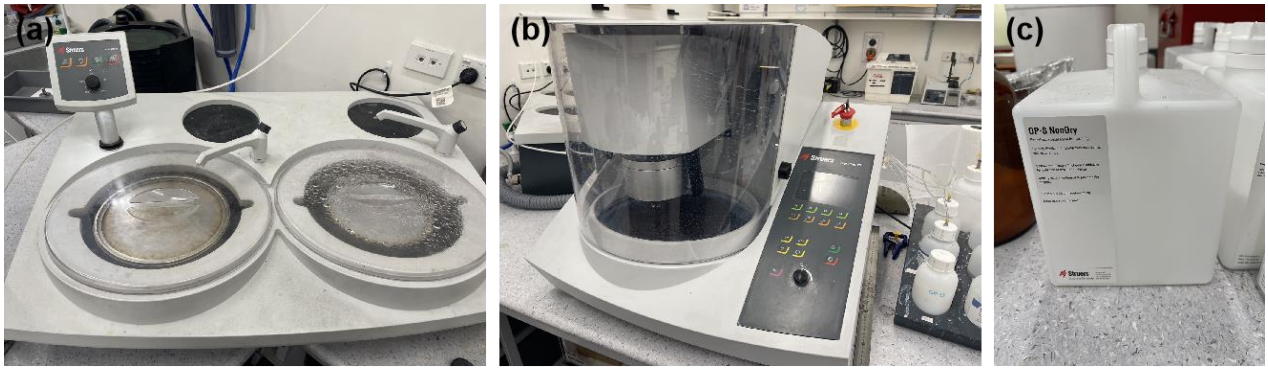

Fig 3.5 (a) Struers Labopol-60 Polishing Table; (b) Struers Tegramin-25 Automatic Polisher; (c) OPS-Non day (oxide polishing suspension)

3.2.3 X-ray diffraction (XRD)/Rietveld refinement method

X-ray diffraction (XRD) is a widely used characterization technique for analyzing the crystal structure of high-entropy alloys (HEAs). XRD works by measuring the diffraction angles of X-rays as they interact with the crystal planes of a material, allowing researchers to determine its phase composition and crystal structure parameters [200]. In this study, a Panalytical Empyrean X-ray diffractometer show in Fig 3.6 (Malvern, United Kingdom) with a Cu Kα radiation source (λ = 0.154157 nm) was employed to perform the analysis. To ensure high-resolution XRD patterns, the instrument was operated at a high voltage of 40 mA and 55 kV, with a slow scan rate and a step size of 0.003°, which helps capture subtle variations in crystal phases and structural details.

Fig 3.6 Panalytical Empyrean X-ray diffractometer

This high-precision XRD setup provides a wealth of information about the crystal structure, particularly useful in studying multiphase systems or lattice distortions. The slow scanning mode and high voltage settings enable the precise identification of various phases, as well as the detection of crystal defects or distortions, offering deeper insights into the relationship between the microstructure and the performance of the HEAs.

The analysis of X-ray diffraction data was further refined using the Rietveld refinement method [201]. This widely applied full-profile fitting technique is based on the least squares method, optimizing the crystal structure parameters by minimizing the differences between the theoretical and experimental diffraction patterns. In this study, MADU software was used for XRD refinement, leveraging its robust data processing capabilities to handle complex multiphase systems [202].

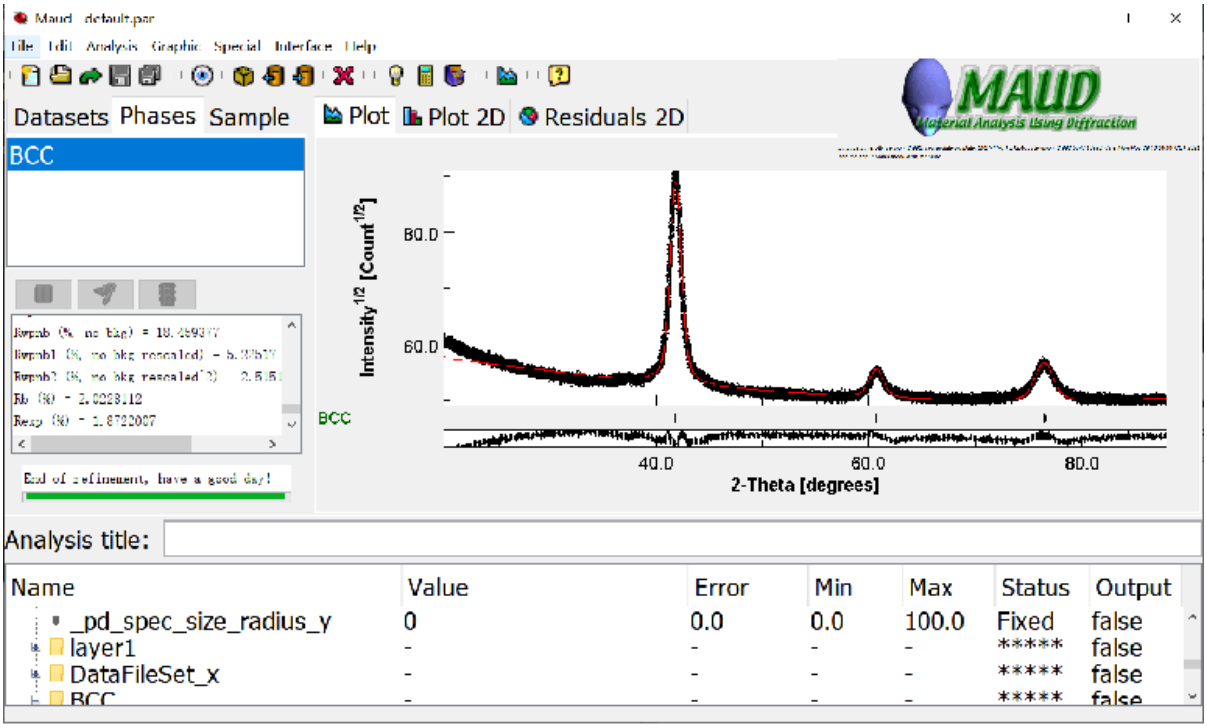

Fig 3.7 The user interface of the MAUD software

Through refinement with MADU (Fig 3.7), the XRD patterns were accurately fitted, providing detailed information on the crystal structure. This process allowed for the determination of phase compositions, lattice parameters, and other critical structural features [202]. Such information is crucial for further understanding the relationship between the microstructure and performance of high-entropy alloys (HEAs), offering theoretical support and insight into their structural properties.

3.2.4 Scanning electron microscopy (SEM)/Transmission electron microscopy (TEM)

Scanning electron microscopy (Ultra-High Resolution Scanning Electron Microscope (UHR-SEM, Regulus, SU8230)) was employed as a key tool for characterizing the microstructure of the high-entropy alloys (HEAs). SEM utilizes an electron beam to interact with the surface of the sample [203], generating high-resolution images that reveal the morphology and microstructural features of the HEAs. One of the main advantages of SEM is its high magnification capability combined with a large depth of field, which allows for detailed

microstructural analysis.

In this experiment, SEM was used to observe samples after grinding and polishing, with the parameters such as accelerating voltage (20 kV), backscatter mode and working distance (8 - 15 mm) optimized to ensure image clarity and contrast based on the specific requirements of the sample. Eenergy-dispersive X-ray spectroscopy (EDS) was integrated to analyze the elemental distribution within the alloy further. By combining backscattered electron (BSE) imaging with EDS, it was possible to obtain microstructural images and analyze elemental content and distribution across the sample. Finally, the SEM images were utilized to compare microstructural changes under different experimental conditions, and the results were combined with other characterization techniques such as XRD and TEM to provide a comprehensive analysis of the structural evolution of the alloys. Additionally, to obtain clearer images and prevent the sample from drifting during high-magnification observation, a thin layer of conductive metal coating is typically applied to the sample surface. In this experiment, a platinum (Pt) coating was used. Platinum, with its excellent electrical conductivity, effectively eliminates the charge accumulation that would otherwise occur on the non-conductive resin surface, thus ensuring clear imaging and accurate data acquisition.

The JEOL 2100F transmission electron microscopy (TEM) was used to characterize the microstructure of the high-entropy alloys (HEAs), particularly for observing nanoscale phase structures. Unlike scanning electron microscopy (SEM), TEM allows the electron beam to penetrate the sample, producing high-resolution images that provide detailed information about the crystal structure [204]. During TEM analysis, samples often require the preparation of ultra-thin sections; however, the preparation process for powder samples is relatively complex. The powder is suspended in alcohol and subjected to repeated ultrasonic treatment, after which the upper clear liquid is collected and dropped onto a copper grid for drying [205]. TEM not only offers microstructural images but can also be coupled with energy-dispersive X-ray spectroscopy (EDX) to analyze the local elemental distribution and chemical composition of the sample. Additionally, selected area electron diffraction (SAED) can be used to further

determine the crystal orientation, phase composition, and related structural information. The results obtained from TEM are combined with data from other characterization techniques such as XRD and SEM, providing a more comprehensive analysis and helping to reveal the relationship between the alloy's microstructure and its hydrogen storage performance.

3.2.5 Particle size distribution

The particle size distribution of the alloy after ball milling were measured using laser diffraction technology. Laser diffraction is a commonly used method for particle size analysis, determining particle size by measuring the scattering angle and intensity of a laser beam as it interacts with the particles. The basic principle of this technique is that larger particles scatter light at smaller angles, while smaller particles scatter light at larger angles. By analyzing the distribution of scattered light, the particle size and its distribution can be accurately calculated. In this experiment, a Malvern Panalytical Mastersizer 3000 (Fig 3.8) particle size analyzer was used for the measurements. The as milled HEAs powder, after ball milling, was dispersed in a liquid medium (water or ethanol) with continuous ultrasonication to prevent particle agglomeration during the measurement process. The measurements were repeated three times, and the average value was obtained. Data analysis was performed using the SOP Architect software.

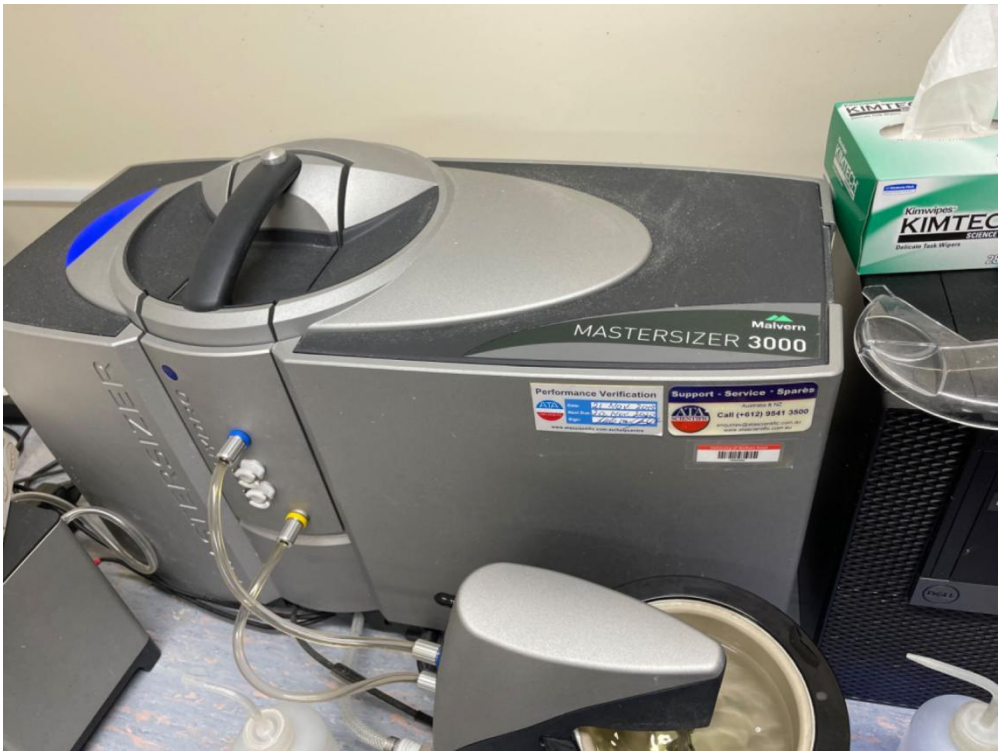

Fig 3.8 The Malvern Panalytical Mastersizer 3000 particle size analyzer

3.3 Thermodynamic characterization

3.3.1 Differential scanning calorimetry (DSC)

Differential scanning calorimetry (DSC) show in Fig 3.9 was employed for thermodynamic characterization, with the primary aim of determining the phase transition temperatures of the high-entropy alloys (HEAs) to guide subsequent heat treatment processes. DSC is a widely used thermal analysis technique that measures the heat absorbed or released by a sample during heating or cooling, allowing for the identification of phase transitions, reaction processes, and thermal stability of the material. In this study, the heating rate was set to 10°C/min, with the temperature range spanning from room temperature (approximately 25°C) to 1300°C, covering the temperatures at which various solid-state phase transitions may occur in the HEAs.

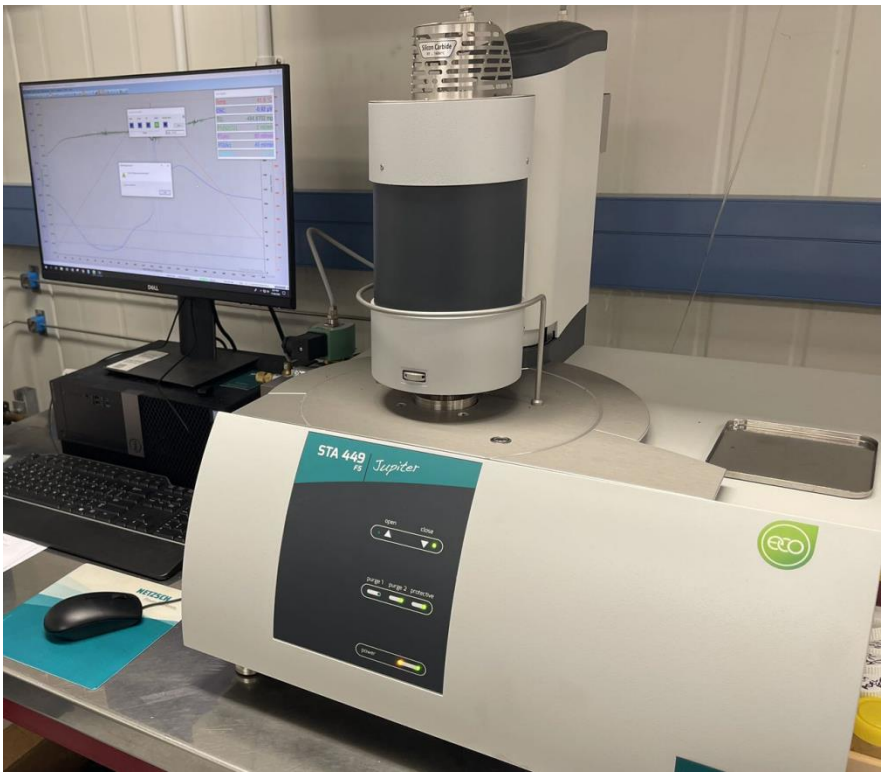

Fig 3.9 The Simultaneous Thermal Analysis (Netzsch Jupiter STA449 F5)

3.3.2 Heat Treatment

In this experiment, the samples were heat-treated using a vacuum sintering furnace (Fig 3.10) with a vacuum level reaching 10^-3 Pa. This high-vacuum environment effectively prevents the samples from reacting with impurities such as oxygen and nitrogen in the air at elevated temperatures. To ensure consistency with the heating conditions of the DSC, the heating rate for the heat treatment was also set to 10°C/min, allowing for a uniform temperature increase and precise control of phase transformations. The heat treatment temperatures were set at 300°C, 600°C, and 900°C, aimed at observing the evolution in phase structures at different temperature stages. Each sample was held at the target temperature for 3 hours to ensure that the phases became more stable and uniform.

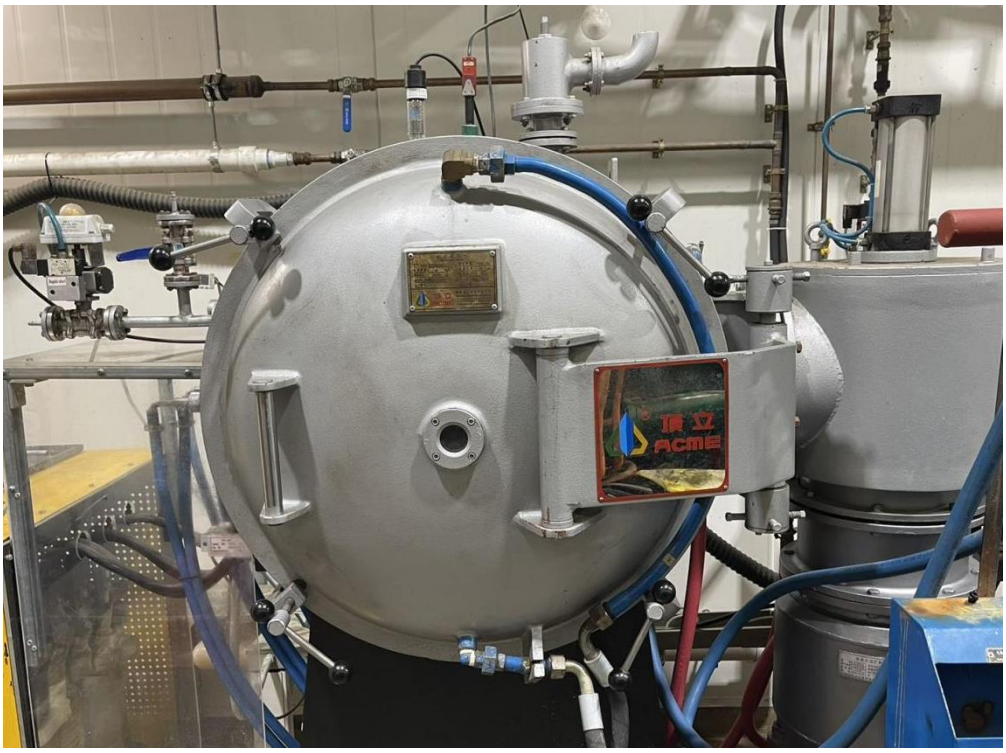

Fig 3.10Vacuum sintering furnace

3.3.3 Calculations of phase diagram (CALPHAD)

In this experiment, Thermo-Calc software was used for phase diagram calculations, utilizing the TCHEA6 database provided by Inner Mongolia University of Science and Technology. Thermo-Calc is a computational tool based on thermodynamic and phase equilibrium theories, widely applied in alloy design, phase diagram prediction, and heat treatment process optimization [206]. The software calculates phase transitions, phase compositions, and thermodynamic parameters under equilibrium conditions, enabling researchers to analyze the phase behavior of multicomponent alloy systems.

The core principle of Thermo-Calc relies on the minimization of Gibbs free energy to achieve thermodynamic equilibrium [207]. By minimizing the total free energy of the system, the software can determine the stable phases at various temperatures and predict phase compositions under multiphase equilibrium conditions. This approach is particularly effective for investigating complex alloy systems, especially high-entropy alloys (HEAs), where phase

diagram calculations provide critical theoretical guidance for predicting phase composition in these multicomponent systems.

3.4 Hydrogen storage performance

3.4.1 High-Pressure (H_2 condition) differential scanning calorimetry (HDSC)

In this experiment, the first hydrogen absorption temperature of the alloy was determined by placing the sample in a high-pressure differential scanning calorimeter (NETZSCH High-Pressure DSC (DSC 204 HP Phoenix)) under a hydrogen atmosphere, and gradually increasing the temperature. The specific procedure involved heating the sample at a constant rate of 10°C per minute. Since hydrogen absorption is an exothermic reaction, a distinct exothermic peak appears on the DSC curve when the alloy begins to absorb hydrogen. By observing and recording the temperature at which this exothermic peak occurs, the initial hydrogen absorption temperature of the alloy can be identified. The first hydrogen absorption temperature of the alloy provides valuable information for guiding the subsequent activation of the alloy and comparing the activation difficulty of different alloys.

3.4.2 Hydrogen storage performance testing

In this experiment, the hydrogen absorption and desorption performance were evaluated using an H-Sorb 2600 high-pressure gas adsorption analyzer (Beijing CI-Ultrametrics Technology Co., Ltd.), which is a Sievert-type apparatus. The Sievert method [208] is a classical gas adsorption measurement technique widely used for characterizing hydrogen storage materials. It determines the material’s capacity to absorb or desorb hydrogen by measuring the changes in gas volume. The principle of the Sievert-type apparatus involves placing the sample in a sealed pressure vessel and gradually varying the gas pressure to observe the sample's hydrogen absorption or desorption behavior. During hydrogen absorption, as the pressure increases, hydrogen molecules are absorbed by the material, and the equipment monitors the changes in

gas pressure and volume to calculate the hydrogen uptake. Conversely, when the pressure is reduced, the hydrogen stored in the material is released, and the equipment records the pressure changes and gas volume to determine the amount of hydrogen desorbed. The PCT test of the HEAs was conducted within a hydrogen pressure range of 0.01 to 5 MPa to obtain its pressure-composition isotherms. During the hydrogen absorption process, the pressure was increased in increments of 0.5 MPa, with an absorption time of 30 minutes for each step. The desorption process followed the reverse procedure, where the pressure was reduced by 0.5 MPa per step, with a desorption time of 30 minutes. All PCT measurements were performed after the complete activation. The cyclic performance tests of the alloys were conducted using GASPRO, Setaram Kep Technologies, France equipment at the University of Waikato, New Zealand, with the activation method remaining unchanged. For the as-milled alloys, after activation and hydrogen absorption at room temperature, the temperature was increased to 300°C under vacuum, followed by cooling to room temperature for testing. For the arc-melted alloys, the vacuum treatment was performed at 400°C.

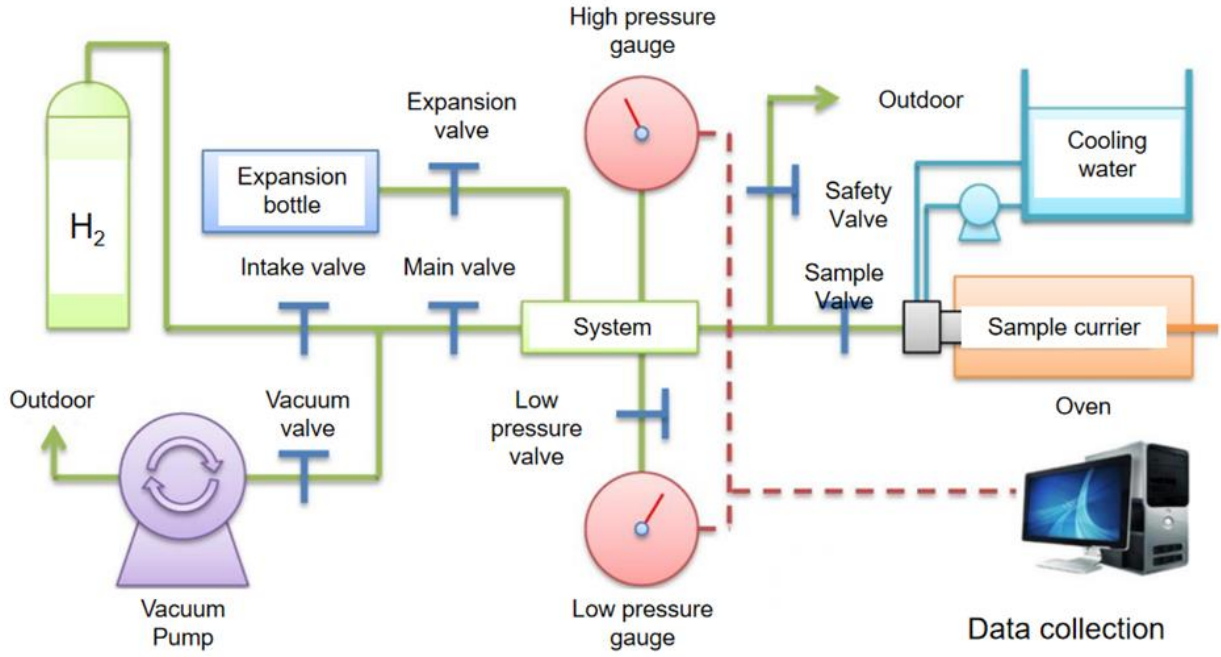

Fig 3.11 Schematic diagram of hydrogen storage device

3.4.2.1 Hydrogen storage activation process

The hydrogen activation process was conducted at 300°C under a pressure of 5 MPa for a duration of two hours, followed by vacuum treatment for one hour. This process was repeated three times. The activation was considered successful when the hydrogen absorption curve from the final cycle closely matched the previous one, indicating that the material had been fully activated. After completing the activation process, the sample was subjected to vacuum at 300°C for an additional two hours to ensure complete hydrogen desorption from the alloy at that condition.

3.4.2.2 Hydrogen storage absorption/desorption testing

In this experiment, the hydrogen absorption/desorption kinetics of the HEAs were measured under 5 MPa of hydrogen pressure, with the testing temperature adjusted according to specific requirements. The XRD measurements for the fully hydrogenated state were conducted at the alloy's maximum hydrogen absorption temperature, which is room temperature, to determine the formation of hydrides. The XRD for the desorbed state was performed after vacuum treatment at 300°C for two hours, ensuring that all absorbed hydrogen had been fully released from the alloy at that condition.

3.4.2.3 Hydrogen storage pressure–concentration–temperature (PCT) test

In this experiment, the pressure-composition-temperature (PCT) tests were conducted after the alloy had been fully activated and completely desorption. The procedure involved incrementally increasing the pressure by 0.2 MPa during the hydrogen absorption process, until reaching the final pressure of 5 MPa. During the desorption process, the pressure was gradually reduced, also in steps of 0.2 MPa, until atmospheric pressure or vacuum conditions were achieved. Due to the excellent kinetics of the alloy, a waiting time of 30 minutes was sufficient after each pressure increase or decrease to allow the system to reach equilibrium.

4. Investigation on fabrication of HEAs powders via mechanical milling

In the field of materials science, ball milling is an efficient mechanical alloying method widely used for refining and alloying metal powders. This process introduces high-energy mechanical forces to facilitate cold welding, fracture, and rewelding of powder particles, thereby achieving atomic-level mixing and phase transformation. Key parameters in the ball milling process, such as milling ball/jar material, milling time, ball-to-powder ratio, and rotational speed, significantly influence the phase structure of the alloy. Optimizing these parameters is crucial for obtaining the desired phase structure.

In this study, we systematically investigate the effects of different ball milling parameters on the phase composition of the $Ti_{15}V_{35}(CrMnFe)_{50}$ HEA. Based on previous research on synthesis of NiMnFeCr high entropy alloy using ball milling in our research group [209], this study initially selected a milling time of 15 hours, a ball-to-powder ratio of 10:1, a rotational speed of 350 rpm, and 1 wt% process control agent (ethanol) as the baseline conditions. Through a systematic investigation, the effects of milling material, milling time, ball-to-powder ratio, rotational speed, and process control agent on the phase composition of the alloy were investigated. Following the successful optimization of the $Ti_{15}V_{35}(CrMnFe)_{50}$ alloy, these findings will be applied to the fabrication of other high-entropy alloy compositions.

4.1 Morphology of raw material

In ball milling processes, the initial particle size of the powder is typically selected based on the specific requirements of the process and the desired characteristics of the final material. Generally, a particle size range of 10 to 100 μm is considered optimal [210]. Larger particles may hinder certain elements from dissolving fully into the matrix or require extended mechanical alloying time to achieve the desired results, which increases the risk of

contamination in the alloy powder. In such cases, intermittent milling may be required to mitigate this issue. On the other hand, smaller particle sizes can lead to agglomeration during the early stages of mechanical alloying, resulting in uneven alloy distribution [211]. Therefore, selecting an appropriate particle size is a critical factor in improving both the efficiency and success rate of mechanical alloying. Fig 4.1 shows the morphology of the raw powder, with specific parameters provided in the research methodology section. The particle sizes are uniformly distributed, with all diameters less than 45 microns. No excessively large or small particles were observed, indicating that the powder size distribution is optimal for the milling process. This uniform size selection helps ensure the stability of the ball milling process and promotes homogeneous alloying. An appropriate particle size not only enhances the efficiency of mechanical alloying but also minimizes potential issues such as agglomeration or incomplete alloying during the milling process.

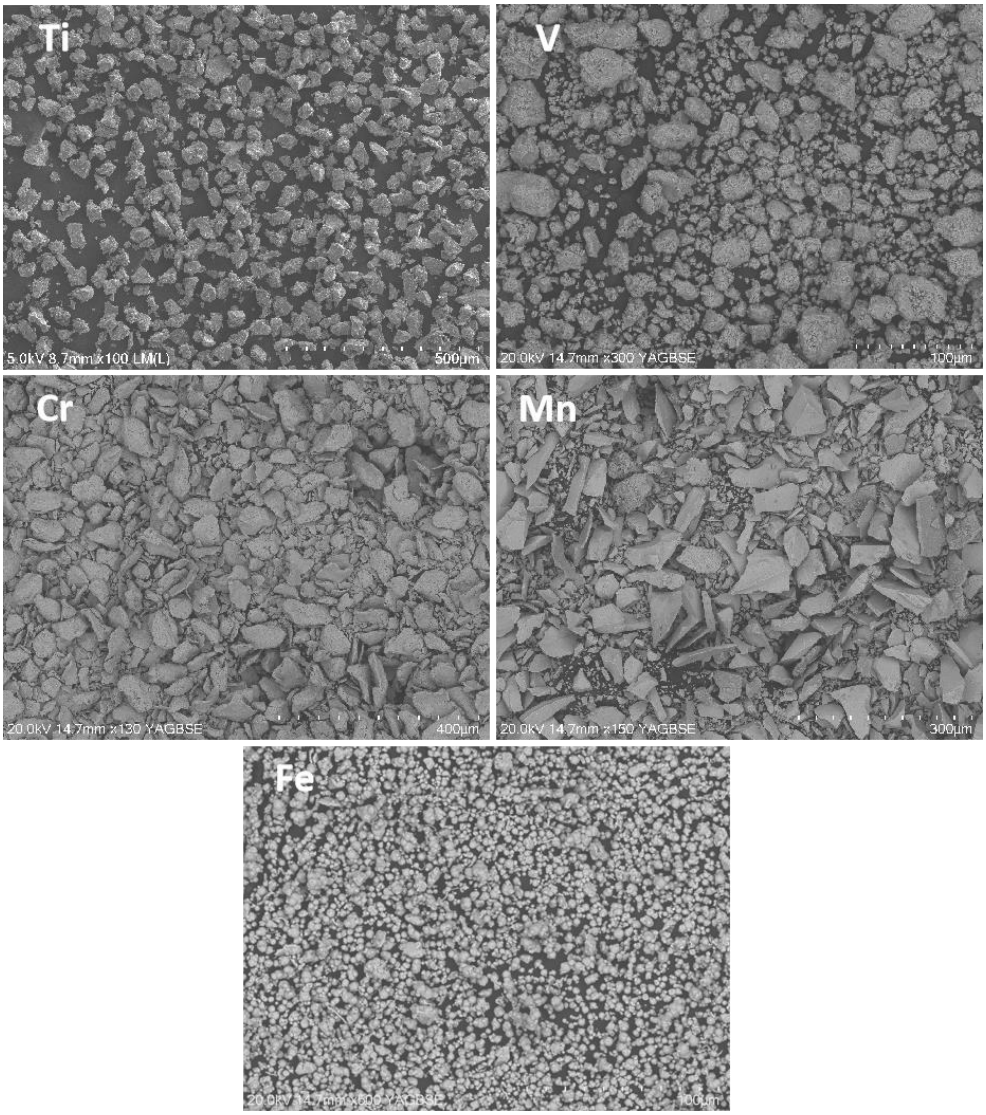

Fig 4.1 SEM Morphology of raw elemental powder: (a) Ti; (b) V; (c) Cr; (d) Mn; (e) Fe

4.2 Material of the milling balls and jars

In the ball milling process, the material of the milling balls and milling jars has a significant impact on the final composition of the alloy. This is especially in high-energy ball milling, where the hardness of the materials used for the milling media greatly influences the extent of contamination introduced during the mechanical alloying process. Typically, milling jars and milling balls are made of the same material to ensure uniform wear and minimize contamination. In this study, we explored the effects of milling balls and jars made from two different materials (304 stainless steel and high carbon chrome steel), with varying hardness

levels, on the final composition of the HEA. Fig 4.2 and 4.3 present the elemental distribution of high-entropy alloys (HEAs) milled with different materials. From the figures, it is evident that Fe enrichment occurred in the alloys milled using 304 stainless steels as the grinding material. This is likely due to wear on the grinding media during the milling process, causing Fe to be introduced into the alloy, leading to contamination. In contrast, the alloys milled with high-carbon chromium steel show a more uniform elemental distribution, with no visible Fe enrichment. This can be attributed to the lower hardness of 304 stainless steel (20 HRC), which is more prone to wear when colliding with harder elements such as V (45 HRC) and Cr (60 HRC), resulting in Fe contamination. However, the higher hardness of high-carbon chromium steel (65 HRC) prevents significant Fe wear, and thus no Fe enrichment was observed.

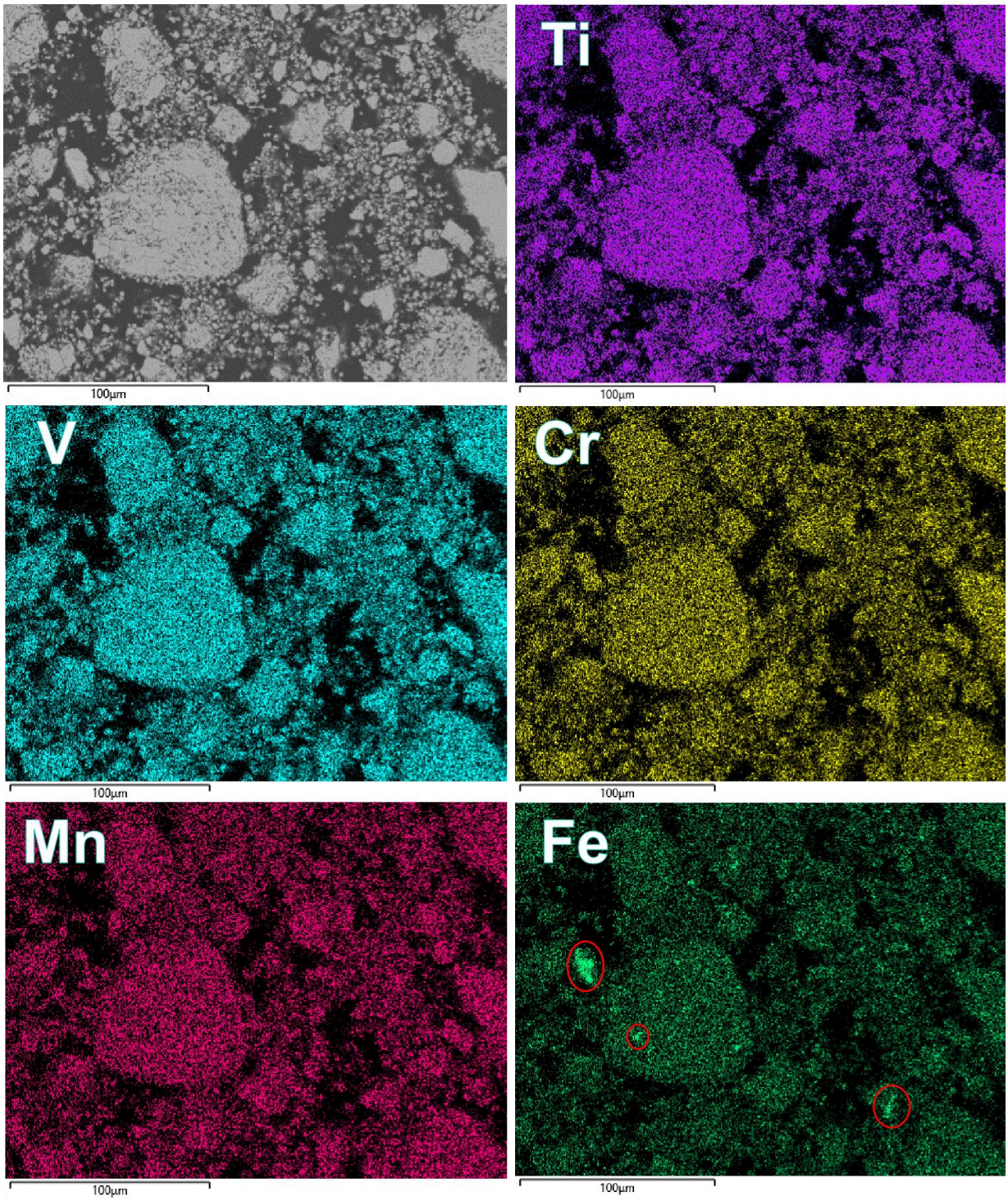

Fig 4.2 The BSE image and elements distribution of HEA milled by 304 stainless steels

Fig 4.4 (a) and (b) illustrate the atm% of individual elements in the high-entropy alloys (HEAs) fabricated using different materials. It is evident from the figures that the Cr and Fe content in the alloys milled with 304 stainless steel ball/jar is significantly higher than the designed composition, due to the fact that Fe and Cr are the primary constituents of 304 stainless steel.

In contrast, the HEA fabricated using high-carbon chromium steel show element concentrations that closely align with the nominal values, indicating much lower contamination.

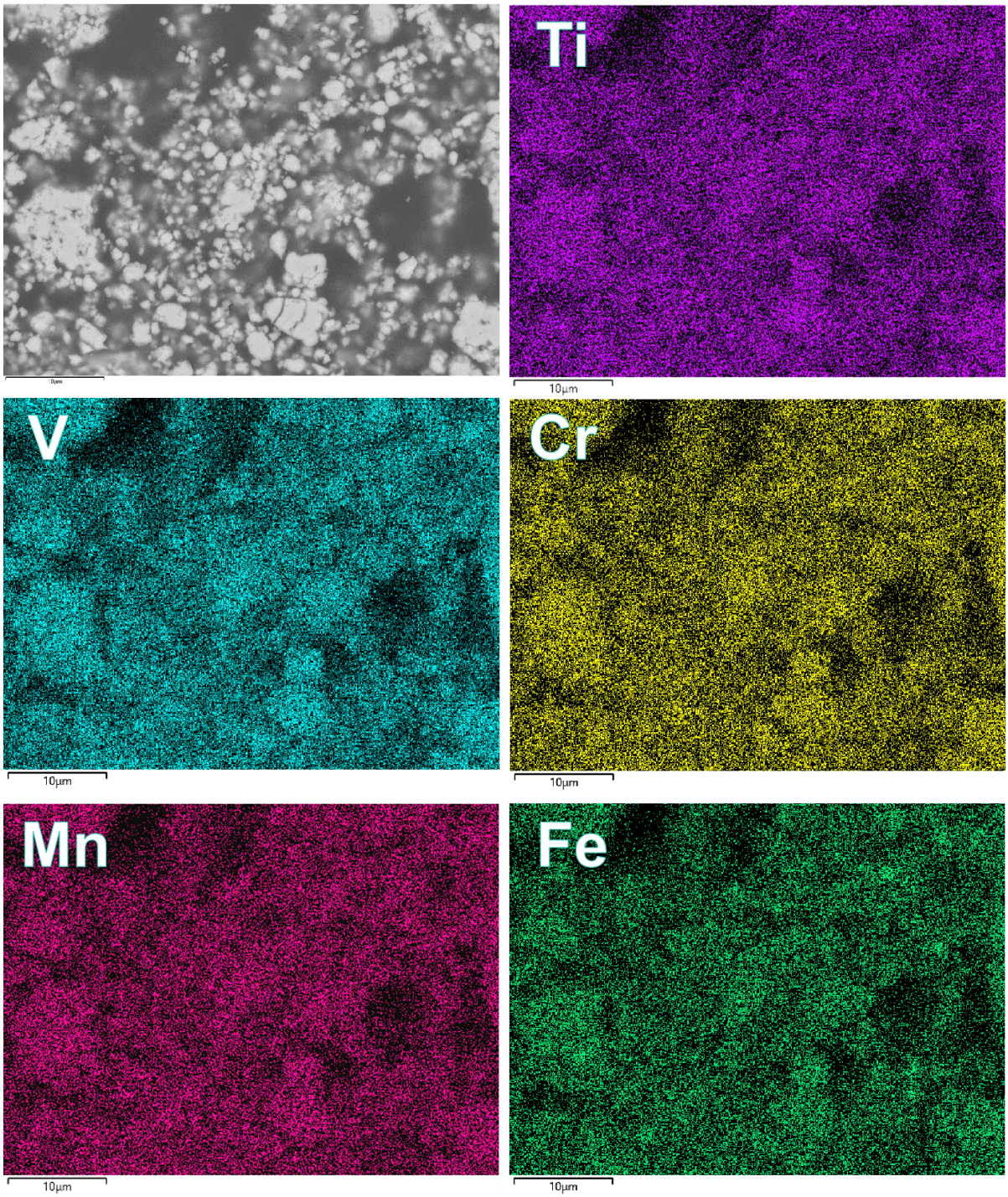

Fig 4.3 The BSE image and elements distribution of HEA milled by high carbon chrome steel

Furthermore, the excessive incorporation of Cr and Fe leads to a reduction in the lattice constant

of the body-centered cubic (BCC) structure. This occurs because Cr and Fe have smaller atomic radii, and their extensive solid solution into the alloy matrix decreases the overall average atomic radius, consequently reducing the lattice constant (show in Fig 4.4 c). Based on this analysis, high-carbon chromium steel will be selected as the preferred milling material for future alloy preparation. Its use results in minimal contamination, yielding alloys with more uniform elemental distribution and element concentrations that are closer to the designed values.

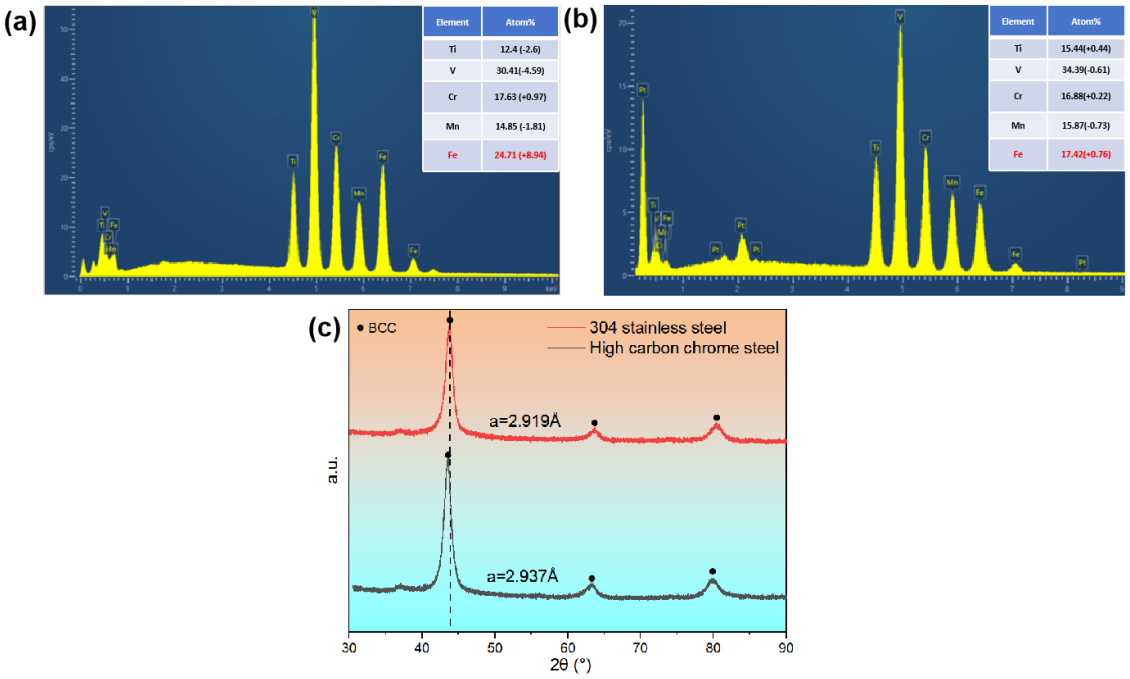

Fig 4.4 (a) The measured atm% values and EDS spectrums of HEA milled by 304 stainless steels; (b) the measured atm% values and EDS spectrums of HEA milled by high carbon chrome steel; (c) the XRD patterns of HEA after ball milling by different materials

4.3 Effect of milling time on phase evolution of $Ti_{15}V_{35}(CrMnFe)_{50}$ HEA

Milling time is one of the critical parameters in the ball milling process, directly influencing the microstructure and the phase composition of the alloy [171, 212]. Typically, the milling time needs to strike a balance between particle fracture and cold welding, leading to the formation of a stable phase structure [213]. The required milling time depends on various factors, including the type of milling machine used, the ball-to-powder ratio, and the rotational speed, all of which contribute to the energy input and material response during the milling process. However, a lot of studies have shown that once the phase structure stabilizes, extending the milling time does not further improve material properties. Instead, it can lead to contamination from wear of the milling balls or jars, increasing the risk of impurity introduction [209]. Moreover, prolonged milling may induce unwanted phase transformations [214]. Therefore, the optimal strategy is to precisely control the milling time, processing the powder only for the necessary duration. Avoiding excessive milling time helps minimize contamination and prevent negative effects on the material caused by unnecessary prolongation.

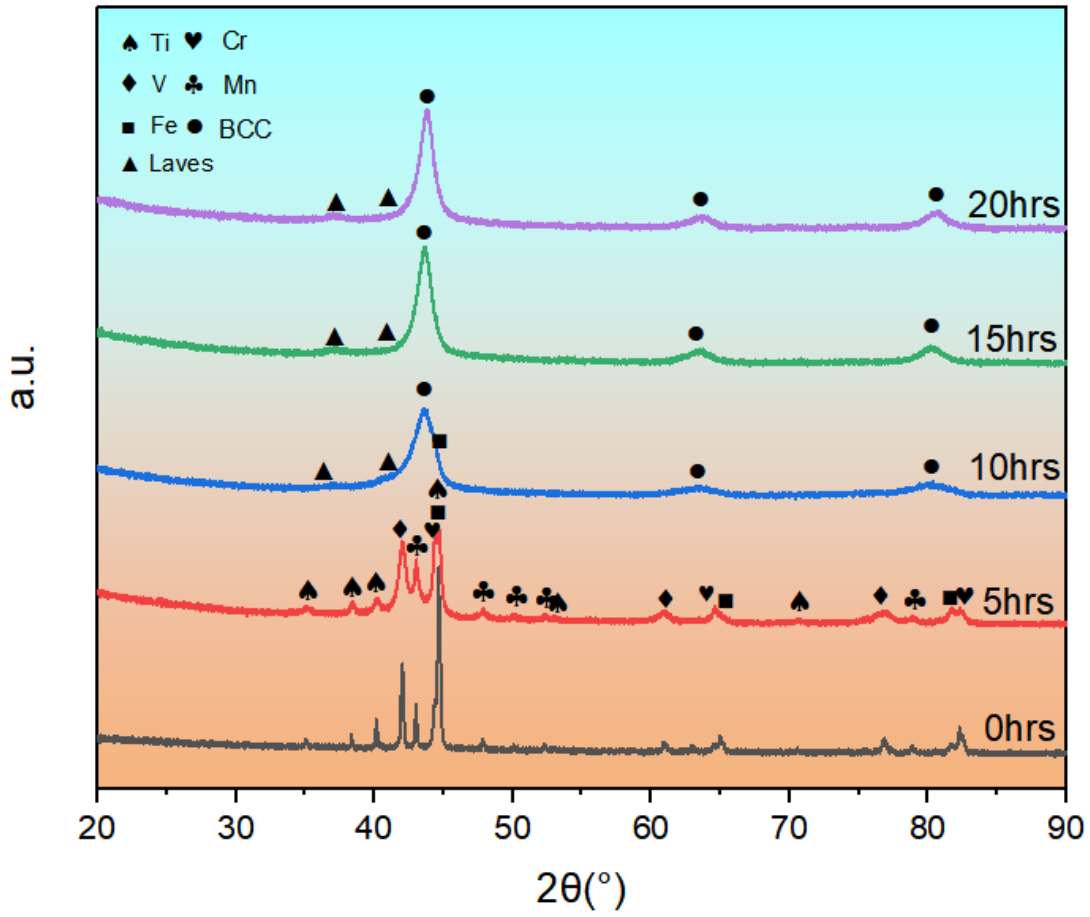

Fig 4.5 X ray diffraction patterns of the milled $Ti_{15}V_{35}(CrMnFe)_{50}$ HEA with different milling time under BPR 10:1 and milling speed 350rpm

Fig 4.5 illustrates the X-ray diffraction (XRD) patterns of the $Ti_{15}V_{35}(CrMnFe)_{50}$ alloy at different ball milling times. In the un-milled state, the XRD pattern clearly displays the characteristic diffraction peaks corresponding to Ti, V, Cr, Mn, and Fe, indicating the distinct presence of the individual metallic elements. After 5 hours of ball milling, the diffraction peaks of these elements broaden and weaken to varying degrees, signifying the initiation of particle fracture and cold welding processes. However, several distinct elemental peaks are still observable, indicating that the alloy is still in the initial stages of the ball milling process.

As the ball milling time is extended to 10 hours, the XRD patterns reveal prominent peaks corresponding to the body-centered cubic (BCC) structure, along with minor Laves phases and residual Fe element peaks. The presence of Fe is likely attributed to its smallest atomic radius

(124.12 pm), which makes it more difficult for Fe atoms to dissolve into the BCC structure, leaving a trace amount of Fe as a separate phase in the XRD patterns. By the time the ball milling duration reaches 15 hours, the BCC structure becomes the dominant phase, as indicated by the increased intensity of the corresponding diffraction peaks. At this stage, the Fe peaks have largely disappeared, suggesting that Fe has gradually dissolved into the alloy matrix. This shift reflects a stabilization of the BCC phase and a more homogeneous distribution of elements within the alloy

After 20 hours of ball milling, the XRD pattern shows no significant changes compared to that at 15 hours, indicating that a stable phase structure had already been established by the 15 hours. However, a slight shift of the peak positions (BCC phase) toward lower angles is observed, suggesting that the lattice constant may have decreased slightly due to the prolonged ball milling. This peak shift could be attributed to lattice distortion and the accumulation of strain caused by extended milling, or possibly due to contamination from Fe, which could have altered the overall lattice parameters.

Overall, with the increase in ball milling time, the phase structure of the alloy gradually transitions from an initial multi-metal mixture to a structure dominated by the BCC phase, with a small amount of Laves phase as a secondary phase. This indicates that milling time is one of the key factors influencing the phase composition of the $Ti_{15}V_{35}(CrMnFe)_{50}$ alloy. However, excessively long milling times may not further stabilize the phase structure; instead, they may introduce slight lattice distortion and elemental contamination. Therefore, determining the optimal ball milling time is critical for optimizing the phase structure of the alloy.

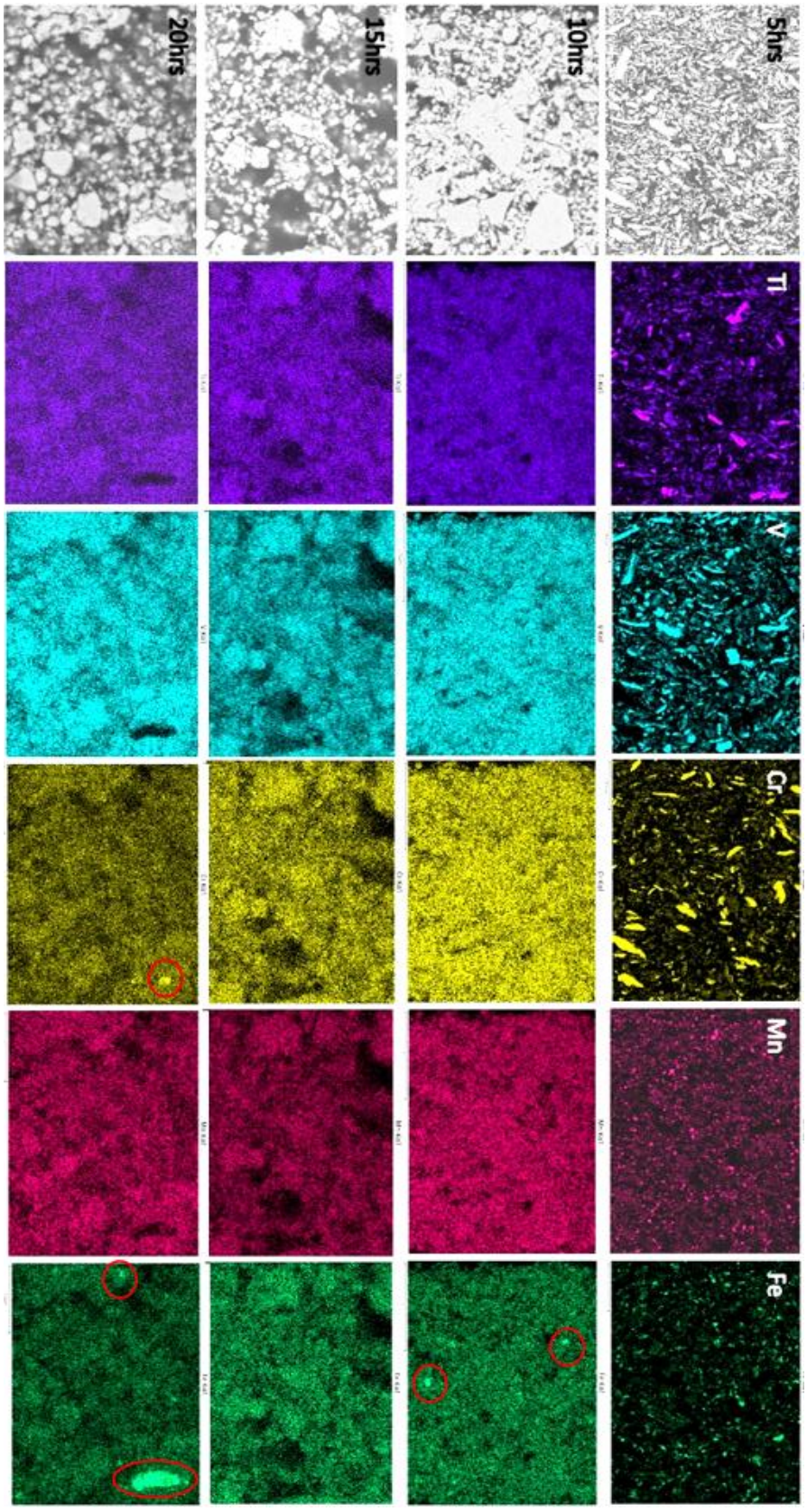

Fig 4.6 The BSE image and EDS elements mapping of the HEAs milling by different hours

The Fig 4.6 presents the distribution of elements (Ti, V, Cr, Mn, Fe) in the Ti15V35(CrMnFe)50 alloy at different ball milling times. After 5 hours of ball milling, the element distribution is uneven, showing significant elemental segregation, indicating that elements diffusion between atomic level has not yet begun. The particle size remains relatively large, but the process of powder fracture and cold welding has initiated (show in Fig 4.7), signaling the early stages of mechanical alloying. As the ball milling time increases (up to 10hrs), the distribution of elements becomes more uniform, indicating that atomic-level diffusion has begun between the elements and that a predominantly BCC structure is gradually forming (show in Fig 4.6). However, minor Fe segregation is still observable, which is consistent with the findings from the XRD pattern (Fig 4.6).

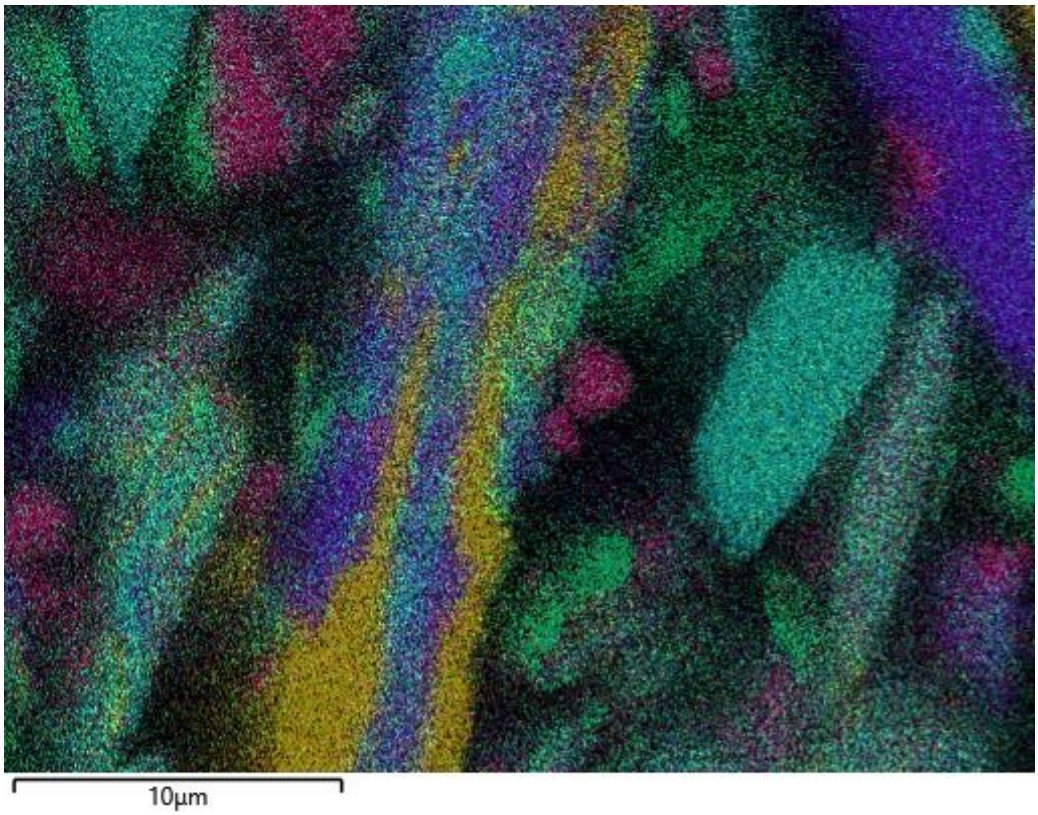

Fig 4.7 The EDS elements over layer mapping image of 5hrs milling (the element types represented by different colors are the same as in Fig 4.6)

After 15 hours of ball milling, the distribution of elements in the alloy becomes uniform, with no evidence of elemental segregation. However, the presence of a second phase cannot be

detected, which may be attributed to the resolution limitations of the scanning electron microscope (SEM) or the extremely low content of the second phase. It is also worth noting that due to the nanoscale grain size and significant lattice distortion in the alloy after ball milling, observing the second phase in transmission electron microscopy (TEM) also be challenging. When the ball milling time up to 20 hours, the EDS mapping reveals a significant accumulation of Fe and Cr elements. This is likely due to excessive wear of the milling balls after the alloy's structure has stabilized, resulting in contamination of the alloy composition. Since the milling balls primarily consist of Fe and Cr, their attrition during prolonged ball milling leads to the enrichment of these elements in the alloy. Table 4.1 presents the specific elemental composition (atm%) of the alloy at different ball milling durations. It can be observed that when the milling time is less than 15 hours, the alloy's elemental composition closely aligns with the designed composition. However, at 20 hours of milling, the contents of Fe and Cr increase significantly, deviating considerably from the intended composition. This deviation suggests that prolonged milling results in contamination due to wear of the milling balls. Based on the XRD analysis, EDS elemental distribution, and the specific elemental contents, 15 hours of milling is identified as the optimal ball milling times, ensuring composition stability with minimal contamination.

Table 4.1 Represents the measured atm% values of each element present in the as-milled $Ti_{15}V_{35}(CrMnFe)_{50}$ HEA

Time	Ti	V	Cr	Mn	Fe
5hrs	**16.63**	**35.78**	**16.60**	**15.32**	**15.68**
10hrs	**15.38**	**35.26**	**16.61**	**15.61**	**17.14**
15hrs	**15.44**	**34.39**	**16.88**	**15.85**	**17.42**
20hrs	**13.64**	**31.85**	**17.55**	**14.33**	**22.63**

Fig 4.8 illustrates the particle size distribution of the alloy at various milling times. It is evident that, in the initial stages of milling, the particle size increases, which is likely due to particle

agglomeration during the cold welding process. However, as milling time increase, the particle size gradually decreases, indicating effective particle fragmentation and refinement during the mechanical milling process. When the milling time reaches 15 hours, the particle size tends to stabilize, with minimal further changes. This suggests that the powder has reached a balanced state between fracturing and cold welding, and extending the milling time has limited impact on further size reduction.

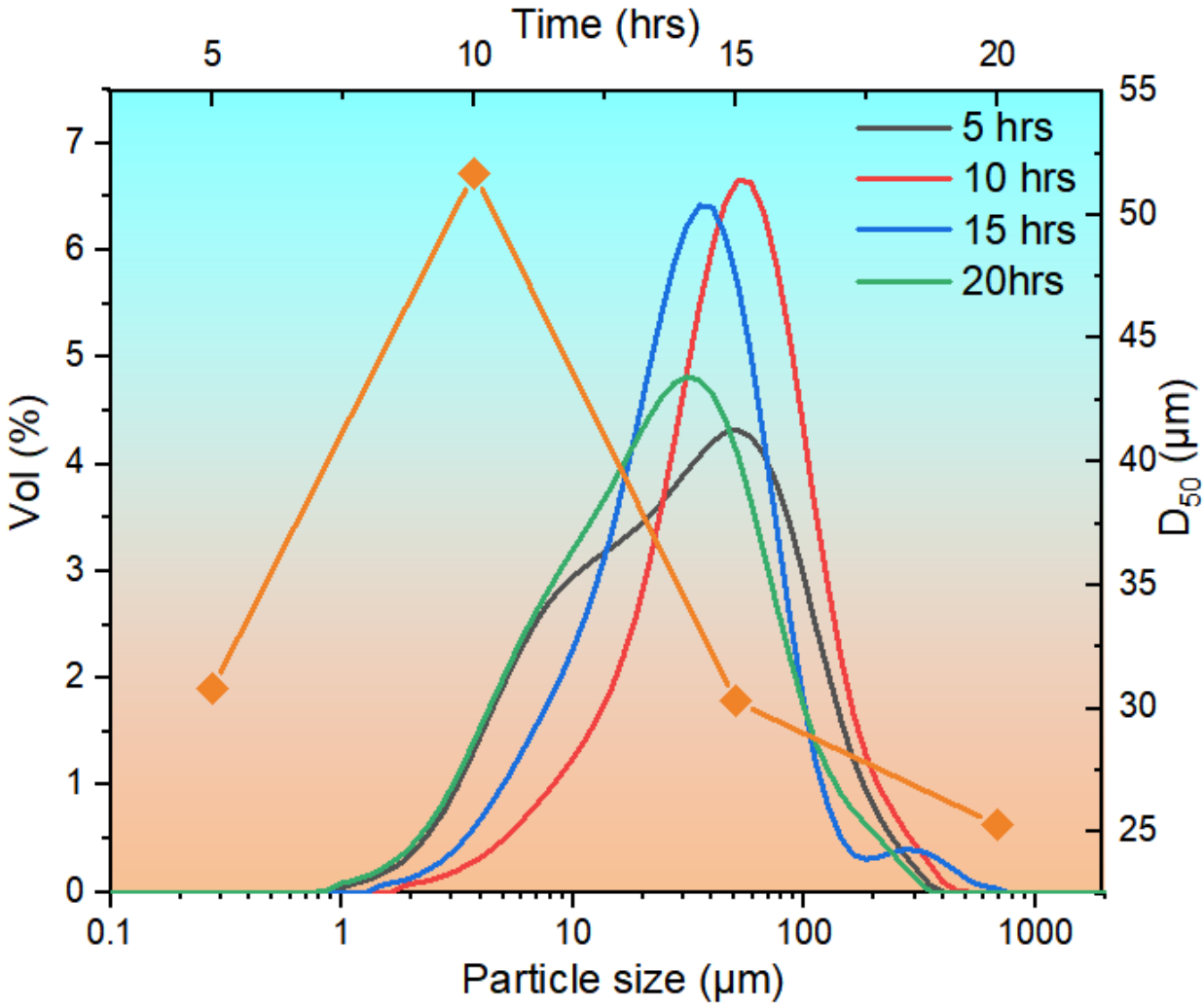

Fig 4.8 The Particle size distribution at different ball milling times

4.4 Effect of Ball-to-Powder weight ratio on phase evolution of $Ti_{15}V_{35}(CrMnFe)_{50}$ HEA

The ball-to-powder ratio (BPR), sometimes referred to as the charge ratio (CR), is a crucial variable in the milling process. Different researchers have suggested various optimal BPR values, ranging from as low as 1:1 to as high as 50:1 [215-218]. A higher BPR increases the frequency of collisions between the milling media and the powder particles within a given time frame, allowing more energy to be transferred to the powder. This accelerates the alloying process and reduces the milling time required for phase stabilization. However, excessively high BPR values can also increase the risk of contamination during the milling process. Conversely, if the BPR is too low, the mechanical energy may be insufficient, slowing down the alloying process or even preventing it from fully occurring. Therefore, identifying the optimal BPR is critical for achieving the desired phase composition, microstructure, and material properties. In this study, various BPR values are controlled to systematically explore their impact on the phase composition of the $Ti_{15}V_{35}(CrMnFe)_{50}$ alloy.

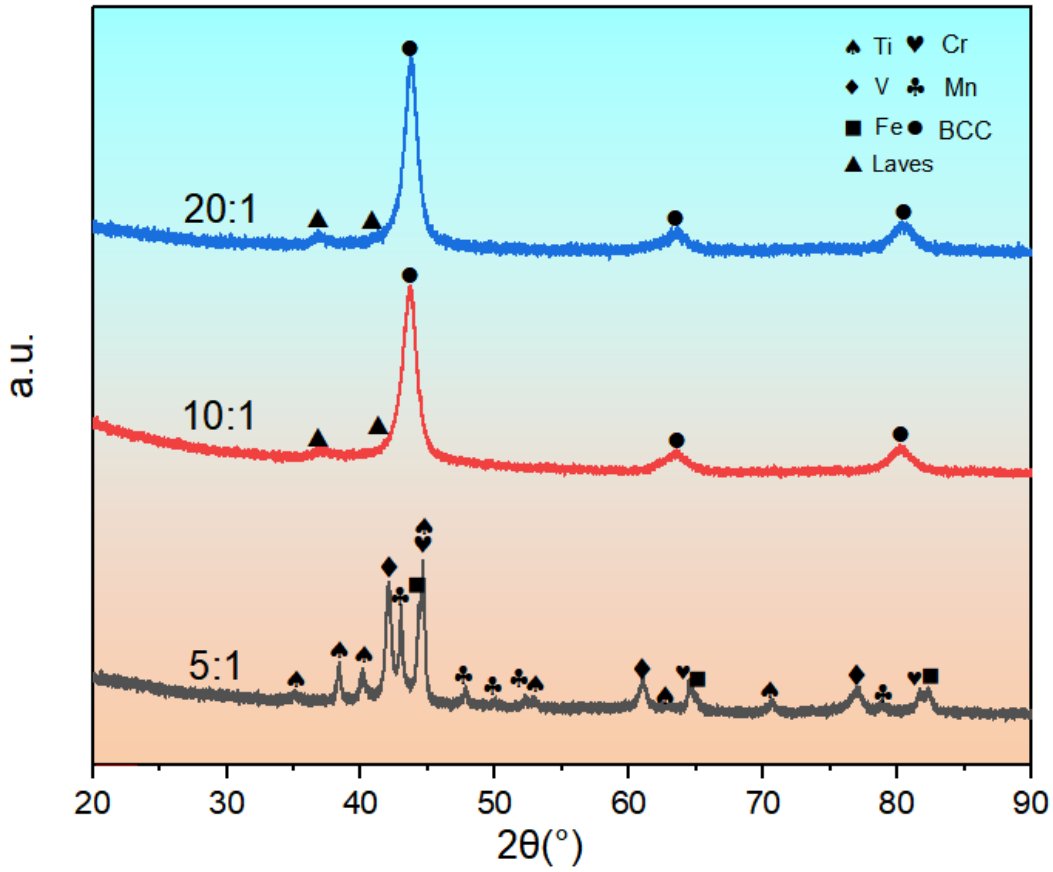

Fig 4.9 X ray diffraction patterns of the milled $Ti_{15}V_{35}(CrMnFe)_{50}$ HEA with different Ball-to-powder weight ratio under 15hrs milling

At the ball-to-powder ratio of 5:1, the XRD patterns exhibit several distinct diffraction peaks (show in Fig 4.9) corresponding to individual elements such as Ti, V, Cr, Mn, and Fe. However, no BCC phase is observed, indicating that the mechanical alloying process is incomplete under these conditions. The relatively low energy input during ball milling with this ratio is insufficient to effectively mix the elemental components into a stable BCC matrix structure.

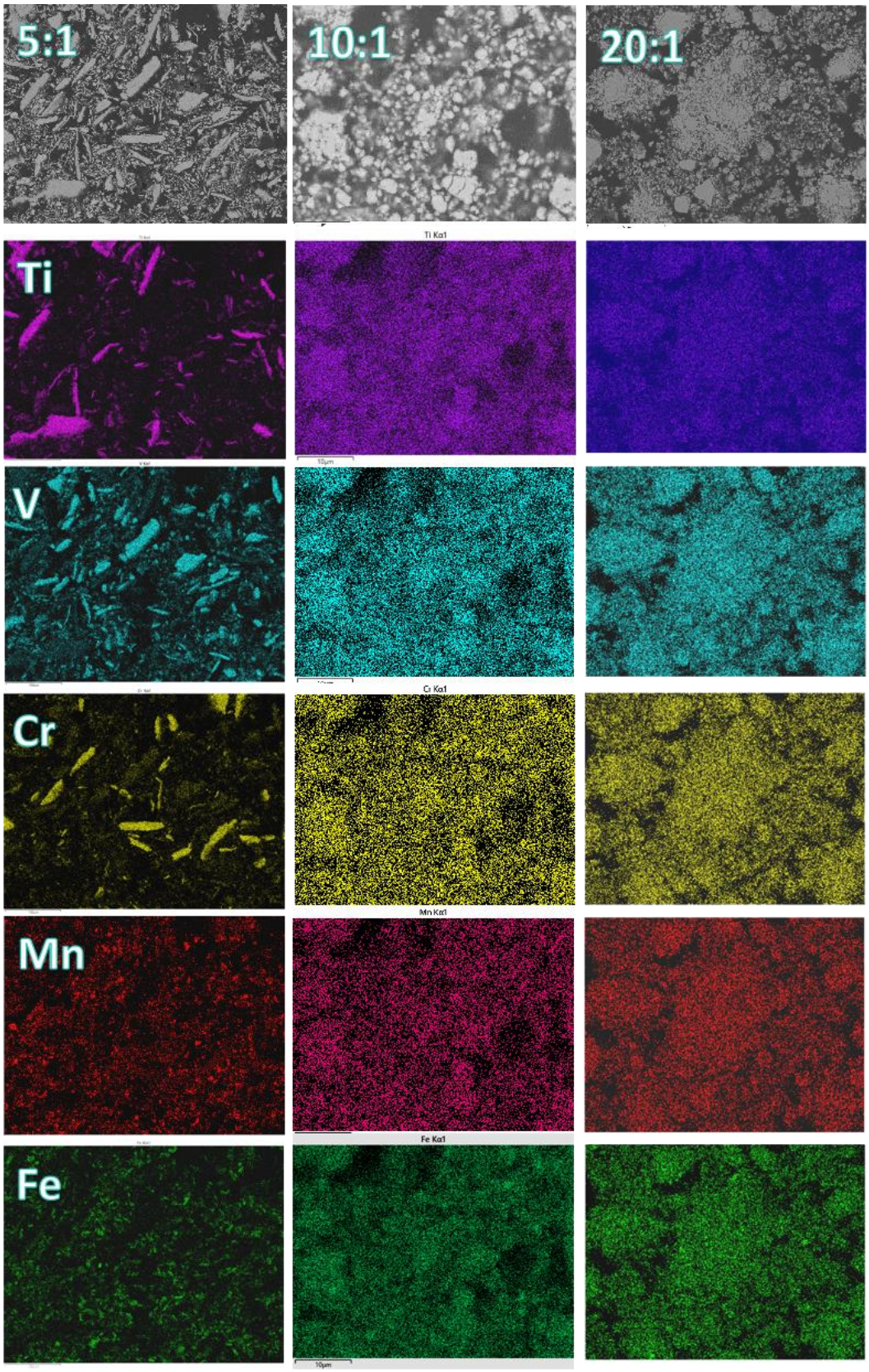

Fig 4.10 The BSE image and EDS elements mapping of the HEAs milling by different ball-to-powder ratio

As the ball-to-powder ratio increases to 10:1, the XRD patterns reveal the emergence of a BCC phase as the primary structure, along with a minor presence of Laves phase. This suggests that the mechanical alloying process has significantly improved, with enhanced elemental diffusion and a higher degree of alloying. When the ball-to-powder ratio is further increased to 20:1, the phase composition remains unchanged, with the BCC structure remaining dominant. However, a slight shift in the BCC peak position toward higher angles is observed, which could be attributed to lattice distortion or stress accumulation due to prolonged milling, or potentially contamination from Fe introduced during the process.

Table 4.2 Represents the measured atm% values of each element present in the as-milled $Ti_{15}V_{35}(CrMnFe)_{50}$ HEA with different BPR

Ratio	Ti	V	Cr	Mn	Fe
5:1	**16.19**	**35.93**	**13.49**	**18.62**	**15.77**
10:1	**15.44**	**34.39**	**16.88**	**15.85**	**17.42**
20:1	**13.66**	**31.73**	**17.10**	**13.35**	**24.16**

Fig 4.10 illustrates the distribution of elements at different ball-to-powder ratios (BPR). At the BPR of 5:1, the distribution maps of Ti, V, Cr, Mn, and Fe reveal significant inhomogeneity, indicating that mechanical alloying has not yet fully occurred. The powder particles are still in the initial stages of fracture and cold welding, and the elements have not been sufficiently mixed. When the BPR is increased to 10:1, the elemental distribution becomes more uniform, and no noticeable element segregation is observed. However, further increasing the BPR (20:1) results in localized enrichment of Fe, suggesting that at higher BPR values, there is an increase in the wear of the milling balls, leading to Fe contamination from the milling media. Table 4.2 is the measured atm% values of each element present in the as-milled $Ti_{15}V_{35}(CrMnFe)_{50}$ HEA with different BPR. As shown in the table, the elemental composition of the alloy is closest to the designed values when the ball-to-powder ratio (BPR) is set to 10:1. However, when the BPR is increased to 20:1, the proportion of other elements (Ti, V, Mn) decreases significantly,

while the Fe and Cr contents rise considerably, resulting in a large deviation from the designed composition. Therefore, taking these factors into consideration, the BPR of 10:1 is selected as the optimal ratio to achieve the desired alloy composition.

4.5 Effect of Milling Speed on phase evolution of $Ti_{15}V_{35}(CrMnFe)_{50}$ HEA.

The rotational speed (rpm) in ball milling is one of the key parameters influencing the energy input during the mechanical alloying process. Changes in speed directly affect the kinetic energy of the milling balls and the frequency of collisions, which in turn have a significant impact on the phase composition of the alloy [219, 220]. At lower rotational speeds, both collision frequency and energy are reduced, leading to insufficient mixing of alloying elements and potentially hindering the formation of the desired phase structure. In contrast, higher rotational speeds increase the kinetic energy of the milling balls, thereby promoting more effective powder fragmentation and cold welding, which accelerates the alloying process. However, excessively high speeds can result in issues such as excessive cold welding, and increased wear of the milling balls and jar, potentially introducing contamination. Therefore, selecting an optimal rotational speed is critical for optimizing the phase composition of the alloy. This study systematically investigates the effect of different rotational speeds on the phase composition of the $Ti_{15}V_{35}(CrMnFe)_{50}$ alloy, aiming to provide theoretical guidance for further optimization of the mechanical alloying process.

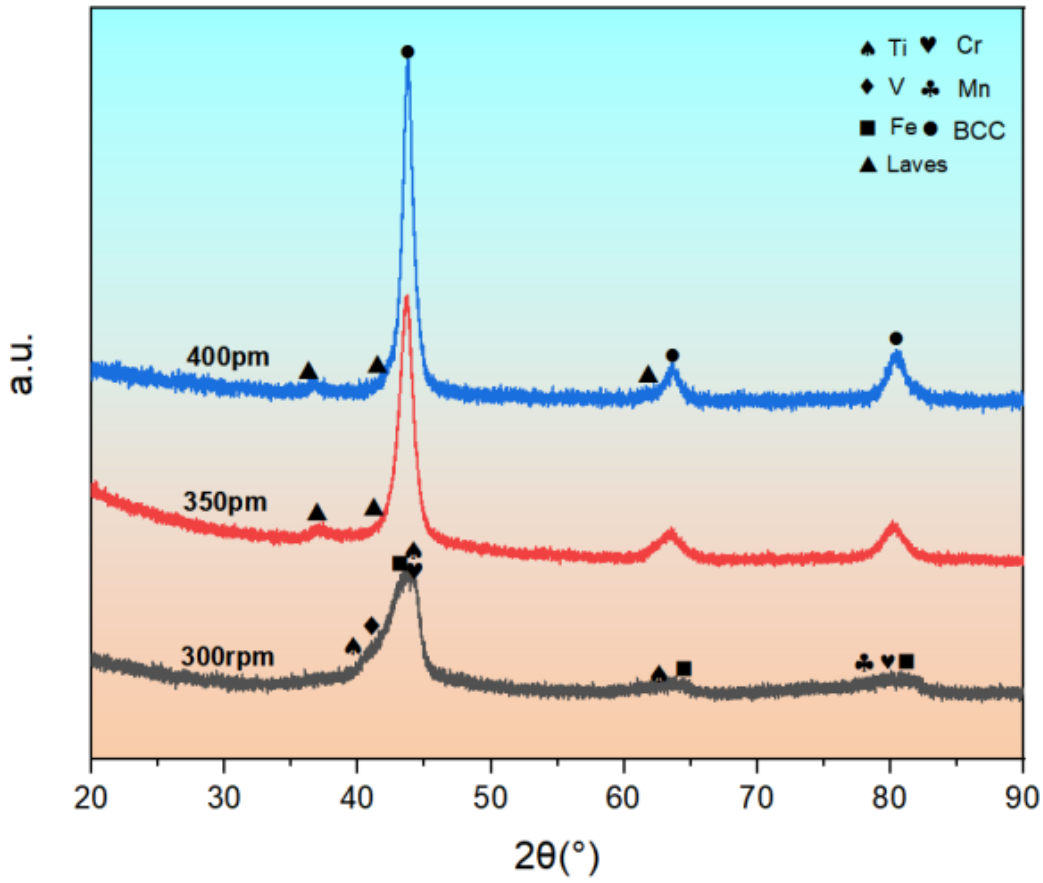

Fig 4.11 X ray diffraction patterns of the milled $Ti_{15}V_{35}(CrMnFe)_{50}$ HEA with different milling speed under BPR 10:1 and 15hrs milling

Fig 4.11 presents the X-ray diffraction (XRD) patterns under different milling speeds. At 300 rpm, the diffraction pattern reveals several characteristic peaks for various elements. Although the alloying degree is improved compared to the conditions with a lower ball-to-powder ratio (5:1), the phase structure has not yet fully transitioned into a stable BCC structure, suggesting that the alloy is still in the early stages of mechanical alloying without achieving a stable phase. When the milling speed is increased to 350 rpm, the XRD pattern clearly exhibits a dominant BCC structure with a minor Laves phase, indicating a significant improvement in the degree of alloying. The elements are more uniformly mixed, and the alloy has achieved a relatively stable phase. Further increasing the speed to 400 rpm shows no significant change in the phase structure, suggesting that the alloy's phase composition stabilizes at 350 rpm. However, a slight peak shift towards larger angles in the BCC structure is observed. This shift, which has also

been noted in cases of overextended milling time or excessive ball-to-powder ratio, is likely caused by contamination from Fe due to the wear of the milling balls.

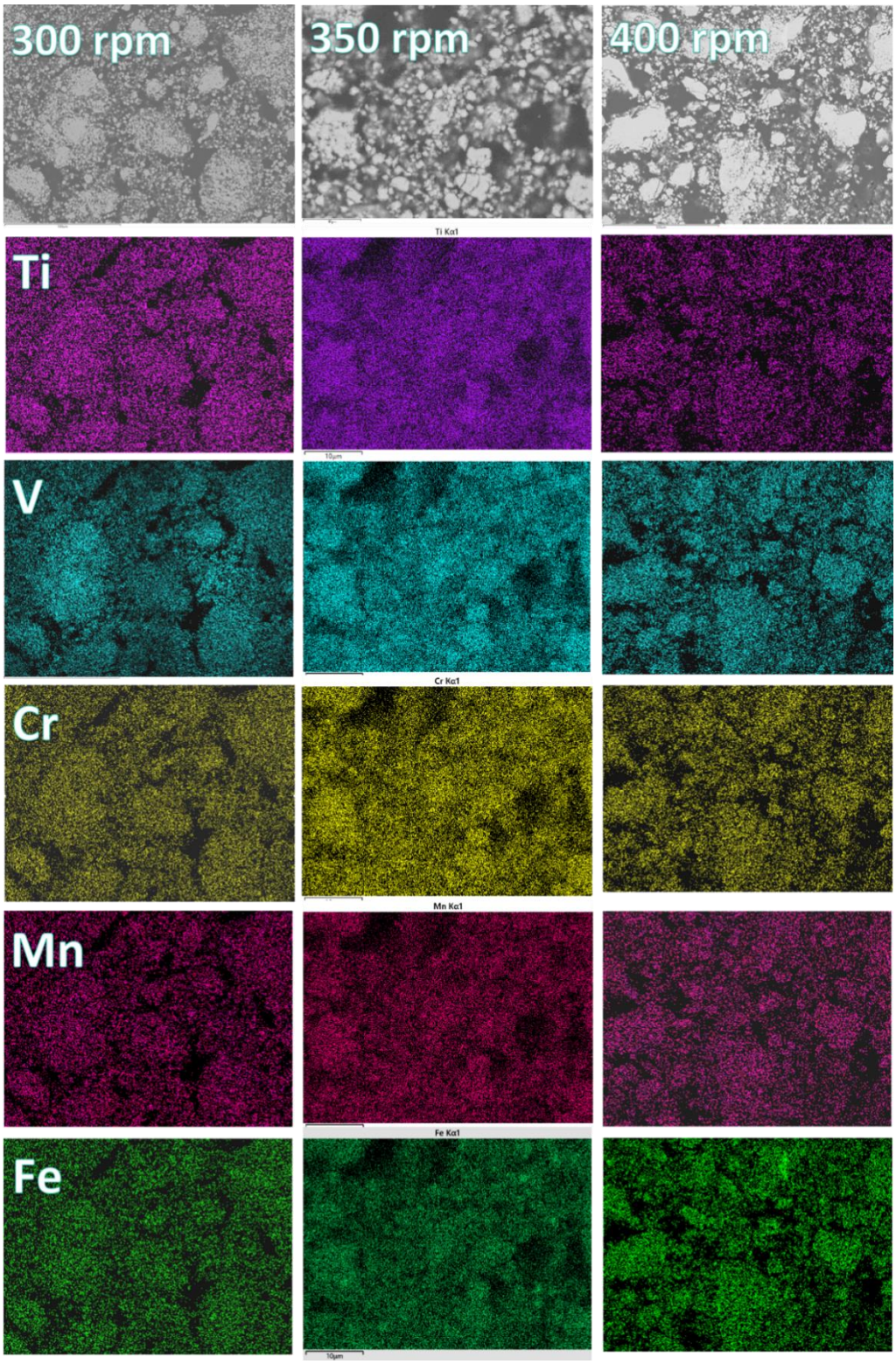

Fig 4.12 The BSE image and EDS elements mapping of the HEAs milling by different rotational speed

Figure 4.12 and Table 4.3 present the elemental distribution and specific elemental content (atm%) of the alloy at various milling speeds. At 300 rpm, it can be observed that the elements are already evenly distributed across the alloy. However, when analyzed the XRD patterns (show in Fig 4.11), it is evident that despite the uniform elemental distribution, the phase structure of the alloy has not yet reached stability. At 350 rpm, the elemental distribution remains uniform, with no signs of significant elemental segregation. According to the XRD results, the alloy's phase structure stabilizes at this milling speed, forming a BCC-dominated structure. This indicates that 350 rpm is an optimal milling speed for the alloy. When the speed is further increased to 400 rpm, a significant Fe enrichment is observed, suggesting that excessive milling speed may cause wear and tear on the milling balls, leading to contamination by Fe. Therefore, considering the combined results, 350 rpm is identified as the optimal milling speed, ensuring uniform elemental distribution, preventing contamination, and forming a stable phase structure

Table 4.3 Represents the measured atm% values of each element present in the as-milled $Ti_{15}V_{35}(CrMnFe)_{50}$ HEA with different BPR

Speed	Ti	V	Cr	Mn	Fe
300	**15.94**	**36.84**	**16.65**	**15.65**	**14.92**
350	**15.44**	**34.39**	**16.88**	**15.85**	**17.42**
400	**12.73**	**29.49**	**17.21**	**13.04**	**27.53**

4.6 Effect of Process control agents (PCA) on powder yield of ball milling

During the ball milling process, powder particles often undergo significant plastic deformation, particularly those with high ductility, which can lead to substantial cold welding. However, effective alloying only occurs when there is a balance between cold welding and particle fracture [221, 222]. Excessive cold welding can result in a significant reduction in milling efficiency and powder yield [223]. To mitigate the impact of cold welding, process control agents (PCAs) are typically added to the powder mixture, with concentrations generally ranging from 1 to 5 wt% [43]. Given the relatively low amounts of PCA used, its effect on the phase composition and stability of the alloy is minimal. However, the introduction of PCA may still introduce external contaminants, which could affect subsequent processing steps or material properties. Therefore, it is advisable to minimize the amount of PCA added, while still ensuring its efficacy in reducing cold welding.

Table 4.4 Effect of PCA content on powder yield of $Ti_{15}V_{35}(CrMnFe)_{50}$ HEA

	Jar (g)		Milling ball (g)		Powder (g)		
Content	**B**	**A**	**B**	**A**	**B**	**A**	**Powder yield (%)**
Without	**3147.5**	**3151**	**165.12**	**167.32**	**15.55**	**9.79**	**63**
0.5wt%	**3147.3**	**3149.1**	**165.10**	**166.08**	**15.36**	**12.59**	**82**
1wt%	**3147.1**	**3147.8**	**165.07**	**165.55**	**15.46**	**14.22**	**92**
1.5wt%	**3147.6**	**3148.4**	**165.06**	**165.33**	**15.52**	**14.43**	**93**

B: before ball milling/A: after ball milling

The Table 4.4 clearly shows that different PCA concentrations (wt%) have a significant impact on the powder yield of $Ti_{15}V_{35}(CrMnFe)_{50}$ HEA. Without PCA, the powder yield is the lowest at only 63%, indicating excessive cold welding during the ball milling process, which severely reduces the powder yield. When 0.5 wt% PCA is added, the yield increases significantly to

82%, suggesting that even a small amount of PCA can mitigate cold welding and enhance the powder yield. As the PCA content increases to 1 wt%, the powder yield further rises to 92%. However, when the PCA concentration is increased to 1.5 wt%, the yield only slightly increases to 93%, showing a marginal improvement over 1 wt%. Thus, the addition of 1 wt% PCA appears to be the optimal choice for maximizing powder yield while minimizing the introduction of external contaminants.

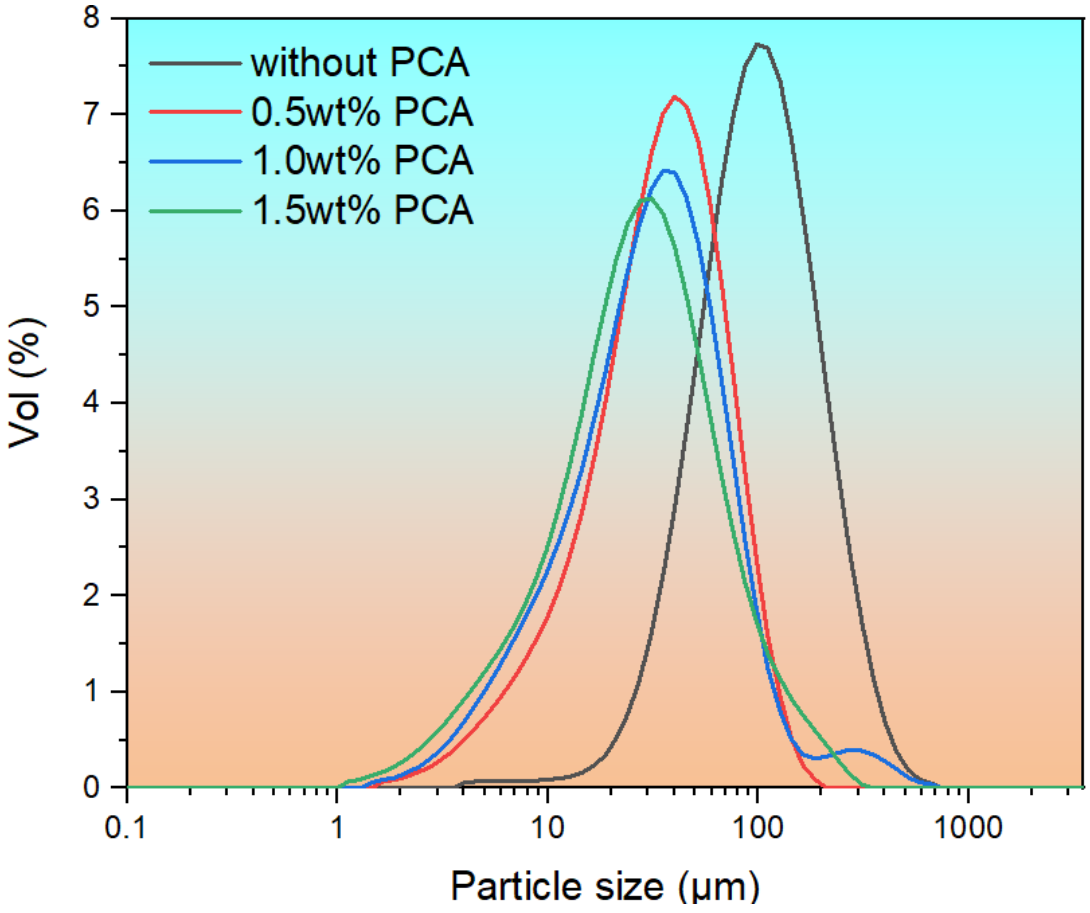

Fig 4.13 The Particle size distribution at different PCA addition

The addition of PCA significantly impacts the particle size distribution of the alloy powders, as shown in the Fig. 4.13. Without PCA, the powder exhibits larger particle sizes (D_{50}=106μm), indicating severe cold welding during the ball milling process. When 0.5 wt% PCA is added, the particle size distribution narrows, and the particle size decreases (D_{50} =37.1μm), suggesting that the PCA effectively reduces cold welding, resulting in finer powder particles. As the PCA content increases to 1.0 wt% (D_{50} =30.3μm) and 1.5 wt% (D_{50} =28.8μm), the particle size

continues to decrease, though the changes are marginal. This indicates that the addition of 1.0 wt% PCA is sufficient to effectively control cold welding, and further increases in PCA content have minimal additional effect on particle size. Therefore, combining the results of powder yield and particle size distribution, adding 1.0 wt% PCA is deemed optimal.

4.7 Summary of Optimized Milling Parameters

4.7.1 Ball-to-Powder Ratio (BPR)

The BPR significantly influences the energy input and degree of alloying during mechanical milling. Experimental results revealed that at a lower BPR of 5:1, elemental mixing was insufficient, as indicated by the presence of residual metallic phases in the XRD patterns. In contrast, increasing the BPR to 20:1 enhanced alloying efficiency; however, excessive wear of the milling media led to severe Fe contamination, causing compositional deviation from the designed alloy. To balance the degree of alloying and minimize contamination, a BPR of 10:1 was identified as the optimal ratio.

4.7.2 Milling Time

Milling time plays a crucial role in determining the extent of particle fracture, cold welding, and phase transformation. The XRD analysis showed a gradual evolution toward a predominant BCC phase with increasing milling duration. When the milling time was less than 10 hours, unalloyed elemental peaks were still observed, indicating incomplete mechanical alloying. At 15 hours, the BCC phase became dominant, with a uniform elemental distribution. However, extending the milling time to 20 hours resulted in negligible changes in phase composition while leading to increased Fe contamination due to prolonged wear of the milling media. Thus, 15 hours was selected as the optimal milling duration to achieve a stable phase structure while minimizing contamination.

4.7.3 Milling Speed

Milling speed directly affects the impact energy of the milling media and the kinetics of mechanical alloying. At a lower speed of 300 rpm, insufficient impact energy resulted in a slower alloying process. Conversely, increasing the speed to 400 rpm enhanced mechanical energy input but also intensified cold welding effects. Additionally, noticeable peak shifts in the XRD patterns were observed, suggesting increased lattice strain, which could influence hydrogen storage kinetics. Moreover, higher milling speeds exacerbated media wear, introducing unwanted impurities. Consequently, a milling speed of 350 rpm was chosen as the optimal condition to balance the degree of alloying and lattice strain while minimizing contamination

4.7.4 Process Control Agent (PCA)

The addition of PCA plays a crucial role in preventing excessive cold welding, improving milling efficiency, and optimizing particle size distribution. Without PCA, the powder yield was only 63%, indicating severe cold welding during milling, which hindered the homogenization process. The introduction of 0.5 wt% PCA significantly improved the powder yield to 82%, while increasing the PCA content to 1.0 wt% further enhanced it to 92%. However, when the PCA content reached 1.5 wt%, the improvement in powder yield was marginal, and excessive PCA could potentially introduce additional carbon contamination. Therefore, 1.0 wt% PCA was determined to be the optimal concentration, ensuring effective milling while minimizing external contamination. Based on the experimental findings, the optimized ball milling parameters for the preparation of Ti-V-Cr-Mn-Fe HEAs are as follows:

Table 4.5 Optimized ball milling parameters

Milling parameters	Details
Milling ball radius	Half ft. (1.5cm)
Manufacturing material	304 stainless steel/high Cr steel
Ball milling time	30 hrs (30min milling/30mins pose)
Ball to powder weight ratio	10:1
Milling speed	350 rpm
Milling atmosphere	Ar gas (99.9wt%)
Process control agents	1 wt% C_2H_5OH

5. Effect of heat treatment on microstructural evolution and hydrogen storage performance of as-milled $Ti_{5+x}V_{35}(CrMnFe)_{60-x}$ (x=0, 10, 20, 30) high-entropy alloys

The investigation focused on the effects of adjusting the ratios between elements A (Ti) and B (Cr, Mn, Fe) on the alloy's hydrogen storage performance. This chapter investigates the microstructural evolution, thermal stability, and hydrogen storage behavior of as-milled Ti5+xV35(CrMnFe)60-x (x=0,10,20,30) high-entropy alloys (HEAs) before and after heat treatment (HT).

Partial contents in this chapter have been published in the journal:

Y.T. Zhai, Y.M. Li, L. Bolzoni, J. Kennedy, ***F. Yang,*** Effect of heat treatment on microstructural evolution and hydrogen storage performance of as-milled $Ti_{5+x}V_{35}(CrMnFe)_{60-x}$ (x=0, 10, 20, 30) high-entropy alloys, International Journal of Hydrogen Energy, Volume 81, 2024, Pages 584-594. https://doi.org/10.1016/j.ijhydene.2024.07.298.

5.1 Microstructural characterization of the as-mill HEA powders

Fig 5.1 (a) depicts the X-ray diffraction (XRD) patterns of mechanically alloyed $Ti_{5+x}V_{35}(CrMnFe)_{60-x}$ (x = 0, 10, 20, 30) HEAs. It is evident that all HEAs consist of a BCC (Im-3m) primary phase and a minor C14 Laves (P63-mmc). Table 5.2 presents the phase concentrations and lattice parameters determined by Rietveld refinement analysis. From the Table 5.1, it can be observed that the proportion of the C14 Laves phase gradually increases with increasing Ti content. This is attributed to the larger atomic radius of Ti (146.15 pm) compared to other metal atoms (V, 131.6 pm; Cr, 121.91 pm; Mn, 135 pm, Fe, 124.12 pm) and its larger formation enthalpy with other elements (show in Table 5.1), leading to increased lattice distortion and formation enthalpy of the alloy, thereby increasing the probability of forming the second phase [49].

Table 5.1 Calculated thermodynamic and geometric parameters of $Ti_{5+x}V_{35}(CrMnFe)_{60-x}$ (x=10, 20, 30) HEAs.

HEA	ΔHmix (kJ/mol)	ΔS (J/K·mol)	VEC	Ω	δ (%)	$\bar{r}$ (pm)	T_m (℃)
$Ti_5V_{35}(CrMnFe)_{60}$	-4.06	12.38	6.15	5.96	4.28	130.17	1690
$Ti_{15}V_{35}(CrMnFe)_{50}$	-5.83	12.86	5.85	4.35	5.37	131.98	1700
$Ti_{25}V_{35}(CrMnFe)_{40}$	-6.76	12.63	5.55	3.71	5.93	133.80	1710
$Ti_{35}V_{35}(CrMnFe)_{30}$	-6.82	11.85	5.25	3.46	6.13	135.61	1720

Furthermore, with the increase in Ti content, the peaks significantly shift to lower angles, indicating lattice constant increases due to Ti atoms having a larger atomic radius compared to other metallic elements in these HEAs [224]. This suggests that, although the increase in Ti content slightly augments the second phase quantity, a substantial portion of Ti atoms remains solvated within the BCC structure.

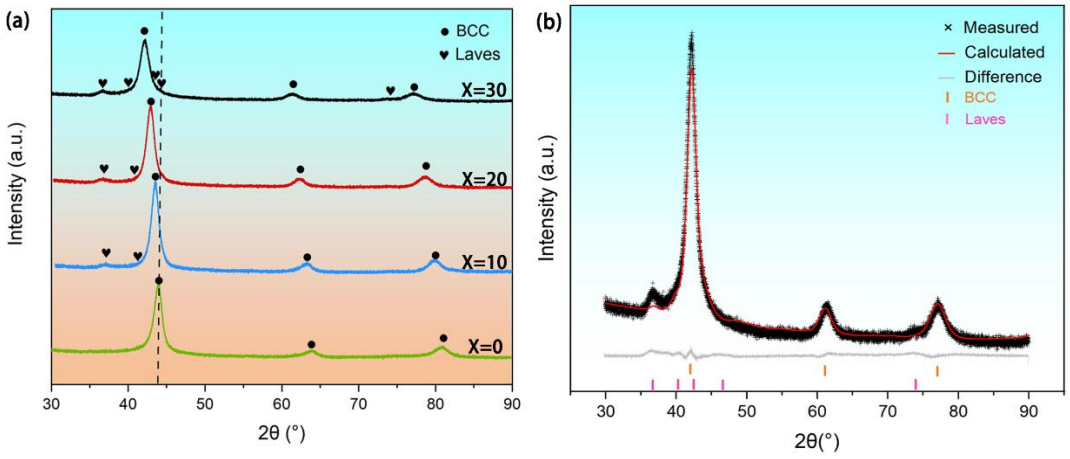

Fig 5.1 (a) XRD patterns of the $Ti_{5+x}V_{35}(CrMnFe)_{60-x}$ (x = 0, 10, 20, 30) alloys; (b) Rietveld refinement of representative of $Ti_{35}V_{35}(CrMnFe)_{30}$ HEA powders.

Table 5.2 Refinement data of the $Ti_{5+x}V_{35}(CrMnFe)_{60-x}$ (x = 0, 10, 20, 30) HEA.

Alloys	Phase	Space group	wt%	Lattice constant(Å)	R_{wp}(%)
x=0	BCC	Im-3m (229)	-	a=2.911	3.01
x=10	BCC	Im-3m (229)	96.81	a=2.937	2.74
	Laves	P63-mmc (194)	3.18	a=4.848/c=7.673	
x=20	BCC	Im-3m (229)	95.30	a=2.969	3.35
	Laves	P63-mmc (194)	4.70	a=4.868/c=7.885	
x=30	BCC	Im-3m (229)	94.87	a=3.021	5.23
	Laves	P63-mmc (194)	5.13	a=4.877/c=8.064	

Fig 5.2 presents the experimental chemical composition of the fabricated HEAs, measured through Energy-Dispersive X-ray Spectroscopy (EDS) analysis and EDS spectra. According to Fig 5.2, it can be observed that the final chemical composition of the alloy after ball milling is close to the nominal composition, except for the Fe content in the $Ti_5V_{35}(CrMnFe)_{60}$

composition, which significantly deviates. This discrepancy is attributed to the high content of the hard element Cr (with a Mohs hardness of 8.5), which increases the wear of the milling balls. Since the primary component of the milling balls is Fe, this results in an increased Fe content in the alloy. The EDS map of randomly selected powder particles, as shown in Fig 5.3, reveals that the distribution of all five elements within each particle is nearly uniform, without any obvious elemental segregation.

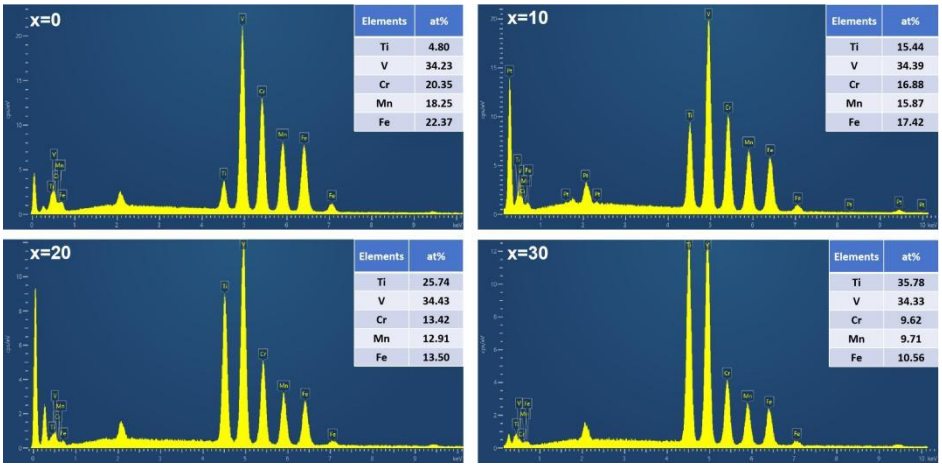

Fig. 5.2 Represents the measured atm% values and EDS spectra of as-milled $Ti_{5+x}V_{35}(CrMnFe)_{60-x}$ (x=0, 10, 20, 30)

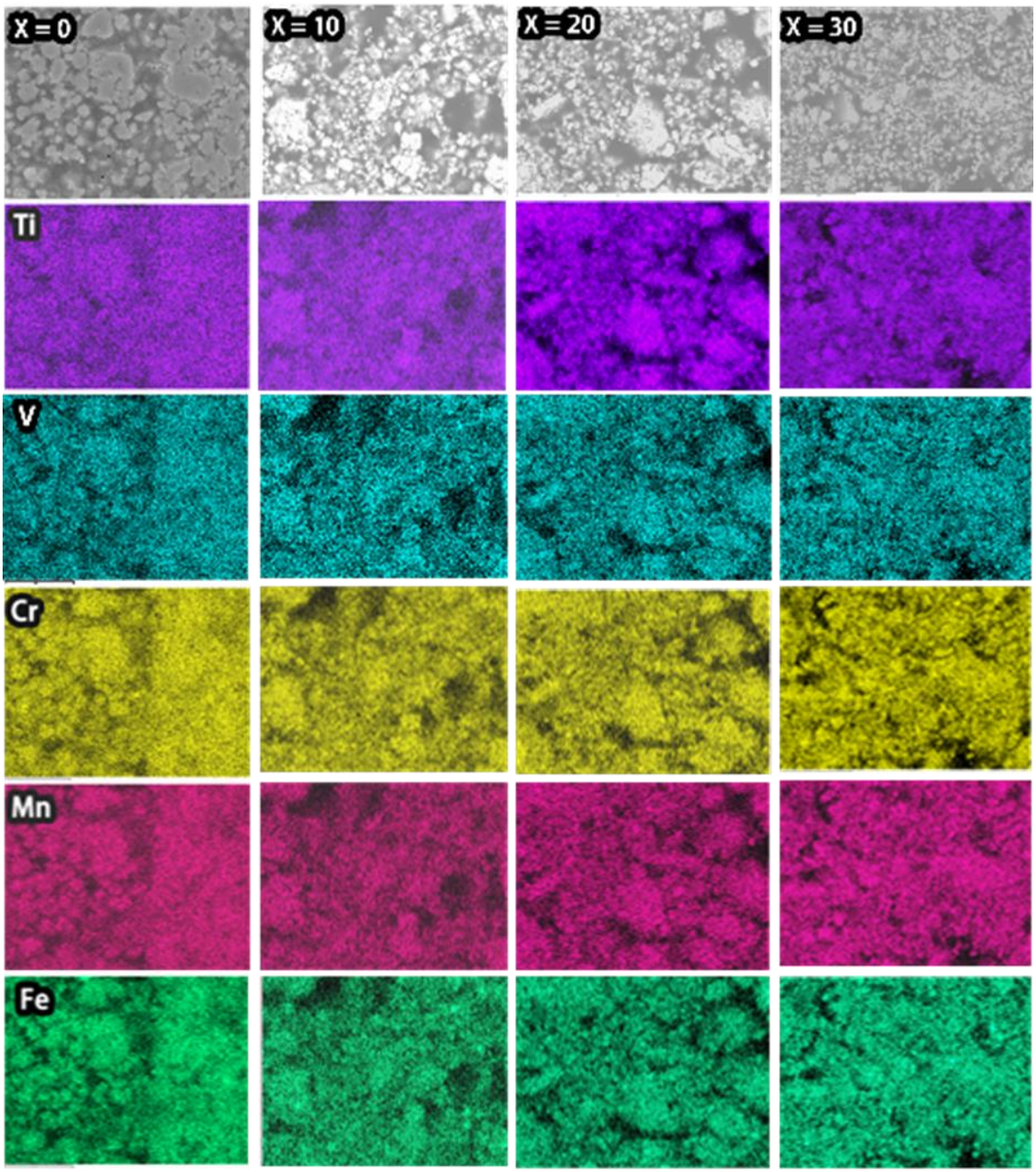

Fig 5.3. BSE/EDS maps of the as-milled $Ti_{5+x}V_{35}(CrMnFe)_{60-x}$ (x = 0, 10, 20, 30) HEA powders

5.2 Thermal stability of the as-mill HEA powders

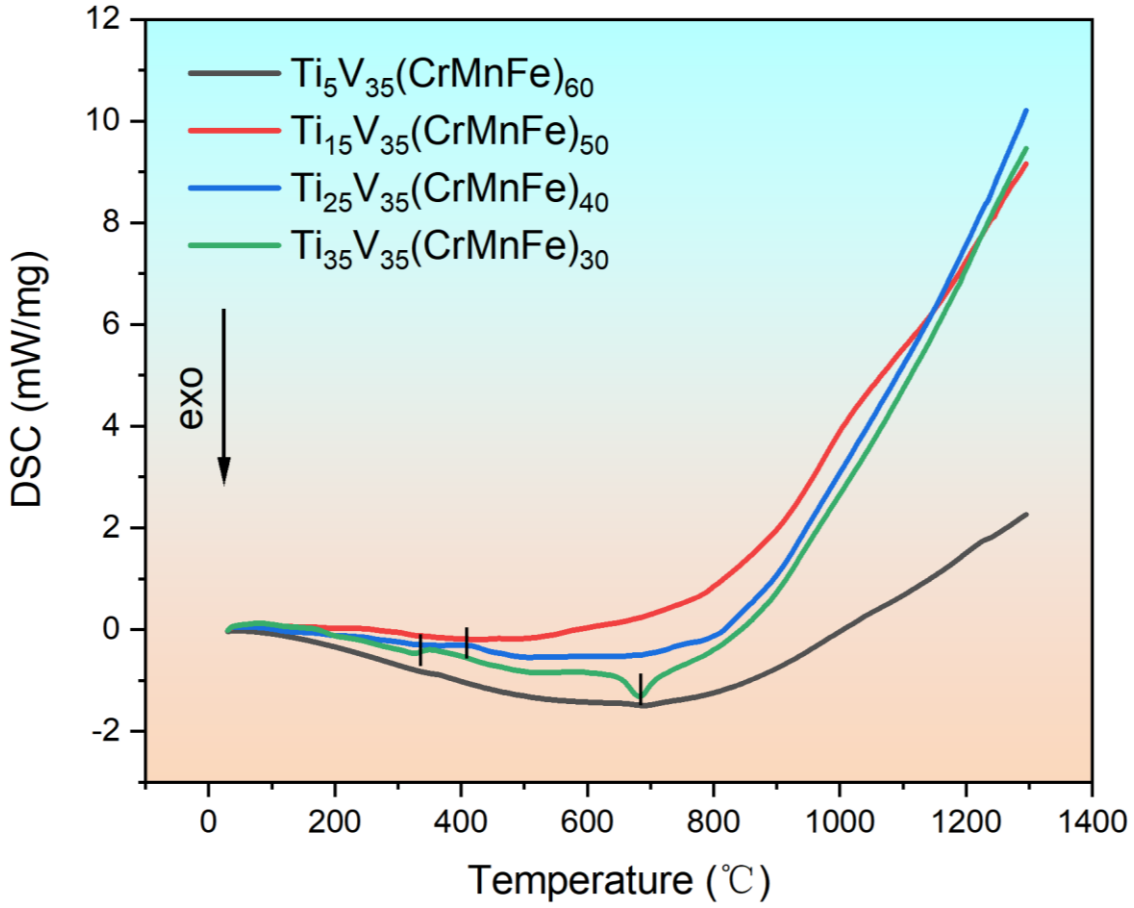

Fig 5.4 The DSC curve of the as-milled $Ti_{5+x}V_{35}(CrMnFe)_{60-x}$ (x = 0, 10, 20, 30) HEAs powders.

The DSC curves (Fig 5.4) of each alloy exhibit similar exothermic and endothermic trend. Initially, an exothermic trend is observed, which can be attributed to the release of internal stresses caused by severe plastic deformation induced by high-energy ball milling [225]. It is worth noting that both the $Ti_{25}V_{35}(CrMnFe)_{40}$ and $Ti_{35}V_{35}(CrMnFe)_{30}$ alloys show fluctuations between 350 and 450 ℃, while the $Ti_{35}V_{35}(CrMnFe)_{30}$ alloy exhibits a distinct exothermic peak between 650 and 700 ℃. To investigate the variation of alloy microstructure at different temperatures, the as-milled HEAs powders were annealed at 300, 600, and 900 ℃, 3 hours to achieve a homogeneous microstructure.

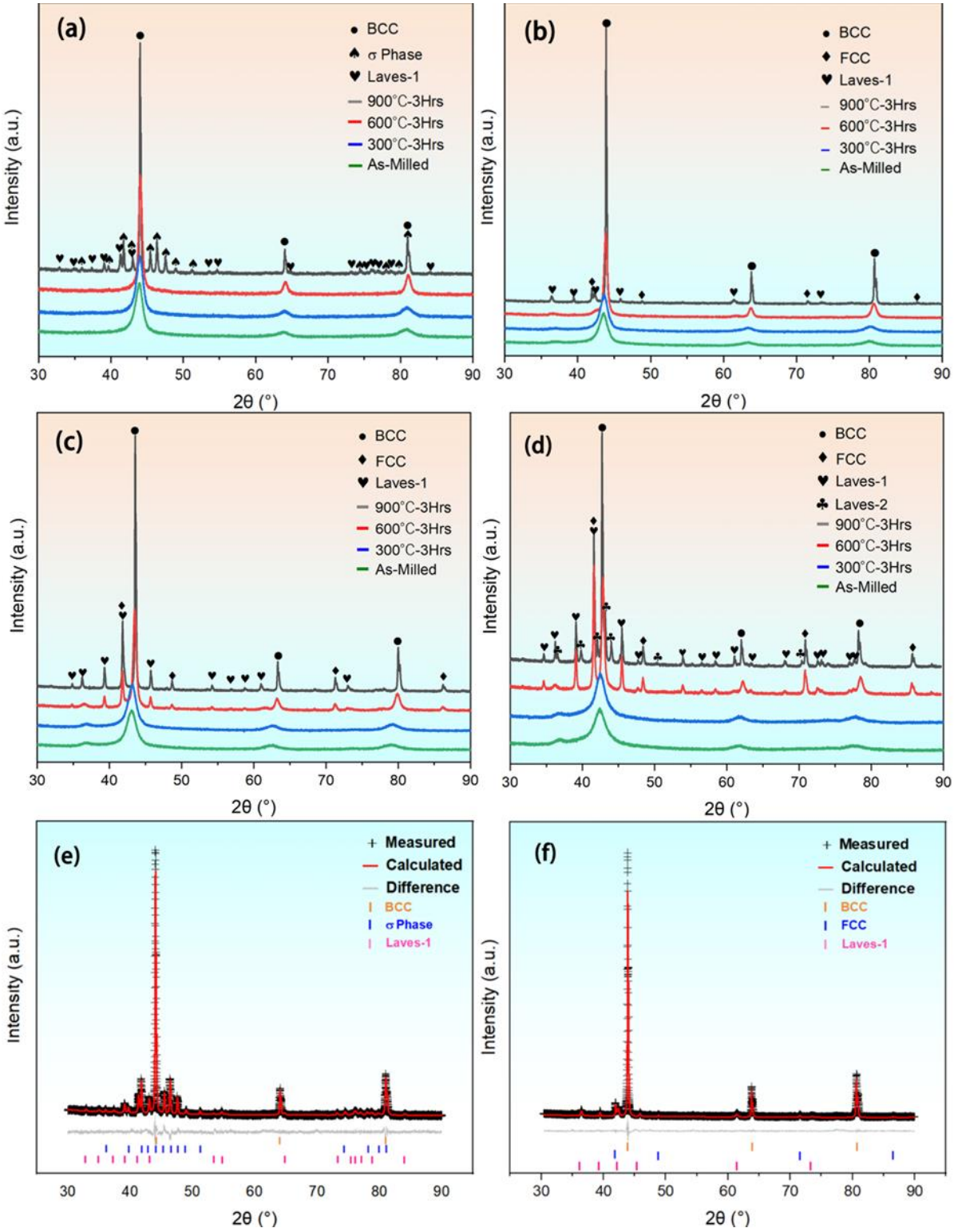

Fig 5.5 XRD patterns of the $Ti_{5+x}V_{35}(CrMnFe)_{60-x}$ (x = 0, 10, 20, 30) HEAs heat treated at different temperature. (a) x=0; (b) x=10; (c) x=20; (d) x=30; (e), (f) Rietveld refinement of representative of $Ti_5V_{35}(CrMnFe)_{60}$ and $Ti_{15}V_{35}(CrMnFe)_{50}$ HEAs heat treated at 900 °C

Fig 5.5. presents the XRD patterns of the as-milled $Ti_{5+x}V_{35}(CrMnFe)_{60-x}$ (x = 0, 10, 20, 30) HEAs after various heat treatments. The XRD pattern of the alloy after HT at 900 ℃ was refined, and the fitting results of the alloy's crystal structure are summarized in Table 5.3. It is worth noting that the $Ti_5V_{35}(CrMnFe)_{60}$ HEA after HT at 900 ℃, a significant amount of σ (P42/mnm, JCPDS 65-4528) phase is identified in the XRD pattern (Fig 5.5 a) By comparing the XRD patterns and the refinement results, it is found that the lattice constant of the BCC phase in the HEA remained almost unchanged (Table 5.3). The decomposition of the alloy phase (BCC phase) typically accompanies a significant shift in peak position [226], and is often accompanied by pronounced fluctuations in the DSC curve. The identified σ phase in the heat-treated HEA is likely already existed in the as-milled $Ti_5V_{35}(CrMnFe)_{60}$. However, the σ phase peak is overlapped in the XRD pattern of the as-milled $Ti_5V_{35}(CrMnFe)_{60}$ HEA, attributed to the low crystallinity and significant broadening of the BCC peak after ball milling [35]. Therefore, it is inferred that the σ phase already exists in the alloy after ball milling. The rest of HEAs are primarily composed of BCC, Laves, and FCC (Fm-3m (225), JCPDS 04-0783) phases after heat treatments, with the FCC phase originating from the decomposition of the BCC phase (after first fluctuation in DSC curve). As the HT temperature increases from 600°C to 900°C, the peak intensity of the FCC in the heat-treated $Ti_{35}V_{35}(CrMnFe)_{30}$ HEA significantly decreases (Fig 5.5 d). This is attributed to the partial precipitation of Laves-2 from the FCC phase in the alloy (around the temperature range that is corresponded to the second peak in the DSC curve), the exitence of Laves-2 to is further confirmed by subsequent SEM observations. Notably, a small amount of FCC in the $Ti_{15}V_{35}(CrMnFe)_{50}$ HEA, but the fluctuations are identified in the DSC curve of the as-milled $Ti_{15}V_{35}(CrMnFe)_{50}$ HEA. This may be due to the inhomogeneous lattice strain in the HEA causing a very minimal amount of BCC decomposition, which is not detectable using DSC.

Table 5.3 Refinement data of the $Ti_{5+x}V_{35}(CrMnFe)_{60-x}$ (x = 0, 10, 20, 30) HEAs heat treated at 900 °C.

Alloys	Phases	Content (wt%)	Lattice parameters (Å)	R_{WP} (%)
$Ti_5V_{35}(CrMnFe)_{60}$	BCC	59.82	a= 2.901	7.65
	σ (P42/mnm)	35.09	a= 8.913/c=4.604	
	Laves-1	5.09	a= 5.201/c=7.750	
$Ti_{15}V_{35}(CrMnFe)_{50}$	BCC	89.20	a= 2.909	2.61
	FCC	2.68	a= 3.722	
	Laves-1	8.12	a= 4.929/c=8.233	
$Ti_{25}V_{35}(CrMnFe)_{40}$	BCC	63.78	a= 2.932	7.03
	FCC	24.05	a= 3.735	
	Laves-1	12.20	a= 5.082/c=8.121	
$Ti_{35}V_{35}(CrMnFe)_{30}$	BCC	46.58	a= 2.991	14.01
	FCC	30.31	a= 3.755	
	Laves-1	14.78	a= 5.165/c=8.203	
	Laves-2	8.33	a= 4.977/c=9.037	

Fig 5.6 illustrates the backscattered electron image (BSE) of the $Ti_{5+x}V_{35}(CrMnFe)_{60-x}$ HEAs after HT at 900°C. There are at least three regions with varying grayscale intensities in the

heat-treated HEAs, which can be attributed to the differences in average atomic number (Z number) of different phases [227]. This suggests that the heat-treated HEAs consists of at least three chemically distinct phases. Table 5.4 lists the proportions of the constituent elements (at%) in different regions, marked with different letters (Fig 5.6). After heat treatment, the crystal size of the alloy remains at the nanoscale.

Table 5.4 The EDS results of the $Ti_{5+x}V_{35}(CrMnFe)_{60-x}$ (x = 0, 10, 20, 30) HEAs heat treated at 900 ℃ (at %).

Alloy	Area	Ti	V	Cr	Mn	Fe
x=0	A	5.14 (0.1)	39.72 (0.5)	18.65 (0.2)	16.49 (0.3)	20.00 (0.2)
	B	4.85 (0.1)	33.16 (0.3)	18.64 (0.2)	18.83 (0.2)	24.52 (0.2)
	C	4.90 (0.1)	34.31 (0.2)	20.32 (0.2)	18.20 (0.2)	22.27 (0.3)
x=10	A	14.68 (0.2)	35.02 (0.3)	16.87 (0.3)	16.15 (0.3)	17.28 (0.2)
	B	15.91 (0.2)	33.95 (0.3)	16.39 (0.4)	16.36 (0.2)	17.39 (0.3)
	C	18.30 (0.2)	33.24 (0.3)	16.07 (0.2)	16.01 (0.2)	16.38 (0.3)
x=20	A	22.70 (0.2)	35.24 (0.4)	14.29 (0.2)	14.52 (0.3)	13.25 (0.3)
	B	25.43 (0.2)	33.52 (0.2)	13.22 (0.2)	13.98 (0.3)	13.85 (0.3)
	C	28.54 (0.4)	31.91 (0.3)	12.59 (0.2)	13.87 (0.2)	13.09 (0.4)
x=30	A	32.81 (0.3)	36.94 (0.3)	10.36 (0.3)	9.87 (0.2)	10.02 (0.3)
	B	35.07 (0.3)	33.45 (0.3)	10.16 (0.3)	10.33 (0.2)	10.99 (0.3)
	C	37.03 (0.3)	32.64 (0.3)	9.18 (0.3)	9.98 (0.2)	11.17 (0.2)
	D	38.89 (0.4)	33.26 (0.3)	9.51 (0.1)	8.85 (0.2)	9.49 (0.1)

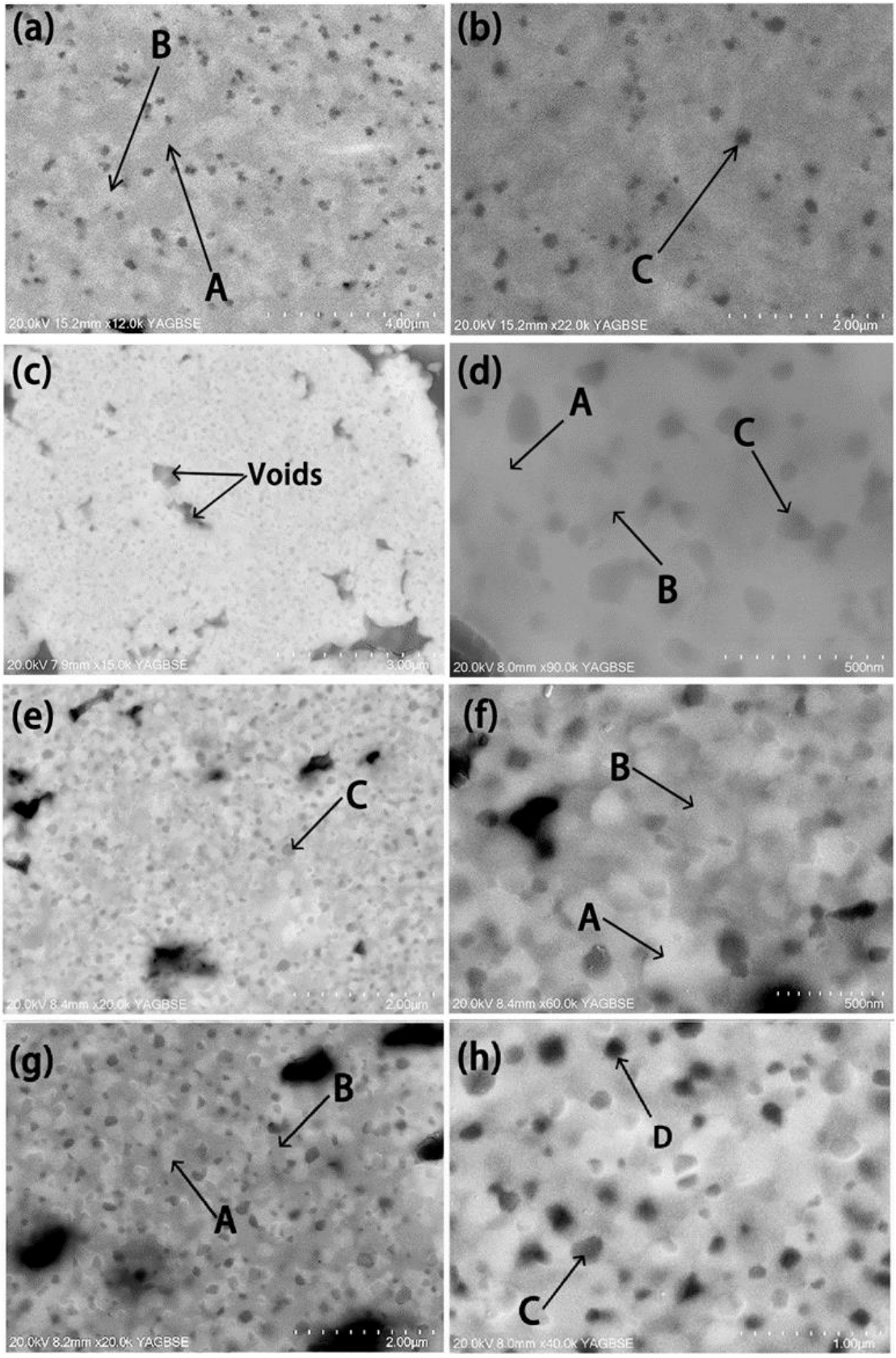

Fig. 5.6 The Back-scattered Electron images of the $Ti_{5+x}V_{35}(CrMnFe)_{60-x}$ (x = 0, 10, 20, 30) HEAs heat treated at 900 °C. (a), (b) x=0; (c), (d) x=10; (e), (f) x=20; (g), (h) x=30.

By comparing the refined phase proportions in Table 5.3 and Fig 5.6 (a) and (b), it can be determined that region A in the $Ti_5V_{35}(CrMnFe)_{60}$ HEA corresponds to the BCC, region B corresponds to the σ ((P42/mnm), and region C corresponds to the Laves-1. Fig 5.6 (c) - (h) depict the microstructures of the $Ti_{5+x}V_{35}(CrMnFe)_{60-x}$ (x = 10, 20, 30) HEAs, and it can be observed that their overall microstructures are similar. It is determined that region A corresponds to the BCC, region B corresponds to the FCC, and region C corresponds to the Laves-1. It is noteworthy that in region B (FCC) of Fig 5.6 (h), some precipitate phases are observed, which are attributed to the Laves-2, consistent with the trend observed in the XRD data. After heat treatment, the elemental compositions among different HEAs exhibit consistent trends. Specifically, the V content in the BCC is relatively higher compared to other elements; in the FCC, Ti content is higher than in BCC but lower than in the Laves. Within the Laves phase, the titanium content is the highest among all structures. The variation in Ti content within the same alloy can be attributed to the decomposition of the initial BCC. After decomposition, the Ti content decreases and the V content increases in the resulting BCC structure, leading to a reduction in the average atomic size of the alloy and consequently a decrease in the lattice parameter of the decomposed BCC. However, due to the differing initial Ti content in the alloys, the lattice parameters of the various structures exhibit higher values in alloys with higher initial Ti content.

Fig 5.7 presents the TEM analysis of the $Ti_{35}V_{35}(CrMnFe)_{30}$ HEAs after heat treatment. From the elemental distribution map in Fig 5.7 (b) and (g), it is evident that the alloy consists of four distinct phase regions: region A with higher V content, region B with relatively uniform Ti, V distribution, region C with relatively high Ti content, and region D with the highest Ti enrichment. To confirm further the types of phases in each region, corresponding selected area electron diffraction (SAED) patterns were obtained. The SAED patterns confirm that phase A corresponds to the BCC, phase B corresponds to the FCC, phase C corresponds to the Laves-1, and phase D corresponds to the Laves-2, which is consistent with the observations from the backscattered electron and XRD data.

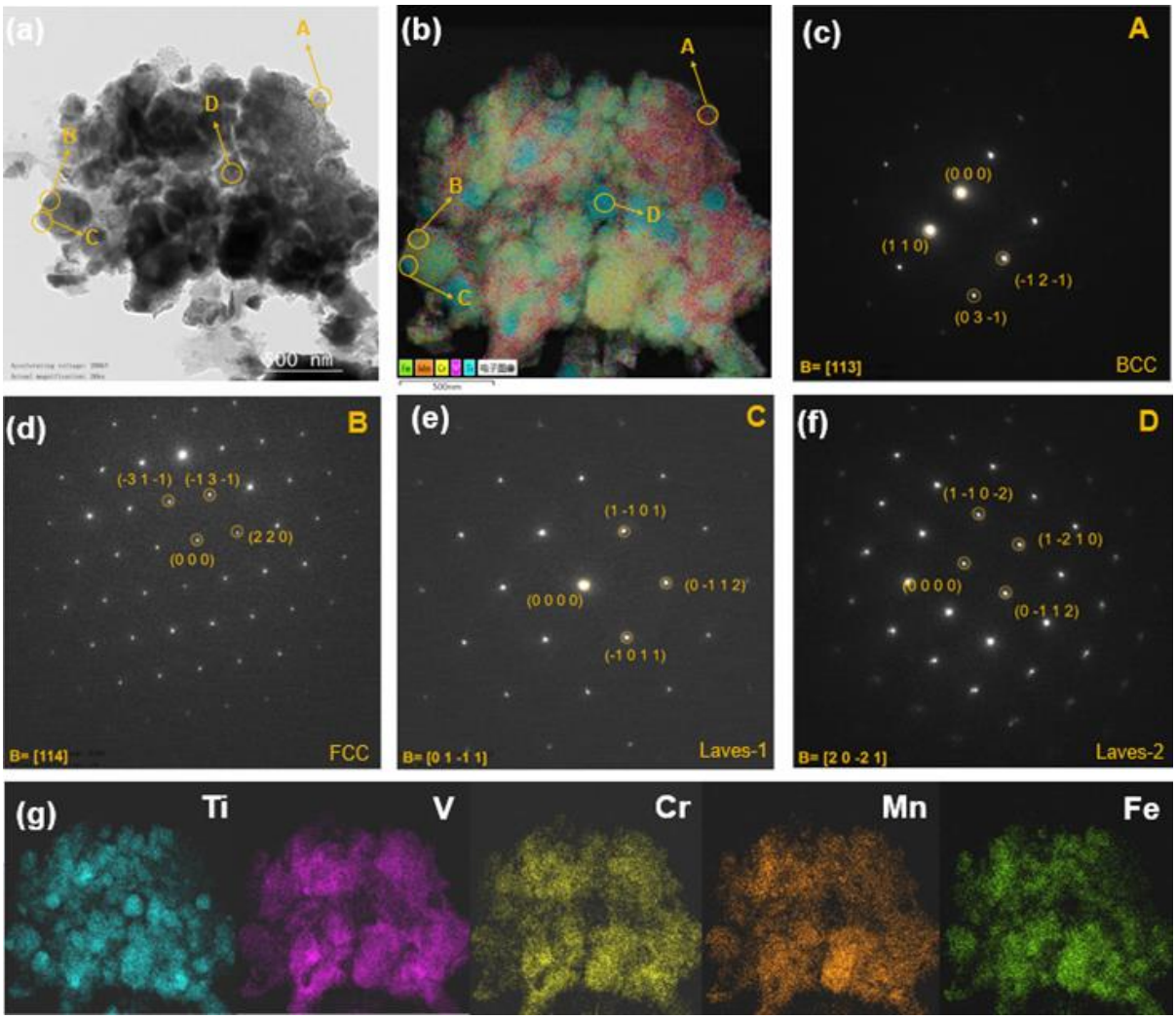

Fig 5.7 The TEM characterization of $Ti_{35}V_{35}(CrMnFe)_{30}$ HEAs after heat treated at 900 °C. (a) bright field image; (b) EDS element distribution overlap image; (c) - (f) SAED pattern of the different points marking from (a) and (b); (g) the EDS element distribution mappings

Based on the analysis above, it is observed that when x = 0, a significant amount of σ (P42/mnm) is detected in the alloy after heat treatment, a phenomenon not observed in other alloys after heat treatments. This is attributed to the abundant presence of chromium (Cr) and iron (Fe) elements in the alloy with x=0, coupled with their relatively low entropy values (1.47 R), facilitating the formation of Cr-Fe σ structure (JCPDS 65-4528) [228, 229]. Conversely, with an increase in titanium (Ti) content, and a corresponding decrease in Cr and Fe content, along with an increase in the overall entropy of the alloy (Table 5.1), subsequent alloys do not exhibit

σ (P42/mnm) structure. From Fig 5.5 and Table 5.4, it can be inferred that at the same temperature (600℃ or 900℃), the content of FCC and Laves increases while the BCC decreases with increasing Ti content (x=10, 20, 30). The slight increase in the Laves can be attributed to the presence of stabilizing elements Ti [17, 22, 230], which promotes the formation of the Laves phase. Additionally, the increased Ti content leads to higher overall lattice (atomic) distortion in the alloy, thereby reducing the stability of the initial BCC. This results in the decomposition of the BCC and an increase in the content of the FCC. Furthermore, by observing the DSC curve, it can be noted that as the Ti content increases from 25 at% to 35 at%, the first fluctuation (BCC decomposition) temperature of the alloy decreases, and an exothermic peak appears around 700 ℃ for the first time. These observations provide further evidence that the increase in Ti content leads to a decrease in the stability of the alloy phases. From Fig 5.6 and Table 5.4, it can be observed that the variation of phases in the alloy is consistent with the observations from XRD patterns. Furthermore, the decomposition phases are mostly accompanied by fluctuations in the Ti element. This can be attributed to the Ti has the largest atomic radius (146.15 pm), the lattice (atomic) distortion is primarily caused by changes in Ti content.

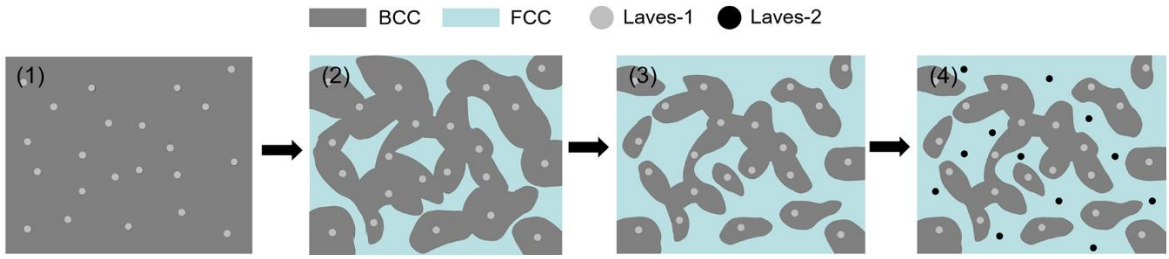

Fig 5.8 Schematic illustrations of phase transition of as milled HEAs at high temperature and different titanium contents

The phase evolution of the as milled HEAs can be summarized into four stages: (1) With the increase in temperature, the pre-existing Laves phases in the alloy grows; (2) With the increase of Ti element content and temperature, the BCC phase decomposes; (3) With further increase in temperature or Ti element content, the FCC phase content increases; (4) At high

temperatures, with an increasing Ti element content, the Laves-2 phases precipitates from the FCC phase.

5.3 Hydrogen storage performance

Fig 5.9 (c)-(f) depict the hydrogen absorption activation curves of $Ti_{5+x}V_{35}(CrMnFe)_{60-x}$ (x = 20, 30) HEAs before and after heat treatments. It can be observed that all alloys require only two absorption/desorption cycles to complete the hydrogen activation process. This is significantly better than similar alloy compositions reported in the literature, which usually require 4 to 5 cycles to be fully activated [29, 36, 231]. Due to the extremely low hydrogen absorption capacity of the alloy (x=0, 10) during activation, and it's almost negligible hydrogen absorption capability at room temperature after activation (shown in Fig 5.9 a and b), those alloys are not discussed in this section. This may be attributed to the low content of A-type elements (i.e., hydrogen-affinitive elements) in the alloy composition, which reduces the overall affinity of the alloy for hydrogen and is therefore unfavorable for effective hydrogen storage and the formation of metal hydrides.

Fig. 7. (e) and (f) illustrate the hydrogen absorption/desorption kinetics curves of the $Ti_{5+x}V_{35}(Cr, Mn, Fe)_{60-x}$ alloy under different conditions. Before heat treatments, the alloy with x=30 exhibits the maximum hydrogen absorption capacity, reaching 1.21 wt%, compared to 0.78 wt% for x=20. However, the alloy's desorption capacity is greater when x = 20 (0.38 wt%) compared to when x = 30 (0.34 wt%). This is because the alloy with x = 30 contains more A-type (hydrogen-affinitive) elements Ti, which lowers the overall electronegativity of the alloy and strengthens its affinity for hydrogen, making hydrogen absorption easier and increase the storage capacity. Conversely, hydrogen desorption becomes more difficult. After heat treatment, a decrease in the maximum hydrogen storage capacity of the alloy (x=20, 30) is observed. This phenomenon is attributed to the decomposition of the initial BCC structure and its reduced fraction after heat treatment. Structural analysis indicates that the lattice constant of the BCC phase decreases upon annealing, which leads to a reduction in the available interstitial volume within the lattice. This decrease in interstitial volume may reduce the stability of hydrogen atoms in the structure. [20, 232].

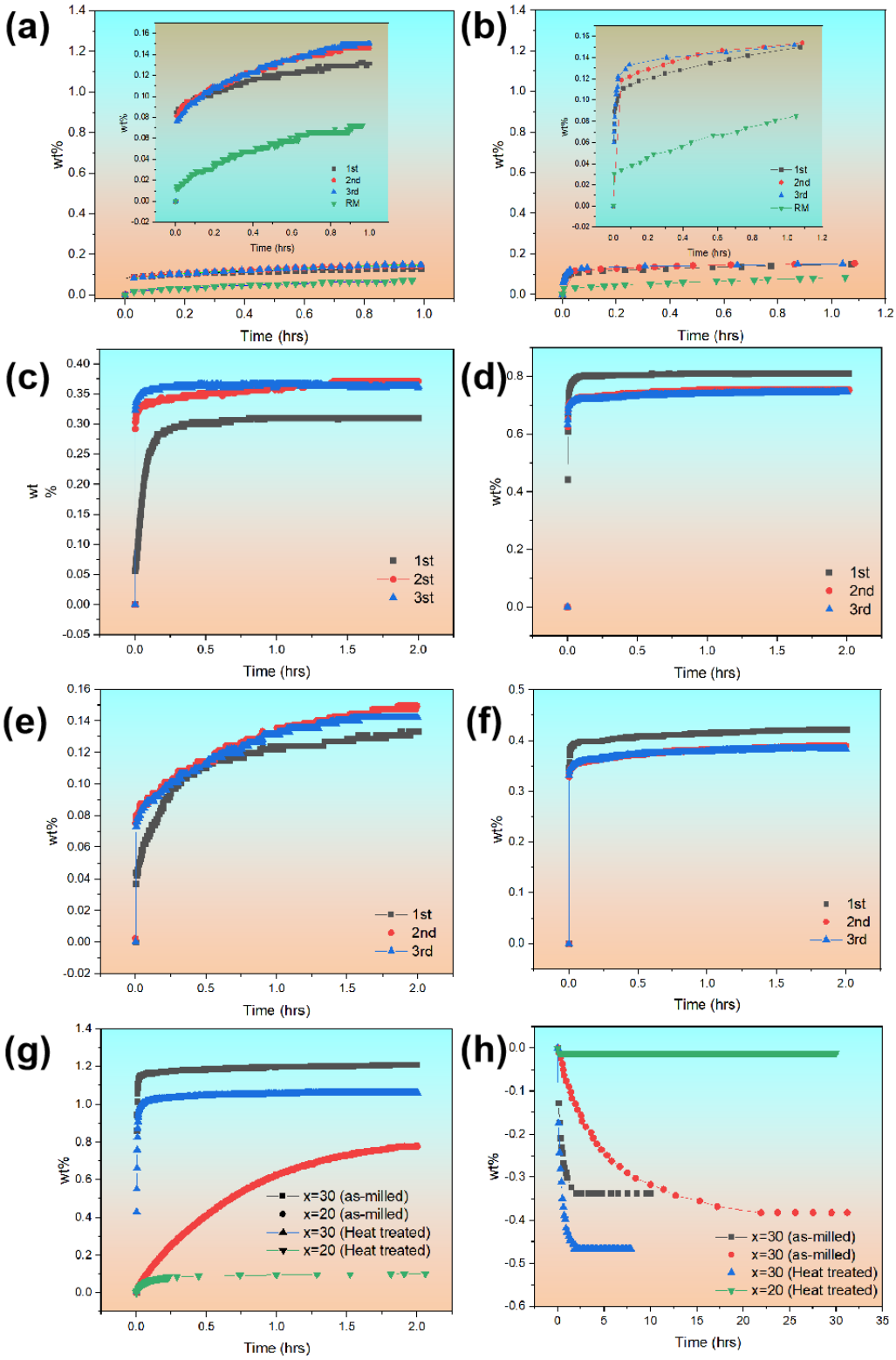

Fig 5.9 Activation hydrogen absorption curve of as-milled $Ti_{5+x}V_{35}(CrMnFe)_{60-x}$ HEAs: (a) x=0; (b) x=10; (c) x=20; (d) x=30; (e) and (f) x = 20 and 30 after heat treatment at 900 ℃ respectively; (g) and (h) The hydrogen absorption/desorption curve at room temperature of the x = 20, 30 HEAs under different conditions

Since the hydrogen storage capacity of x=20 is relatively low before heat treatment, the alloy almost loses its hydrogen storage capacity after heat treatment. It is noteworthy that alloy x=30 exhibits a slight increase in hydrogen desorption capacity (0.46 wt%) after heat treatment, which can be attributed to two factors: (1) the reduction in the lattice constant of the BCC structure leads to a decrease in the atomic spacing within the alloy, thereby reducing the stability of hydrogen atoms within the lattice and making it easier for hydrogen atoms to dissociate from the lattice; (2) the decomposition of the BCC after heat treatment results in an increase in the number of phases within the alloy. The synergistic effect among these phases enhances the hydrogen desorption performance of the alloy[36, 49].

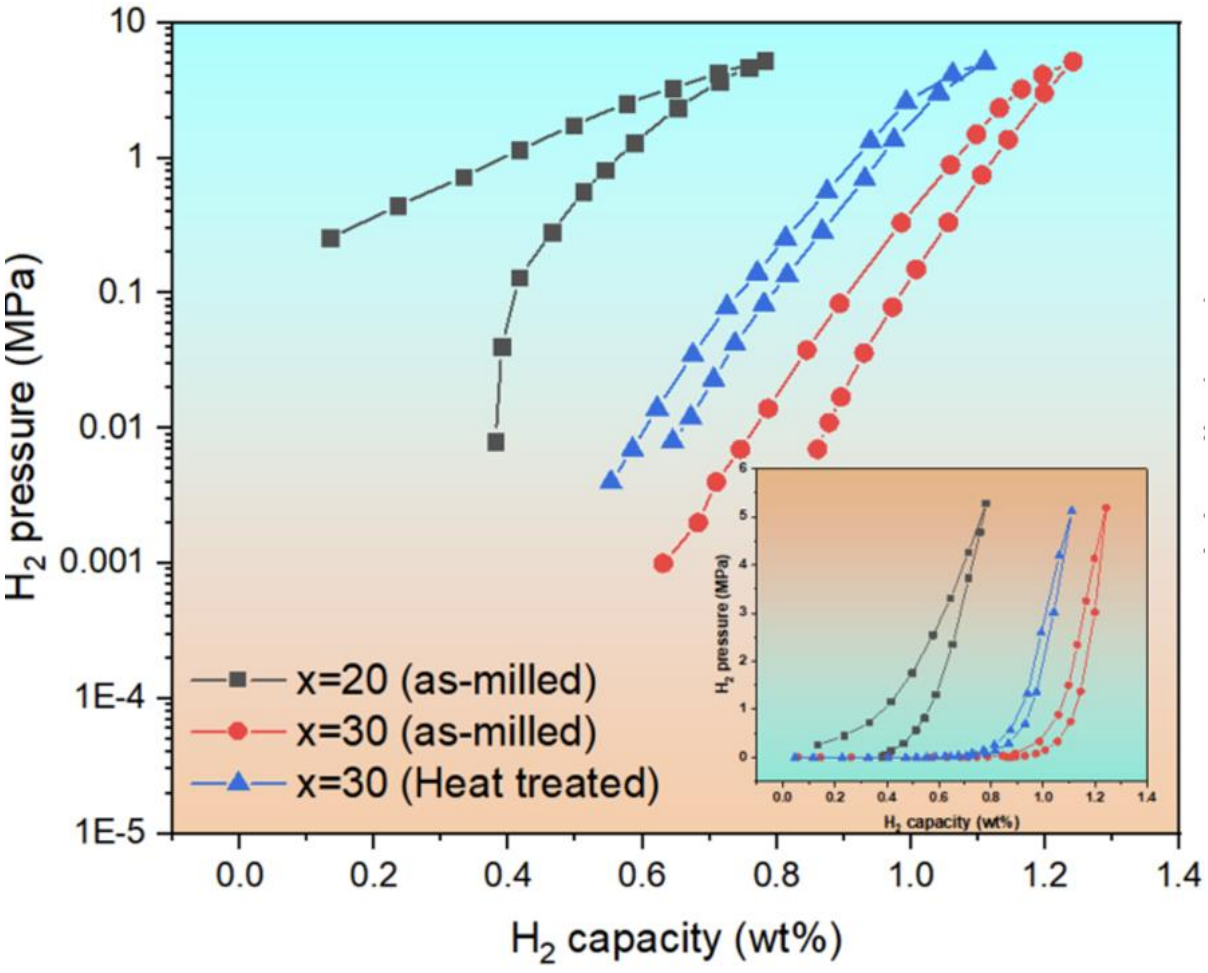

Fig 5.10 Room temperature PCT curves of as-milled $Ti_{5+x}V_{35}(CrMnFe)_{60-x}$ (x = 20, 30) HEAs, and x=30 after heat treated

Fig 5.10 (a) shows the room temperature hydrogen absorption/desorption PCT curve of the $Ti_{5+x}V_{35}(CrMnFe)_{60-x}$ (x = 20, 30) alloy and x=30 alloy after heat treatment. It can be clearly observed that the hydrogen absorption/desorption capacities of the alloy are close with the results of hydrogen storage kinetics tests. The alloys are capable of hydrogen absorption lower than 0.001 MPa hydrogen pressure, indicating that the alloy may start absorbing hydrogen at extremely low pressures, which are below the detection limit of the instrument, which has been observed in numerous studies [35, 233] Additionally, it is observed that compared to traditional hydrogen storage materials, there is a lack of a distinct plateau pressure [26, 33, 233].

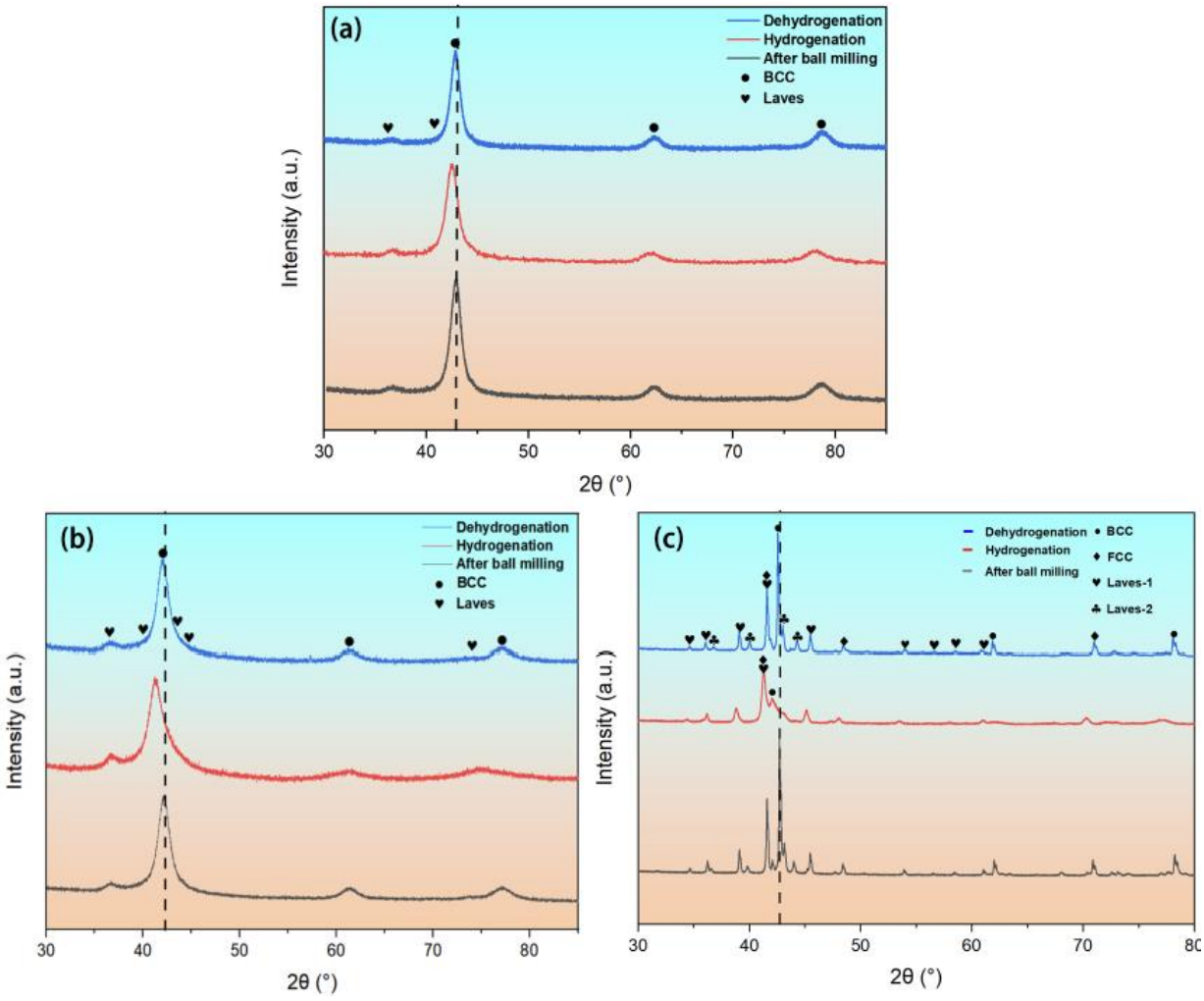

Fig 5.11 The hydrogenation/dehydrogenation XRD patterns of the as-milled alloy: (a) x=20; (b) x=30; (c) 900°C heat treated alloy (x=30)

Fig 5.11 presents the XRD patterns of the alloys after room temperature hydrogen

absorption/desorption, and the lattice parameters are summarized in Table 5. Following hydrogen absorption, a leftward shift in the alloy's XRD patterns is evident, accompanied by an increase in the respective lattice parameters, attributed to lattice expansion during hydrogenation [224]. It is worth noting that the XRD patterns of the as-milled alloys after hydrogen absorption shows obvious changes in the BCC peak, indicating the predominant hydrogen absorption phase as the BCC. This elucidates the significant fluctuations in hydrogen absorption observed with variations in BCC phase content and lattice constants. Furthermore, the XRD patterns after hydrogen absorption does not unveil the presence of BCT or FCC, implying the alloy's incapacity to form stable metal hydrides.

Table 5.5 Phase lattice parameters of hydrogenated/dehydrogenated of $Ti_{5+x}V_{35}(CrMnFe)_{60-x}$ (x = 20, 30) as-milled HEAs and heat-treated HEA (x=30).

Alloy		$a_{bcc/fcc}$ (Å)	a_{Laves} (Å)	c_{laves} (Å)	R_{wp} (%)
Hydrogenated	x=20	2.987^{b}	4.905	7.930	3.91
	x=30	3.093^{b}	4.935	8.101	6.08
	x=30 (Heat treated)	$3.040^{b}/3.787^{f}$	$5.207^{L1}/5.016^{L2}$	$8.242^{L1}/9.069^{L2}$	10.87
Dehydrogenated	x=20	2.971^{b}	4.869	7.887	3.79
	x=30	3.030^{b}	4.879	8.071	5.32
	x=30 (Heat treated)	$2.993^{b}/3.758^{f}$	$5.168^{L1}/4.979^{L2}$	$8.209^{L1}/9.041^{L2}$	9.68

L1/L2: Laves-1 and Laves-2; b/f: BCC and FCC.

Through analysis of PCT curves (Fig.8 a) and XRD data (Fig. 8 c-d), it was observed that the

HEAs did not display noticeable plateau pressures throughout the hydrogen absorption/desorption processes, and changes were limited to lattice constants variations among the phases without any phase transformations (BCT or FCC). This indicates that hydrogen atoms solved within the lattice interstitially, where hydrogen atoms occupy interstitial sites with varying potential energies, leading to a slope plateau [26, 233]. This solid solution mechanism is particularly notable in HEAs, likely due to the complex interactions among multiple elements. Several HEAs systems have observed such phenomena [231, 233-235]. After heat treatment (x=30), the increased number of phases and the synergistic hydrogen absorption/desorption effects among them result in a single slope plateau and increase in plateau pressure, slightly enhancing the hydrogen desorption capacity of the alloy.

5.4 Summary

In summary, our study on Ti5+xV35(CrMnFe)60-x (x=0,10,20,30) high-entropy alloys (HEAs) revealed the following:

1. After milling, the alloy consists predominantly of the BCC, accompanied by a small amount of C14 Laves. The proportion of C14 Laves increasing with the increase of Ti content.

2. Thermal stability evaluation unveiled complex phase transformations during HT (BCC+Laves-1 → BCC+FCC+Laves-1 → BCC+FCC+Laves-1+Laves-2), indicating the dependency of phase stability on Ti content. Nanocrystalline structures are maintained post-heat treatment.

3. Hydrogen absorption/desorption performance before HT primarily depend on the total A (hydrogen affinity) elements content in the alloy. At x=20, absorption reaches 0.78 wt%, and desorption reaches 0.38 wt%. At x=30, absorption reaches 1.21 wt%, with desorption at 0.34 wt%.

4. After heat treatment, the reduction in lattice constant and content of the BCC led to a decrease in the alloy's hydrogen storage capacity. However, its hydrogen desorption capacity has slightly increased at x=30.

6. Hydrogen ab/desorption behavior of the mechanical alloyed Ti-V-Cr-Mn-Fe HEAs with varying Mn/Cr ratio

According to previous research [16, 48, 153], a higher valence electron concentration (VEC) or electronegativity may lead to a reduction in the hydrogen storage capacity of the alloy. In addition, excessive Fe content may promote the formation of C14-type (laves, H/M=1) intermetallic compounds, which exhibit relatively low hydrogen storage capacity, thereby reducing the overall hydrogen storage capacity of the alloy. [19, 20, 29]. Therefore, the Fe content was deliberately kept at a minimum level in this study to minimize its potential adverse effects on the hydrogen storage performance of the alloy. In addition, the ratio between Mn and Cr was adjusted due to the significant difference in their atomic radii—Mn (135pm) having a relatively larger atomic radius, while Cr (124.91pm) is smaller. By varying the Mn/Cr ratio, the lattice constant of the alloy can be effectively tuned, which in turn influences the crystal structure and hydrogen storage performance. This study builds upon our previous research (chapter 5) by systematically adjusting the Cr (124.91pm) and Mn (135pm) content in $Ti_{35}V_{35}(CrMnFe)_{30}$ alloys to investigate their effects on hydrogen storage performance. By fixing the elements on the A side (Ti and V) and adjusting the proportions of Mn/Cr, we investigated the hydrogen storage performance, kinetics performance of the mechanically alloyed $Ti_{35}V_{35}Cr_{20-x}Mn_{5+x}Fe_5$ (x=0, 5, 10, 15) HEAs, and systematically explored the influence of varying Mn/Cr content on the phase structure and the optimization of hydrogen storage properties of the as-milled HEAs.

Partial contents in this chapter have been published in the journal:

Y.T. Zhai, Y.M. Li, Z.C. Liu, L. Bolzoni, J. Kennedy, ***F. Yang***, Hydrogen ab/desorption behavior of the mechanical alloyed Ti-V-Cr-Mn-Fe HEAs with varying Mn/Cr ratio, International Journal of Hydrogen Energy, Volume 109, 2025, page 1008-1022. https://doi.org/10.1016/j.ijhydene.2025.02.139.

6.1 Phase composition and microstructure of $Ti_{35}V_{35}Cr_{20-x}Mn_{5+x}Fe_5$ (x = 0, 5, 10, 15)

Fig 6.1 depicts the X-ray diffraction (XRD) patterns of the as-milled $T_{35}V_{35}Cr_{20-x}Mn_{5+x}Fe_5$ (x = 0, 5, 10, 15) HEAs. These four alloy compositions exhibit a combination of body-centered cubic (BCC) and a small amount of C14 Laves. The phase proportions and lattice parameters were determined through Rietveld refinement analysis using the MAUD software [202], as presented in Table 6.2 The XRD results indicate that the addition of Mn elements suppresses the formation of the C14 Laves. Conversely, with an increase in Cr content, the corresponding number of C14 Laves peaks gradually increases. This phenomenon is attributed to the addition of Cr, which leads to increased lattice distortion (δ) and a higher formation enthalpy (ΔHmix) (as shown in Table 6.1).

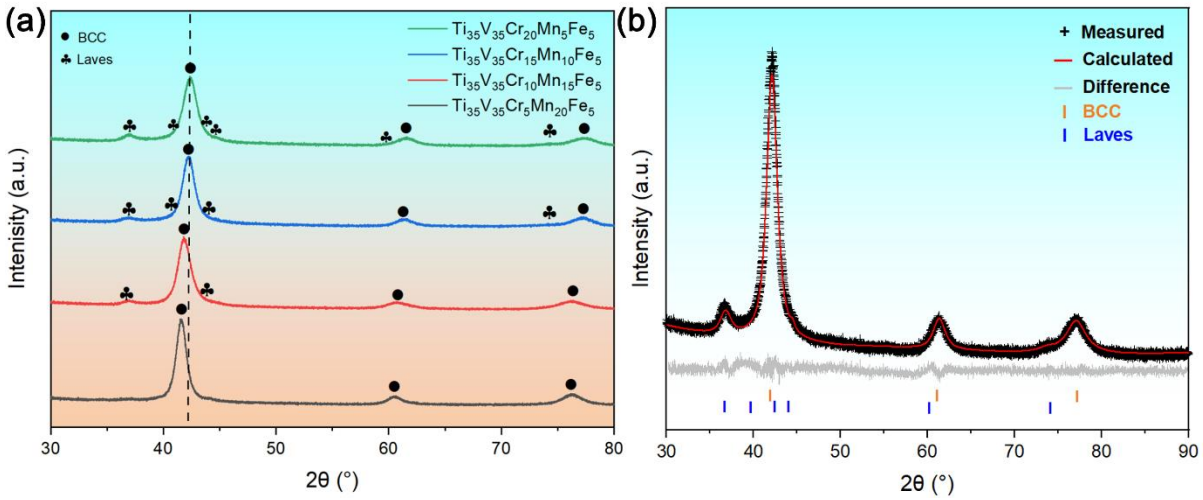

Fig 6.1 (a) XRD patterns of the as-milled $Ti_{35}V_{35}Cr_{20-x}Mn_{5+x}Fe_5$ (x = 0, 5, 10, 15) HEAs; (b) Rietveld refinement of representative of $Ti_{35}V_{35}Cr_{20}Mn_5Fe_5$ HEA

Table 6.1 Calculated thermodynamic and geometric parameters of $Ti_{35}V_{35}Cr_{20-x}Mn_{5+x}Fe_5$ (x = 0, 5, 10, 15) HEAs.

HEAs	$\triangle H_{mix}$ (kJ/mol)	VEC	Ω	δ (%)	$\bar{r}$ (pm)
$Ti_{35}V_{35}Cr_{20}Mn_5Fe_5$ ($Cr_{20}Mn_5$)	-4.71	5.1	4.89	6.35	135.07
$Ti_{35}V_{35}Cr_{15}Mn_{10}Fe_5$ ($Cr_{15}Mn_{10}$)	-4.4	5.15	5.32	6.09	135.57
$Ti_{35}V_{35}Cr_{10}Mn_{15}Fe_5$ ($Cr_{10}Mn_{15}$)	-3.95	5.2	5.83	5.79	136.08
$Ti_{35}V_{35}Cr_5Mn_{20}Fe_5$ (Cr_5Mn_{20})	-3.63	5.25	6.53	5.46	136.58

The elevated formation enthalpy and greater lattice distortion promote the formation of intermetallic compounds, resulting in a slight increase in the content of the Laves phase in the alloy [236]. Furthermore, with the increase in Mn content, the main peak of the BCC gradually shifts to the left. This corresponds to the gradual increase in the BCC lattice parameters, as presented in Table 6.3, due to the substitution of small Cr (124.91pm) atoms by large Mn (135pm) atoms. In this study, the crystallite size was calculated by combining X-ray diffraction (XRD) data with the Scherrer formula. The Scherrer formula is expressed as follows:

$$D = \frac{K * \lambda}{\beta * \cos\theta}$$

Among those :D is the crystallite size (nm); K is the shape factor, which is usually taken as 0.9; λ is the wavelength of the X-ray, and in this study, Cu-Kα radiation with a wavelength of 0.15406 nm was used; β is the full width at half maximum (FWHM) of the main peak; θ is the Bragg angle of the main peak (show in Table 6.2).

Table 6.2 Specific parameters main peak of the bcc phase and crystallite size for different HEAs

Alloys	2θ (°)	FWHM (°)	Crystallite size (mn)
Cr_5Mn_{20}	41.58	1.26	6.74
$Cr_{10}Mn_{15}$	41.87	1.56	5.46
$Cr_{15}Mn_{10}$	42.22	1.61	5.31
$Cr_{20}Mn_5$	42.36	1.73	4.93

The crystallite sizes calculated using the Scherrer formula are presented in Table 2, with the specific formula and parameters detailed in Table 6.2. The results indicate that as the overall lattice distortion (δ) of the alloy increases, the crystallite size decreases. This may be attributed to the larger lattice distortion impeding atomic diffusion, thereby facilitating the formation of finer crystallites [158, 237]. Furthermore, the average particle size (D_{50}) of the alloy powders prepared via mechanical alloying is below 25 μm (morphology and particle size distribution of each alloy are illustrated in Fig. 6.2), which can be attributed to the unique advantages of the mechanical alloying process [238, 239].

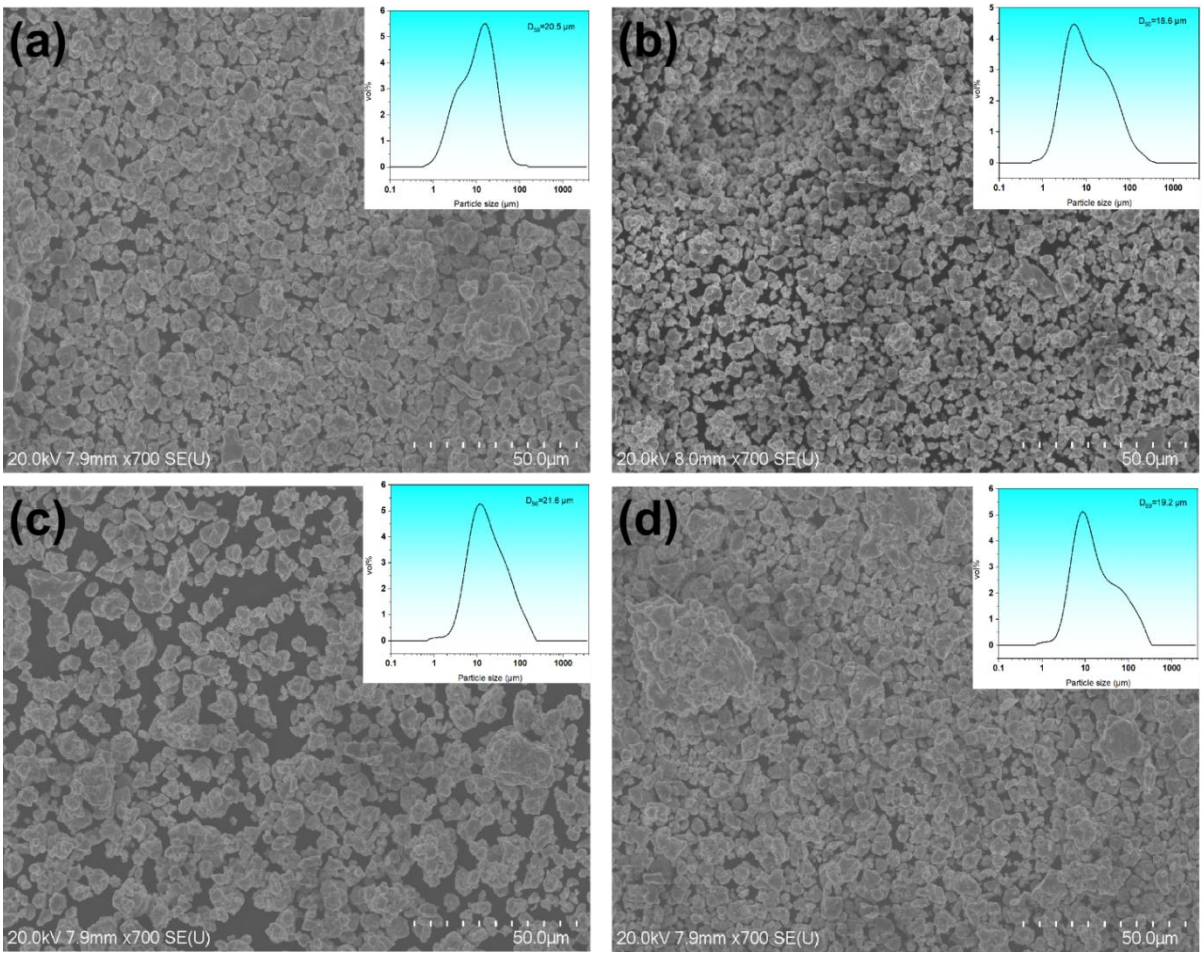

Fig. 6.2 Particle morphology and particle size distribution (detect by Malvern Panalytical Mastersizer 3000) of different HEAs: (a) Cr5Mn20; (b) Cr10Mn15; (c) Cr15Mn10; (d) Cr20Mn5

Fig 6.3 presents the backscattered electron (BSE) images and chemical element distribution maps of the as-milled $T_{35}V_{35}Cr_{20-x}Mn_{5+x}Fe_5$ (x = 0, 5, 10, 15) HEAs. The elemental compositions of these HEAs are listed in Table 3. The elemental distribution mappings reveal the composition distributions are homogeneous in the alloys. The actual chemical compositions of the alloys are closely approximate their nominal compositions, and minor disparities are discernible between the actual and nominal chemical compositions. Notably, in the backscattered electron images of the alloy (Fig. 6.3), no distinct phase structures are observed. This may be due to the low concentration of the Laves phase (Table 6.4). Additionally, during the mechanical alloying process, the severe plastic deformation and mechanical impacts induced by high-energy ball milling result in significant crystal structure distortion and the

formation of extremely fine nanocrystals, making the identification of phase structures by SEM highly challenging [240, 241]. This also align with the results we reported previously that the as-milled HEA alloy can maintain nanostructure even after heat treatment at high temperatures [58].

Table 6.3 Refinement data of the $T_{35}V_{35}Cr_{20-x}Mn_{5+x}Fe_5$ (x = 0, 5, 10, 15) HEAs.

Alloys	Phase	Space group	wt%	Lattice constant(Å)	Crystallite size (mn)	Rwp%
$Cr_{20}Mn_5$	BCC	Im-3m (229)	92.38	a=3.017	4.93	6.45
	Laves	P63-mcc (194)	7.62	a=4.836/c=7.938	-	
$Cr_{15}Mn_{10}$	BCC	Im-3m (229)	94.61	a=3.020	5.31	6.83
	Laves	P63-mcc (194)	5.39	a=4.848/c=7.977	-	
$Cr_{10}Mn_{15}$	BCC	Im-3m (229)	96.59	a=3.025	5.46	6.99
	Laves	P63-mcc (194)	3.41	a=4.898/c=8.021	-	
Cr_5Mn_{20}	BCC	Im-3m (229)	-	a=3.034	6.74	5.88

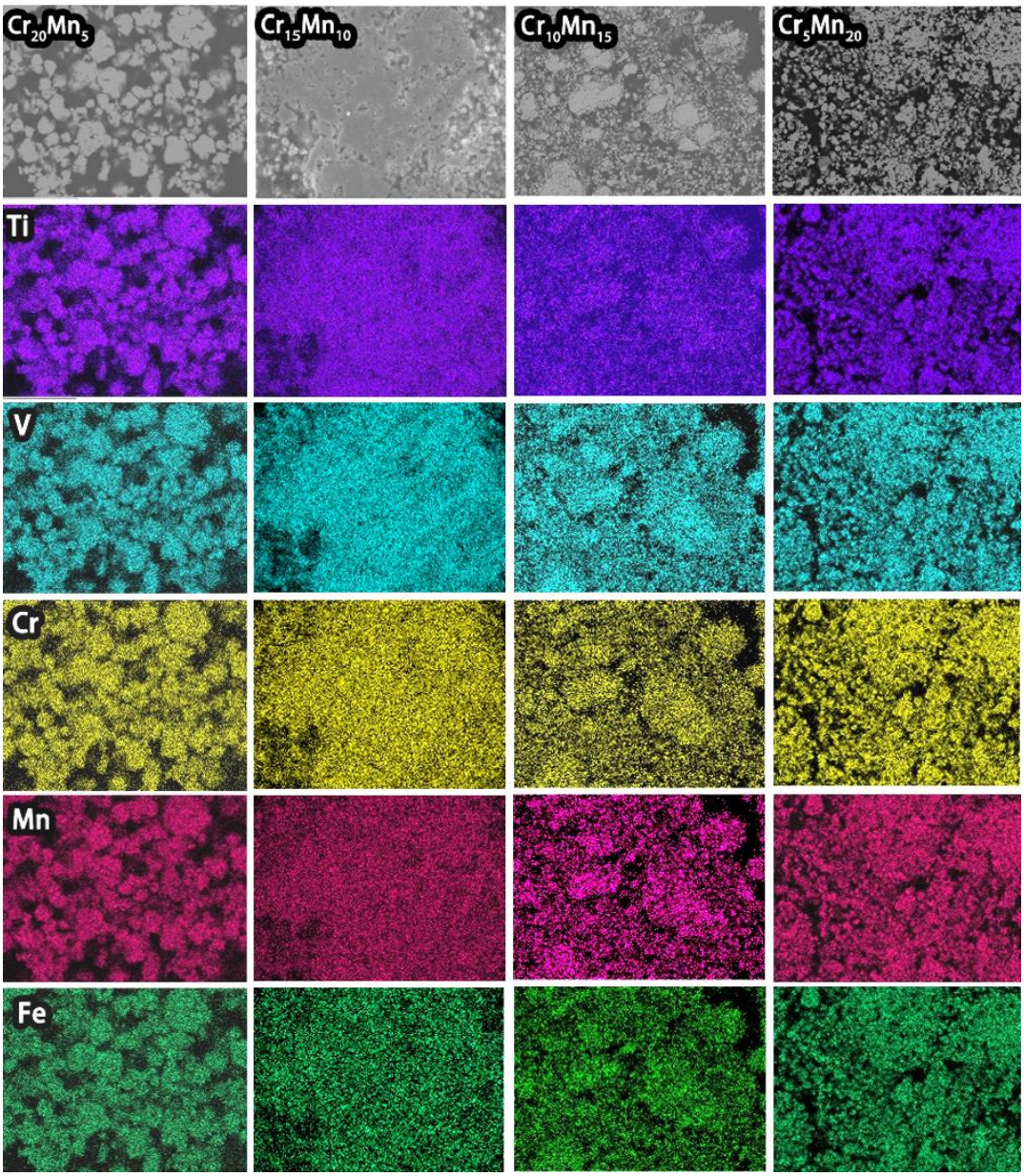

Fig 6.3 BSE/EDS maps of the as-milled $T_{35}V_{35}Cr_{20-x}Mn_{5+x}Fe_5$ (x = 0, 5, 10, 15) HEAs

Table 6.4 Represents the measured at% values of each element present in the as-milled $T_{35}V_{35}Cr_{20-x}Mn_{5+x}Fe_5$ (x = 0, 5, 10, 15) HEAs.

Alloy	Ti	V	Cr	Mn	Fe
$Cr_{20}Mn_5$	35.53	34.77	19.77	4.98	4.95
$Cr_{15}Mn_{10}$	35.67	34.85	14.82	9.98	4.68
$Cr_{10}Mn_{15}$	35.56	34.92	10.16	14.49	4.87
Cr_5Mn_{20}	35.85	34.94	4.79	19.53	4.89

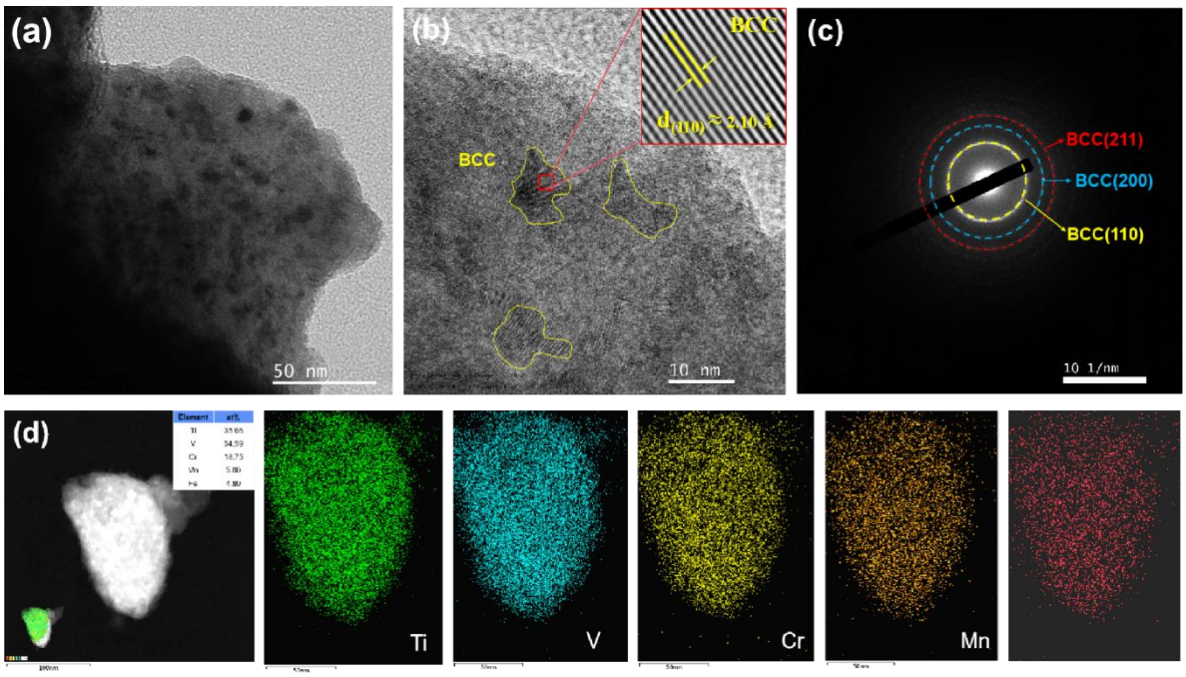

Fig 6.4 TEM characterization of as-milled $Ti_{35}V_{35}Cr_{20}Mn_5Fe_5$ ($Cr_{20}Mn_5$) HEA: (a) bright-field image; (b) high-resolution TEM image (FFT image of red frame); (c) SEAD pattern; (d) the element distribution mappings

In order to explore more details of the microstructure present in the alloys, TEM investigation have been performed. Fig 6.4 presents the TEM analysis of the $Cr_{20}Mn_5$ high-entropy alloy. Fig 6.4 a and b reveal the presence of numerous nanocrystalline structures within the alloy, with sizes ranging approximately 10 nanometers and exhibiting irregular shapes. Additionally, it is confirmed that the alloy is predominantly composed of a BCC structure after ball milling. However, it is noteworthy that the Laves structure remains difficult to observe under TEM, which could be due to its low content or the inherent limitations of the TEM observation range. Fig 6.4 d further illustrates that the elemental distribution in the as-milled HEA is uniform, with no elemental segregation regions observed, and the elemental composition matches to the designed composition. These findings are consistent with those observed under SEM.

6.2 Hydrogen activation performances

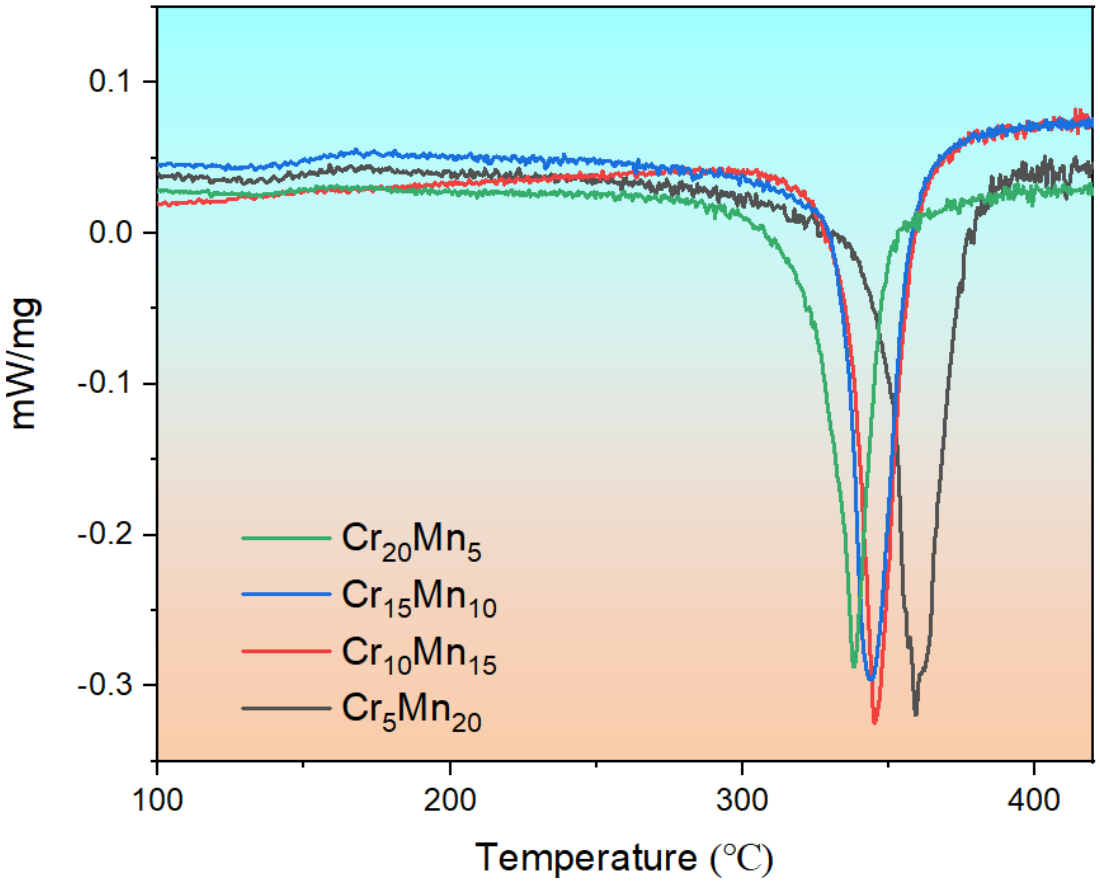

Fig 6.5 The first hydrogen absorption high-pressures (H_2) differential scanning calorimetry (HPDSC) curve of $T_{35}V_{35}Cr_{20-x}Mn_{5+x}Fe_5$ (x = 0, 5, 10, 15) HEAs.

Fig 6.5 a present the DSC curves for the initial hydrogen absorption of the fabricated HEAs under a 3 MPa hydrogen atmosphere. It is evident that as the Cr content increases, the optimal temperature for initial hydrogen absorption decreases. This suggests that the addition of Cr improves the alloy's initial activation performance. Fig 6.6 (a) - (d) shows the activation curves for the fabricated HEAs. It can be observed that as the Mn content gradually increases, the initial hydrogen absorption during activation slightly increases. This is attributed to the substitution of smaller atoms (Cr) with larger atoms (Mn), results in an increase in the lattice constant of the HEAs. As lattice constant increases, the unit cell volume expands accordingly, providing more interstitial space for hydrogen atoms. This alleviates the repulsive interactions between hydrogen atoms within the lattice, thereby enhancing their thermodynamic

stability[242, 243]. Furthermore, all four alloy compositions achieved their maximum hydrogen absorption capacity during the first activation. After three activations, the hydrogen absorption capacity is slightly lower than the first activation, attributed to the formation of relatively stable hydrides during hydrogen absorption and they cannot be fully decomposed during the 2-hour vacuum treatment at 300°C.

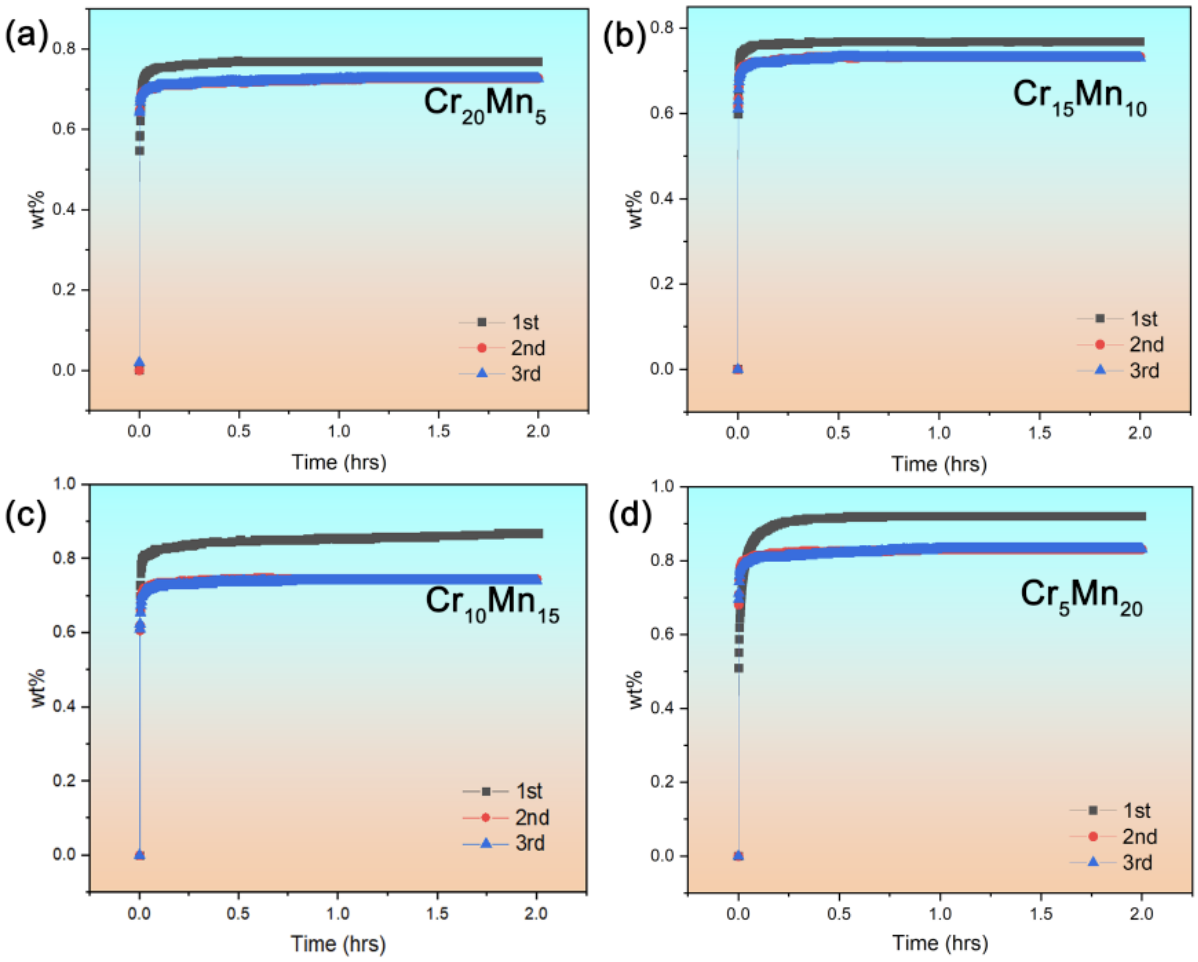

Fig 6.6 The activation curve of $T_{35}V_{35}Cr_{20-x}Mn_{5+x}Fe_5$ (x = 0, 5, 10, 15) HEAs

6.3 Hydrogen ab/desorption capacity of $T_{35}V_{35}Cr_{20-x}Mn_{5+x}Fe_5$ (x = 0, 5, 10, 15) HEAs

Fig 6.7 shows the hydrogen absorption/desorption curves of the $Ti_{35}V_{35}Cr_{20-x}Mn_{5+x}Fe_5$ (x = 0, 5, 10, 15) alloy after activation at different temperatures. From Fig 6.7 (a) - (c), it can be observed that as the Mn content increases, the overall hydrogen absorption capacity gradually increases. The hydrogen absorption capacities of $Cr_{20}Mn_5$, $Cr_{15}Mn_{10}$, $Cr_{10}Mn_{15}$, and Cr_5Mn_{20} at room temperature are 1.08 wt%, 1.12 wt%, 1.23 wt%, and 1.39 wt% (show in Table 6.5), respectively. This phenomenon is caused by two factors: (1) The addition of Mn increases the BCC content and decreases the Laves content. Since the theoretical hydrogen storage capacity of the BCC (~ 4wt% [48]) is larger than the Laves (~ 1.8wt% [22]), the overall hydrogen storage capacity of the alloy increases; (2) The lattice constant of the BCC structure increases, resulting in an increase in the unit cell volume. This provides more space, increasing the distance between hydrogen atoms, reducing their mutual repulsion in the lattice, thus allowing more hydrogen atoms to be accommodated within the lattice [20, 244, 245]. Comparing hydrogen absorption capacity at various temperatures reveals that absorption capacity decreases with increasing the temperature. This phenomenon occurs because hydrogen absorption is an exothermic reaction, and elevated temperatures will inhibit the reaction [36]. Conversely, hydrogen desorption is an endothermic reaction, thus higher temperatures facilitate the desorption process, resulting in an increased of hydrogen desorption capacity [52].

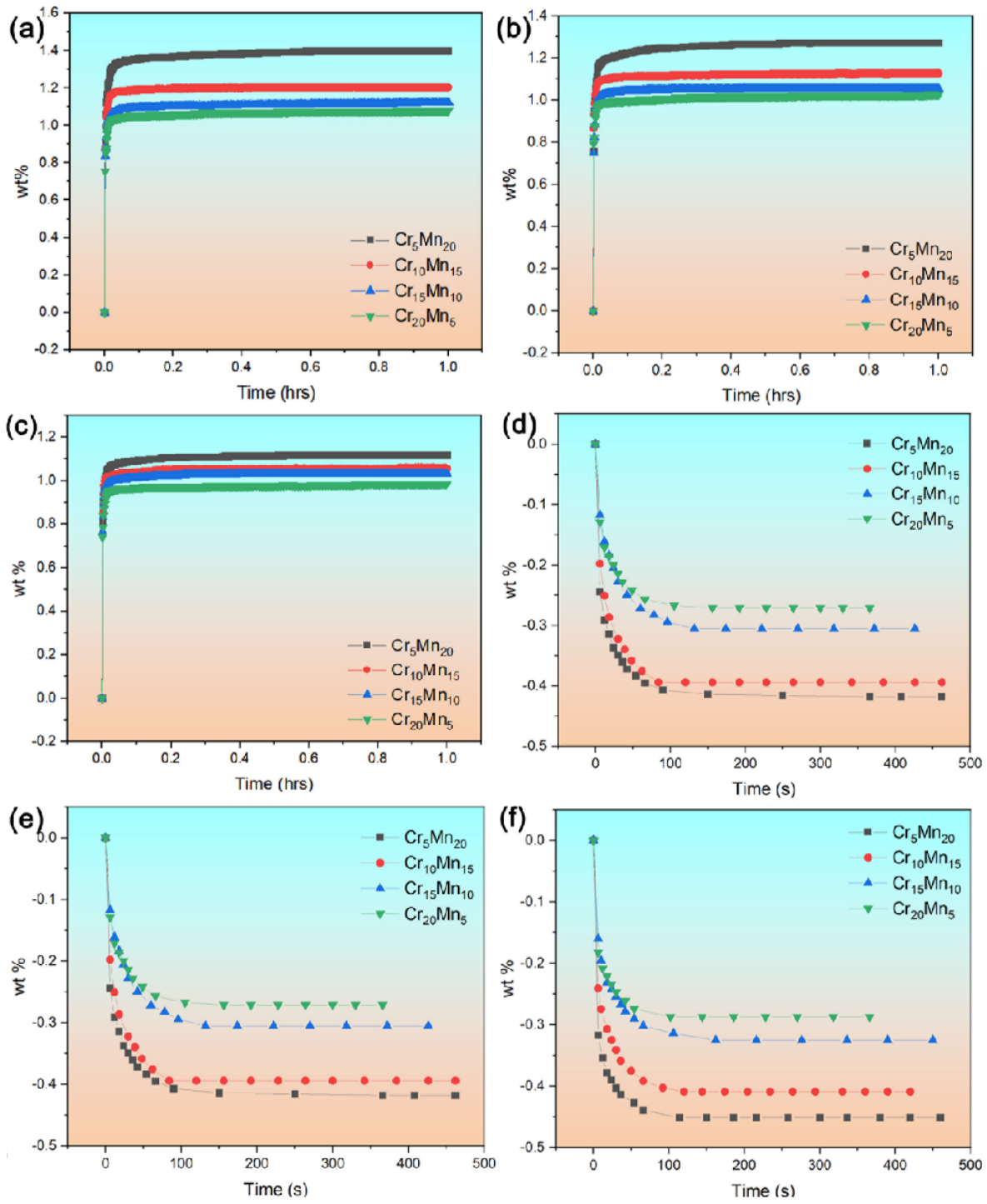

Fig 6.7 Hydrogen absorption and desorption curves of the alloy at different temperatures: (a), (d) room temperature; (b), (e) 50°C, (c), (f) 75°C.

Table 6.5 Hydrogen absorption/desorption capacity of $T_{35}V_{35}Cr_{20-x}Mn_{5+x}Fe_5$ (x = 0, 5, 10, 15) HEAs at different temperature.

HEAs	Capacity (wt%)	Temperature		
		Room temperature	50°C	75°C
$Cr_{20}Mn_5$	Abs	1.08	1.03	0.98
	Des	0.26	0.27	0.29
$Cr_{15}Mn_{10}$	Abs	1.12	1.06	1.01
	Des	0.3	0.31	0.33
$Cr_{10}Mn_{15}$	Abs	1.23	1.13	1.06
	Des	0.38	0.40	0.41
Cr_5Mn_{20}	Abs	1.39	1.27	1.12
	Des	0.40	0.42	0.45

6.4 Hydrogen storage kinetic performances

The hydrogen absorption process is typically divided into two stages. The first stage is controlled by surface reactions and interfacial processes [236, 246]. The second stage involves the nucleation and growth of the metal hydrides [127, 247]. Fig 6.8 presents the fitting results of different models applied to various stages of the hydrogen absorption process of the Cr_5Mn_{20} HEA at room temperature. It is evident that the degree of fit varies among models. Detailed formulas for each model can be found in Table 2.1 of Chapter 2. By comparing the R^2 values from the fitting results, it is clear that the Hirooka's first-order kinetic equation provides the highest R^2 (0.9741) value for the first stage of hydrogen absorption, indicating that this model most accurately reflects the alloy's behavior during this stage I. In contrast, the JMAK equation achieves the best fit (R^2=0.9608) for the second stage of hydrogen absorption. Consequently, to maintain consistency across experiments, the Hirooka's first-order kinetic equation will be used for fitting the first stage, while the JMAK equation will be applied to the second stage of hydrogen absorption in subsequent analyses at various temperatures.

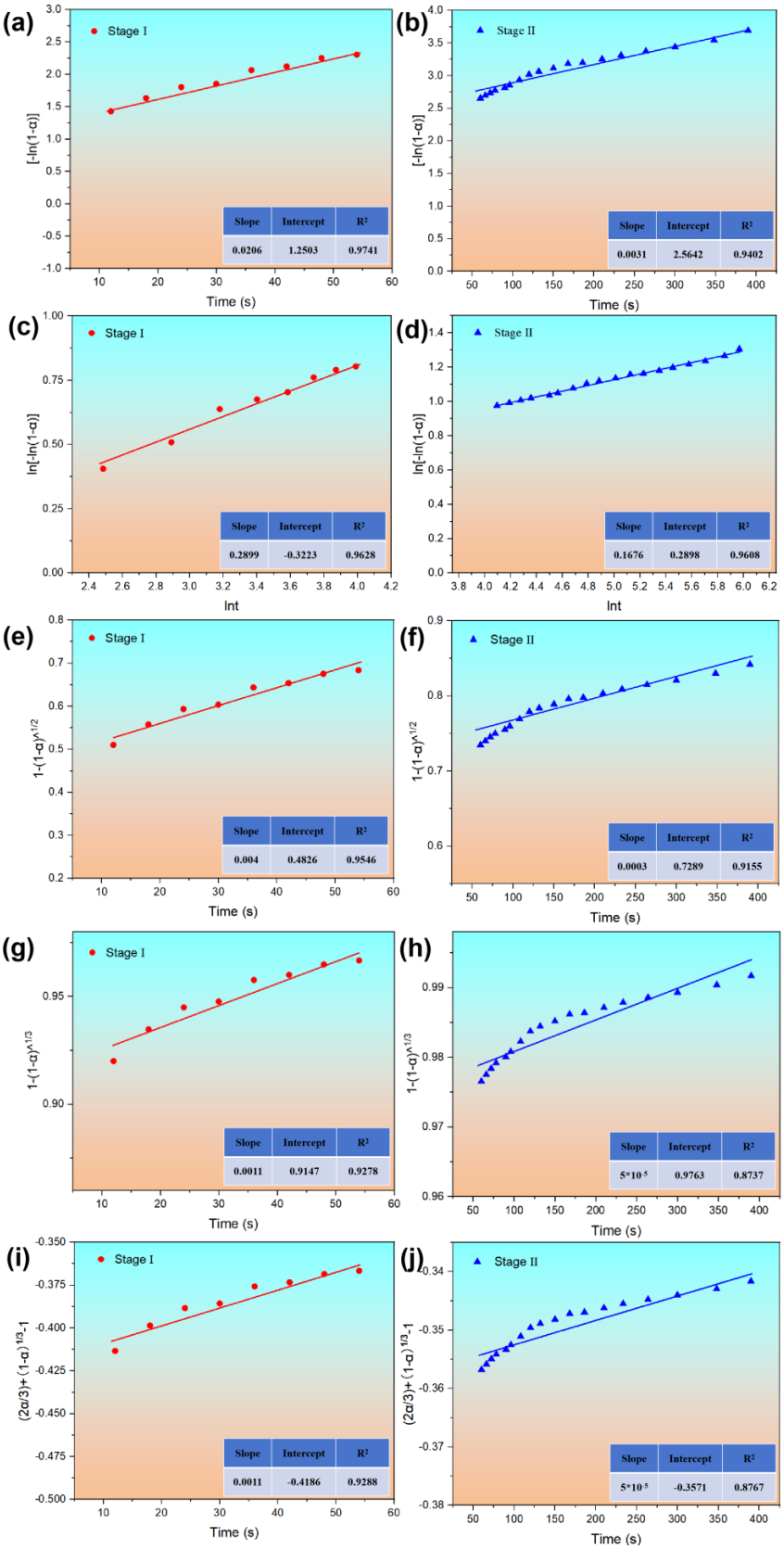

Fig 6.8 The corresponding fittings model of the hydrogenation kinetics by different hydrogenation stages

In this study, Hirooka's first-order kinetic equation to analyze the hydrogen absorption kinetics during the first stage. The specific equation is as follows [246]:

$$-\ln(1-\alpha) = kt \quad (1)$$

Where α is the reaction fraction at time t; t is the time k is the reaction rate constant, which characterizes the hydrogenation reaction rate parameter. The second stage of hydrogen absorption in the alloy was fitted using the JMAK (Johnson-Mehl-Avrami-Kolmogorov) equation. The specific equation is as follows [127]:

$$\alpha = 1 - \exp(-kt)^{\eta} \quad (2)$$

$$\ln[-\ln(1-\alpha)] = \eta \ln t + \eta \ln k \quad (3)$$

Where α is the reaction fraction at time t; k is the reaction rate constant, which characterizes the hydrogenation reaction rate parameter; η is the Avrami exponent, indicating the complexity of the reaction. It can be observed that the different stages of hydrogen absorption at each temperature are well-fitted by the different equations. The specific fitting results are shown in Fig 6.9

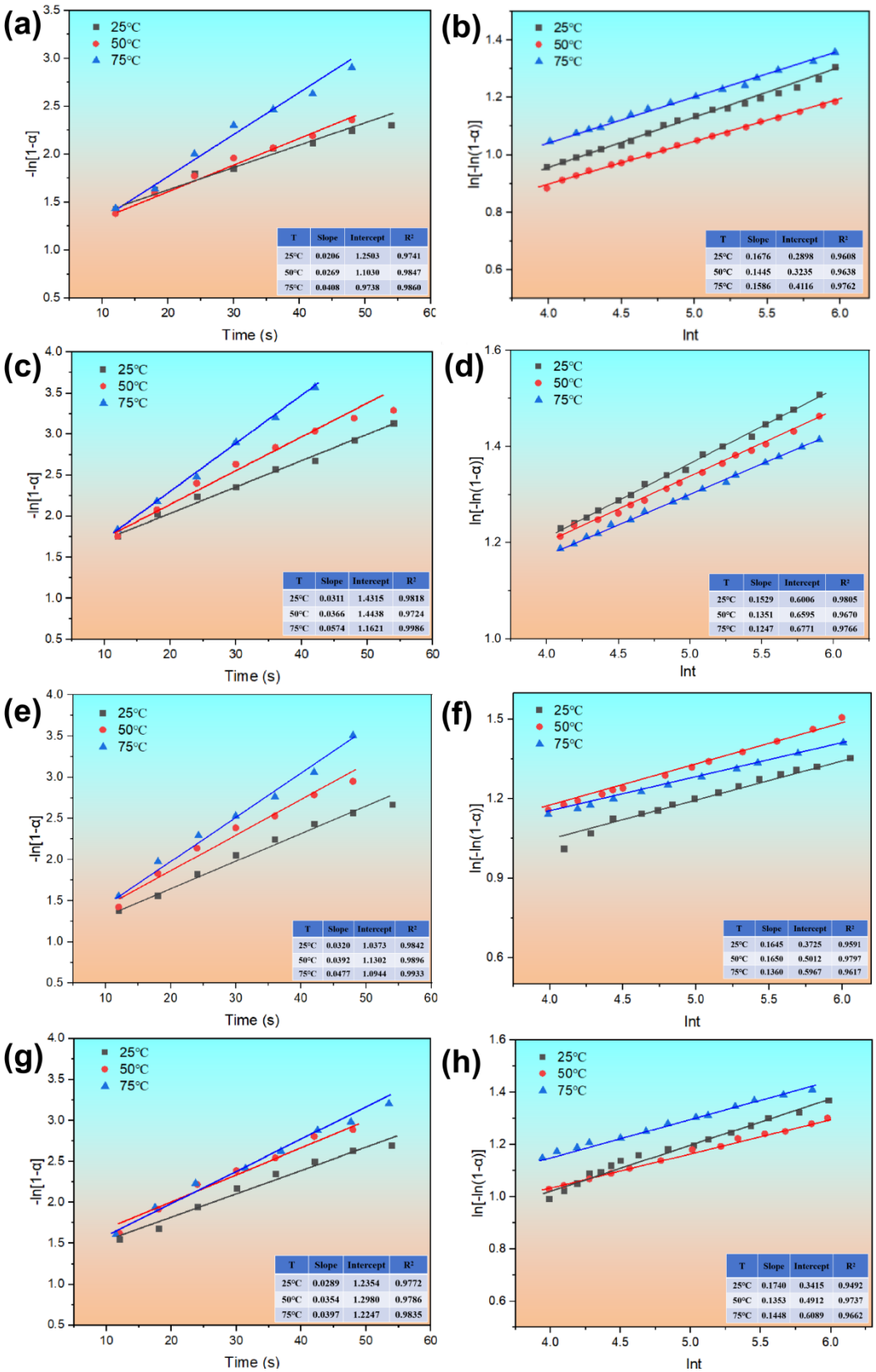

Fig 6.9 The fitting curve of different stages by Hirooka's first-order kinetic equation (a, c, e, f) and JMAK equation (b, d, f, h): (a), (b) Cr_5Mn_{20}; (c), (d) $Cr_{10}Mn_{15}$; (e), (f) $Cr_{15}Mn_{10}$; (g), (h) $Cr_{20}Mn_5$

To analyze the activation energy of $T_{35}V_{35}Cr_{20-x}Mn_{5+x}Fe_5$ (x = 0, 5, 10, 15) during the hydrogenation reaction, linear fitting is performed using the Arrhenius equation based on the Hirooka's first-order kinetic equation and JMAK equation fitting. The linear relationship of lnk with 1000/RT is obtained, and the activation energy (E_a) of each alloy is determined by calculating the slope of the curve. The Arrhenius equation is given by Equation [248]:

$$\boldsymbol{k = Ae^{-\frac{E_a}{RT}}} \quad \textbf{(3)}$$

$$\boldsymbol{lnk = -\frac{Ea}{RT} + lnA} \quad \textbf{(4)}$$

where $\boldsymbol{k}$ is the rate constant, **A** is the pre-exponential factor, $\mathbf{E_a}$ is the activation energy, **T** is the temperature and **R** is the universal gas constant (8.314 kJ/mol). The specific fitting results are shown in Fig 6.10.

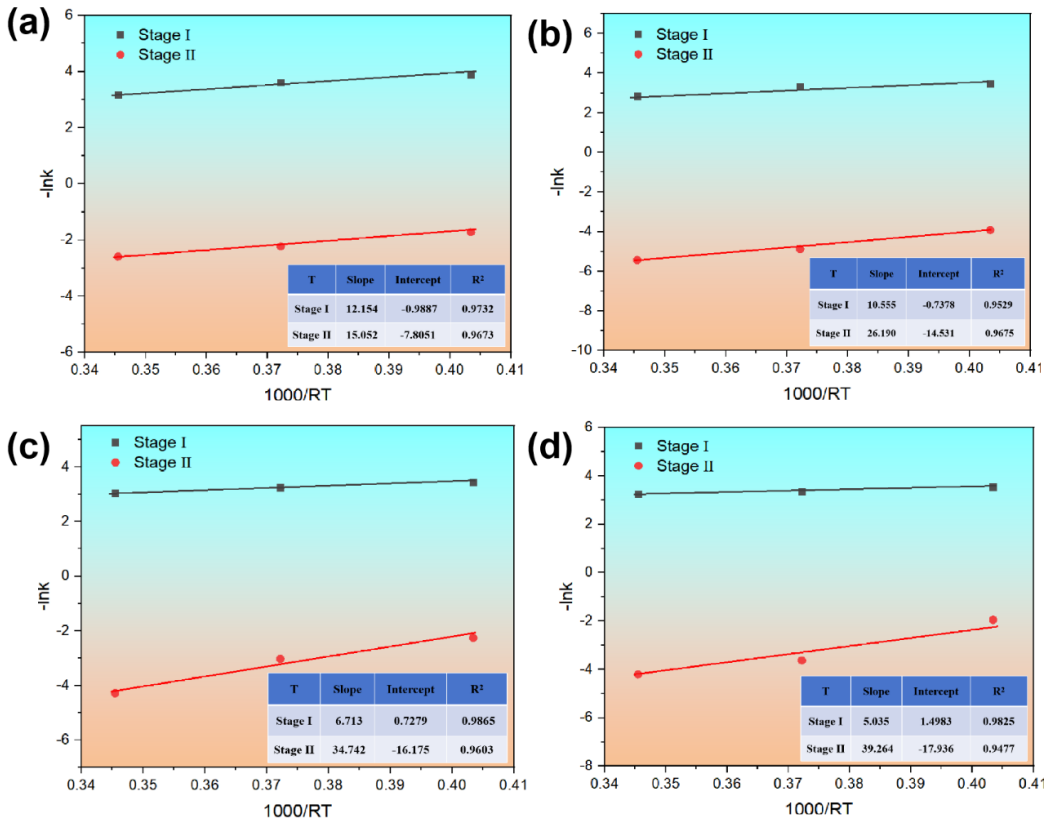

Fig 6.10 Corresponding Arrhenius plots of lnk vs 1000/RT for the apparent activation energies of stage I and stage II of hydrogenation processes: (a) Cr_5Mn_{20}; (b) $Cr_{10}Mn_{15}$; (c) $Cr_{15}Mn_{10}$; (d) $Cr_{20}Mn_5$

By comparing the absorption activation energies (E_a) of the same alloy at different stages, it can be observed that the nucleation and growth of the metal hydrides (Stage II) has the highest activation energy (show in table 6.6), indicating that this stage is the rate-limiting step in the hydrogen absorption process [233]. Additionally, comparing the activation energies of different alloys reveals that the activation energy in the stage I decreases with increasing Cr content. This suggests that the addition of Cr enhances the surface reactions and interfacial processes [249, 250]. This is because the addition of Cr increases the content of the second (C14 Laves) phase (show in Table 6.3), and the presence of more second phase in the alloy facilitates the initiation and propagation of cracks during hydrogenation [49]. These cracks between the phases serve as diffusion pathways for hydrogen atoms, enhancing the kinetic performance during the first stage [251]. During the second stage of hydrogen absorption in the alloy, the activation energy gradually increases. This phenomenon can be attributed to the increase in overall lattice distortion (δ) of the alloy (show in Table 6.1), which disrupts the high symmetry of interstitial sites [252], and alter the diffusion pathways of hydrogen atoms within the crystal structure, slowing hydrogen accumulation and inhibiting the nucleation and growth of metal hydrides [253, 254].

Table 6.6 The activation energies of $Ti_{35}V_{35}Cr_{20-x}Mn_{5+x}Fe_5$ (x = 0, 5, 10, 15) HEAs.

Alloys	Activation energies (kJ/mol)		
	A_b (stage I)	A_b(stageII)	D_e
Cr_5Mn_{20}	12.15	15.05	-19.93
$Cr_{10}Mn_{15}$	10.55	26.19	-16.11
$Cr_{15}Mn_{10}$	6.71	34.74	-15.87
$Cr_{20}Mn_5$	5.03	39.26	-14.76

PS: The positive and negative signs in the table are used solely to distinguish between the hydrogenation and dehydrogenation processes of the HEAs.

Fig 6.11 illustrates the hydrogen desorption kinetics analysis of the $T_{35}V_{35}Cr_{20-x}Mn_{5+x}Fe_5$ (x = 0, 5, 10, 15) alloys. Typically, only a single stage is observed, as the desorption process is more rapidity than desorption process [52, 124, 255]. It can be seen that the desorption process at each temperature is well-fitted by the JMAK equation. The specific fitting results are shown in Fig 6.11 (a) to (b). From Fig 6.11 (e), the hydrogen desorption activation energies (E_d) for Cr_5Mn_{20}, $Cr_{10}Mn_{15}$, $Cr_{15}Mn_{10}$, and $Cr_{20}Mn_5$ are -19.93 kJ/mol, -16.12 kJ/mol, -15.88 kJ/mol, and -14.76 kJ/mol, respectively. The clear trend is that with the increase in Cr content, the dehydrogenation activation energy decreases. This is because that the lattice constant of the HEAs decreases as the Cr content increases. As the lattice constant decreases, the distance between hydrogen atoms also decreases, which increases the repulsive force between hydrogen atoms [244]. Additionally, the reduction in the lattice constant leads to a decrease in the stability of hydrogen atoms within the crystal structure [256]. These factors collectively make the dehydrogenation reaction easier to occur, thereby reducing the energy required for hydrogen atom desorption.

Table 6.7 summarizes the activation energy for hydrogen absorption/desorption in various multi-component hydrogen storage alloys primarily based on the different fabrication process and main phase (structure) of the alloys content ($>$ 90%). High-entropy alloys (HEAs) fabricated by mechanical alloying exhibit significantly lower activation energies compared to other alloys. This is due to the mechanical alloying process, which creates a roughened surface [238], increasing specific surface area and providing more absorption sites and potential active centers [257]. Additionally, the intense plastic deformation, repeated fracturing, and welding during the high energy ball milling process result in the formation of nanocrystalline structures [258], which facilitate the hydrogen absorption and desorption processes in the alloy [259]. Consequently, hydrogen storage alloys produced through mechanical alloying exhibit excellent activation performance and lower hydrogen absorption/desorption activation energies. This makes mechanically alloyed hydrogen storage alloys highly promising as catalytic materials for traditionally difficult-to-activate hydrogen storage alloys [241, 260].

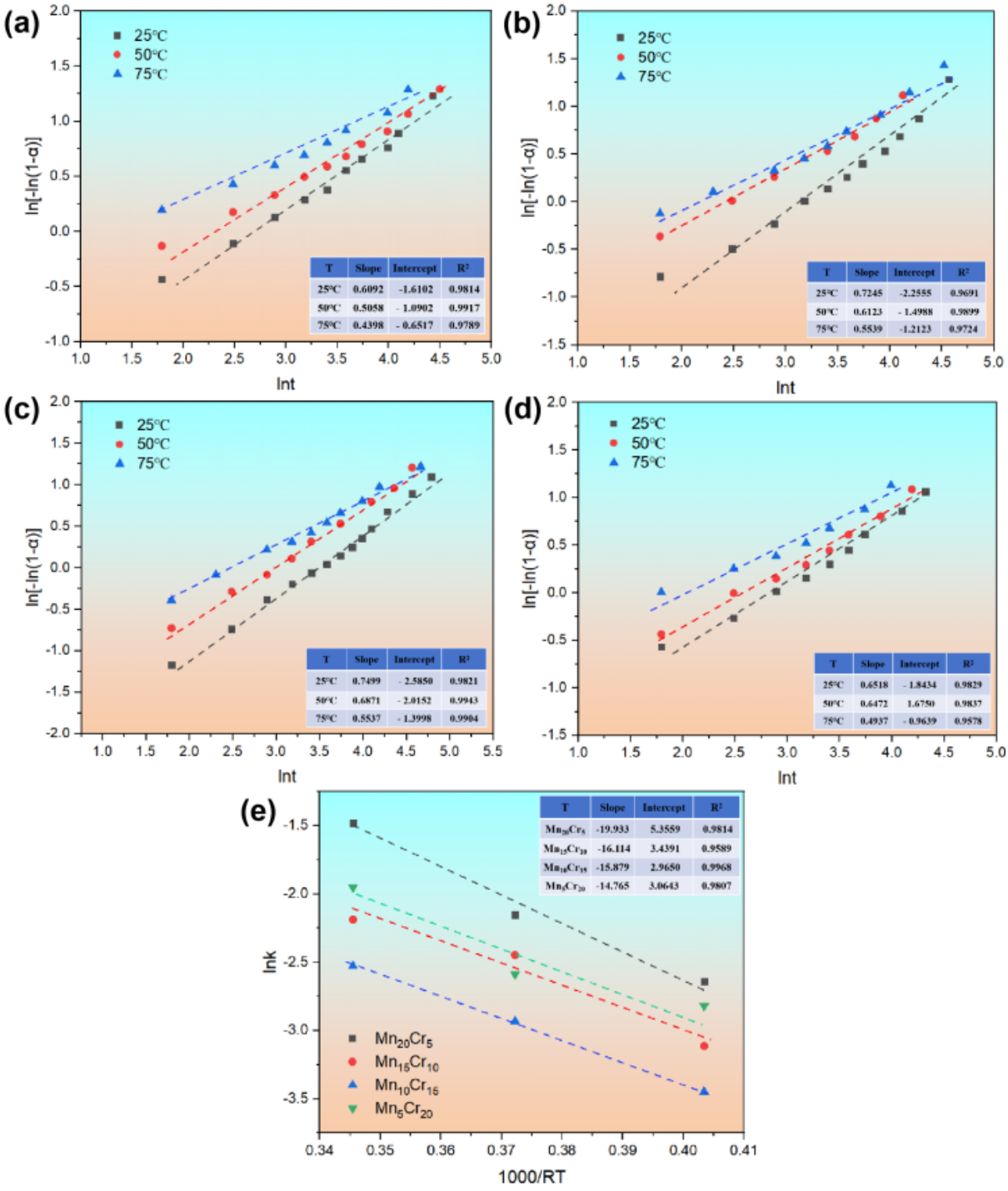

Fig 6.11 The relationship between ln (-ln (1-α)) and ln (t) in the process of hydrogen desorption process: (a) Cr_5Mn_{20}; (b) $Cr_{10}Mn_{15}$; (c) $Cr_{15}Mn_{10}$; (d) $Cr_{20}Mn_5$ and (e) corresponding Arrhenius plots of lnk vs. 1000/RT for the apparent activation energies of dehydrogenation processes

Table 6.7 The summary of hydrogen absorption/desorption activation energy (Ea) of different hydrogen storage alloys

Alloys	Activation energy (kJ/mol)		Fabrication process	Main structure	Ref.
	$E_{a\ (stage\ I)}$	E_d			
Cr_5Mn_{20}	12.15	-19.93	BM	BCC	This study
$Cr_{10}Mn_{15}$	10.55	-16.11	BM	BCC	This study
$Cr_{15}Mn_{10}$	6.71	-15.87	BM	BCC	This study
$Cr_{20}Mn_5$	5.03	-14.76	BM	BCC	This study
$Ti_{35}V_{35}Cr_{10}Fe_{10}Sc_{10}$	-	-50	AM	BCC	[242]
$Ti_{35}V_{35}Cr_{10}Fe_{10}Ni_{10}$	-	-66	AM	BCC	[242]
$(Ti_{32.5}V_{27.5}Zr_{7.5}Nb_{32.5})_{0.97}Ni_{0.03}$	36.12	-	AM	BCC	[49]
$(Ti_{32.5}V_{27.5}Zr_{7.5}Nb_{32.5})_{0.94}Ni_{0.06}$	24.41	-	AM	BCC	[49]
$Ti_{25}V_{30}Nb_{10}Cr_{33}Mo_2$	-	-55.85	AM	BCC	[255]
$Ti_{25}V_{30}Nb_{10}Cr_{33}Mo_2$	-	-44.21	AM	BCC	[255]
$Ti_{25}V_{30}Nb_{10}Cr_{33}Ni_2$	-	-93.8	AM	BCC	[124]
$Ti_{25}V_{30}Nb_{10}Cr_{31}Ni_4$	-	-28.5	AM	BCC	[124]

$TiCr_3V_{16}$	27.19	-	AM	BCC	[261]
$TiCr_3V_{16}Ce_{0.2}$	39.16	-	AM	BCC	[261]
$Ti_{20}V_{30}Nb_{30}Cr_{20}$	-	-39.12	AM	BCC	[262]
$(ZrTiVFe)_{0.95}Cu_{0.05}$	6.16	-	AM+BM	Laves (c14)	[251]
$(ZrTiVFe)_{0.90}Cu_{0.10}$	11.96	-	AM+BM	Laves (c14)	[251]
TiVZrNbFe	11.27		AM+BM	Laves (c14)	[127]

6.5 Hydrogen storage thermodynamic performances

The PCT (Pressure-Composition-Temperature) curve is a crucial characteristic for evaluating the thermodynamics performance of hydrogen storage materials. It provides valuable insights into the stability of metal hydrides and the ease of hydrogen absorption/desorption in alloys. Fig 6.12 (a) presents the PCT curves of the Cr_5Mn_{20} HEA at various temperatures. It can be observed that, regardless of the temperature, the as-milled HEA does not exhibit a stable plateau pressure, indicating a specific characteristic of this alloy. This phenomenon is frequently observed in high entropy alloys, due to the complex interactions among the constituent elements [127, 234, 263]. However, the variations in the PCT curve can still provide important information regarding the stability of hydrogen atoms within the crystal structure and the ease of hydrogen absorption and desorption. Specifically, a lower PCT curve (towards lower hydrogen pressures) suggests that hydrogen absorption is relatively easy while desorption is more difficult. Conversely, a higher PCT curve indicates that hydrogen desorption is relatively easy while absorption is more difficult [264]. Therefore, since hydrogen absorption is an exothermic reaction and hydrogen desorption is an endothermic reaction, increasing the temperature hinders hydrogen absorption in the alloy while facilitating hydrogen desorption, leading to an overall upward shift (towards higher hydrogen pressures) of the PCT curve (Fig 6.12 a).

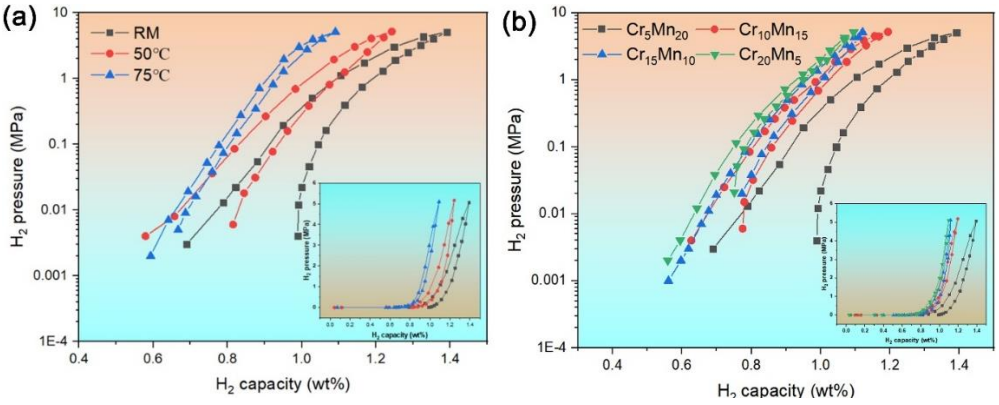

Fig 6.12 (a) The PCT curve of as-milled Cr_5Mn_{20} HEA at different temperature; (b) the PCT curve of as-milled $Ti_{35}V_{35}Cr_{20-x}Mn_{5+x}Fe_5$ (x = 0, 5, 10, 15) HEAs at RMT

Fig 6.12 b shows the PCT curve of the $Ti_{35}V_{35}Cr_{20-x}Mn_{5+x}Fe_5$ (x = 0, 5, 10, 15) HEAs at room temperature. It can be observed that as the Cr content increases, the PCT curve shifts progressively towards higher hydrogen pressures. This indicates that hydrogen desorption becomes easier while hydrogen absorption becomes more difficult. This is due to increased lattice distortion and decreased lattice constant with Cr addition, reducing the stability of hydrogen atoms in the crystal structure. Although thermodynamics and kinetics are distinct concepts, the changes in the PCT curve with varying Cr content can indirectly reflect and corroborate the trends in the hydrogen storage kinetics of the alloy.

6.6 Phase composition of hydrogenation/dehydrogenation

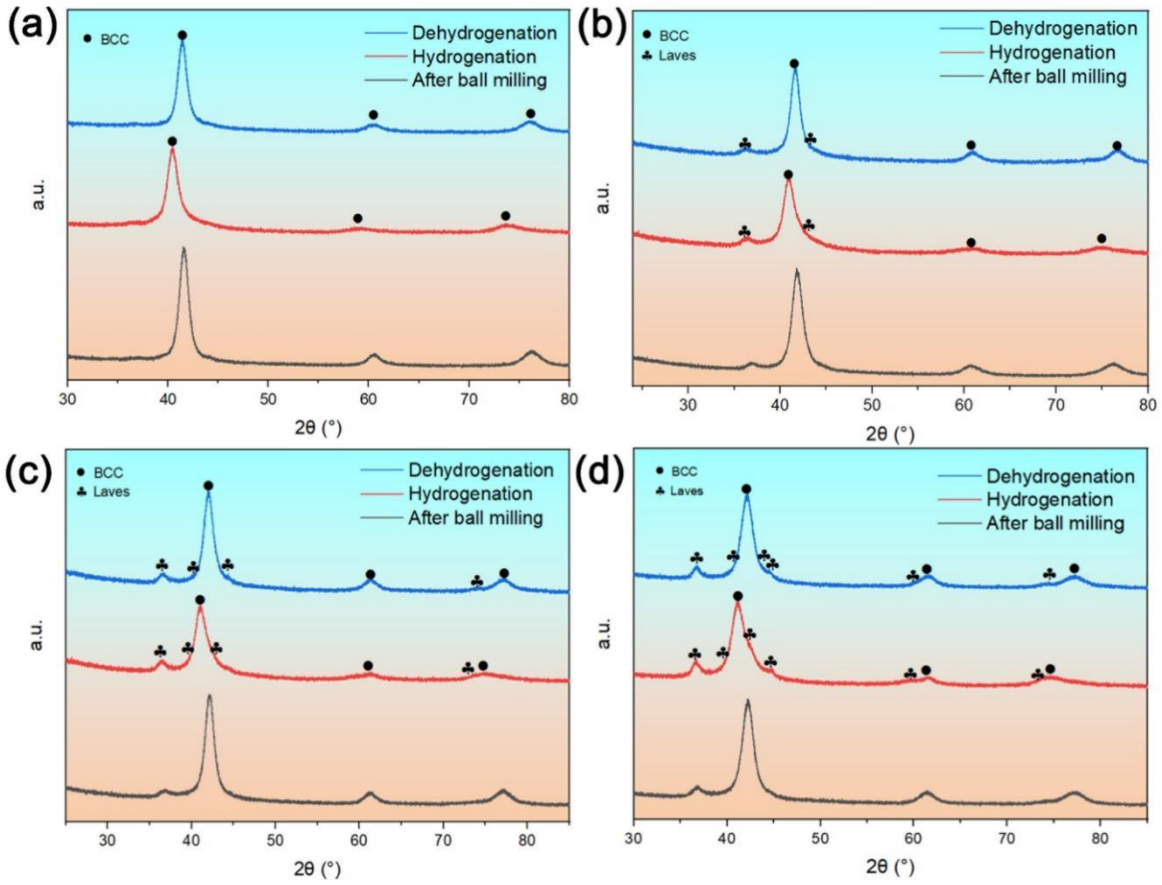

Fig 6.13 Phase structure of HEAs before and after hydrogenation: (a) Cr_5Mn_{20}; (b) $Cr_{10}Mn_{15}$; (c) $Cr_{15}Mn_{10}$; (d) $Cr_{20}Mn_5$

The XRD patterns of the HEAs after hydrogen absorption/desorption process are shown in Fig 6.13, with the lattice parameters of each structure summarized in Table 6.8 From Fig 6.13, it

can be observed that after hydrogenation, the XRD pattern of the alloy shifts significantly to the left (move to small angle), and the lattice parameters increase is attributed to lattice expansion during hydrogenation. The XRD patterns of the as-milled HEAs after hydrogen absorption exhibit significant alterations in the BCC peak, indicating that the BCC is the predominant hydrogen-absorbing structure. This clarifies the fluctuations in hydrogen absorption observed with changes in the BCC content and lattice parameters. Notably, the XRD patterns of the HEAs after hydrogen absorption do not exhibit the BCT or FCC structures. This is due to the overall hydrogen absorption capacity of the alloy has not reached the levels required for the formation of BCT (H/M=1~2wt%) or FCC (H/M=2~4wt%) structures [48]. The lattice parameters of the HEAs slightly increases after hydrogen desorption. This increase may be attributed to the repeated expansion and contraction of the lattice or due to the presence of a small amount of residual hydrogen atoms within the alloys [49, 124].

Table 6.8 Phase lattice parameters of hydrogenated and dehydrogenated HEAs

Alloy		a_{bcc} (Å)	a_{Laves} (Å)	c_{Laves} (Å)	R_{wp}%
Hydrogenated	**Cr_5Mn_{20}**	**3.142**	**-**		**6.32**
	$Cr_{10}Mn_{15}$	**3.079**	**4.983**	**8.125**	**7.25**
	$Cr_{15}Mn_{10}$	**3.067**	**4.918**	**8.047**	**6.85**
	$Cr_{20}Mn_5$	**3.055**	**4.906**	**7.973**	**6.82**
Dehydrogenated	**Cr_5Mn_{20}**	**3.062**	**-**	**-**	**5.81**
	$Cr_{10}Mn_{15}$	**3.037**	**4.921**	**8.069**	**7.62**
	$Cr_{15}Mn_{10}$	**3.027**	**4.878**	**7.978**	**7.12**
	$Cr_{20}Mn_5$	**3.024**	**4.870**	**7.966**	**6.82**

6.7 Hydrogen absorption/desorption cycle performance

Fig 6.14 a and b illustrate the room temperature hydrogen storage cycling performance and the phase structure after complete hydrogen desorption of the Cr_5Mn_{20} alloy, respectively. As shown in Fig 6.14 a, the hydrogen absorption/desorption performance of the alloy remains unchanged after 10 cycles, which can be attributed to the alloy's unique interstitial solid-solution hydrogen absorption mechanism [35, 263]. The post-cycling XRD pattern (Fig.6.14 b) reveals that the phase structure of the alloy remains stable after 10 hydrogenation/dehydrogenation cycles, with only a slight increase observed in the lattice constant of the BCC structure. This minor lattice expansion may result from residual hydrogen in the alloy structure or pulverization induced during the cycling process [265].

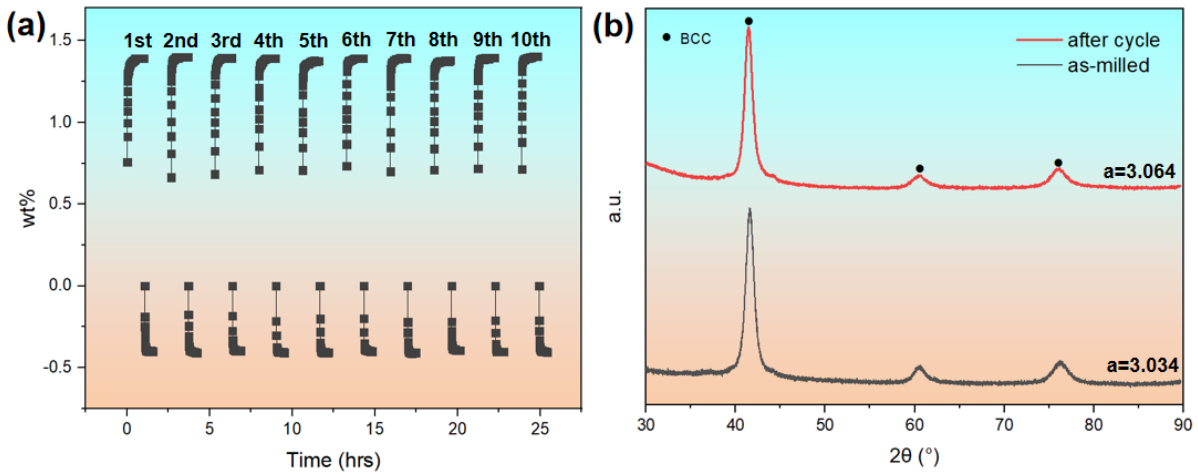

Fig 6.14 The hydrogen absorption/desorption cycle performance (room temperature) and the phase structure after cycle of Cr_5Mn_{20} HEA

6.8 Summary

In summary, our study on $Ti_{35}V_{35}Cr_{20-x}Mn_{5+x}Fe_5$ (x = 0, 5, 10, 15) high-entropy alloys (HEAs) revealed the following:

1. The increase in Mn content effectively suppressed the formation of the C14 Laves phase in the $Ti_{35}V_{35}Cr_{20-x}Mn_{5+x}Fe_5$ (x = 0, 5, 10, 15) high-entropy alloys, and increasing the BCC phase content.

2. Increasing the Cr content enhances the initial activation performance of the HEAs, reducing both the initial hydrogen absorption temperature, and the surface reactions and interfacial processes activation energy.

3. $Ti_{35}V_{35}Cr_{20}Mn_5Fe_5$ HEAs via mechanical alloying exhibited highest hydrogen storage capacity (1.39wt%), easy activation and lower activation energy ($E_{a\ (stage\ I)}$ /E_d = 12.15/19.93 kJ/mol) for hydrogen absorption/desorption due to their nanocrystalline structures, demonstrating their potential as catalytic materials for hydrogen storage alloys that are not easy to activate.

4. $Ti_{35}V_{35}Cr_{20}Mn_5Fe_5$ HEA demonstrates excellent hydrogen absorption/desorption cycling performance. After 10 cycles, both the hydrogen storage capacity and the phase structure remain largely unchanged, primarily due to its unique interstitial hydrogen storage mechanism.

7. Investigation of the influence of fabrication methods on the phase structure, thermal stability, and hydrogen storage performance of $Ti_{25}V_{35}(CrMnFe)_{40}$ high entropy alloy

The differences in fabrication processes significantly impact the phase composition, microstructure, and hydrogen storage performance of high-entropy alloys (HEAs). Mechanical alloying (ball milling) and arc-melting are two commonly used methods [23, 24]. Mechanical alloying typically refines the grain size, increases the specific surface area, and introduces numerous lattice defects and distortions [25-27]. These characteristics theoretically enhance the hydrogen storage performance of the alloys. However, numerous studies have shown that despite the microstructural advantages of ball-milled alloys, their actual hydrogen storage capacity is significantly lower than that of arc-melted alloys [28-30]. This phenomenon has not yet been fully explored and understanded.

Therefore, this study systematically compares the phase composition, thermodynamic stability, and hydrogen storage performance of the $Ti_{25}V_{35}(CrMnFe)_{40}$ HEA with identical compositions fabricated by ball milling and arc melting. The goal is to elucidate the effects of different fabrication processes on the phase structure and hydrogen storage performance of the HEAs, though integrating experimental investigations.

Partial contents of this chapter are being prepared for submission to this journal:

Y.T. Zhai, Y.M. Li, L. Bolzoni, J. Kennedy, ***F. Yang***, Investigation of different fabrication methods on the phase structure, thermal stability, and hydrogen storage kinetic performance of $Ti_{25}V_{35}(CrMnFe)_{40}$ high entropy alloy, International Journal of Hydrogen Energy.

7.1 Phase constitutions and Microstructure characterizations

The alloy was conducted with the assistance of CALPHAD calculations using the Thermo-Calc software. The relationship between the calculated equilibrium phase fractions and temperature is shown in Fig 7.1. The alloy primarily consists of the BCC and C14 Laves. When the temperature exceeds 1050°C, the alloy mainly comprises the BCC. As the temperature decreases, the C14 Laves gradually precipitates. At room temperature, the ratio of the BCC to C14 Laves in the HEA is approximately 0.62:0.38.

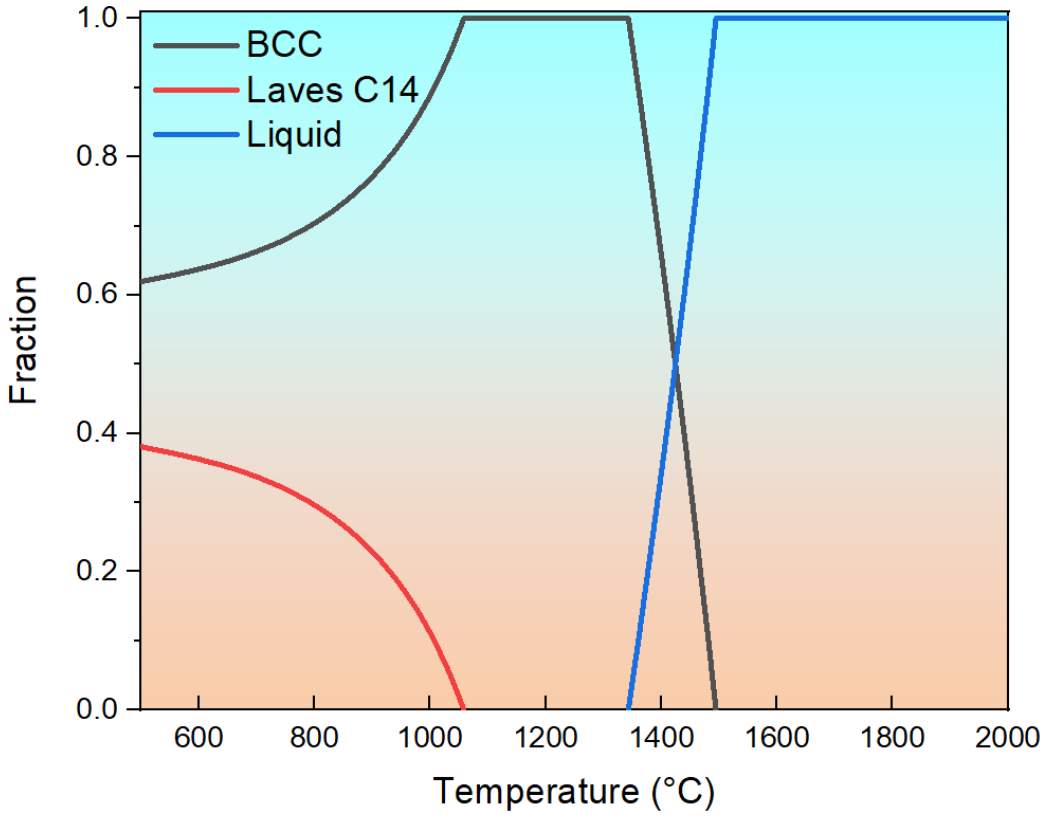

Fig 7.1 Phase diagram of $Ti_{25}V_{35}(CrMnFe)_{40}$ HEA calculated by CALPHAD method using Thermo-Calc software (TCHEA6 database)

Fig 7.2 (a) shows the XRD patterns of $Ti_{25}V_{35}(CrMnFe)_{40}$ high-entropy alloys fabricated by different methods (mechanical alloying and arc-melting). Table 7.1 lists the phase concentrations and lattice constants and so on determined through Rietveld refinement analysis [202]. It is evident from Fig 7.2 (a) and Table 7.1 that these two fabrication methods significantly influence the phase composition and crystal structure of the alloys. Compared to

the arc-melting process, the HEA fabricated by mechanical alloying exhibit significantly reduced characteristic peaks of the Laves and broader peaks of the BCC structure, indicating greater lattice distortion (show in Table 7.1). This is primarily because mechanical alloying (ball milling) involves repeated high-frequency collisions, shearing, and cold welding of the as-milled powders, and introduces a large number of deformation and internal stress in the materials system, [266], thus promoting the formation of BCC solid solution phase and suppressing the formation of secondary phases such as the Laves phase. This is a possible reason to explain the distinct differences in phase composition observed between the ball-milled alloys and those produced by arc melting, however, more detailed research in this regard needs to be attended in the future. XRD peaks of the arc-melted alloy are narrower, indicating higher crystallinity and less lattice distortion. The phase composition of the alloy closely matches the theoretical calculations (show in Fig 7.1). This is due to the high temperatures during the arc melting process, which facilitate sufficient atomic diffusion and rearrangement [37], leading to a more stable crystal structure and the phase ratio that is more reached with thermodynamics simulation.

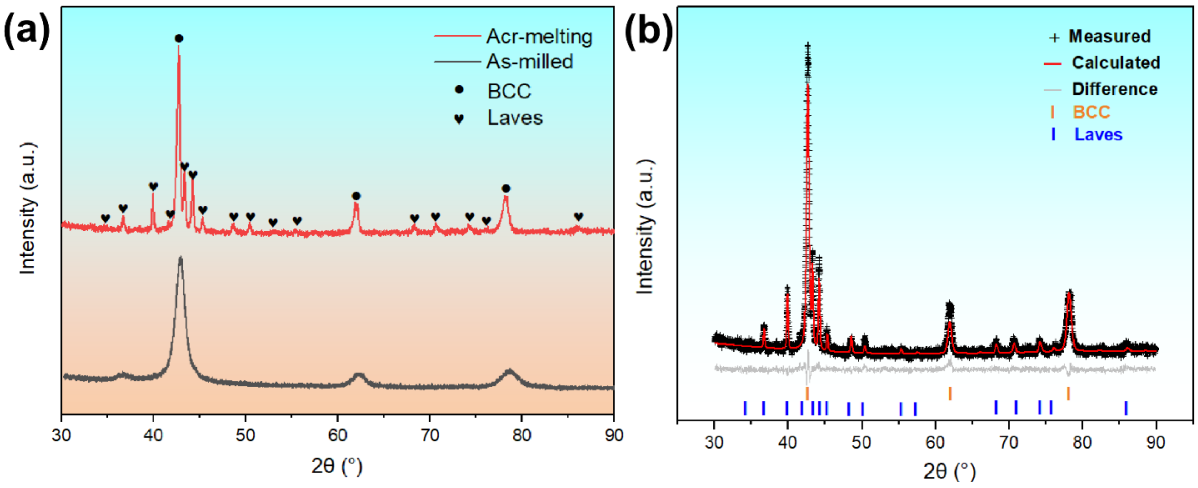

Fig 7.2 (a) The XRD patterns of HEAs fabricated by different method; (b) Rietveld refinement of representative of arc-melting $Ti_{25}V_{35}(CrMnFe)_{40}$ HEA

Table 7.1 Refinement data of the $Ti_{25}V_{35}(CrMnFe)_{40}$ HEA fabricated by different method

Alloys	Structure	Space group	wt%	Lattice constant(Å)	Strain (%)	R_{wp}%
As-milled	BCC	Im-3m (229)	95.30	a=2.969	0.46	3.35
	Laves	P63-mmc (194)	4.70	a=4.868/c=7.885	-	
Arc-melting	BCC	Im-3m (229)	64.05	a=2.995	0.21	4.13
	Laves	P63-mmc (194)	35.95	a=4.893/c=8.009	0.11	

Fig 7.3 shows the backscattered electron images of the $Ti_{25}V_{35}(CrMnFe)_{40}$ alloy fabricated by different fabricated methods. Fig 7.3 (a) depicts the microstructure after mechanical alloying, where no distinct second phase (Laves) is observed. This may be due to the low concentration of the Laves phase (show in Table 7.1). Additionally, the intense mechanical impact and stress during the mechanical alloying process can induce severe deformation, leading to the formation of numerous nanocrystalline, which further complicates the identification of secondary phases [241]. After mechanical alloying, the elemental composition of the alloy closely matches the designed specifications (show in Table 7.2), with no obvious areas of elemental enrichment, indicating that mechanical alloying effectively promotes homogeneous atomic-level mixing of the elements [267].

Table 7.2 Represents the measured atm% values of each element present in the as-milled and as-melted HEA

Alloy	Area	Ti	V	Cr	Mn	Fe
As-milled	-	25.74	34.43	13.42	12.91	13.50
As-melted	A	23.87	39.01	14.19	11.31	11.61
	B	31.82	21.25	12.53	14.14	20.26

Fig 7.3 (b) shows the microstructure after arc melting, clearly distinguishing two different regions, labeled as areas A and B. Combining the phase content from Table 7.1 and the elemental distribution from Table 7.2, it can be determined that area A corresponds to the BCC structure, while area B corresponds to the Laves structure. The BCC structure exhibits a higher content of vanadium (V), as vanadium is a BCC stabilizing element [129]. In the Laves structure, the titanium (Ti) content is relatively high. This is because during the high-temperature melting process, the thermodynamically stable structure formed by Ti with Cr and Mn are Laves structure (AB_2) [140, 256]

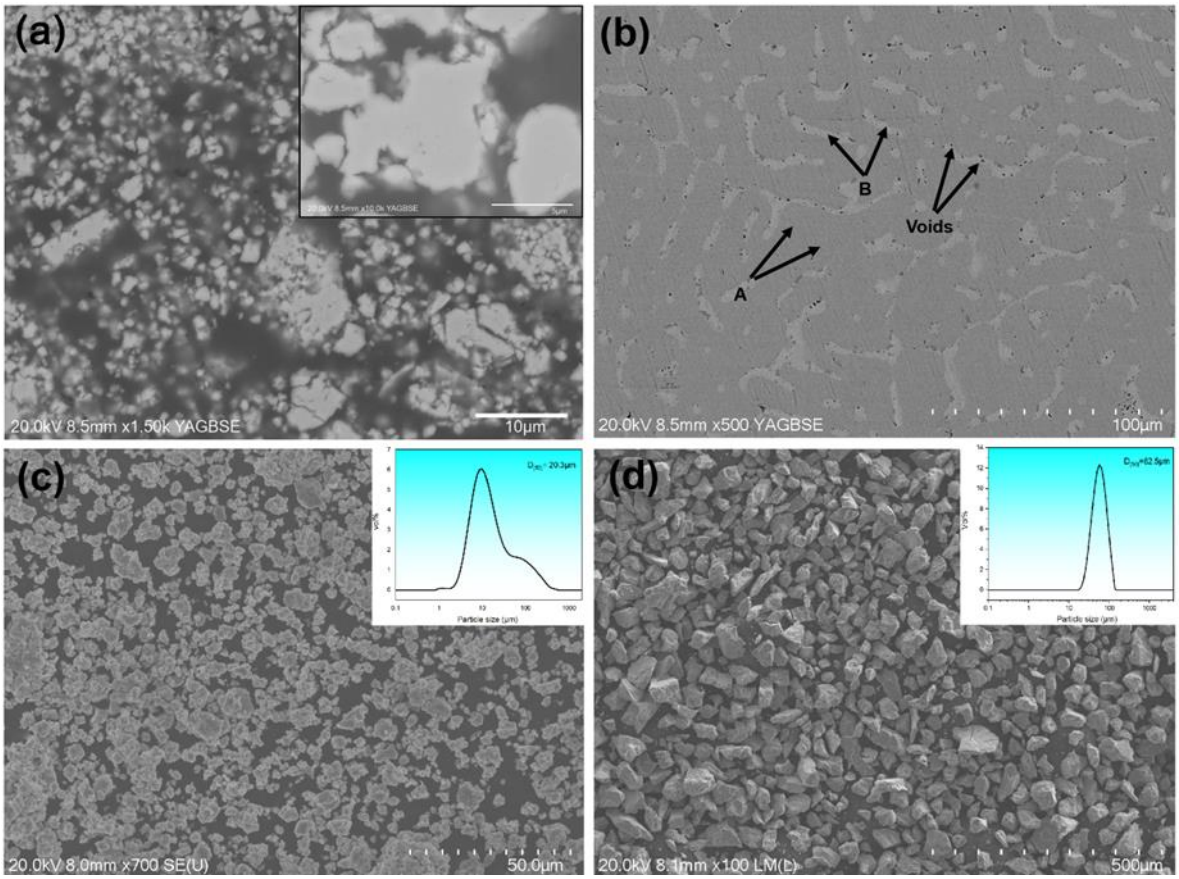

Fig 7.3 The back-scattered electron images and particle size of the $Ti_{25}V_{35}(CrMnFe)_{40}$ HEA fabricated by different method: (a), (c) as-milled; (c), (d) as-melted

Additionally, during the high-temperature melting process, the thermodynamically stable structure formed by Ti with Cr and Mn are also Laves structure [89, 149]. Fig 7.3 (c) and d illustrate the differences in particle size of the alloy under different fabrication processes. It is evident that the particle size of the alloy after mechanical alloying (D_{50} =20.3 μm) is significantly smaller compared to the particle size obtained after arc melting (D_{50} = 62.5 μm; crushing and sieving through a 200-mesh screen).

7.2 Thermal stability

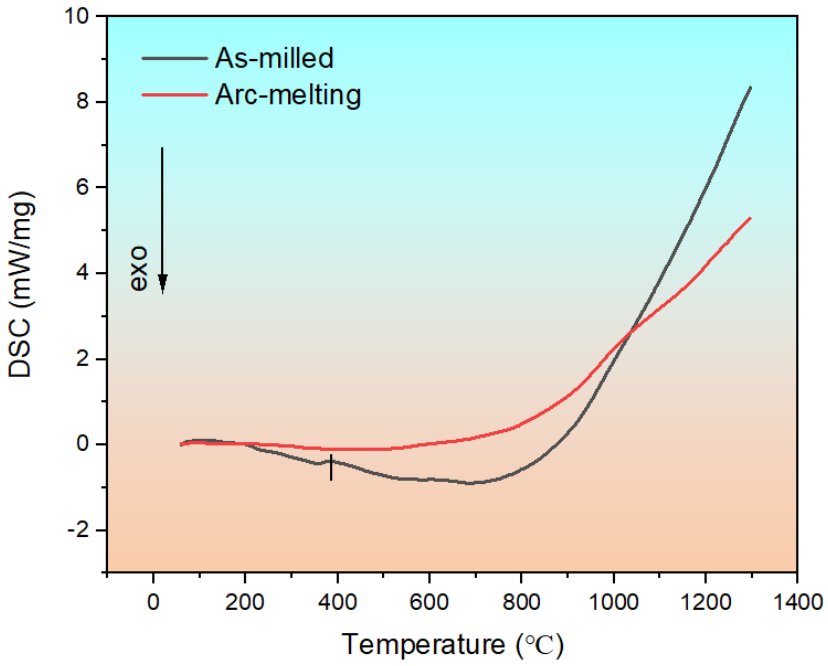

Fig 7.4 The DSC curve of the $Ti_{25}V_{35}(CrMnFe)_{40}$ HEA fabricated by different method

Fig 7.4 shows the DSC curves of $Ti_{25}V_{35}(CrMnFe)_{40}$ HEA fabricated by different methods. Compared to the relatively smooth initial stage of the arc-melted sample, the mechanically alloyed sample exhibits a distinct exothermic trend, which can be attributed to the release of internal stresses caused by severe plastic deformation induced by high-energy ball milling [268]. At approximately 400°C, a noticeable endothermic peak (black line) appears in the mechanically alloyed sample. This indicates that following ball milling, the alloy's phase structure is in a non-equilibrium or metastable state, prompting a transition to more stable phase structure at elevated temperatures. In the final stage, both fabrication methods show varying extents of endothermic, attributed to phase (grain) growth and element diffusion within the alloys [269, 270]. Based on previous experiences, as-milled samples do not exhibit further changes in crystallinity after heat treatment at 900°C, facilitating the observation of the alloy's phase structure. Therefore, the HEAs fabricated by different methods heat-treated at 900°C to ensure experimental consistency.

Fig 7.5 shows the XRD spectra of $Ti_{25}V_{35}(CrMnFe)_{40}$ high-entropy alloys fabricated by different methods after heat treatment at 900°C. Table 7.3 lists the phase concentrations and lattice constants etc. determined by Rietveld refinement. By comparing the XRD patterns (Fig 7.5 a) and DSC curves of alloys with different preparation methods before and after heat treatment at 900°C, it can be seen that the internal stress introduced during the ball milling process is released during heat treatment, leading to the decomposition of the BCC structure into BCC and FCC, and an increase in the crystallinity and content of pre-existing Laves. In contrast, the phase compositions of arc-melted samples showed minimal changes before and after heat treatment, with an increase in the Laves content due to the element diffusion. The significant internal stress from the ball milling process promoted recovery and recrystallization, resulting in lower strain (%) in ball-milled samples compared to the arc-melted samples.

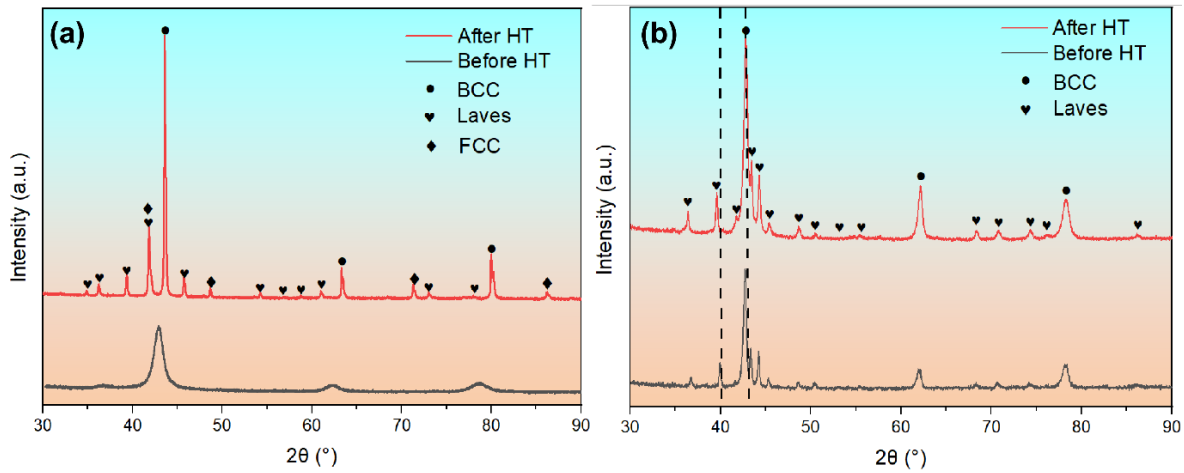

Fig 7.5 The XRD patterns of $Ti_{25}V_{35}(CrMnFe)_{40}$ HEA fabricated by different methods after heat treatment at 900°C: (a) as-milled; (b) as-melted

Table 7.3 Refinement data of the $Ti_{25}V_{35}(CrMnFe)_{40}$ HEA by different methods after heat treatment at 900°C.

Alloys	Structure	Space group	wt%	Lattice constant(Å)	R_{wp}%
As-milled	BCC	Im-3m (229)	63.78	a=2.932	7.03
	FCC	Fm-3m (225)	24.05	a=3.735	
	Laves	P63-mmc (194)	12.20	a=5.082/c=8.121	
Arc-melting	BCC	Im-3m (229)	57.45	a=2.978	3.98
	Laves	P63-mmc (194)	42.55	a=4.912/c=8.015	

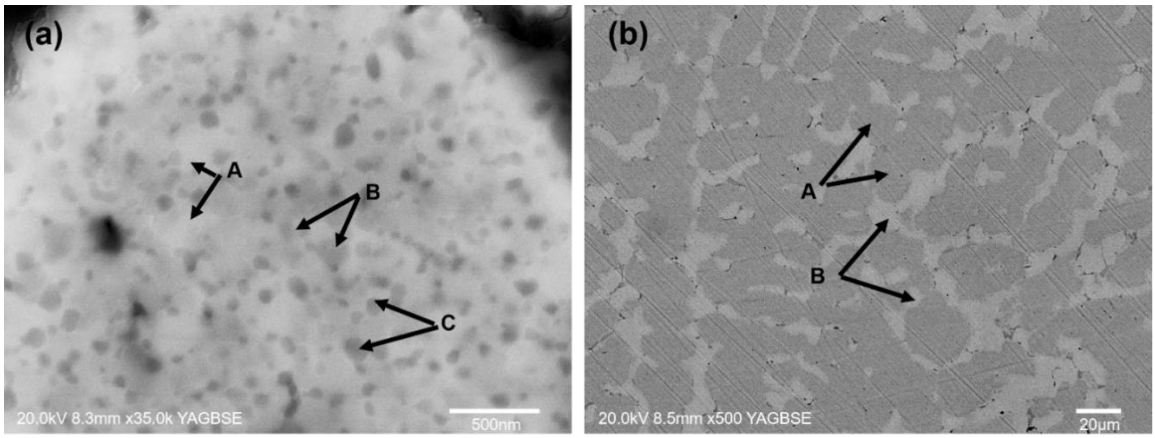

Fig 7.6 The Back-scattered Electron images of the $Ti_{25}V_{35}(CrMnFe)_{40}$ HEA fabricated by different methods after heat treatment at 900°C: (a) as-milled; (b) as-melted.

Fig 7.6 presents backscattered electron (BSE) micrographs of alloys subjected to different fabrication processes after heat treatment at 900°C, with the specific elemental distributions (at%) of each phase detailed in Table 7.4. From Fig 7.6 (a), we observe three regions within the alloy that exhibit distinct color contrasts. By integrating the information from Tables 7.3 and 7.4, it can identify that region A corresponds to the BCC structure, region B to the FCC

structure, and region C to the Laves structure. By comparing the elemental content of different regions in the heat-treated (as-milled) samples, it is evident that the primary difference in phase structures within the alloy is the Ti content. This is because Ti (146.15 pm) has the largest atomic radius in this alloy system (V 131.6 pm; Cr 124.91 pm; Mn 135 pm; Fe 124.12 pm) and its larger formation enthalpy with other elements (Cr, Mn) [58].

Table 7.4 Represents the measured at% values of each element present in the as-milled and as-melted HEA after heat treatment at 900 °C

Alloy	Area	Ti	V	Cr	Mn	Fe
As-milled	A	22.70	35.24	14.29	14.52	13.25
	B	25.43	33.52	13.22	13.98	13.85
	C	28.54	31.91	12.59	13.87	13.09
As-melted	A	22.11	40.76	14.78	11.49	10.86
	B	34.12	19.55	10.54	14.64	21.15

By comparing Fig 7.6 b and Fig 7.3 b, it can be observed that the phase compositions in the as-melted HEA did not change after heat treated at 900°C. However, the content of the BCC structure decreased and the content of the Laves structure increased (shown in Table 7.3) due to the diffusion of Ti atoms. The reason for the diffusion of Ti atoms is consistent with that in the as-milled HEA. During the heat treatment process, the diffusion of Ti atoms led to a decrease in Ti content in the BCC structure and an increase in Ti content in the Laves structure (show in Table 7.4). This resulted in a reduction in the average atomic radius and lattice constant of the BCC structure, and an increase in the average atomic radius and lattice constant of the Laves structure. These observations are consistent with the results observed from XRD pattern show in Fig 7.4 b (the BCC peaks shift towards higher angles, while the Laves structure peaks shifts towards lower angles).

7.3 Hydrogen storage performance

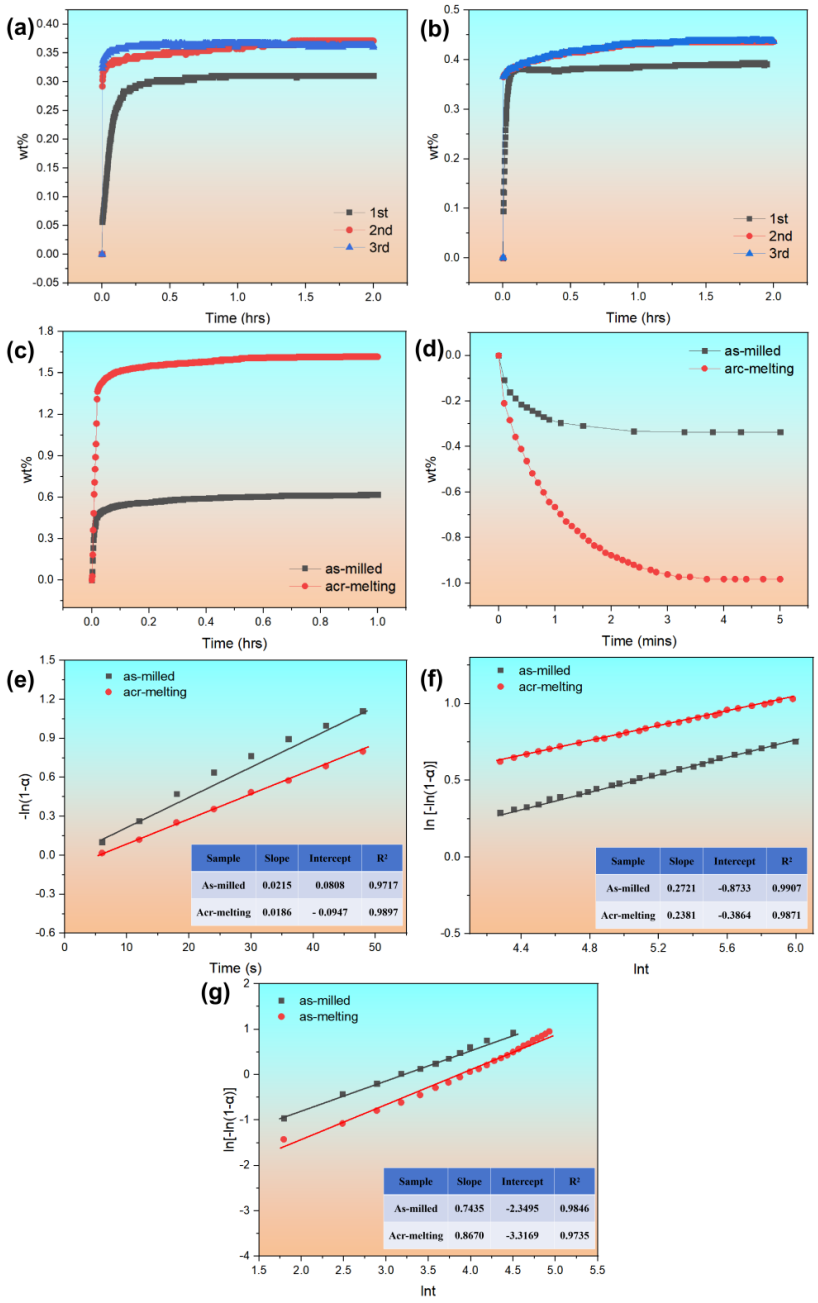

Fig 7.7 The hydrogen storage performances of $Ti_{25}V_{35}(CrMnFe)_{40}$ HEA fabricated by different processes: (a), (b) the hydrogen storage activation curve of as-milled and as-melted samples respectively; (c), (d) the hydrogen storage absorption/desorption curve at 50 °C; (e), (f) The fitting curve of different stages by Hirooka's first-order kinetic equation (e) and JMAK equation (f); (g) the JMAK fitting curve of hydrogen desorption process

Fig 7.7 (a) and (b) shows the activation curves of $Ti_{25}V_{35}(CrMnFe)_{40}$ HEA fabricated by different methods. It can be observed that all alloys exhibit excellent hydrogen activation performance, achieving full activation in just two cycles. However, the reasons for their outstanding activation performance may different. For the ball-milled alloys, mechanical alloying significantly refines the grain size, forming a nanocrystalline structure [267]. The smaller grain size increases the grain boundary area, providing more active sites for hydrogen activation [259]. Additionally, the ball milling process increases the density of surface defects in the alloy [258, 271], which also serve as hydrogen activation sites, thereby enhancing the activation performance of the material. Compared to the as-milled HEA, the superior activation performance of the arc-melted HEA is primarily attributed to the content and morphology of the second phase (Laves) [247]. This is because hydrogen storage alloys with a Laves structure exhibit better activation performance and hydrogen absorption/desorption kinetics than BCC structure. Therefore, the content of the second phase (Laves) significantly influences the hydrogen storage activation performance of the alloy. Additionally, the morphology of the second phase also affects the hydrogen storage kinetics of the alloy. Different structures of hydrogen storage alloys exhibit varying degrees of lattice expansion during hydrogen absorption/desorption. This lattice expansion creates fine cracks between the two phases during the hydrogen absorption process, providing additional diffusion pathways for hydrogen atoms and thus enhancing the activation performance of the alloy.

Table 7.5 The hydrogen storage performance of $Ti_{25}V_{35}(CrMnFe)_{40}$ HEA fabricated by different processes

Alloys		Capacity (wt%)	Reaction rate (k)	
			Stage I	Stage II
As-milled	Absorption	0.619 (t_{90}=8.1mins)	0.0215	0.0403
	Desorption	0.336 (t_{90}=1.5mins)	0.0424	–
As-melted	Absorption	1.617 (t_{90}=2.7mins)	0.0186	0.1973
	Desorption	0.983 (t_{90}=2mins)	0.0218	–

Fig 7.8 (c) and (d) show the hydrogen absorption/desorption curves of $Ti_{25}V_{35}(CrMnFe)_{40}$ HEA fabricated by different methods at 323K. As observed in Fig 7.7 (c), the arc-melted alloy exhibits a higher hydrogen storage capacity (Table 7.5). Although Fig 7.2 and Table 7.1 indicates that the ball-milled HEA has a higher BCC content than the arc-melted HEA, which theoretically should result in higher hydrogen storage capacity, the actual results are contrary. This phenomenon may be attributed to the excessive lattice distortion introduced during the ball milling process. A lot of studies have shown that ball milling time significantly influences the hydrogen storage performance of alloys [272-274]. As ball milling time increases, the grain size and particle size of the alloys gradually decrease, which typically enhances their hydrogen storage kinetics [275]. However, further extension of ball milling time leads to a continuous increase in lattice distortion and a potential rise in the amorphous phase content within the alloy structure, ultimately resulting in a reduction in hydrogen storage capacity [272, 274, 276]. Therefore, this may be one possible reason why the as-milled HEA shows a relatively low hydrogen storage capacity compared to the arc-melted alloy, although no amorphous phase was detected in the as-milled $Ti_{25}V_{35}(CrMnFe)_{40}$ alloy by XRD and TEM [277]. Furthermore, the reduction in hydrogen storage capacity could be also attributed to alloy poisoning or contamination. A lot of studies have shown that the hydrogen storage capacity of alloys is highly sensitive to the oxygen content[82, 278-280]. Oxygen atoms can occupy hydrogen

storage sites within the alloy and, through their additional electrons, increase the electron density at these sites, thereby hindering storage capacity [279, 280]. In the ball milling process, the PCA (alcohol), primarily consists of C and O elements. These atoms may dissolve into the interstitial sites of the alloy lattice during mechanical alloying, reducing the hydrogen storage capacity the as-milled HEA. More detailed research in this regard will be explored in our research group in the future.

The hydrogen absorption process is generally divided into two stages. The first stage is dominated by surface reactions and interfacial processes[236, 246], while the second stage encompasses the nucleation and growth of metal hydrides [127, 247]. In this study, Hirooka's first-order kinetic equation was employed to analyze the kinetics of hydrogen absorption during the first stage. The equation is presented as follows in chapter 6 [246]. For the second stage, the JMAK (Johnson-Mehl-Avrami-Kolmogorov) equation was applied. The equations used are as follows in chapter 6 [127]. It can be observed that the different stages of hydrogen absorption are well-fitted by the different equations. The specific fitting results are shown in Fig 7.7 (e) and (f). Fig 7.7 (g). illustrates the hydrogen desorption kinetics analysis of the HEAs fabricated by different method. Typically, only one stage is observed, as the desorption process is significantly faster than absorption [52, 124, 255] and the desorption process is well-fitted by the JMAK equation.

By comparing the $\boldsymbol{k}$ values of alloys fabricated using different methods at various stages, it was found that the as-milled HEAs exhibited slightly higher $\boldsymbol{k}$ values in the first stage (surface reactions and interfacial processes) compared to arc-melted samples. This is primarily due to the smaller particle size of the ball-milled samples, which provides a larger specific surface area [281]. Additionally, the smaller grain size (nano sizes) of the ball-milled alloy offers more diffusion pathways for hydrogen atoms [247, 259, 281]. However, in the second stage (nucleation and growth of metal hydrides), the $\boldsymbol{k}$ value of the as-milled HEA is significantly lower than arc-melted HEA. This may be due to the presence of a large amount of kinetically

favorable Laves phase in the cast HEA, whereas the as-milled HEA primarily exhibits a single-phase BCC structure. Compared to the BCC, the Laves phase generally possesses superior kinetic properties, resulting in a higher overall ***k*** value for the cast HEA in this stage. Furthermore, by comparing the t_{90} values of the as-milled and arc-melted alloys, it is evident that the hydrogen absorption rate of the arc-melted HEA is higher than as-milled HEA. This further indicates that the hydrogen absorption of the arc-melted alloy mainly occurs in the second stage, and the phases composition and content may play a dominant role in the overall hydrogenation kinetics of the alloy. These factors collectively influence the kinetic performance of the ball-milled alloy during hydrogen storage [34, 263, 280]. Fig 7.7 (g) presents the hydrogen desorption kinetics analysis of the $Ti_{25}V_{35}(CrMnFe)_{40}$ alloys fabricated by different methods. Since the desorption process is significantly faster than the absorption process, only a single stage is typically observed [255, 282, 283]. The specific fitting results are shown in the Fig 7.7 (g). As indicated in Table 7.5, the desorption rate of the as-milled HEA is larger than arc-melted HEA. This may be due to the smaller lattice constant in the as-milled condition, which reduces the distance between hydrogen atoms in the crystal structure, increasing the repulsive force between them and facilitating faster desorption [244].

7.4 Phase composition of hydrogenation/dehydrogenation.

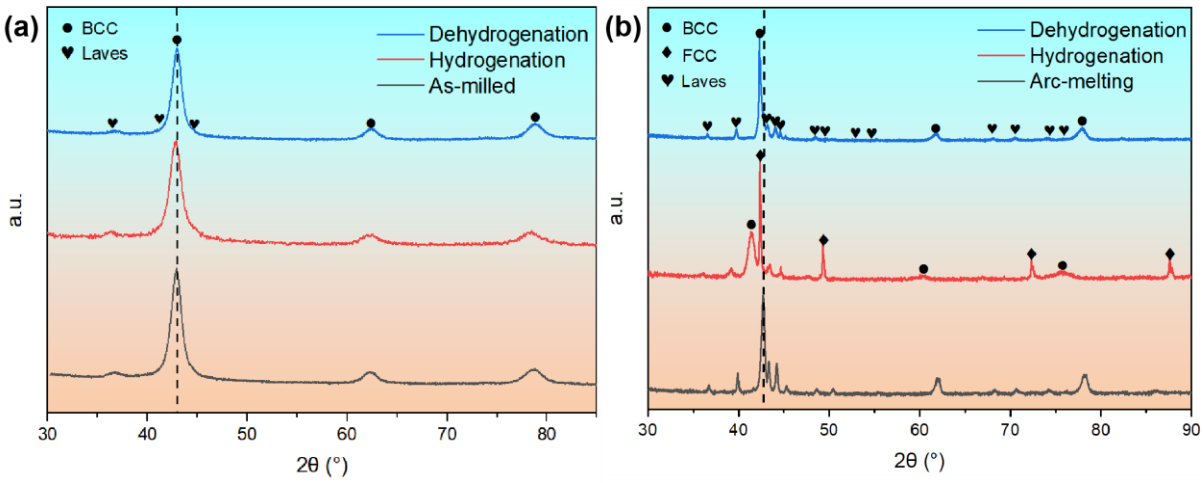

Fig 7.8 Phase structure of $Ti_{25}V_{35}(CrMnFe)_{40}$ HEA fabricated by different processes before and after hydrogenation: (a) ball-milled; (b) arc-melted

Fig. 7.8 (a) shows the XRD patterns of the ball-milled alloy after hydrogen absorption at room temperature and subsequent vacuum treatment at 300 °C for 2 hours. It can be observed that the XRD peak positions exhibit only slight shifts following hydrogen absorption/desorption. This behavior is primarily attributed to the alloy's low hydrogen absorption capacity and the interstitial solid solution mechanism of hydrogen absorption [26]. Previous studies have demonstrated that no stable metal hydrides are formed for this series of high-entropy alloys made by mechanical alloying [58]. Fig. 7.8 (b) presents the hydrogen absorption/desorption XRD patterns of the arc-melted HEA. It is observed that the XRD peaks shift towards lower angles (lattice constant increase) after hydrogen absorption. Additionally, after hydrogen absorption, a coexistence of BCC and FCC structures was observed in the HEA (as shown in Fig. 7.8 (b) and Table 7.6), indicating that only certain BCC structures underwent a phase transformation during hydrogenation process. This phenomenon is likely due to the disordered arrangement of elements in the high-entropy alloy [284, 285]. In addition, this observation suggests that both interstitial solid solution and phase transformation hydrogen absorption mechanisms are present in the BCC structure of the as-cast HEA. Following vacuum treatment at 300°C for 2 hours, the lattice constants of the BCC and Laves phases nearly returned to their pre-hydrogenation values, with only a slight increase, which could be due to a minimal amount of residual hydrogen atoms remaining in the lattice interstices.

Table. 7.6 Phase lattice parameters of hydrogenated/dehydrogenated of $Ti_{25}V_{35}(CrMnFe)_{40}$ HEA fabricated by different processes.

Alloy		a (Å)	a/c $_{Laves}$ (Å)
Hydrogenated	As-milled	a^b=2.982	4.892/7.918
	Arc-melted	a^b=3.082 (51.68)	4.987/8.147 (32.95)
		a^f=3.690 (15.37)	
Dehydrogenated	As-milled	a^b=2.970	4.870/7.886
	Arc-melted	a^b=3.008 (64.73)	4.902/8.015 (35.27)

a^b/a^f: Lattice constants of BCC and FCC structures; the values in brackets are the wt% of each structure.

7.5 Hydrogen absorption/desorption cycle performance

Fig. 7.9 a and b illustrate the hydrogen absorption/desorption cycling performance of alloys prepared by different fabrication methods. As shown in the figures, both alloys exhibit excellent cycle performance. The arc-melted alloy retains approximately 88% (1.43 wt%) of its maximum hydrogen storage capacity after 10 absorption/desorption cycles, whereas the ball-milled alloy demonstrates almost no change in its maximum hydrogen storage capacity after the same number of cycles. Fig. 7.9 c and d show the dehydrogenated XRD patterns of alloys prepared using different methods after 10 hydrogen absorption/desorption cycles. The results indicate that, after 10 cycles, the XRD peaks of all alloys shift slightly toward lower angles, suggesting a slight increase in lattice constants. This phenomenon may be attributed to the cumulative effect of repeated lattice expansion and contraction during cycling, or possibly due to residual hydrogen that could not be fully desorbed. Notably, the peak shift is more pronounced in the arc-melting alloy fabricated to the ball-milled alloy after cycling. This observation (more residual hydrogen cannot be released) may explain why the cycling performance of the cast alloy deteriorates more significantly than that of the ball-milled alloy. In addition, the decline in hydrogen storage capacity during cycling is generally attributed to various factors, such as disproportionation reactions [265, 286], higher defect concentration [287, 288], and the formation of vacancies clusters and dislocations [289, 290]. The arc-melted alloy undergoes significant phase transformations during the hydrogen absorption/desorption process, making it potentially more susceptible to these factors compared to the solid-solution-based hydrogen storage mechanism of the ball-milled alloy, leading to a slight reduction in its maximum hydrogen storage capacity.

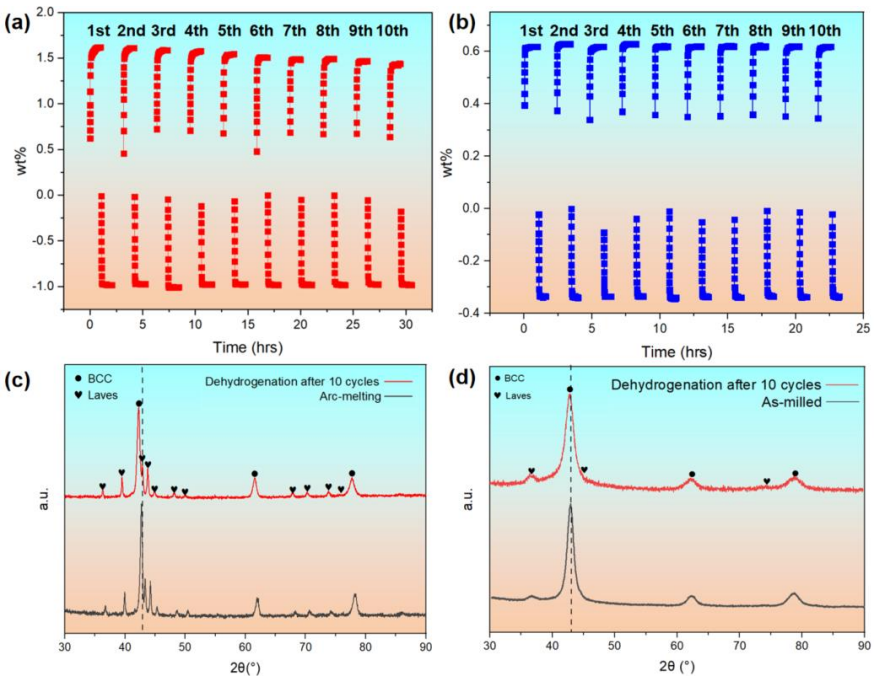

Fig. 7.9 The hydrogen absorption/desorption cycle performance and XRD pattern of Ti25V35(CrMnFe)40 HEA fabricated by different processes: (a), (c) arc-melted; (b), (d) ball-milled

7.6 Summary

In summary, our study on different fabrication methods on $Ti_{25}V_{35}(CrMnFe)_{40}$ high-entropy alloys (HEAs) revealed the following:

1. Mechanical alloying, as a typical non-equilibrium synthesis technique, introduces substantial deformation and internal stresses through repeated high-energy collisions, it enhances element solubility in BCC structures, promotes the formation of metastable solid solutions, and suppresses the precipitation of secondary phases Laves phase. However, the increased lattice strain also reduces the thermal stability of the alloys, making them more prone to phase decomposition at elevated temperatures.

2. The nanocrystalline structure and large specific surface area induced by the ball milling process contribute to enhanced kinetic performance during the first stage of hydrogenation. However, in the second stage of hydrogenation, the hydrogen absorption kinetics of the alloy are primarily governed by the phase composition and its relative content. Overall, the hydrogenation kinetics of the alloy are likely to be more dependent on its phase composition and phase fraction.

8. Conclusions and perspectives

8.1 Conclusions

In this thesis, Ti-V-Cr-Mn-Fe high-entropy alloys (HEAs) were fabricated using mechanical alloying. A systematic investigation was conducted to explore the effects of ball milling parameters, heat treatment processes, different fabrication methods, and alloy composition on the phase structure and hydrogen storage performance of the alloys. The relationships between these factors and the hydrogen storage properties of the alloys were clarified. The specific conclusions are as follows:

1. After mechanical ball milling, the alloy composition predominantly exhibits a body-centered cubic (BCC) structure, accompanied by a minor proportion of the C14 Laves phase. As the Ti content increases, the overall lattice distortion (δ (%)) and formation enthalpy ($\triangle H_{mix}$) of the alloy rise, leading to an increased proportion of the C14 Laves phase.

2. Thermal stability evaluations reveal complex phase transformations during heat treatment (BCC+Laves-1 → BCC+FCC+Laves-1 → BCC+FCC+Laves-1+Laves-2), with phase stability dependent on overall lattice distortion (δ (%)). The nanocrystalline structure is retained after high temperature (900°C) heat treatment.

3. Increased Mn content effectively suppresses the formation of the C14 Laves phase, enhancing the BCC phase content. Additionally, increasing Cr content improves the alloy's initial activation performance, reducing both the initial hydrogen absorption temperature and the activation energy of surface and interfacial reactions.

4. The $Ti_{35}V_{35}Cr_5Mn_{20}Fe_5$ HEA fabricated by mechanical alloying displays the highest hydrogen storage capacity (1.39 wt%), excellent activation performance, and lower

activation energies for hydrogen absorption/desorption (Ea (stage I) /E_d = 12.15/19.93 kJ/mol). These properties suggest its potential as a catalytic material for hydrogen storage alloys that are challenging to activate.

5. Investigations on different fabrication methods for $Ti_{25}V_{35}(CrMnFe)_{40}$ HEAs demonstrate that mechanical alloying introduces significant lattice strain, which improves the solubility of elements in the BCC structure, thereby enabling the formation of high-entropy hydrogen storage alloys that cannot be synthesized through conventional melting methods.

8.2 Perspectives

1. Due to the ease of activation and fine particle size of mechanically alloyed alloys, an innovative approach could involve embedding this material, using ball milling, on the surface of hydrogen storage alloys that are less readily activated. This would create effective hydrogen storage pathways, potentially enhancing the overall hydrogen absorption kinetics of the alloy.

2. The reduction in hydrogen storage capacity of ball-milled alloys may be attributed to the contamination from C and O in the process control agent (PCA). Therefore, research on how impurities influence Ti-V-Fe-Cr-Mn high entropy alloys' hydrogen ab-/desorption behaviors need to be performed.

3. The research on practical applications of Ti-V-Fe-Cr-Mn hydrogen storage materials in different working environments need to be conducted.

References

[1] Y. Wei, C. Xu, G. He, R. Hua, Z. Xie, D. Liu, X. Li, R. Zhang, H. Tang, J. Li, D. Qu, Influence of structural and chemical environmental factors on electrochemical hydrogen storage in carbon materials, Electrochimica Acta 433 (2022).

[2] K. Abbasi, P. Ali, V. Barbour, T. Benfield, K. Bibbins-Domingo, S. Hancocks, R. Horton, L. Laybourn-Langton, R. Mash, P. Sahni, W. Mohammad Sharief, P. Yonga, C. Zielinski, Time to treat the climate and nature crisis as one indivisible global health emergency, Gaceta Sanitaria 37 (2023).

[3] M. Sarroukh, K. Lahlou, M. Farah, M. Kebir, Effect of global warming and new equivalent temperature zoning maps for asphalt pavement design in Morocco, Energy and Buildings 303 (2024).

[4] M.R. Hossain, S. Singh, G.D. Sharma, S.-A. Apostu, P. Bansal, Overcoming the shock of energy depletion for energy policy? Tracing the missing link between energy depletion, renewable energy development and decarbonization in the USA, Energy Policy 174 (2023).

[5] K. Halttunen, R. Slade, I. Staffell, What if we never run out of oil? From certainty of "peak oil" to "peak demand", Energy Res Soc Sci 85 (2022) 102407.

[6] I.P. Jain, Hydrogen the fuel for 21st century, International Journal of Hydrogen Energy 34(17) (2009) 7368-7378.

[7] S. Hu, L. Lv, G. Yang, W. Liu, H. Miao, H. Cheng, X. Han, Z. Lin, Improvement in hydrogen storage performance of Mg by mechanical grinding with molten salt etching Ti3C2Cl, Progress in Natural Science: Materials International 33(2) (2023) 211-224.

[8] S.C. Wijayasekera, K. Hewage, F. Razi, R. Sadiq, Fueling tomorrow's commute: Current status and prospects of public bus transit fleets powered by sustainable hydrogen, International Journal of Hydrogen Energy 66 (2024) 170-184.

[9] L. Yin, H. Yang, Y. Ju, Review on the key technologies and future development of insulation structure for liquid hydrogen storage tanks, International Journal of Hydrogen Energy 57 (2024) 1302-1315.

[10] D. Cirrone, D. Makarov, V. Molkov, Rethinking “BLEVE explosion” after liquid hydrogen storage tank rupture in a fire, International Journal of Hydrogen Energy 48(23) (2023) 8716-8730.

[11] J. Danebergs, S. Deledda, Can hydrogen storage in metal hydrides be economically competitive with compressed and liquid hydrogen storage? A techno-economical perspective for the maritime sector, International Journal of Hydrogen Energy 50 (2024) 1040-1054.

[12] H. Fu, C. Lv, J. Meng, M. He, J. Wu, L. Gong, Strength and fatigue study of on-board type III cryo-compressed hydrogen storage cylinder, International Journal of Hydrogen Energy 57 (2024) 1081-1088.

[13] V.N. Verbetsky, T.A. Zotov, A.V. Tatarintsev, E.A. Movlaev, Hydrogen sorption properties of V1 − x Cr x (x = 0.1–0.5) alloys, Inorganic Materials 49(2) (2013) 149-152.

[14] T. Hagi, Y. Sato, M. Yasuda, K. Tanaka, Structure and Phase Diagram of Ti–V–H System at Room Temperature, Transactions of the Japan Institute of Metals 28(3) (1987) 198-204.

[15] S. Ono, K. Nomura, Y. Ikeda, The reaction of hydrogen with alloys of vanadium and titanium, Journal of the Less Common Metals 72(2) (1980) 159-165.

[16] Y.T. Zhai, Y.M. Li, S.H. Wei, I. Tolj, J. Kennedy, F. Yang, Progress in V-BCC based solid solution hydrogen storage alloys, Journal of Energy Storage 109 (2025).

[17] S. Banerjee, A. Kumar, C.G.S. Pillai, Improvement on the hydrogen storage properties of ZrFe2 Laves phase alloy by vanadium substitution, Intermetallics 51 (2014) 30-36.

[18] J.W. Yeh, S.K. Chen, S.J. Lin, J.Y. Gan, T.S. Chin, T.T. Shun, C.H. Tsau, S.Y. Chang, Nanostructured High-Entropy Alloys with Multiple Principal Elements: Novel Alloy Design Concepts and Outcomes, Advanced Engineering Materials 6(5) (2004) 299-303.

[19] T. Tamura, T. Kazumi, A. Kamegawa, H. Takamura, M. Okada, Protium absorption properties and protide formations of Ti–Cr–V alloys, Journal of Alloys and Compounds 356-357 (2003) 505-509.

[20] Y. Yan, Y. Chen, X. Zhou, H. Liang, C. Wu, M. Tao, Some factors influencing the hydrogen storage properties of 30V–Ti–Cr–Fe alloys, Journal of Alloys and Compounds 453(1-2) (2008)

428-432.

[21] O.N. Senkov, S.V. Senkova, C. Woodward, D.B. Miracle, Low-density, refractory multi-principal element alloys of the Cr–Nb–Ti–V–Zr system: Microstructure and phase analysis, Acta Materialia 61(5) (2013) 1545-1557.

[22] W. Li, E. Wu, P. Ma, K. Sun, D. Chen, Hydrogen storage properties of Ti1−xScxMnCr Laves phase alloys, International Journal of Energy Research 37(7) (2013) 686-697.

[23] M. Sahlberg, D. Karlsson, C. Zlotea, U. Jansson, Superior hydrogen storage in high entropy alloys, Sci Rep 6 (2016) 36770.

[24] D. Karlsson, G. Ek, J. Cedervall, C. Zlotea, K.T. Moller, T.C. Hansen, J. Bednarcik, M. Paskevicius, M.H. Sorby, T.R. Jensen, U. Jansson, M. Sahlberg, Structure and Hydrogenation Properties of a HfNbTiVZr High-Entropy Alloy, Inorg Chem 57(4) (2018) 2103-2110.

[25] Z. Wang, Q. Fang, J. Li, B. Liu, Y. Liu, Effect of lattice distortion on solid solution strengthening of BCC high-entropy alloys, Journal of Materials Science & Technology 34(2) (2018) 349-354.

[26] R. Floriano, G. Zepon, K. Edalati, G.L.B.G. Fontana, A. Mohammadi, Z. Ma, H.-W. Li, R.J. Contieri, Hydrogen storage in TiZrNbFeNi high entropy alloys, designed by thermodynamic calculations, International Journal of Hydrogen Energy 45(58) (2020) 33759-33770.

[27] X. Yang, Y. Zhang, Prediction of high-entropy stabilized solid-solution in multi-component alloys, Materials Chemistry and Physics 132(2-3) (2012) 233-238.

[28] T.R. Somo, M.V. Lototskyy, V.A. Yartys, M.W. Davids, S.N. Nyamsi, Hydrogen storage behaviours of high entropy alloys: A Review, Journal of Energy Storage 73 (2023).

[29] R.R. Chen, X.Y. Chen, X. Ding, X.Z. Li, J.J. Guo, H.S. Ding, Y.Q. Su, H.Z. Fu, Effects of Ti/Mn ratio on microstructure and hydrogen storage properties of Ti-V-Mn alloys, Journal of Alloys and Compounds 748 (2018) 171-178.

[30] J.F. Lynch, G.G. Libowitz, A.J. Maeland, Thermodynamic anomalies in hydrides of Niobium-Vanadium alloys, Materials Letters 2(4, Part A) (1984) 294-295.

[31] Y.Q. Hu, H.F. Zhang, C. Yan, L. Ye, B.Z. Ding, Z.Q. Hu, Preparation and hydrogenation

of body-centered-cubic TiCr2 alloy, Materials Letters 58(5) (2004) 783-786.

[32] D.F. S.M. L.Pontonnier, J.L.Soubeyroux, A.Baudry, P.Boyer, Structural study of hyperstoichiometric alloys ZrMn2+x and their hydrides, Journal of Alloys and Compounds 186(2) (1995) 241-248.

[33] R. Floriano, G. Zepon, K. Edalati, G.L.B.G. Fontana, A. Mohammadi, Z. Ma, H.-W. Li, R.J. Contieri, Hydrogen storage properties of new A3B2-type TiZrNbCrFe high-entropy alloy, International Journal of Hydrogen Energy 46(46) (2021) 23757-23766.

[34] P. Edalati, R. Floriano, A. Mohammadi, Y. Li, G. Zepon, H.-W. Li, K. Edalati, Reversible room temperature hydrogen storage in high-entropy alloy TiZrCrMnFeNi, Scripta Materialia 178 (2020) 387-390.

[35] J. Chen, Z. Li, H. Huang, Y. Lv, B. Liu, Y. Li, Y. Wu, J. Yuan, Y. Wang, Superior cycle life of TiZrFeMnCrV high entropy alloy for hydrogen storage, Scripta Materialia 212 (2022).

[36] L. Luo, F. Yang, Y. Li, L. Li, Y. Li, Investigation of the microstructure and hydrogen storage behavior of V48Fe12Ti15+Cr25- (x=0, 5, 10, 15) alloys, International Journal of Hydrogen Energy 47(16) (2022) 9653-9671.

[37] S. Arun, N. Radhika, B. Saleh, Advances in vacuum arc melting for high entropy alloys: A review, Vacuum 226 (2024).

[38] J. Zhang, Y. Hu, Q. Wei, Y. Xiao, P. Chen, G. Luo, Q. Shen, Microstructure and mechanical properties of RexNbMoTaW high-entropy alloys prepared by arc melting using metal powders, Journal of Alloys and Compounds 827 (2020).

[39] X.Y. Chen, R.R. Chen, X. Ding, H.Z. Fang, J.J. Guo, H.S. Ding, Y.Q. Su, H.Z. Fu, Crystal structure and hydrogen storage properties of Ti-V-Mn alloys, International Journal of Hydrogen Energy 43(12) (2018) 6210-6218.

[40] L. Luo, L. Chen, L. Li, S. Liu, Y. Li, C. Li, L. Li, J. Cui, Y. Li, High-entropy alloys for solid hydrogen storage: a review, International Journal of Hydrogen Energy 50 (2024) 406-430.

[41] A. Kumar, A. Singh, A. Suhane, Mechanically alloyed high entropy alloys: existing challenges and opportunities, Journal of Materials Research and Technology 17 (2022) 2431-2456.

[42] D.Y. Kovalev, N.A. Kochetov, I.I. Chuev, Fabrication of high-entropy carbide (TiZrHfTaNb)C by high-energy ball milling, Ceramics International 47(23) (2021) 32626-32633.

[43] N. Yazdani, M.R. Toroghinejad, A. Shabani, P. Cavaliere, Effects of Process Control Agent Amount, Milling Time, and Annealing Heat Treatment on the Microstructure of AlCrCuFeNi High-Entropy Alloy Synthesized through Mechanical Alloying, Metals 11(9) (2021).

[44] Z. Hussain, Comparative Study on Improving the Ball Mill Process Parameters Influencing on the Synthesis of Ultrafine Silica Sand: A Taguchi Coupled Optimization Technique, International Journal of Precision Engineering and Manufacturing 22(4) (2021) 679-688.

[45] J.F. de Carvalho, S.N. de Medeiros, M.A. Morales, A.L. Dantas, A.S. Carriço, Synthesis of magnetite nanoparticles by high energy ball milling, Applied Surface Science 275 (2013) 84-87.

[46] C. Suryanarayana, A.A. Al-Joubori, Z. Wang, Nanostructured Materials and Nanocomposites by Mechanical Alloying: An Overview, Metals and Materials International 28(1) (2021) 41-53.

[47] Y. Xu, Y. Deng, W. Liu, X. Zhao, J. Xu, Z. Yuan, Research progress of hydrogen energy and metal hydrogen storage materials, Sustainable Energy Technologies and Assessments 55 (2023).

[48] S. Kumar, A. Jain, T. Ichikawa, Y. Kojima, G.K. Dey, Development of vanadium based hydrogen storage material: A review, Renewable and Sustainable Energy Reviews 72 (2017) 791-800.

[49] J. Liang, G. Li, X. Ding, Y. Li, Z. Wen, T. Zhang, Y. Qu, The synergistic effect of Ni and C14 Laves phase on the hydrogen storage properties of TiVZrNbNi high entropy hydrogen storage alloy, Intermetallics 164 (2024).

[50] D.H. Lee, H.-T. Im, H.G. Kwon, S.-M. Park, R.H. Kwak, C.-S. Park, K.B. Park, S.S. Sohn, H.-K. Park, A study on the first hydrogenation behavior of TiFe0.9Cr0.1 hydrogen storage alloy with the laves phase, International Journal of Hydrogen Energy 56 (2024) 864-870.

[51] S. Zhang, X. Ding, R. Chen, J. Zhang, Y. Su, S. Wu, J. Guo, Modification of nano-eutectic structure and the relation on hydrogen storage properties: A novel Ti–V–Zr medium entropy alloy, International Journal of Hydrogen Energy 47(81) (2022) 34533-34544.

[52] X. Dong, Y. Li, Y. Zhai, Z. Liu, G. Zhang, F. Yang, Study on Microstructure and Hydrogen Storage Properties of Mg80Ni16−xAlxY4 (x = 2, 4, 8) Alloys, Metals 14(1) (2024).

[53] J. Cermak, L. Kral, P. Roupcova, Significantly decreased stability of MgH2 in the Mg-In-C alloy system: Long-period-stacking-ordering as a new way how to improve performance of hydrogen storage alloys?, Renewable Energy 150 (2020) 204-212.

[54] H. Yong, X. Wei, Y. Wang, S. Guo, Z. Yuan, Y. Qi, D. Zhao, Y. Zhang, Phase evolution, thermodynamics and kinetics property of transition metal (TM = Zr, Ti, V) catalyzed Mg–Ce–Y–Ni hydrogen storage alloys, Journal of Physics and Chemistry of Solids 144 (2020).

[55] Y. Zhang, M. Ji, Z. Yuan, J. Gao, Y. Qi, X. Dong, S. Guo, A comparison study of hydrogen storage performances of SmMg 11 Ni alloys prepared by melt spinning and ball milling, Journal of Rare Earths 36(4) (2018) 409-417.

[56] A.Z. Louis Schlapbach, Hydrogen-storage materials for mobile applications, nature 414 (2001) 353-358.

[57] P. Lv, J. Huot, Hydrogenation improvement of TiFe by adding ZrMn2, Energy 138 (2017) 375-382.

[58] Y.T. Zhai, Y.M. Li, L. Bolzoni, J. Kennedy, F. Yang, Effect of heat treatment on microstructural evolution and hydrogen storage performance of as-milled Ti5+xV35(CrMnFe)60-x (x=0, 10, 20, 30) high-entropy alloys, International Journal of Hydrogen Energy 81 (2024) 584-594.

[59] Z. Lu, H. Liu, H. Luo, Z. Wu, H. Ning, Y. Fan, X. Wang, X. Huang, C. Huang, Z. Lan, W. Zhou, J. Guo, Effect of Ti0.9Zr0.1Mn1.5V0.3 alloy catalyst on hydrogen storage kinetics and cycling stability of magnesium hydride, Chemical Engineering Journal 479 (2024).

[60] S.L. Li, H.H. Cheng, X.X. Deng, W. Chen, D.M. Chen, K. Yang, Investigation of hydrogen absorption/desorption properties of ZrMn0.85−xFe1+x alloys, Journal of Alloys and Compounds 460(1-2) (2008) 186-190.

[61] J. Liu, K. Li, H. Cheng, K. Yan, Y. Wang, Y. Liu, H. Jin, Z. Zheng, New insights into the hydrogen storage performance degradation and Al functioning mechanism of LaNi5-Al alloys, International Journal of Hydrogen Energy 42(39) (2017) 24904-24914.

[62] J. Lang, M. Eagles, M.S. Conradi, J. Huot, Hydrogenation rate limiting step, diffusion and thermal conductivity in cold rolled magnesium hydride, Journal of Alloys and Compounds 583 (2014) 116-120.

[63] X.H. An, Y.B. Pan, Q. Luo, X. Zhang, J.Y. Zhang, Q. Li, Application of a new kinetic model for the hydriding kinetics of LaNi5−xAlx (0≤x≤1.0) alloys, Journal of Alloys and Compounds 506(1) (2010) 63-69.

[64] S. Khajavi, M. Rajabi, J. Huot, Effect of cold rolling and ball milling on first hydrogenation of Ti0.5Zr0.5 (Mn1-xFex) Cr1, x = 0, 0.2, 0.4, Journal of Alloys and Compounds 775 (2019) 912-920.

[65] Y. Pang, Q. Li, A review on kinetic models and corresponding analysis methods for hydrogen storage materials, International Journal of Hydrogen Energy 41(40) (2016) 18072-18087.

[66] T. Kimura, H. Miyaoka, T. Ichikawa, Y. Kojima, Hydrogen absorption of catalyzed magnesium below room temperature, International Journal of Hydrogen Energy 38(31) (2013) 13728-13733.

[67] G. Liu, D. Chen, Y. Wang, K. Yang, Experimental and computational investigations of LaNi 5-x Al x (x = 0, 0.25, 0.5, 0.75 and 1.0) tritium-storage alloys, Journal of Materials Science & Technology 34(9) (2018) 1699-1712.

[68] Q. Yao, Y. Tang, H. Zhou, J. Deng, Z. Wang, S. Pan, G. Rao, Q. Zhu, Effect of rapid solidification treatment on structure and electrochemical performance of low-Co AB5-type hydrogen storage alloy, Journal of Rare Earths 32(6) (2014) 526-531.

[69] M.H. Dhaou, S. Belkhiria, N. Sdiri, A. Mallah, S. Al-Thoyaib, A. Jemni, S. Ben Nasrallah, Thermodynamic and electric study of the LaNi3,6Al0,4Co0,7Mn0,3 alloy, International Journal of Hydrogen Energy 42(4) (2017) 2209-2214.

[70] H.I. T. Yamamoto, M. Yamaguchi, Deformation of LaNi5 by uniaxial compression and

hydrogenation, Intermetallics 9(10-11) (2001) 987-991.

[71] Z. Łodziana, A. Dębski, G. Cios, A. Budziak, Ternary LaNi4.75M0.25 hydrogen storage alloys: Surface segregation, hydrogen sorption and thermodynamic stability, International Journal of Hydrogen Energy 44(3) (2019) 1760-1773.

[72] L. Yin, Y. Guo, X. Guo, Cocktail effect on RT5-type (R = rare earth, T = 3d transition metal) high entropy intermetallic compounds, Journal of Magnetism and Magnetic Materials 563 (2022).

[73] J.B.Y.C.Y.T.G.K.M.G.D.W.O.A.P.W.J. James, Electronic structures and magnetism of LaNi5-xFex compounds, Journal of Applied Physics 89(11) (2001) 7311-7313.

[74] J.H.N.K. Van Vucht, F A; Bruning, H C.A.M., Reversible room-temperature absorption of lage quantities of hydrogen by intermetallic compounds, Philips Res. Repts 25 (1970) 133-140.

[75] E.A.U. R.A.S. V.N.Verbetsky, Absorption of hydrogen by MmNi5 alloys, International Journal of Hydrogen Energy 21(11-12) (1996) 935-938.

[76] K.N.R. M.N.M. R.Balasubramaniam, Hydriding properties of MmNi5 system with aluminium, manganese and tin substitutions, Journal of Alloys and Compounds 196(1-2) (1993) 63-70.

[77] G. Han, Y. Kwon, J.B. Kim, S. Lee, J. Bae, E. Cho, B.J. Lee, S. Cho, J. Park, Development of a high-energy-density portable/mobile hydrogen energy storage system incorporating an electrolyzer, a metal hydride and a fuel cell, Applied Energy 259 (2020).

[78] Y. Li, E. Teliz, F. Zinola, V. Díaz, Design of a AB5-metal hydride cylindrical tank for hydrogen storage, International Journal of Hydrogen Energy 46(68) (2021) 33889-33898.

[79] V. Iosub, M. Latroche, J. Joubert, A. Percheronguegan, Optimisation of MmNi5-xSnxMmNi5-xSnx (Mm=LaMm=La, Ce, Nd and Pr, 0.27<x<0.50.27<x<0.5) compositions as hydrogen storage materials, International Journal of Hydrogen Energy 31(1) (2006) 101-108.

[80] V.A. Yartys, M.V. Lototskyy, Laves type intermetallic compounds as hydrogen storage materials: A review, Journal of Alloys and Compounds 916 (2022).

[81] J. Bodega, J.F. Fernández, F. Leardini, J.R. Ares, C. Sánchez, Synthesis of hexagonal C14/C36 and cubic C15 ZrCr2 Laves phases and thermodynamic stability of their hydrides,

Journal of Physics and Chemistry of Solids 72(11) (2011) 1334-1342.

[82] M.W. Davids, T. Martin, M. Lototskyy, R. Denys, V. Yartys, Study of hydrogen storage properties of oxygen modified Ti- based AB2 type metal hydride alloy, International Journal of Hydrogen Energy 46(25) (2021) 13658-13663.

[83] C. Wan, X. Jiang, X. Yin, X. Ju, High-capacity Zr-based AB2-type alloys as metal hydride battery anodes, Journal of Alloys and Compounds 828 (2020).

[84] M. Tliha, C. Khaldi, S. Boussami, N. Fenineche, O. El-Kedim, H. Mathlouthi, J. Lamloumi, Kinetic and thermodynamic studies of hydrogen storage alloys as negative electrode materials for Ni/MH batteries: a review, Journal of Solid State Electrochemistry 18(3) (2013) 577-593.

[85] G. A. Pebler, E A, Thermochemical and structural aspects of the reaction of hydrogen with alloys and intermetallic compounds of zirconium, Electrochemical Technology (U.S.) Absorbed by J. Electrochem. Soc. 4 (1966) 211-215, (1966).

[86] R. Pedicini, Gatto, I., Passalacqua, E., Biffi, C., Coduri, M., & Tuissi, A, Investigation of TiCr Hydrogen Storage Alloy, Journal of Technology Innovations in Renewable Energy 7 (2018) 35-41.

[87] F.P. Ming Au, S.G. Sankar, W.E. Wallace, Lian Zhang, TiMn2-based alloys as high hydrogen storage materials, Materials Science and Engineering: B 33(2-3) (1995) 53-57.

[88] X. Zhang, B. Li, L. Wang, W. Xiong, J. Li, S. Zhou, J. Xu, Y. Zhao, X. He, H. Yan, Hydrogen storage properties of AB2 type Ti–Zr–Cr–Mn–Fe based alloys, International Journal of Hydrogen Energy 51 (2024) 193-201.

[89] W. Jiang, C. He, X. Yang, X. Xiao, L. Ouyang, M. Zhu, Influence of element substitution on structural stability and hydrogen storage performance: A theoretical and experimental study on TiCr2-xMnx alloy, Renewable Energy 197 (2022) 564-573.

[90] P. Zhou, Z. Cao, X. Xiao, L. Zhan, S. Li, Z. Li, L. Jiang, L. Chen, Development of Ti-Zr-Mn-Cr-V based alloys for high-density hydrogen storage, Journal of Alloys and Compounds 875 (2021).

[91] H.-Y.J. Jeong-Gun Park, Sang-Cheol Han, Paul S. Lee, Jai-Young Lee, Hydrogen storage

properties of TiMn2-based alloys for metal hydride heat pump, Materials Science and Engineering: A 329-331 (2002) 351-55.

[92] F. Guo, K. Namba, H. Miyaoka, A. Jain, T. Ichikawa, Hydrogen storage behavior of TiFe alloy activated by different methods, Materials Letters: X 9 (2021).

[93] F.H.A.A. Mubarak, Hydrogen storage in the TiCo and TiNi alloys, International Journal of Modern Physics C 28(12) (2017) 1750148.

[94] T. Nobuki, J.-C. Crivello, F. Cuevas, J.-M. Joubert, Fast synthesis of TiNi by mechanical alloying and its hydrogenation properties, International Journal of Hydrogen Energy 44(21) (2019) 10770-10776.

[95] R.H.W. J. J. Reilly, Formation and Properties of Iron Titanium Hydride, Inorganic Chemistry 13(1) (1973) 218-222.

[96] A.K. Patel, B. Tougas, P. Sharma, J. Huot, Effect of cooling rate on the microstructure and hydrogen storage properties of TiFe with 4 wt% Zr as an additive, Journal of Materials Research and Technology 8(6) (2019) 5623-5630.

[97] E.A. Berdonosova, V.Y. Zadorozhnyy, M.Y. Zadorozhnyy, K.V. Geodakian, M.V. Zheleznyi, A.A. Tsarkov, S.D. Kaloshkin, S.N. Klyamkin, Hydrogen storage properties of TiFe-based ternary mechanical alloys with cobalt and niobium. A thermochemical approach, International Journal of Hydrogen Energy 44(55) (2019) 29159-29165.

[98] J.L. Soubeyroux, Fruchart, D., Lorthioir, G., Ochin, P., & Colin, D, Structural study of the hydrides NiTiHx (X = 1.0 and 1.4), Journal of Alloys and Compounds 196(1-2) (1993) 127-132.

[99] P. Jain, C. Gosselin, J. Huot, Effect of Zr, Ni and Zr 7 Ni 10 alloy on hydrogen storage characteristics of TiFe alloy, International Journal of Hydrogen Energy 40(47) (2015) 16921-16927.

[100] K. Ishikawa, S. Watanabe, K. Aoki, Microstructure and hydrogen permeability in Nb–TiFe alloys, Journal of Alloys and Compounds 566 (2013) 68-72.

[101] E.M. Dematteis, D.M. Dreistadt, G. Capurso, J. Jepsen, F. Cuevas, M. Latroche, Fundamental hydrogen storage properties of TiFe-alloy with partial substitution of Fe by Ti

and Mn, Journal of Alloys and Compounds 874 (2021).

[102] E.M. Dematteis, F. Cuevas, M. Latroche, Hydrogen storage properties of Mn and Cu for Fe substitution in TiFe0.9 intermetallic compound, Journal of Alloys and Compounds 851 (2021).

[103] Y.-h. Zhang, C. Li, Z.-m. Yuan, Y. Qi, S.-h. Guo, D.-l. Zhao, Research progress of TiFe-based hydrogen storage alloys, Journal of Iron and Steel Research International 29(4) (2022) 537-551.

[104] Y. Xinglin, L. Xiaohui, Z. Jiaqi, H. Quanhui, Z. Junhu, Progress in improving hydrogen storage properties of Mg-based materials, Materials Today Advances 19 (2023).

[105] J.H. Jörg Kapischk, Measurement of the effective thermal conductivity of a Mg–MgH2 packed bed with oscillating heating, Experimental Thermal and Fluid Science 17(4) (1998) 347-355.

[106] T.K. Nielsen, Manickam, Kandavel, Hirscher, Michael, Besenbacher, Flemming, Jensen, Torben R., Confinement of MgH2 Nanoclusters within Nanoporous Aerogel Scaffold Materials, ACS Nano 3(11) (2009) 3521-8.

[107] Y. Zhang, X. Wei, W. Zhang, Z. Yuan, J. Gao, Y. Qi, H. Ren, Effect of milling duration on hydrogen storage thermodynamics and kinetics of Mg-based alloy, International Journal of Hydrogen Energy 45(58) (2020) 33832-33845.

[108] L.R. Siarhei Kalinichenka, Thomas Riedl, Thomas Gemming, Thomas Weißgärbe, Bernd Kieback, Microstructure and hydrogen storage properties of melt-spun Mg–Cu–Ni–Y alloys, International Journal of Hydrogen Energy 36(2) (2011) 1592-1600.

[109] T. Yang, P. Wang, C. Xia, Q. Li, C. Liang, Y. Zhang, Characterization of microstructure, hydrogen storage kinetics and thermodynamics of a melt-spun Mg86Y10Ni4 alloy, International Journal of Hydrogen Energy 44(13) (2019) 6728-6737.

[110] E.A. Lass, Hydrogen storage measurements in novel Mg-based nanostructured alloys produced via rapid solidification and devitrification, International Journal of Hydrogen Energy 36(17) (2011) 10787-10796.

[111] M.M. H.Y. T. Matumura, Alloying effects on the electronic structures of VH and VH2,

Journal of Alloys and Compounds 284 (1999) 82-88.

[112] S. Kumar, G.P. Tiwari, N. Krishnamurthy, Tailoring the hydrogen desorption thermodynamics of V2H by alloying additives, Journal of Alloys and Compounds 645 (2015) S252-S256.

[113] W.C. C.S.H. Sung, Choong Nyeon Park, Etsuo Akiba, The hydrogen storage characteristics of Ti–Cr–V alloys, Journal of Alloys and Compounds 288 (1999) 294-298.

[114] T. Kuriiwa, T. Maruyama, A. Kamegawa, M. Okada, Effects of V content on hydrogen storage properties of V–Ti–Cr alloys with high desorption pressure, International Journal of Hydrogen Energy 35(17) (2010) 9082-9087.

[115] H. Itoh, H. Arashima, K. Kubo, T. Kabutomori, K. Ohnishi, Improvement of cyclic durability of BCC structured Ti–Cr–V alloys, Journal of Alloys and Compounds 404-406 (2005) 417-420.

[116] B. Massicot, M. Latroche, J.M. Joubert, Hydrogenation properties of Fe–Ti–V bcc alloys, Journal of Alloys and Compounds 509(2) (2011) 372-379.

[117] G. Song, M.D. Dolan, M.E. Kellam, D. Liang, S. Zambelli, V–Ni–Ti multi-phase alloy membranes for hydrogen purification, Journal of Alloys and Compounds 509(38) (2011) 9322-9328.

[118] Y. Yan, Y. Chen, H. Liang, X. Zhou, C. Wu, M. Tao, L. Pang, Hydrogen storage properties of V–Ti–Cr–Fe alloys, Journal of Alloys and Compounds 454(1-2) (2008) 427-431.

[119] Y.T. T. Tamura , K. Matsumoto, T. Fuda, T. Kuriiwa, A. Kamegawa, H. Takamura, M. Okada, Protium absorption properties of Ti–V–Cr–Mn alloys with a b.c.c. structure, Journal of Alloys and Compounds 330-332 (2002) 522-525.

[120] H.E. Sung Wook Cho, Etsuo Akiba Effect of Fe addition on hydrogen storage characteristics of Ti-Zr-Cr-V alloy, Journal of Alloys and Compounds 307 (2000) 304–310.

[121] Y. Wu, W. Zhao, L. Jiang, Z. Li, X. Guo, J. Ye, B. Yuan, S. Wang, L. Hao, Effect of Fe and Al on hydrogen storage properties of 75 V-Ti-Cr alloys, Journal of Alloys and Compounds 887 (2021).

[122] C. Zlotea, M.A. Sow, G. Ek, J.P. Couzinié, L. Perrière, I. Guillot, J. Bourgon, K.T. Møller,

T.R. Jensen, E. Akiba, M. Sahlberg, Hydrogen sorption in TiZrNbHfTa high entropy alloy, Journal of Alloys and Compounds 775 (2019) 667-674.

[123] B. Cantor, I.T.H. Chang, P. Knight, A.J.B. Vincent, Microstructural development in equiatomic multicomponent alloys, Materials Science and Engineering: A 375-377 (2004) 213-218.

[124] B. Cheng, L. Kong, H. Cai, Y. Li, Y. Zhao, D. Wan, Y. Xue, Exploring microstructure variations and hydrogen storage characteristics in TiVNbCrNi high-entropy alloys with different Ni incorporation, International Journal of Hydrogen Energy 72 (2024) 29-40.

[125] L. Luo, H. Han, D. Feng, W. Lv, L. Chen, L. Li, T. Zhai, S. Liu, S. Sun, Y. Li, W. Pei, J. Cui, Y. Li, Nanocrystalline High Entropy Alloys with Ultrafast Kinetics and High Storage Capacity for Large-Scale Room-Temperature-Applicable Hydrogen Storage, Renewables 2(2) (2024) 138-149.

[126] X. Ma, X. Ding, R. Chen, W. Cao, Q. Song, Study on hydrogen storage property of (ZrTiVFe) Al high-entropy alloys by modifying Al content, International Journal of Hydrogen Energy 47(13) (2022) 8409-8418.

[127] X. Ma, X. Ding, R. Chen, X. Chen, Q. Song, H. Cui, Study on microstructure and the hydrogen storage behavior of a TiVZrNbFe high-entropy alloy, Intermetallics 157 (2023).

[128] J.Z.C. X.B. Yu, Z. Wu, B.J. Xia, N.X. Xu, Effect of Cr content on hydrogen storage properties for Ti-V-based BCC-phase alloys, International Journal of Hydrogen Energy 29(13) (2004) 1377-1381.

[129] X.B. Yu, Z. Wu, B.J. Xia, N.X. Xu, Enhancement of hydrogen storage capacity of Ti–V–Cr–Mn BCC phase alloys, Journal of Alloys and Compounds 372(1-2) (2004) 272-277.

[130] X.Y. Chen, R.R. Chen, X. Ding, H.Z. Fang, X.Z. Li, H.S. Ding, Y.Q. Su, J.J. Guo, H.Z. Fu, Effect of phase formation on hydrogen storage properties in Ti-V-Mn alloys by zirconium substitution, Energy 166 (2019) 587-597.

[131] H. Shen, J. Hu, P. Li, G. Huang, J. Zhang, J. Zhang, Y. Mao, H. Xiao, X. Zhou, X. Zu, X. Long, S. Peng, Compositional dependence of hydrogenation performance of Ti-Zr-Hf-Mo-Nb high-entropy alloys for hydrogen/tritium storage, Journal of Materials Science & Technology

55 (2020) 116-125.

[132] J. Yoo, G. Shim, S. Cho, C. Park, Effects of desorption temperature and substitution of Fe for Cr on the hydrogen storage properties of Ti0.32Cr0.43V0.25Ti0.32Cr0.43V0.25 alloy, International Journal of Hydrogen Energy 32(14) (2007) 2977-2981.

[133] S. Basak, K. Shashikala, P. Sengupta, S. Kulshreshtha, Hydrogen absorption properties of Ti–V–Fe alloys: Effect of Cr substitution, International Journal of Hydrogen Energy 32(18) (2007) 4973-4977.

[134] J.-H. Yoo, G. Shim, C.-N. Park, W.-B. Kim, S.-W. Cho, Influence of Mn or Mn plus Fe on the hydrogen storage properties of the Ti-Cr-V alloy, International Journal of Hydrogen Energy 34(22) (2009) 9116-9121.

[135] M.M. Nygård, M.H. Sørby, A.A. Grimenes, B.C. Hauback, The Influence of Fe on the Structure and Hydrogen Sorption Properties of Ti-V-Based Metal Hydrides, Energies 13(11) (2020).

[136] I. ANSARA, Thermodynamic modelling of solution phases and
phase diagram calculations Pure & Appl. Chem 62(1) (1990) 71-78.

[137] J.-W. Yeh, S.-Y. Chang, Y.-D. Hong, S.-K. Chen, S.-J. Lin, Anomalous decrease in X-ray diffraction intensities of Cu–Ni–Al–Co–Cr–Fe–Si alloy systems with multi-principal elements, Materials Chemistry and Physics 103(1) (2007) 41-46.

[138] A. Munitz, L. Meshi, M.J. Kaufman, Heat treatments' effects on the microstructure and mechanical properties of an equiatomic Al-Cr-Fe-Mn-Ni high entropy alloy, Materials Science and Engineering: A 689 (2017) 384-394.

[139] Z. Fu, W. Chen, H. Wen, D. Zhang, Z. Chen, B. Zheng, Y. Zhou, E.J. Lavernia, Microstructure and strengthening mechanisms in an FCC structured single-phase nanocrystalline Co25Ni25Fe25Al7.5Cu17.5 high-entropy alloy, Acta Materialia 107 (2016) 59-71.

[140] D.B. Miracle, O.N. Senkov, A critical review of high entropy alloys and related concepts, Acta Materialia 122 (2017) 448-511.

[141] Q. Li, H. Zhang, D. Li, Z. Chen, S. Huang, Z. Lu, H. Yan, W(x)NbMoTa Refractory

High-Entropy Alloys Fabricated by Laser Cladding Deposition, Materials (Basel) 12(3) (2019).

[142] P.K.L. J.W.Y. Michael C. Gao, Yong Zhang, Chapter 3: Physical Metallurgy, High-Entropy Alloys: Fundamentals and Applications, (2016) 56-57.

[143] K.Y. Tsai, M.H. Tsai, J.W. Yeh, Sluggish diffusion in Co–Cr–Fe–Mn–Ni high-entropy alloys, Acta Materialia 61(13) (2013) 4887-4897.

[144] S. Ranganathan, Alloyed pleasures: Multimetallic cocktails, Current Science 85(5) (2003) 1404-1406.

[145] Y.-F. Kao, T.-J. Chen, S.-K. Chen, J.-W. Yeh, Microstructure and mechanical property of as-cast, -homogenized, and -deformed AlxCoCrFeNi ($0 \leq x \leq 2$) high-entropy alloys, Journal of Alloys and Compounds 488(1) (2009) 57-64.

[146] X. Ye, Z. Diao, H. Lei, L. Wang, Z. Li, B. Li, J. Feng, J. Chen, X. Liu, D. Fang, Multi-phase FCC-based composite eutectic high entropy alloy with multi-scale microstructure, Materials Science and Engineering: A 889 (2024).

[147] F. Liu, P. Liaw, Y. Zhang, Recent Progress with BCC-Structured High-Entropy Alloys, Metals 12(3) (2022).

[148] Y.J. Zhao, J.W. Qiao, S.G. Ma, M.C. Gao, H.J. Yang, M.W. Chen, Y. Zhang, A hexagonal close-packed high-entropy alloy: The effect of entropy, Materials & Design 96 (2016) 10-15.

[149] A.I. Akira Takeuchi, Classification of Bulk Metallic Glasses by Atomic Size Difference, Heat of Mixing and Period of Constituent Elements and Its Application to Characterization of the Main Alloying Element, Materials Transactions 46(12) (2005).

[150] Y. Zhang, Y.J. Zhou, J.P. Lin, G.L. Chen, P.K. Liaw, Solid-Solution Phase Formation Rules for Multi-component Alloys, Advanced Engineering Materials 10(6) (2008) 534-538.

[151] Y. Zhang, Z.P. Lu, S.G. Ma, P.K. Liaw, Z. Tang, Y.Q. Cheng, M.C. Gao, Guidelines in predicting phase formation of high-entropy alloys, MRS Communications 4(2) (2014) 57-62.

[152] X. Yang, S.Y. Chen, J.D. Cotton, Y. Zhang, Phase Stability of Low-Density, Multiprincipal Component Alloys Containing Aluminum, Magnesium, and Lithium, Jom 66(10) (2014) 2009-2020.

[153] S. Guo, C. Ng, J. Lu, C.T. Liu, Effect of valence electron concentration on stability of

fcc or bcc phase in high entropy alloys, Journal of Applied Physics 109(10) (2011).

[154] B. Pan, X. Xu, J. Yang, H. Zhan, L. Feng, Q. Long, Q. Yao, J. Deng, L. Cheng, Z. Lu, H. Zhou, Effect of Nb, Ti, and V on wear resistance and electrochemical corrosion resistance of AlCoCrNiM (M=Nb, Ti, V) high-entropy alloys, Materials Today Communications 39 (2024).

[155] W. Luo, Y.g. Li, Q. Zou, L. Dai, H. Jia, Y.a. Luo, Effect of V on microstructure and properties of Fe1.25CoNiAlMn0.21Vx magnetic high-entropy alloys, Materials Characterization (2024).

[156] A. Záděra, J. Sopoušek, J. Buršík, J. Čupera, P. Brož, V. Jan, Influence of substitution of Cr by Cu on phase equilibria and microstructures in the Fe–Ni–Co–Cr high-entropy alloys, Intermetallics 174 (2024).

[157] S.E. Sünbül, K. İçin, F.Z. Şeren, Ö. Şahin, D.D. Çakil, R. Sezer, S. Öztürk, Determination of structural, tribological, isothermal oxidation and corrosion properties of Al–Co–Cr–Fe–Ni–Ti–Cu high-entropy alloy, Vacuum 187 (2021).

[158] C.C. Koch, Nanocrystalline high-entropy alloys, Journal of Materials Research 32(18) (2017) 3435-3444.

[159] Y. Zou, J.M. Wheeler, H. Ma, P. Okle, R. Spolenak, Nanocrystalline High-Entropy Alloys: A New Paradigm in High-Temperature Strength and Stability, Nano Lett 17(3) (2017) 1569-1574.

[160] S. Liu, G. Feng, L. Xiao, Y. Guan, W. Song, Shock-induced dynamic response in single and nanocrystalline high-entropy alloy FeNiCrCoCu, International Journal of Mechanical Sciences 239 (2023).

[161] N. Kumar, C.S. Tiwary, K. Biswas, Preparation of nanocrystalline high-entropy alloys via cryomilling of cast ingots, Journal of Materials Science 53(19) (2018) 13411-13423.

[162] S. Varalakshmi, M. Kamaraj, B.S. Murty, Processing and properties of nanocrystalline CuNiCoZnAlTi high entropy alloys by mechanical alloying, Materials Science and Engineering: A 527(4-5) (2010) 1027-1030.

[163] Q.-W. Xing, Y. Zhang, Amorphous phase formation rules in high-entropy alloys, Chinese Physics B 26(1) (2017).

[164] M.A. Tunes, H.T. Vo, J.K.S. Baldwin, T.A. Saleh, S.J. Fensin, O. El-Atwani, Perspectives on novel refractory amorphous high-entropy alloys in extreme environments, Applied Materials Today 32 (2023).

[165] J. Jiang, W. Sun, N. Luo, Molecular dynamics study of microscopic deformation mechanism and tensile properties in AlxCoCrFeNi amorphous high-entropy alloys, Materials Today Communications 31 (2022).

[166] S. Guo, Q. Hu, C. Ng, C.T. Liu, More than entropy in high-entropy alloys: Forming solid solutions or amorphous phase, Intermetallics 41 (2013) 96-103.

[167] J. Joseph, T. Jarvis, X. Wu, N. Stanford, P. Hodgson, D.M. Fabijanic, Comparative study of the microstructures and mechanical properties of direct laser fabricated and arc-melted Al x CoCrFeNi high entropy alloys, Materials Science and Engineering: A 633 (2015) 184-193.

[168] J. Cieslak, J. Tobola, K. Berent, M. Marciszko, Phase composition of AlxFeNiCrCo high entropy alloys prepared by sintering and arc-melting methods, Journal of Alloys and Compounds 740 (2018) 264-272.

[169] T.M. Butler, M.L. Weaver, Oxidation behavior of arc melted AlCoCrFeNi multi-component high-entropy alloys, Journal of Alloys and Compounds 674 (2016) 229-244.

[170] M. Vaidya, G.M. Muralikrishna, B.S. Murty, High-entropy alloys by mechanical alloying: A review, Journal of Materials Research 34(5) (2019) 664-686.

[171] L. Wei, X. Liu, Y. Gao, X. Peng, N. Hu, M. Chen, Phase, microstructure and mechanical properties evaluation of AlCoCrFeNi high-entropy alloy during mechanical ball milling, Intermetallics 138 (2021).

[172] S.N. Addepalli, S. Joladarashi, M.R. Ramesh, S.B. Arya, Effect of Mechanical Alloying on the Microstructure of CoCrNiTiMox High Entropy Alloy, Journal of Thermal Spray Technology 31(4) (2022) 1045-1055.

[173] P.-O. Delzant, P. Chapelle, A. Jardy, J. Jourdan, J. Jourdan, Y. Millet, Investigation of arc dynamics during vacuum arc remelting of a Ti64 alloy using a photodiode based instrumentation, Journal of Materials Processing Technology 266 (2019) 10-18.

[174] F.J. Baldenebro-Lopez, J.M. Herrera-Ramírez, S.P. Arredondo-Rea, C.D. Gómez-

Esparza, R. Martínez-Sánchez, Simultaneous effect of mechanical alloying and arc-melting processes in the microstructure and hardness of an AlCoFeMoNiTi high-entropy alloy, Journal of Alloys and Compounds 643 (2015) S250-S255.

[175] J.-H. Pi, Y. Pan, L. Zhang, H. Zhang, Microstructure and property of AlTiCrFeNiCu high-entropy alloy, Journal of Alloys and Compounds 509(18) (2011) 5641-5645.

[176] T. Matsushita, Electromagnetic Induction, Electricity and Magnetism: New Formulation by Introduction of Superconductivity, Springer International Publishing, Cham, 2021, pp. 257-282.

[177] L. Shiqi, L. Weili, X. Kuangdi, Induction Furnace Melting, in: K. Xu (Ed.), The ECPH Encyclopedia of Mining and Metallurgy, Springer Nature Singapore, Singapore, 2022, pp. 1-4.

[178] R. Mishra, Synthesis of Materials by Induction Heating, in: A.K. Tyagi, R.S. Ningthoujam (Eds.), Handbook on Synthesis Strategies for Advanced Materials : Volume-I: Techniques and Fundamentals, Springer Singapore, Singapore, 2021, pp. 215-228.

[179] J. Zhouhua, D. Yanwu, X. Kuangdi, Vacuum Metallurgy, in: K. Xu (Ed.), The ECPH Encyclopedia of Mining and Metallurgy, Springer Nature Singapore, Singapore, 2022, pp. 1-8.

[180] B.-M. Moon, J.H. Seo, H.-J. Lee, K.H. Jung, J.H. Park, H.-D. Jung, Method of recycling titanium scraps via the electromagnetic cold crucible technique coupled with calcium treatment, Journal of Alloys and Compounds 727 (2017) 931-939.

[181] S.M. Thompson, L. Bian, N. Shamsaei, A. Yadollahi, An overview of Direct Laser Deposition for additive manufacturing; Part I: Transport phenomena, modeling and diagnostics, Additive Manufacturing 8 (2015) 36-62.

[182] Z. Tian, C. Zhang, D. Wang, W. Liu, X. Fang, D. Wellmann, Y. Zhao, Y. Tian, A Review on Laser Powder Bed Fusion of Inconel 625 Nickel-Based Alloy, Applied Sciences 10(1) (2019).

[183] J. Maya, K. Sivaprasad, G. Sarath Kumar, R. Baitimerov, P. Lykov, K. Prashanth, Microstructure, Mechanical Properties, and Corrosion Behavior of 06Cr15Ni4CuMo Processed by Using Selective Laser Melting, Metals 12(8) (2022).

[184] K. Li, C. Ji, S. Bai, B. Jiang, F. Pan, Selective laser melting of magnesium alloys:

Necessity, formability, performance, optimization and applications, Journal of Materials Science & Technology 154 (2023) 65-93.

[185] J. Shen, W. Sun, L. Xie, S. Yang, B. Yu, M. Chen, F. Wang, Achieving well-balanced mechanical properties and oxidation resistance of an oxide dispersion strengthened nickel-based alloy via in-situ solid-state reaction, Ceramics International 50(13) (2024) 22514-22523.

[186] W. He, F. Liu, L. Tan, Z. Tian, Z. Qin, L. Huang, X. Xiao, G. Wang, P. Chen, B. Liu, Optimizing the Thermomechanical Process of Nickel-Based ODS Superalloys by an Efficient Method, Materials (Basel) 15(12) (2022).

[187] S. Huang, Development Of Oxide-Dispersion-Strengthened Nickel-Based Super Alloy Powders For Additive Manufacturing, Graduate Theses, Dissertations, and Problem Reports. (2018) 3699.

[188] X.-R. Tan, G.-P. Zhang, Q. Zhi, Z.-X. Liu, Effects of milling on the microstructure and hardness of Al2NbTi3V2Zr high-entropy alloy, Materials & Design 109 (2016) 27-36.

[189] S. Li, W. Yin, Y. Qiao, Enhanced electrochemical properties of ball-milled LaY2Ni9.5Mn0.5Al0.5 hydrogen storage alloy with graphene, Journal of Physics and Chemistry of Solids 160 (2022).

[190] C. Sun, P. Li, S. Xi, Y. Zhou, S. Li, X. Yang, A new type of high entropy alloy composite Fe18Ni23Co25Cr21Mo8WNb3C2 prepared by mechanical alloying and hot pressing sintering, Materials Science and Engineering: A 728 (2018) 144-150.

[191] A. Fourmont, S. Le Gallet, O. Politano, C. Desgranges, F. Baras, Effects of planetary ball milling on AlCoCrFeNi high entropy alloys prepared by Spark Plasma Sintering: Experiments and molecular dynamics study, Journal of Alloys and Compounds 820 (2020).

[192] T. Qureshi, M.M. Khan, H.S. Pali, The future of hydrogen economy: Role of high entropy alloys in hydrogen storage, Journal of Alloys and Compounds 1004 (2024).

[193] H.-Y. Kong, Q.-F. Xie, C.-L. Wu, Y. Wang, Y.-G. Chen, H.-W. Li, Y.-G. Yan, Vanadium-based alloy for hydrogen storage: a review, Rare Metals (2024).

[194] X. Wang, W. Guo, Y. Fu, High-entropy alloys: emerging materials for advanced functional applications, Journal of Materials Chemistry A 9(2) (2021) 663-701.

[195] J. Matsuda, E. Akiba, Lattice defects in V–Ti BCC alloys before and after hydrogenation, Journal of Alloys and Compounds 581 (2013) 369-372.

[196] F.K. Mustafa Okumuş Effect of Ti content and ball-milling time on the microstructural, thermal, and microhardness properties of AlCoCuNiTi high entropy alloys, Materials Chemistry and Physics 311 (2024) 128591.

[197] S. Motozuka, H. Sato, H. Kuwata, M. Bito, Y. Okazaki, Effects of interfacial interactions between metal and process control agents during ball milling on the microstructure of the milled Fe-based nanocrystalline alloy powder, Heliyon 8(8) (2022) e10325.

[198] E.G. Volkova, K.A. Kozlov, B.D. Antonov, A.M. Murzakaev, V.A. Zavalishin, V.A.Y. A.A. Livinets, Alloying of Al2Au intermetallic compound with Cu by the ball milling technique, Journal of Alloys and Compounds 900 (2022) 163429.

[199] P. Echlin, Sample Embedding and Mounting, Handbook of Sample Preparation for Scanning Electron Microscopy and X-Ray Microanalysis, Springer US, Boston, MA, 2009, pp. 47-63.

[200] J. Epp, 4 - X-ray diffraction (XRD) techniques for materials characterization, in: G. Hübschen, I. Altpeter, R. Tschuncky, H.-G. Herrmann (Eds.), Materials Characterization Using Nondestructive Evaluation (NDE) Methods, Woodhead Publishing2016, pp. 81-124.

[201] F. Izumi, Chapter 7 The rietveld method and its applications to synchrotron X-ray powder data, in: H. Saisho, Y. Gohshi (Eds.), Analytical Spectroscopy Library, Elsevier1996, pp. 405-452.

[202] A.I. Saville, A. Creuziger, E.B. Mitchell, S.C. Vogel, J.T. Benzing, J. Klemm-Toole, K.D. Clarke, A.J. Clarke, MAUD Rietveld Refinement Software for Neutron Diffraction Texture Studies of Single- and Dual-Phase Materials, Integr Mater Manuf Innov 10(3) (2021).

[203] W. Zhou, R. Apkarian, Z.L. Wang, D. Joy, Fundamentals of Scanning Electron Microscopy (SEM), in: W. Zhou, Z.L. Wang (Eds.), Scanning Microscopy for Nanotechnology: Techniques and Applications, Springer New York, New York, NY, 2007, pp. 1-40.

[204] C.Y. Tang, Z. Yang, Chapter 8 - Transmission Electron Microscopy (TEM), in: N. Hilal, A.F. Ismail, T. Matsuura, D. Oatley-Radcliffe (Eds.), Membrane Characterization,

Elsevier2017, pp. 145-159.

[205] P. Tizro, C. Choi, N. Khanlou, Sample Preparation for Transmission Electron Microscopy, in: W.H. Yong (Ed.), Biobanking: Methods and Protocols, Springer New York, New York, NY, 2019, pp. 417-424.

[206] J.O. Andersson, T. Helander, L. Höglund, P. Shi, B. Sundman, Thermo-Calc & DICTRA, computational tools for materials science, Calphad 26(2) (2002) 273-312.

[207] Chapter 5 - Thermodynamic Models for Solution and Compound Phases, in: N. Saunders, A.P. Miodownik (Eds.), Pergamon Materials Series, Pergamon1998, pp. 91-126.

[208] T. Voskuilen, Y. Zheng, T. Pourpoint, Development of a Sievert apparatus for characterization of high pressure hydrogen sorption materials, International Journal of Hydrogen Energy 35(19) (2010) 10387-10395.

[209] A. Kumar, M. Mucalo, L. Bolzoni, Y. Li, F. Kong, F. Yang, Fabrication, Microstructure, Mechanical, and Electrochemical Properties of NiMnFeCu High Entropy Alloy from Elemental Powders, Metals 12(1) (2022).

[210] C. Suryanarayana, Mechanical alloying and milling, Progress in Materials Science 46(1) (2001) 1-184.

[211] J.Y. Huang, Y.K. Wu, A.Q. He, H.Q. Ye, Direct evidence of nanocrystal enhanced complete mutual solubility in mechanically alloyed Co□Cu powders, Nanostructured Materials 4(3) (1994) 293-302.

[212] S. Daryoush, H. Mirzadeh, A. Ataie, Amorphization, mechano-crystallization, and crystallization kinetics of mechanically alloyed AlFeCuZnTi high-entropy alloys, Materials Letters 307 (2022).

[213] O.D. Neikov, Chapter 3 - Mechanical Alloying, in: O.D. Neikov, S.S. Naboychenko, N.A. Yefimov (Eds.), Handbook of Non-Ferrous Metal Powders (Second Edition), Elsevier, Oxford, 2019, pp. 91-124.

[214] C. Suryanarayana, Does a disordered γ-TiAl phase exist in mechanically alloyed TiAl powders?, Intermetallics 3(2) (1995) 153-160.

[215] H. Wu, Y. Ji, Y. Chen, Y. Zhang, H. Yong, Y. Zhang, Microstructure, hydrogen storage

properties, and thermodynamic characterization of ball-milled Mg90Ni5Y5 alloy, Journal of Physics and Chemistry of Solids 195 (2024).

[216] M. Akmal, A. Malik, W. Jeong, H.J. Ryu, Incorporating microstructural and mechanical heterogeneity to Ti–Zr–Nb alloy by partial high-energy ball milling, Materials Chemistry and Physics 315 (2024).

[217] D.L. Chen, F. Chen, F.H. Chen, M. Zarinejad, Y.X. Tong, Phase transformation and magnetocaloric properties of Ni–Co–Mn–In alloy particles fabricated by conventional ball milling, Current Applied Physics 59 (2024) 33-38.

[218] N. Yurchenko, D. Shaysultanov, E. Povolyaeva, D. Moskovskikh, S. Zherebtsov, N. Stepanov, Structure and mechanical properties of low-density AlCrFeTiX (X = Co, Ni, Cu) high-entropy alloys produced by spark plasma sintering, Journal of Alloys and Compounds 1007 (2024).

[219] B.E. Nilssen, R.A. Kleiv, Silicon Powder Properties Produced in a Planetary Ball Mill as a Function of Grinding Time, Grinding Bead Size and Rotational Speed, Silicon 12(10) (2020) 2413-2423.

[220] Z. Wu, Y. Liang, E. Fu, J. Du, P. Wang, Y. Fan, Y. Zhao, Effect of Ball Milling Parameters on the Refinement of Tungsten Powder, Metals 8(4) (2018).

[221] M. Huang, J. Jiang, Y. Wang, Y. Liu, Y. Zhang, Effects of milling process parameters and PCAs on the synthesis of Al0.8Co0.5Cr1.5CuFeNi high entropy alloy powder by mechanical alloying, Materials & Design 217 (2022).

[222] L. Zhang, X. Guo, Effects of Process Control Agents on the Mechanical Alloying Behavior of Nb-Ti-Si Based Alloy, Materials Transactions 59(4) (2018) 528-537.

[223] Z. Mao, J. Li, S. Liu, L. Xiong, Effect of Process Control Agent on Microstructures and High-Temperature Oxidation Behavior of a Nickel-Based ODS Alloy, Metals 12(6) (2022).

[224] A. Kumar, M. Abu Shaz, N.K. Mukhopadhyay, T.P. Yadav, Phase transformation of AB5 to AB2 type phase on substitution of Mn with Zr in TiVCoNi (ZrxMn2-x) (x = 0, 0.3, 0.6, 1.0) high entropy alloys, Materials Chemistry and Physics 318 (2024).

[225] A. Kumar, M. Mucalo, L. Bolzoni, Y. Li, Y. Qu, F. Yang, Facile synthesis of a

NiMnFeCrCu high entropy alloy for electrocatalytic oxygen evolution reactions, Materials Today Sustainability 22 (2023).

[226] S. Mohanty, N.P. Gurao, K. Biswas, Sinter ageing of equiatomic Al20Co20Cu20Zn20Ni20 high entropy alloy via mechanical alloying, Materials Science and Engineering: A 617 (2014) 211-218.

[227] P.G.T. Howell, K.M.W. Davy, A. Boyde, Mean atomic number and backscattered electron coefficient calculations for some materials with low mean atomic number, Scanning 20(1) (2006) 35-40.

[228] K.-C. Cheng, J.-H. Chen, S. Stadler, S.-H. Chen, Properties of atomized AlCoCrFeNi high-entropy alloy powders and their phase-adjustable coatings prepared via plasma spray process, Applied Surface Science 478 (2019) 478-486.

[229] S. Mohanty, T.N. Maity, S. Mukhopadhyay, S. Sarkar, N.P. Gurao, S. Bhowmick, K. Biswas, Powder metallurgical processing of equiatomic AlCoCrFeNi high entropy alloy: Microstructure and mechanical properties, Materials Science and Engineering: A 679 (2017) 299-313.

[230] N. Yurchenko, N. Stepanov, G. Salishchev, Laves-phase formation criterion for high-entropy alloys, Materials Science and Technology 33(1) (2016) 17-22.

[231] L. Serrano, M. Moussa, J.-Y. Yao, G. Silva, J.-L. Bobet, S.F. Santos, K.R. Cardoso, Development of Ti-V-Nb-Cr-Mn high entropy alloys for hydrogen storage, Journal of Alloys and Compounds 945 (2023).

[232] U. Ulmer, K. Asano, T. Bergfeldt, V.S.K. Chakravadhanula, R. Dittmeyer, H. Enoki, C. Kübel, Y. Nakamura, A. Pohl, M. Fichtner, Effect of oxygen on the microstructure and hydrogen storage properties of V–Ti–Cr–Fe quaternary solid solutions, International Journal of Hydrogen Energy 39(35) (2014) 20000-20008.

[233] G. Andrade, G. Zepon, K. Edalati, A. Mohammadi, Z. Ma, H.-W. Li, R. Floriano, Crystal structure and hydrogen storage properties of AB-type TiZrNbCrFeNi high-entropy alloy, International Journal of Hydrogen Energy 48(36) (2023) 13555-13565.

[234] A. Bishnoi, P. Sharma, Large-scale production of BCC solid solution hydrogen storage

alloy, International Journal of Hydrogen Energy 75 (2024) 294-302.

[235] A. Kumar, T.P. Yadav, M.A. Shaz, N.K. Mukhopadhyay, Hydrogen Storage Performance of C14 Type Ti0.24V0.17Zr0.17Mn0.17Co0.17Fe0.08 High Entropy Intermetallics, Transactions of the Indian National Academy of Engineering 9(3) (2023) 585-593.

[236] M. Zhang, R. Hu, T. Zhang, H. Kou, J. Li, X. Xue, Hydrogenation properties of Pd-coated Zr-based Laves phase compounds, Vacuum 109 (2014) 191-196.

[237] K. Lu, Y.H. Zhao, Experimental evidences of lattice distortion in Nanocrystalline Materials, Nanostructured Materials 12(1) (1999) 559-562.

[238] P.K. Verma, A. Singh, A. Kumar, Microstructure characterization and phase evolution of equiatomic AlCoMoFeNi high entropy alloy synthesized by mechanical alloying, Materials Chemistry and Physics 318 (2024).

[239] M.S. El-Eskandarany, Ball milling as a powerful nanotechnological tool for fabrication of nanomaterials, Mechanical Alloying2015, pp. 84-112.

[240] M.d.B. Ferraz, W.J. Botta, G. Zepon, Synthesis, characterization and first hydrogen absorption/desorption of the Mg35Al15Ti25V10Zn15 high entropy alloy, International Journal of Hydrogen Energy 47(54) (2022) 22881-22892.

[241] M. Balcerzak, J. Ternieden, M. Felderhoff, Synthesis, thermal stability, and hydrogen storage properties of poorly crystalline TiVFeCuNb multi-principal element alloy, Journal of Alloys and Compounds 943 (2023).

[242] L. Luo, H. Han, D. Feng, W. Lv, L. Chen, L. Li, T. Zhai, S. Liu, S. Sun, Y. Li, W. Pei, J. Cui, Y. Li, Nanocrystalline High Entropy Alloys with Ultrafast Kinetics and High Storage Capacity for Large-Scale Room-Temperature-Applicable Hydrogen Storage, Renewables (2024) 1-12.

[243] J. Liang, G. Li, X. Ding, Z. Wen, T. Zhang, Y. Li, Y. Qu, Formation of Zr-rich BCC phase and its relation on the hydrogen storage properties of TiVNbZr high entropy alloy, International Journal of Hydrogen Energy 48(86) (2023) 33610-33619.

[244] D.G. WESTLAKE, A geometric model for the stoichiometry and interstitial site occupancy in hydrides (deuterides) of LaNi5, LaNi4Al and LaNi4Mn, Journal of the Less-

Common Metals 91 (1983) 275-292.

[245] F.R. J.R.J. J.J Reilly, J.F Lynch, J Tanaka, R.H Wiswall,, Lattice expansion as a measure of surface segregation and the solubility of hydrogen in α-FeTiHx, Journal of the Less Common Metals 73(1) (1980) 175-782.

[246] Y. Zhang, J. Li, T. Zhang, T. Wu, H. Kou, X. Xue, Hydrogenation thermokinetics and activation behavior of non-stoichiometric Zr-based Laves alloys with enhanced hydrogen storage capacity, Journal of Alloys and Compounds 694 (2017) 300-308.

[247] J. Liang, G. Li, X. Ding, Y. Li, Z. Wen, T. Zhang, Y. Qu, Effect of C14 Laves/BCC on microstructure and hydrogen storage properties of (Ti32.5V27.5Zr7.5Nb32.5) 1-xFex (x = 0.03, 0.06, 0.09) high entropy hydrogen storage alloys, Journal of Energy Storage 73 (2023).

[248] P. Ruz, S. Banerjee, R. Halder, A. Kumar, V. Sudarsan, Thermodynamics, kinetics and microstructural evolution of Ti 0.43 Zr 0.07 Cr 0.25 V 0.25 alloy upon hydrogenation, International Journal of Hydrogen Energy 42(16) (2017) 11482-11492.

[249] S. Suwarno, J.K. Solberg, J.P. Maehlen, B. Krogh, V.A. Yartys, Influence of Cr on the hydrogen storage properties of Ti-rich Ti–V–Cr alloys, International Journal of Hydrogen Energy 37(9) (2012) 7624-7628.

[250] M. Balcerzak, M. Wagstaffe, R. Robles, M. Pruneda, H. Noei, Effect of Cr on the hydrogen storage and electronic properties of BCC alloys: Experimental and first-principles study, International Journal of Hydrogen Energy 45(53) (2020) 28996-29008.

[251] X. Ma, X. Ding, R. Chen, J. Zhang, Q. Song, H. Cui, Microstructural features and improved reversible hydrogen storage properties of ZrTiVFe high-entropy alloy via Cu alloying, International Journal of Hydrogen Energy 48(7) (2023) 2718-2730.

[252] Z. Song, J. Ru, R. Ma, M. Wan, J. Zhou, Q. Xie, First-principles studies of behavior of hydrogen and mechanical properties of TiCrTaV high-entropy alloys, Materials Today Communications 35 (2023).

[253] Z. Xie, Y. Wang, C. Lu, L. Dai, Sluggish hydrogen diffusion and hydrogen decreasing stacking fault energy in a high-entropy alloy, Materials Today Communications 26 (2021).

[254] Z. Pu, Y. Chen, L.H. Dai, Strong resistance to hydrogen embrittlement of high-entropy alloy, Materials Science and Engineering: A 736 (2018) 156-166.

[255] B. Cheng, L. Kong, H. Cai, Y. Li, Y. Zhao, D. Wan, Y. Xue, Pushing the Boundaries of solid-state hydrogen storage: A Refined study on TiVNbCrMo high-entropy alloys, International Journal of Hydrogen Energy 60 (2024) 282-292.

[256] W. Jiang, S. Chen, H. Shen, Z. Cao, C. He, X. Yang, L. Ouyang, Influence of Fe substitution on structural stability and hydrogen storage/compression performance: A theoretical and experimental study on TiCr1.5-Mn0.5Fe alloys, Chemical Engineering Journal 494 (2024).

[257] Y. Chen, J.S. Williams, Formation of metal hydrides by mechanical alloying, Journal of Alloys and Compounds 217(2) (1995) 181-184.

[258] M.S. El-Eskandarany, 4 - Ball milling as a powerful nanotechnological tool for fabrication of nanomaterials, in: M.S. El-Eskandarany (Ed.), Mechanical Alloying (Second Edition), William Andrew Publishing, Oxford, 2015, pp. 84-112.

[259] X. Yao, Z.H. Zhu, H.M. Cheng, G.Q. Lu, Hydrogen diffusion and effect of grain size on hydrogenation kinetics in magnesium hydrides, Journal of Materials Research 23(2) (2008) 336-340.

[260] S. Wu, Y. Chen, W. Kang, X. Cai, L. Zhou, Hydrogen storage properties of MgTiVZrNb high-entropy alloy and its catalytic effect upon hydrogen storage in Mg, International Journal of Hydrogen Energy 50 (2024) 1113-1128.

[261] X. Xue, C. Ma, Y. Liu, H. Wang, Q. Chen, Impacts of Ce dopants on the hydrogen storage performance of Ti-Cr-V alloys, Journal of Alloys and Compounds 934 (2023).

[262] B. Cheng, Y. Li, X. Li, H. Ke, L. Wang, T. Cao, D. Wan, B. Wang, Y. Xue, Solid-State Hydrogen Storage Properties of Ti–V–Nb–Cr High-Entropy Alloys and the Associated Effects of Transitional Metals (M = Mn, Fe, Ni), Acta Metallurgica Sinica (English Letters) 36(7) (2022) 1113-1122.

[263] S. Dangwal, K. Edalati, High-entropy alloy TiV2ZrCrMnFeNi for hydrogen storage at room temperature with full reversibility and good activation, Scripta Materialia 238 (2024).

[264] L. Schlapbach, A. Züttel, Hydrogen-storage materials for mobile applications, Nature 414(6861) (2001) 353-358.

[265] A. Kumar, K. Shashikala, S. Banerjee, J. Nuwad, P. Das, C.G.S. Pillai, Effect of cycling on hydrogen storage properties of Ti2CrV alloy, International Journal of Hydrogen Energy 37(4) (2012) 3677-3682.

[266] A. Sarkar, A. Srinivasan, P.S. Robi, Processing and characterization of TiNbMoTaW refractory high entropy alloy by mechanical alloying, Advanced Powder Technology 34(12) (2023).

[267] H. Kalantari, M. Zandrahimi, M. Adeli, H. Ebrahimifar, The production of nanocrystalline AlCoCrFeNiTiZn high entropy alloy via mechanical alloying: Study of the formation mechanism, microstructural evolution, and magnetic properties of the alloy, Intermetallics 150 (2022).

[268] A. Kumar, M. Mucalo, L. Bolzoni, Y. Li, Y. Qu, F. Yang, Electronic structure tuning for enhanced oxygen evolution performance of a NiMnFeCr medium entropy alloy, International Journal of Hydrogen Energy 48(66) (2023) 25755-25769.

[269] W.H. Liu, Y. Wu, J.Y. He, T.G. Nieh, Z.P. Lu, Grain growth and the Hall–Petch relationship in a high-entropy FeCrNiCoMn alloy, Scripta Materialia 68(7) (2013) 526-529.

[270] M. Meng, H. Yang, X.G. Fan, S.L. Yan, A.M. Zhao, S. Zhu, On the modeling of diffusion-controlled growth of primary alpha in heat treatment of two-phase Ti-alloys, Journal of Alloys and Compounds 691 (2017) 67-80.

[271] K.K. Behera, K.G. Pradeep, S.R. Bakshi, Effect of High-Energy Ball Milling in Toluene on the Morphology, Phase Evolution, and Contamination for Some Elemental Powders, Metallurgical and Materials Transactions A 55(1) (2023) 303-319.

[272] Z. Yuan, C. Liu, X. Li, Y. Sui, Z. Han, T. Zhai, D. Feng, Y. Zhang, Effect of Ball Milling Time on Microstructure and Hydrogen Storage Properties of Nd5Mg41Ni Alloy, Acta Metallurgica Sinica (English Letters) 37(7) (2024) 1201-1214.

[273] L. Ruihan, H. Feng, W. Ran, X. Jianyi, X. Jin, H. Zhonghui, Z. Min, B. Junyu, Z. Yanghuan, Effect of ball-milling time on hydrogen storage properties of NdMg12-Ni alloy,

International Journal of Hydrogen Energy 98 (2025) 1262-1274.

[274] Z. Yuan, Y. Sui, Q. Yuan, Z. Qi, T. Zhai, X. Li, T. Li, Effects of ball milling time on the microstructure and hydrogen storage performances of Ti21.7Y0.3Fe16Mn3Cr alloy, International Journal of Hydrogen Energy 48(30) (2023) 11340-11351.

[275] H. Yuan, Y. An, G. Xu, C. Chen, Hydriding behavior of magnesium-based hydrogen storage alloy modified by mechanical ball-milling, Materials Chemistry and Physics 83(2-3) (2004) 340-344.

[276] Z. Yuan, X. Li, T. Li, T. Zhai, Y. Lin, D. Feng, Y. Zhang, Improved hydrogen storage performances of nanocrystalline RE5Mg41-type alloy synthesized by ball milling, Journal of Energy Storage 46 (2022).

[277] Y.T. Zhai, Y.M. Li, Z.C. Liu, L. Bolzoni, J. Kennedy, F. Yang, Hydrogen ab/desorption behavior of the mechanical alloyed Ti–V–Cr–Mn–Fe HEAs with varying Mn/Cr ratio, International Journal of Hydrogen Energy 109 (2025) 1008-1022.

[278] F.S. Yang, X.Y. Chen, Z. Wu, S.M. Wang, G.X. Wang, Z.X. Zhang, Y.Q. Wang, Experimental studies on the poisoning properties of a low-plateau hydrogen storage alloy LaNi 4.3 Al 0.7 against CO impurities, International Journal of Hydrogen Energy 42(25) (2017) 16225-16234.

[279] Y. Nakamura, J. Nakamura, K. Sakaki, K. Asano, E. Akiba, Hydrogenation properties of Ti–V–Mn alloys with a BCC structure containing high and low oxygen concentrations, Journal of Alloys and Compounds 509(5) (2011) 1841-1847.

[280] K. Xiao, J. Yang, X. Kong, L. Zhou, D. Luo, J. Song, Influence of oxygen on the hydrogen storage performance of Zr2Fe: Mechanism, diffusion pathway and DFT calculations, Journal of Alloys and Compounds 1009 (2024).

[281] L. Luo, C. Wu, S. Yang, J. Zhou, Y. Chen, F. Yang, Y. Xu, P. Liu, Decaying behaviors of V40(TiCr)51Fe8Mn hydrogen storage alloys with different particle sizes, Journal of Alloys and Compounds 645 (2015) S178-S183.

[282] M. Wei, Y. Liu, X. Xing, Z. Zhang, T. Liu, (TiVZrNb)83Cr17 high-entropy alloy as catalyst for hydrogen storage in MgH2, Chemical Engineering Journal 476 (2023).

[283] X. Liu, S. Wu, X. Cai, L. Zhou, Hydrogen storage behaviour of Cr- and Mn-doped Mg2Ni alloys fabricated via high-energy ball milling, International Journal of Hydrogen Energy 48(45) (2023) 17202-17215.

[284] J. Liu, J. Xu, S. Sleiman, F. Ravalison, W. Zhu, H. Liu, H. Cheng, J. Huot, Hydrogen storage properties of V0.3Ti0.3Cr0.25Mn0.1Nb0.05 high entropy alloy, International Journal of Hydrogen Energy 47(61) (2022) 25724-25732.

[285] J. Liu, J. Xu, S. Sleiman, X. Chen, S. Zhu, H. Cheng, J. Huot, Microstructure and hydrogen storage properties of Ti–V–Cr based BCC-type high entropy alloys, International Journal of Hydrogen Energy 46(56) (2021) 28709-28718.

[286] B.H. Silva, W.J. Botta, G. Zepon, Achieving room temperature hydrogen storage reversibility in Nb-rich alloys of the Nb-Cr-Mn system, Journal of Alloys and Compounds 1005 (2024).

[287] L. Hao, C. Yungui, Y. Yigang, W. Chaoling, T. Mingda, Cyclic properties of hydrogen absorption and desorption in V–Ti–Cr–Fe(Al,Si) alloy, Materials Science and Engineering: A 448(1) (2007) 128-134.

[288] K. Iwase, N. Terashita, K. Mori, S. Tsunokake, T. Ishigaki, Crystal structure and cyclic properties of hydrogen absorption–desorption in Pr2MgNi9, International Journal of Hydrogen Energy 37(23) (2012) 18095-18100.

[289] R.B. Strozi, M. Witman, V. Stavila, J. Cizek, K. Sakaki, H. Kim, O. Melikhova, L. Perriere, A. Machida, Y. Nakahira, G. Zepon, W.J. Botta, C. Zlotea, Elucidating Primary Degradation Mechanisms in High-Cycling-Capacity, Compositionally Tunable High-Entropy Hydrides, ACS Appl Mater Interfaces 15(32) (2023) 38412-38422.

[290] K. Sakaki, H. Araki, Y. Shirai, Recovery of Hydrogen Induced Defects and Thermal Desorption of Residual Hydrogen in LaNi₅, MATERIALS TRANSACTIONS 43(7) (2002) 1494-1497.